Long-Term Dynamics of High Mass Ratio Multiples

Long-term Dynamics of High Mass Ratio Multiples

A dissertation presented

by

Gongjie Li

to

The Department of Astronomy

in partial fulfillment of the requirements

for the degree of

Doctor of Philosophy

in the subject of

Astronomy & Astrophysics

Harvard University

Cambridge, Massachusetts

April 2015

Dissertation Advisor: Professor Avi Loeb Gongjie Li

Long-term Dynamics of High Mass Ratio Multiples

Abstract

This thesis presents a series of studies on the dynamics of high mass ratio multiples, with applications to planetary systems orbiting stars and stellar systems orbiting supermassive black holes (SMBHs).

Almost two thousand exoplanetary systems have recently been discovered, and their configurations gave rise to new puzzles related to planetary formation theories. We studied the dynamics of planetary systems aiming to understand how the configuration of planetary system is sculptured and to probe the origin of planetary systems. First, we discussed hierarchical three-body dynamics, which can be applied to planets that are orbiting a star while perturbed by a planet or a star that is farther away. The perturbation from the farther object can flip the planetary orbits and produce counter orbiting hot Jupiters, which cannot be formed in the framework of classical planetary formation theory. In addition, we have studied the stellar encounters with planetary systems in star clusters, which produce eccentric and inclined planets. Moreover, we investigated the obliquity variation of the Earth, and the developed formalism can be applied to exoplanetary systems. We note that the obliquity variation is important to the habitability of the exoplanets.

Long term dynamics is also central to understanding stellar systems orbiting SMBHs. SMBHs are common in the centers of galaxies and lead to rich dynamical interactions with nearby stars. At the same time, dynamical features of nearby stars

reveal important properties of SMBHs. The aforementioned hierarchical three-body dynamics can be applied to stars near SMBH binaries, which are natural consequences of galaxy mergers. We found that the distribution of stars surrounding one of the SMBHs results in the shape of a torus due to the perturbation from the other SMBH, and the dynamical interactions contribute to an enhancement of tidal disruption rates, which can help identify the SMBH binaries. In addition, we investigated the heating of stars near SMBHs, where the heating of stars due to gravitational waves as the SMBHs merge may mark the merger, and provide an electromagnetic counterpart for gravitational wave detection. Moreover, the accumulated tidal heating of stars may cause the stars to be more vulnerable for tidal disruptions, as the stars orbit around a SMBH in an eccentric orbit.

Contents

Abstract **iii**

Acknowledgments **x**

Dedication **xii**

1 Introduction **1**

1.1 Dynamics of Planetary Systems 2

1.1.1 Origin of Planetary Systems 5

1.1.2 Spin-axis Dynamics of Planets 9

1.2 Interactions between Stars and Supermassive Black Holes 11

1.2.1 Implications for Stars Surrounding Supermassive Black Hole Binaries 12

1.2.2 Heating of Stars Surrounding Supermassive Black Holes 13

Section I. Planets around Stars **15**

2 Eccentricity Growth and Orbit Flip in Near-coplanar Hierarchical Three-body Systems **16**

2.1 Introduction 17

2.2 Coplanar Flip 19

2.2.1 Analytical Derivation 22

2.3 Systematic Study of 180° Flips 27

2.4 Application to Exoplanets and Tidal Disruption Events 28
2.4.1 Counter Orbiting Hot Jupiters 28
2.4.2 Tidal Disruption Events - Systematic Study 32
2.5 Conclusion 35

3 Chaos in the Test Particle Eccentric Kozai-Lidov Mechanism 49
3.1 Introduction 50
3.2 Overview of the Eccentric Kozai-Lidov Mechanism in the Test-particle Limit 53
3.3 Surfaces of Section 56
3.4 The Maximum Eccentricity and the Flip Condition 61
3.5 Chaotic Regions 65
3.6 Conclusion 66
3.7 Acknowledgments 69
3.8 Appendix 69

4 The Dynamics of the Multi-planet System Orbiting Kepler-56 75
4.1 Introduction 76
4.2 The Obliquity Distribution Function 79
4.3 Obliquity and Inclination Evolution in the Presence of an Outer Perturber 82
4.3.1 Overview of the System Architecture 82
4.3.2 Dynamics of Kepler 56 83
4.3.3 Inferring the Inclination Distribution Function from Observations . 88
4.4 Tidal and Stellar Evolution 92
4.5 Discussion 98
4.6 Acknowledgments 100

5 Cross Sections for Planetary Systems Interacting with Passing Stars and Binaries 101

5.1 Introduction . . . 102
5.2 Formulation of the Problem . . . 105
5.3 Results for the Cross Sections . . . 110
5.4 Analysis and Scaling Laws . . . 135
5.5 The Solar Birth Aggregate . . . 157
5.6 Conclusion . . . 166
5.6.1 Summary of Results . . . 166
5.6.2 Discussion . . . 171

6 On the Spin-axis Dynamics of a Moonless Earth 176
6.1 Introduction . . . 177
6.2 A Simplified Perturbative Model . . . 179
6.2.1 Large Chaotic Regions: $0^\circ - 45^\circ$ & $65^\circ - 85^\circ$ . . . 180
6.2.2 Bridge Region: $45^\circ - 65^\circ$ . . . 185
6.3 Results . . . 187
6.3.1 Analytical Estimates . . . 187
6.3.2 Numerical Results . . . 190
6.4 Conclusion . . . 193
6.5 Acknowledgments . . . 195

References 196
6.6 Appendix . . . 200
6.6.1 Dynamics of the Unsimplified Hamiltonian . . . 200
6.6.2 Double Resonances and Triple Resonances . . . 201

7 Pre-LHB Evolution of the Earth's Obliquity 205
7.1 Introduction . . . 206
7.2 Spectral Analysis . . . 210

7.3 Numerical Integrations 214
7.4 Conclusion 215

Section II. Stars around Supermassive Black Holes 220

8 Implications of the Eccentric Kozai-Lidov Mechanism for Stars Surrounding Supermassive Black Hole Binaries 221

8.1 Introduction 222
8.2 Method 226
8.2.1 Comparison of Timescales 226
8.2.2 Equations of Motion 234
8.3 SMBH-binary System 238
8.4 SMBH-IMBH System 242
8.5 Conclusion 245

9 Accumulated Tidal Heating of Stars Over Multiple Pericenter Passages Near SgrA* 253

9.1 Introduction 254
9.2 Heating of Stars by Tidal Excitation of Modes 256
9.2.1 Mode Excitation and Interference in Multiple Pericenter Passages . 256
9.2.2 Tidal Heating of Stars 264
9.3 Results 267
9.4 Conclusion 271

10 Gravitational Wave Heating of Stars and Accretion Disks 281

10.1 Introduction 282
10.2 Method 284
10.3 Results 289
10.4 Discussion 294

References **297**

Acknowledgments

I would like to express the deepest appreciation to my advisor, Avi Loeb. He shared his passion in astrophysics with me, and his wise advises taught me how to be an astrophysicist. I am grateful that I have had the great honor to work with him for these years.

I am indebted to my close collaborators and mentors, Smadar Naoz, Konstantin Batygin, Bence Kocsis, Fred Adams, Josh Winn, Matt Holman, Charlie Conroy, Dimitrios Psaltis, John Johnson, Edo Berger, Jason Steffen, Francesca Valsecchi and Fred Rasio for inspiring conversations and helpful supports. In particular, Smadar Naoz and Konstantin Batygin have taught me important techniques in dynamics. This dissertation cannot be possible without them.

I would like to thank my committee members, Matt Holman, John Johnson, Mark Reid and Scott Tremaine for insightful feedbacks on my research projects. Their comments significantly improved this dissertation.

I would like to express my gratitude to Sterl Phinney and Nice Scoville, who introduced me to the world of astrophysics when I was an undergrad. In addition, I want to thank them for their continuing care and support.

It gives me great pleasure in acknowledging Peg Herlihy, Donna Adams, Robb Scholten, Nina Zonnevylle, Peg Hedstrom, Uma Mirani, Mark Palmer, members of CFhelp, CfA and ITC staff for their assistance and words of encouragement throughout these years. In addition, I thank all the past and current astronomy graduate students, post docs and my friends at Harvard for years of laughter, inspiration, and support.

Particularly, Widusha Illeperuma, Sumin Tang, Hyungsuk Tak, Hiro Yoshie, Carissa Kang, Hu Zhang, Xuening Bai, Yanfei Jiang, Peter Blanchard, Aaron Bray, Hope Chen, Pierre Christian, Eddie Chua, Ian Czekala, Marion Dierickx, Jason Dittmann, Courtney Dressing, Gregory Green, Meng Gu, Xinyi Guo, Kirit Karkare, Luke Zoltan Kelley, Tanmoy Laskar, Ryan Loomis, Ragnhild Lunnan, Maxwell Moe, Dylan Nelson, Elisabeth Newton, Ana-Maria Piso, Stephen Portillo, Sukrit Ranjan, Vicente Rodriguez-Gomez, Katherine Rosenfeld, Sarah Rugheimer, Laura Schaefer, Yutong Shan, Zachary Slepian, Joshua Suresh, Meng Su, Yuan-Sen Ting, Anjali Tripathi, Andrew Vanderburg, Xiawei Wang, Sarah Wellons, Lauren Woolsey, Li Zeng, Shangjun Zhang and Yucong Zhu.

Last but not least, I would like to express my immense gratitude to my parents, Xin Shao and Jiayu Li, and my husband Molei Tao for their unconditional love, endless patience and care.

To my dear family and friends. Thank you for all of your support along the way.

Chapter 1

Introduction

The study of dynamics can be dated back to the time of Newton, who studied the motion of objects and inquired fundamental questions, such as the stability of our Solar System due to the interaction of planets and comets. There are significant progresses in the studies of dynamics throughout the years, such as secular theories by Lagrange and Laplace, who provided a landmark description of the long-term (secular) dynamics of solar system, and later the foundations of chaos by Poincare, as he investigated three-body interactions. Many challenges, such as the great inequality of Jupiter and Saturn, have been solved along with the significant progresses in analytical studies. However, despite the important breakthroughs in dynamical studies, many of the questions still remain unanswered till today. For instance, some of them are due to the complex nature of chaotic systems (see a review in Laskar 2013).

It is possible to answer some of the fundamental questions today, such as the stability of our Solar System, thanks to the development in numerical algorithms and improvement in computational power. For example, one may simulate the chaotic

systems with high precision and predict the behavior of the chaotic system in a statistical sense by obtaining a large number of trajectories with similar initial conditions. In addition to the improvements in computation, solving dynamical problems is stimulated by interesting topics in astrophysics today, including probing the characteristics of planetary systems outside of our solar system (exoplanetary systems) and the properties of supermassive black holes.

In this thesis, I have utilized both analytical methods and numerical simulations to study the dynamics of high mass ratio multiples, which are prevalent in our universe. In particular, I have studied the dynamics of planetary systems (§1.1, section I: chapter 2-7) and stellar systems orbiting around supermassive black holes (§1.2, section II: chapter 8-10).

1.1 Dynamics of Planetary Systems

Since the first few exoplanet observed in the late 1980s to the early 1990s (Campbell et al. 1988; Latham et al. 1989; Wolszczan & Frail 1992; Mayor & Queloz 1995), 1890 confirmed exoplanets in 1189 planetary systems have been discovered today (as of Feb 20, 2015 shown in Figure 1.1, `http://exoplanet.eu/`). Occurrence studies of the explanatory systems suggest that on average there is one exoplanet per star (e.g., Dressing & Charbonneau 2013). Along with the exciting detections, theories of planetary formation have been confronted: massive planets have been detected to orbit their host star in the order of days (the so-called "hot-Jupiters", e.g., Mayor & Queloz 1995; Marcy et al. 1997), where they could not be formed (Rafikov 2006), and the planets may have eccentric orbits and/or orbit misaligned from the spin axis of the star (e.g., Hébrard

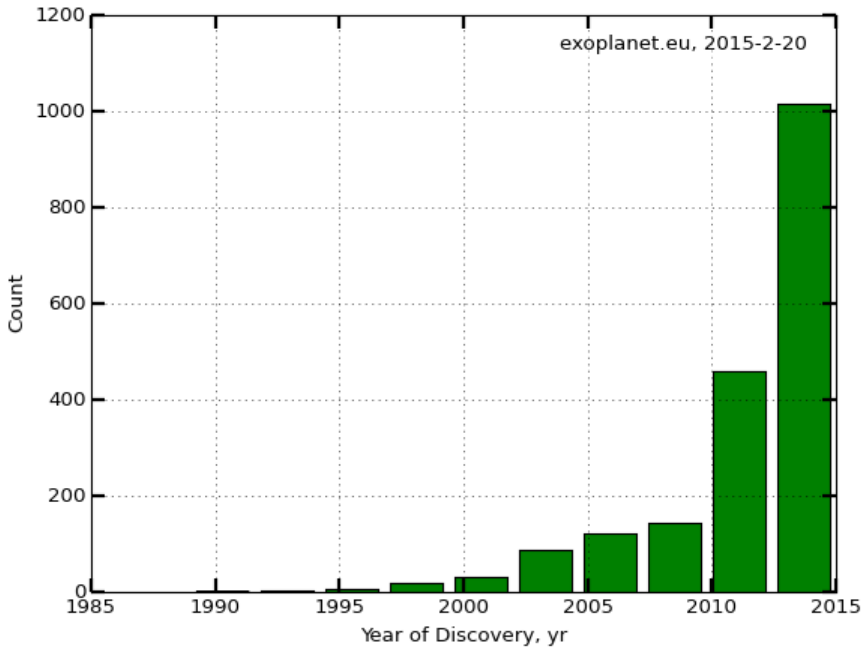

Figure 1.1: The number of exoplanets discovered v.s. year of discovery.

et al. 2008), contrary to the classical planetary formation theory. This wide diversity of the exoplanetary systems has given rise to numerous new puzzles that require theoretical explanations.

Many of these features can be explained by dynamical studies, which in turn improve our understanding on planetary formation. In particular, for solar system dynamics earlier on, the formation of eccentric orbits due to the hierarchical three-body interactions has been proven to be critical. For example, it may cause crashes of artificial satellites orbiting the Earth while perturbed by the Moon and can explain the asteroids orbiting the Sun in eccentric orbits while perturbed by Jupiter (Lidov 1962; Kozai 1962). Recently, further studies of this three-body interaction (the "Kozai-Lidov" mechanism) explain the origin of eccentric orbits for explanatory systems, such as 16 Cyg Bb and

HD80606 (Holman et al. 1997; Wu & Murray 2003) and the formation of retrograde hot Jupiters, which orbit in the opposite direction from the spin of the star (e.g., Naoz et al. 2011).

In addition to the origin of planetary systems, dynamics is important for the habitability of planets, and investigating the habitability of the detected planets can finally allow humankind to answer fundamental questions, such as whether we are alone in the universe. In the late 1950s, astronomers speculated the habitability of planets orbiting other stars (e.g., Huang 1959). The definition of habitability at that time varied from one author to another. Today, according to the definition by NASA, habitable zone refers to regions where liquid water can exist on the surface of an exoplanet. The size of the habitable zone for planets orbiting main sequence stars has been investigated in the literature (Kasting et al. 1993), and it has been recently found that there are 0.2-0.4 planets per M dwarf habitable zone (Bonfils et al. 2013; Dressing & Charbonneau 2015). However, the climate condition on the planets may still be unpleasant inside the habitable zone, since many other factors, such as dynamical instability may render the planets inhabitable. Thus, further studies on the dynamical stability of these planets, including the obliquity variation of the planets (e.g., Laskar & Robutel 1993; Li & Batygin 2014a), may put another constraint on the habitability of planetary systems (e.g., Spiegel et al. 2009).

1.1.1 Origin of Planetary Systems

Hierarchical Three-body Dynamics and Stellar Spin-orbit Misalignment

In this thesis, I studied the spin-orbit misalignment as a probe for the origin of planetary system. According to the classical planetary formation theory, the spin of the star should align with the orbit of the planets as the planetary system form in one molecular cloud, which has a preferred direction of rotation. In contrast with our own solar system, where the misalignment between the spin of the Sun and the planetary orbits is small ($\sim 7^\circ$), exoplanetary systems may exhibit large misalignments (e.g., Fabrycky & Winn 2009; Morton & Johnson 2011). To date, many mechanisms involving the dynamics of protoplanetary disks, perturbation of a farther object, oscillation modes of stars and tides have been proposed in the literature to explain the spin-orbit misalignment (e.g., Bate et al. 2010; Winn et al. 2010; Naoz et al. 2011; Batygin 2012; Albrecht et al. 2012; Dawson 2014; Fielding et al. 2014; Petrovich 2015), and it is likely that the observations show signatures of more than one mechanism (Li et al. 2014c). A coherent understanding of planetary system formation and evolution is essential, and contributes to estimating how unique our own solar system is in the universe.

In particular, hierarchical three-body system dynamics is one of the mechanisms that can explain the misalignment between the planets orbit and the spin of the star (e.g., Fabrycky & Tremaine 2007; Naoz et al. 2012; Li et al. 2014a). The configuration is shown in Figure 1.2, and this kind of configuration is common in the universe as a result of their inherent stability. The dynamics of a hierarchical three-body system is complex. For instance, it has been found in the literature that when the mutual inclination between an inner binary and the perturber is above $\sim 40^\circ$, the inner binary's

orbit undergoes large amplitude oscillations in eccentricity and inclination (Kozai 1962; Lidov 1962), and may flip across 90° if the perturbers orbit is non-circular, or when none of the components in the close binary is a test particle (e.g., Naoz et al. 2011; Katz et al. 2011; Lithwick & Naoz 2011; Naoz & Fabrycky 2014).

The hierarchical three-body interaction can explain many astrophysical phenomena. For stellar systems, some of the binary stars are at separations closer than the minimum separation they can be formed, so there is a need for a mechanism to bring the two stars closer to each other after they are formed. The eccentricity of the inner orbit can be enhanced through the hierarchical three-body interaction, and the distance between the two objects at pericenter can be reduced. Thus, the two stars can be brought closer due to the perturbation from an outer companion, and this interaction helps explain the formation of short period binaries (e.g., Ford et al. 2000; Fabrycky & Tremaine 2007; Shappee & Thompson 2013).

In addition, this mechanism can help explain the origin of blue stragglers and type Ia supernovae. Blue stragglers are stars that are hotter and bluer than the main sequence stars in a cluster. They can be formed through collisions. However, the collision rates are too low to explain the origin of the blue stragglers. Since the two stars can be brought closer and have the potential to collide with each other via the hierarchical three-body interaction, this interaction can enhance the collision rate and help explain the origin of blue stragglers (e.g., Perets & Fabrycky 2009; Naoz & Fabrycky 2014). Similarly, one of the ways to produce type Ia supernovae is through collisions of two white dwarfs. This interaction can enhance the collision rate and help produce type Ia supernovae (e.g., Katz & Dong 2012).

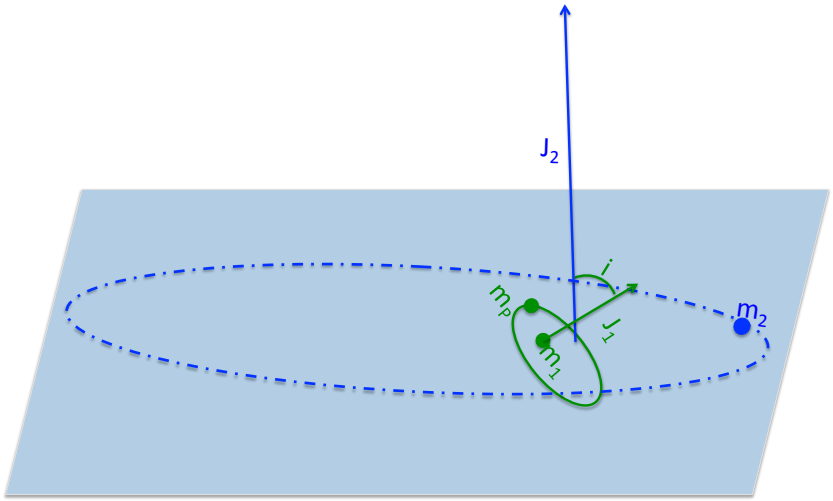

Figure 1.2: The configuration of a hierarchical three-body system. m_1 and m_p form the inner binary, and m_2 is the outer perturber.

For binary black holes of high eccentricity, the merger timescale of the binary black holes can be significantly reduced. Thus, this interaction can enhance the black hole merger rate, as it excites the eccentricity of the binary black holes (e.g., Blaes et al. 2002; Bode & Wegg 2013). Moreover, stars can be brought closer to a supermassive black hole and be tidally disrupted through hierarchical three-body interactions. This has the potential to enhance the tidal disruption rates of stars near SMBH binaries (Ivanov et al. 2005; Chen et al. 2011; Wegg & Bode 2011).

In this thesis, we investigate the hierarchical three-body dynamics, and we have found a new mechanism that allows the orbit to flip from an almost co-planar configuration by $\sim 180°$, and to increase its eccentricity to $\sim 1 - 10^{-6}$ during the flip

(Li et al. 2014a). This increases the parameter space for the interesting phenomena. In addition, assuming one of the objects in the close binary is massless, the system can be reduced to be one degree of freedom, and the flip timescale and the flip criteria can be derived analytically. Moreover, we have analyzed the parameter space for the hierarchical three-body dynamics in the test particle limit, and identified the underlying resonances for the flip (Li et al. 2014b).

For planetary systems in three-body hierarchical configuration, the close binary is composed of a host star and an exoplanet, which is perturbed by an outer planet or an outer star. The planets orbit may flip according to the hierarchical three body dynamics. As the spin axis of the star is not affected, this mechanism will change the spin orbit misalignment. Meanwhile, the eccentricity of the close binary increases during the flip, and this reduces the distance between the planet and the star at the pericenter to allow tides to operate. Specifically, tides will circularize the orbit and shrink the orbit, halting the eccentricity and inclination oscillations. This way, an exoplanet with a spin-orbit misalignment can be produced. If the planet starts in a coplanar configuration with the perturbing object, we found that the planetary orbit may flip by $\sim 180^\circ$ and form a counter orbiting hot Jupiter (Li et al. 2014a).

The variation of the stellar spin-orbit misalignment due to planetary orbital precession caused by planetary interaction is also important in explaining the observed spin-orbit misalignment. In particular, we have studied the exoplanetary system, Kepler-56, which is a multi-planet system containing an outer planet and two coplanar inner planets that are in orbits misaligned with respect to the spin axis of the host star (Li et al. 2014c). We constrained the distribution of the mutual inclination between the inner two planets and the outer planet using the observed misalignment between the

stellar spin and the inner planetary orbits, and requiring the system to be dynamical stable. Moreover, we discussed this distribution as a function of the initial stellar spin variation. As a side note, we investigated the future evolution of this system and found the inner two planets will be engulfed in ~ 129 Myr and ~ 155 Myr. This is the first exoplanetary system observed where two of its planets are going to be engulfed.

Scattering Encounter in Clusters

Scattering encounters play important roles in determining the final orbital distributions of planets, since most stars and planetary systems form in clusters surrounded by a large number of neighboring stars (e.g., Heggie & Rasio 1996; Adams & Laughlin 2001; Spurzem et al. 2009). For instance, our solar system likely formed in a large stellar group, since there are large amount of short-lived radioactive species present during the formation of the solar system, inferred from meteoritic measurements. However, in a crowded cluster, the solar system can be disrupted. To constrain the birth environment of the solar system, we've calculated the averaged cross section for the disruption of solar system using N-body simulations (Li & Adams 2015). In addition, we've also obtained the expression of the disruption cross section as a function of the planetary system properties, such as the planet-star distance and the mass of the star, which can be applied to exoplanetary systems in general.

1.1.2 Spin-axis Dynamics of Planets

The habitability of an exoplanet depends on various conditions, where the planets orbital configuration and spin-axis dynamics plays a significant role (e.g., Spiegel et al. 2009).

In particular, the obliquity variation of planets is important because it determines the latitudinal distribution of the stellar radiation received on the planet. This has been studied extensively for objects in our Solar System (e.g., Laskar et al. 1993; Touma & Wisdom 1993). For instance, Earth's obliquity (the angle between Earths spin axis and its orbit) is stabilized by the Moon and would undergo chaotic variations and reach ~ 80 degrees in the Moon's absence (Laskar & Robutel 1993). However, according to the recent numerical simulations, without the Moon, the obliquity of the Earth stays low ($\lesssim 40$ degrees) over $\sim$Gyr timescales (Lissauer et al. 2012). Accordingly, in (Li & Batygin 2014a), we re-examined the spin-axis evolution of a Moonless Earth within the context of a simplified perturbative framework, and found the chaotic diffusion timescale to be as long as 6 billion years when the obliquity is between $\sim 40 - 60$ degrees. This demonstrated that even in the absence of the Moon, the stochastic change in Earth's obliquity is sufficiently slow to not preclude long-term habitability.

As an extension, we studied the past variation of the Earths obliquity and found that the Earth obtained its current obliquity during the formation of the Moon (Li & Batygin 2014b). It is likely that the architecture of the Solar System underwent a dynamical instability-driven transformation, where the primordial configuration was more compact (e.g., Tsiganis et al. 2005; Morbidelli et al. 2005; Gomes et al. 2005). Thus, the perturbation of the Earths obliquity due to the other planets can be different, potentially allowing for large amplitude variation in the Earths obliquity. Our calculations suggest that the system avoided resonant encounters throughout its evolution, indicating that the Earths obliquity was stable since the formation of the Moon.

1.2 Interactions between Stars and Supermassive Black Holes

SMBHs are common in the center of galaxies, and the features of the SMBH are correlated with the properties of the host galaxy (e.g., the well-known $M - \sigma$ relation) (Ferrarese & Merritt 2000; Gebhardt et al. 2000; Tremaine et al. 2002). In addition to the host galaxy as a whole, the SMBHs affect stars surrounding them. The existence of the SMBH can explain puzzling phenomena, such as the origin of hypervelocity stars in the center of our galaxy, which can be produced during a close encounter between the SMBH and a stellar binary, where one of the stars gets captured by the SMBH and the other star gets ejected with extremely high velocity (e.g., Hills 1988; Yu & Tremaine 2003; Brown et al. 2005). On the other hand, the properties of the stars reveal valuable information about the SMBHs. For instance, the mass of the SMBH can be measured from the stellar orbits (for Sgr A*) or the collective dynamics of nearby stars (e.g., Valluri et al. 2004; Ferrarese & Ford 2005; Ghez et al. 2008; Genzel et al. 2010), and the mass function of the SMBHs can be estimated from tidal disruption rate of stars (Stone & Metzger 2014). In this thesis, I have focused on the distribution of stars surrounding SMBH binaries due to hierarchical three-body interactions, and the heating of stars surrounding SMBHs.

1.2.1 Implications for Stars Surrounding Supermassive Black Hole Binaries

SMBH binaries (SMBHB) are natural consequences of galaxy mergers, since SMBHs are common in the center of galaxies. Spatially-resolved active galactic nuclei have been observed (Komossa et al. 2003; Bianchi et al. 2008; Green et al. 2010; Koss et al. 2011; Fabbiano et al. 2011) (an example is shown in Figure 1.3). In addition, spectroscopic surveys (Comerford et al. 2009; Smith et al. 2010; Liu et al. 2010b) and observations that combine ground-based imaging show numerous systems containing compelling SMBHB candidates with pc to kpc separations (Rodriguez et al. 2006; Liu et al. 2010a; Shen et al. 2011; Fu et al. 2011; McGurk et al. 2011). At sub-parsec distance, it is very difficult to detect the SMBHB observationally, yet one may identify the SMBHB from the dynamical interactions between the SMBHB and the stars. For example, it has been found that the dynamical interactions between the SMBHB and the stars may increase the rate of tidal disruption events (e.g., Ivanov et al. 2005; Chen et al. 2011; Wegg & Bode 2011). The tidal disruption events provide a viable way to probe the dormant SMBH.

Stars, which orbit one of the SMBHs and are perturbed by the other SMBH, reside in a hierarchical three-body configuration. For stars surrounding SMBHB, the aforementioned hierarchical three-body interactions can affect the distribution of stars surrounding a supermassive black hole binary (SMBHB). To characterize the parameter space where the eccentricity can be excited, we systematically studied the number of stars vulnerable to tidal disruption for a wide range of SMBHB configurations (Li et al. 2015). We found that the the eccentricity increase is stronger for stars orbiting the less massive SMBH. Moreover, as it is more effective when the mutual inclination between

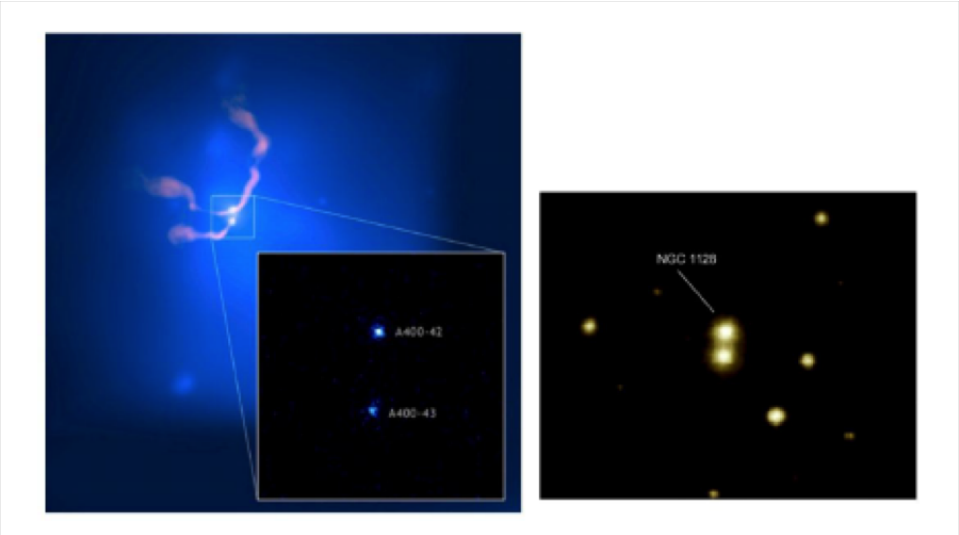

Figure 1.3: An example of SMBH binary in galaxy cluster Abel 400 (figure 1 in Colpi & Dotti (2011)).

the planets orbit and the orbit of the SMBHB is high ($\sim 40 - 140$ degrees), stars with high mutual inclination are more likely to be disrupted and this will cause the final survived stars to distribute in the shape of a torus.

1.2.2 Heating of Stars Surrounding Supermassive Black Holes

As mentioned above, SMBHBs have been observed and are natural consequences of the mergers of galaxies. The SMBHBs may merge and produce gravitational waves (GWs), which are ripples in space time, predicted by General Relativity. GWs generally determine sky positions only to the order of degrees. To better identify the source of the GWs and to interpret the GW data, one needs the electromagnetic (EM) counter part of GW, which can determining the host galaxy redshift and the environment of the sources (Kocsis et al. 2006; Phinney 2009). A large variety of EM signatures have been proposed

to accompany the coalescence of SMBHBs (e.g., Schnittman 2011; Haiman et al. 2009). For instance, the recoil of the black hole remnant changes the tidal disruption rate of stars due to the refilling of the loss cone as the black hole remnant wanders (Stone & Loeb 2011a, 2012; Li et al. 2012), and we studied the dissipation of the GW energy in stars during the merger of the SMBHs, and the consequent heating of the stars(Li, Kocsis & Loeb 2012).

In addition to GW heating, stars can be tidally heated as they orbit close to SMBHs. For instance, many stars exist in the Galactic Center of our own Milky Way and orbit the supermassive black hole, SgrA*, in eccentric orbits (Genzel et al. 2010). For the stars close to SgrA*, the modes inside the star can be tidally excited every time it passes the pericenter of the orbit, and the dissipated heat from the excited modes are accumulated over many passages. Li & Loeb (2013) calculated the coupling of the stellar modes with their orbits, and showed that the gravitational interaction with background stars leads to a linear growth of the tidal excitation energy with the number of pericentre passages near SgrA*. Using both analytical estimation and numerical simulation with stellar evolution code MESA, we found that the accumulated heat deposited by excitation of modes can lead to a runaway disruption of the star at a pericentre distance that is four to five times farther than the standard tidal disruption radius. The accumulated heating may explain the lack of massive ($\gtrsim 10M_{\odot}$) S-stars closer than several tens of AU from SgrA*.

Section I. Planets around Stars

Chapter 2

Eccentricity Growth and Orbit Flip in Near-coplanar Hierarchical Three-body Systems

This thesis chapter originally appeared in the literature as

Li, G., Naoz, S., Kocsis, B. & Loeb, A. Eccentricity Growth and Orbit Flip in Near-coplanar Hierarchical Three-body Systems, *The Astrophysical Journal*, 785, 116, 2014

It is presented here with minor modifications.

Abstract

The dynamical evolution of a hierarchical three body system is well characterized by the eccentric Kozai-Lidov mechanism, where the inner orbit can undergo large eccentricity

and inclination oscillations. It was shown before that starting with a circular inner orbit, large mutual inclination ($40^\circ - 140^\circ$) can produce long timescale modulations that drives the eccentricity to extremely large value and can flip the orbit. Here, we demonstrate that starting with an almost coplanar configuration, for eccentric inner and outer orbits, the eccentricity of the inner orbit can still be excited to high values, and the orbit can flip by $\sim 180^\circ$, rolling over its major axis. The $\sim 180^\circ$ flip criterion and the flip timescale are described by simple analytic expressions that depend on the initial orbital parameters. With tidal dissipation, this mechanism can produce counter-orbiting exo-planetary systems. In addition, we also show that this mechanism has the potential to enhance the tidal disruption or collision rates for different systems.

2.1 Introduction

The Kozai-Lidov mechanism (Kozai 1962; Lidov 1962) has proven very useful for interpreting different astrophysical systems. For example, it has been shown that its application can explain Hot Jupiters configurations and obliquity (e.g. Holman et al. 1997; Wu & Murray 2003; Fabrycky & Tremaine 2007; Veras & Ford 2010; Correia et al. 2011; Naoz et al. 2011, 2012). Furthermore, close stellar binaries with two compact objects are likely produced through triple evolution, and secular effects may play key role in these systems and in their remnants (e.g. Harrington 1969; Mazeh & Shaham 1979; Soderhjelm 1982; Kiseleva et al. 1998; Ford et al. 2000; Eggleton & Kiseleva-Eggleton 2001; Fabrycky & Tremaine 2007; Perets & Fabrycky 2009; Thompson 2011; Katz & Dong 2012; Shappee & Thompson 2013; Naoz et al. 2013a; Naoz & Fabrycky in prep.). Secular effects have been proposed as an important element both in the growth of black

holes at the centre of dense star clusters and the formation of short-period binaries black hole (Blaes et al. 2002; Miller & Hamilton 2002; Wen 2003) and tidal disruption events (Chen et al. 2009, 2011; Wegg & Bode 2011; Bode & Wegg 2013).

The Kozai-Lidov mechanism was first discussed by Kozai (1962) and Lidov (1962), who applied the mechanism for specific configurations where the outer orbit was circular and one of the members inner binary was a test (massless) particle. In this situation, the component of the inner orbit's angular momentum projected on the total angular momentum of the whole system (z axis) is conserved. To lowest order, the quadrupole approximation provides a valid presentation of the system (Lidov & Ziglin 1974). In that case, the system is integrable and the eccentricity and the inclination undergo large oscillations when $i > 39.2$ degree due to the "Kozai resonance" (Thomas & Morbidelli 1996).

Recently, Naoz et al. (2011, 2012) showed that relaxing either one of these assumptions, (i.e., an eccentric outer orbit, or non-negligible mass binary members) leads to qualitatively different behavior. In this case the z-component of the inner, and outer orbit's angular momentum is not conserved. Considering systems beyond the test particle approximation, or a circular orbit, requires the octupole–level of approximation (Harrington 1968, 1969; Ford et al. 2000; Blaes et al. 2002).

The octupole approximation can lead to extremely large values for the inner orbit's eccentricity (Ford et al. 2000; Naoz et al. 2013a; Teyssandier et al. 2013). Furthermore, the inner orbit's inclination can flip its orientation from prograde to retrograde, with respect to the total angular momentum (Naoz et al. 2011, 2013a). We refer to this process as the *eccentric Kozai–Lidov* (EKL) mechanism. It has been shown in Naoz et al.

(2013a) that the secular approximation can be used as a tool for understanding different astrophysical settings, from massive or stellar compact objects to planetary systems.

We focus on the octupole order when the inclination is set to be almost coplanar. Lee & Peale (2003) considered the case when the mutual inclination is zero, and they showed that the eccentricity can oscillate due to the octupole effects. Here we set the mutual inclination to be non-zero but still very small. We show both numerically and analytically, that an eccentric inner orbit ($e_1 > 0.6$) in almost coplanar configuration with an eccentric outer orbit becomes highly eccentric ($e_1 \gtrsim 0.9999$) due to the octupole effects. Provided that it avoids a direct collision with or tidal disruption by the central object, it undergoes a $\sim 180^\circ$ flip. We apply this mechanism to the retrograde hot jupiters and discuss its application to tidal disruptions.

The paper is organized as follows. In §2, we demonstrate the coplanar flip, and derive the analytical expression for the flip criterion and timescale. In §3, we start the system with a large range of parameter space to study the flip criterion and timescale. Finally, in §4, we discuss the applications of the coplanar flip to exo-planetary systems and tidal disruption events.

2.2 Coplanar Flip

The Kozai-Lidov mechanism relates to the hierarchical three-body system as shown in Figure 2.1. The parameter ϵ,

$$\epsilon = \frac{a_1}{a_2}\frac{e_2}{1-e_2^2}, \tag{2.1}$$

is small, where a is the semi-major axis and e is the eccentricity of the inner "1" and outer "2" orbit (Naoz et al. 2013a).

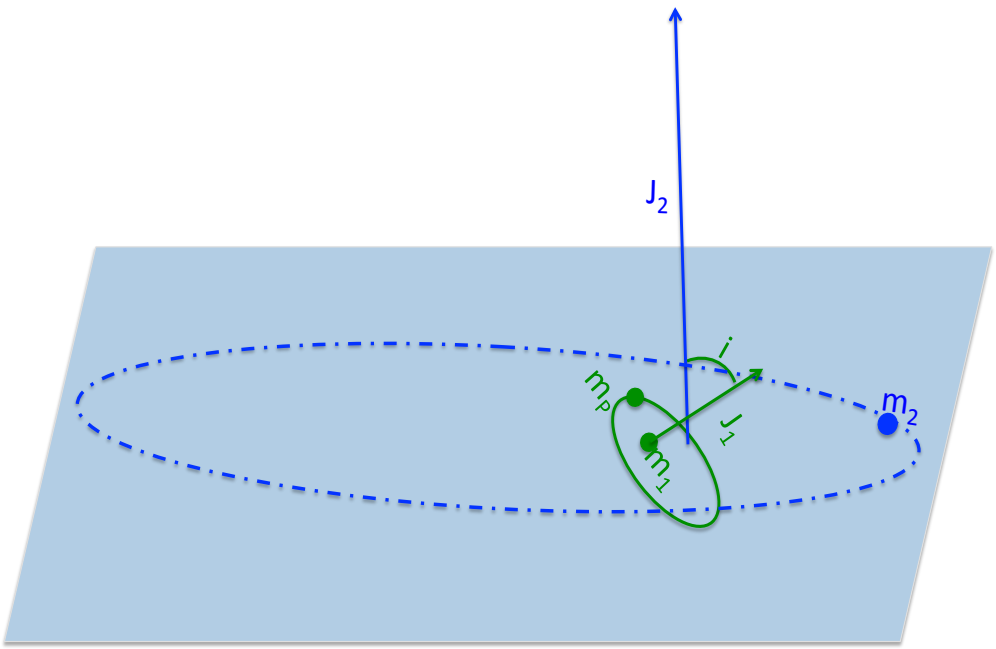

Figure 2.1: *Configuration of the hierarchical 3-body system.* An object m_P orbits around the object m_1 and forms an inner binary. The outer binary is composed of the outqer object m_2 orbiting the center mass of m_1 and m_P. The parameters of the inner and outer binary are denoted by subscripts 1 and 2, respectively. The angle i represents the mutual inclination between the two orbits, and J_1 and J_2 represent the orbital angular momenta of the inner and outer binary. The coolanar case corresponds to $i \sim 0$.

In the test particle quadrupole approximation ($m_P \to 0$, $e_2 = 0$), the Kozai-Lidov resonance is between the longitude of periapsis and the longitude of ascending node of the inner orbit (Kozai 1962). The eccentricity and the inclination oscillate with large

amplitudes when the inclination is over 40 degree. This resonance also exists if the test particle mass is significant. The quadrupole approximation describes the orbital evolution when the outer orbit is circular. When the outer orbit is non-circular, the octupole approximation is needed, inducing variations in eccentricity and inclination on longer timescales, and causes excursions to even higher eccentricities and inclinations above 90° (Naoz et al. 2011, 2013a). However, starting with a circular inner orbit, the inclinations that produce this behavior are restricted to the range of $\sim 40^\circ - 140^\circ$.

Starting with an almost coplanar configuration ($e_1 = 0.8$, $i = 5^\circ$), we find that the inner orbit can still flip if it starts eccentric (the high eccentricity low inclination case: hereafter HeLi). We show the flip in Figure 2.2 using direct N-body integrations, with the MERCURY software package (Chambers97). The remarkable agreement with the integration using the secular approximation up to the octupole order is also shown in Figure 2.2.

The flip in the HeLi case is qualitatively different from the low eccentricity high inclination case (LeHi case, see Figure 2.3 upper panel). Specifically, in the initially coplanar case, the oscillation amplitude of the inclination is small maintaining a coplanar configuration before the flip, as the eccentricity grows monotonically to large values. The timescale for the inclination to cross over 90° (namely the flip timescale) is much shorter. Moreover, the underlying resonances responsible for the flips are different (Li et al. in prep.). The HeLi case is dominated by only octupole order resonances. However, the LeHi case is dominated by both the quadrupole order resonances and the octupole order resonances. As a comparison, we illustrate the difference in the HeLi case in the right panel of Figure 2.3.

To illustrate the orbital evolutions, we show the movies[1] of the inner orbital evolution in the test-particle limit for both cases. We set the z axis to be aligned with the total angular momentum and the x axis is aligned with the ascending node of the outer orbit. In the test particle limit, the outer orbit is stationary. In the movies, the inner orbit is painted according to the value of the mean anomaly. The black arrow represents the normalized orbital angular momentum, and the pink arrow represents the z component of the angular momentum. The orbital flip can be observed in the rapid reorientation of the pink arrow from the $+z$ to the z direction. The black arrow shows the orientation of the orbit. The orbit rolls over its major axis when it flips. This can be understood analytically as dJ_1/dt is perpendicular to the eccentricity vector at $i = 90°$.

2.2.1 Analytical Derivation

The coplanar flip phenomenon can be understood analytically in the test particle approximation (i.e, $m_P \to 0$). In the large inclination regime, it was shown that the behavior associated with the test particle approximation is valid for $m_2/m_P > 7$ (Teyssandier et al. 2013).

This test particle approximation in hierarchical 3-body systems was studied extensively in the past (Lithwick & Naoz 2011; Katz et al. 2011), but only in the regime of large inclinations between the inner and outer orbit's (and for small initial inner eccentricity $e_1 < 0.5$ Lithwick & Naoz 2011). Our initial coplanar configuration simplifies the analytic treatment. The $\sim 180°$ flip occurs due to octupole-level terms, whose

[1] `https://www.cfa.harvard.edu/~gli/images/lowi.mp4`; `https://www.cfa.harvard.edu/~gli/images/lowi.mp4`

importance can be estimated via ϵ.

We follow the equation of motion using a Hamiltonian description for the non-relativistic hierarchical three body problem. We define the energy function as the negative of the Hamiltonian in the secular approximation up to the octupole level (Lithwick & Naoz 2011). The Hamiltonian of such systems is well documented in the literature (e.g. Harrington (1968, 1969); Ford et al. (2000)). The scaled energy function for the hierarchical three-body system in the test particle approximation to this order is $F_{quad} + \epsilon F_{oct}$, where

$$\begin{aligned} F_{quad} &= -(e_1^2/2) + \theta^2 + 3/2 e_1^2\theta^2 \\ &\quad + 5/2 e_1^2(1-\theta^2)\cos(2\omega_1), \end{aligned} \tag{2.2}$$

$$\begin{aligned} F_{oct} &= \frac{5}{16}(e_1 + (3e_1^3)/4) \\ &\quad \times ((1 - 11\theta - 5\theta^2 + 15\theta^3)\cos(\omega_1 - \Omega_1) \\ &\quad + (1 + 11\theta - 5\theta^2 - 15\theta^3)\cos(\omega_1 + \Omega_1)) \\ &\quad - \frac{175}{64} e_1^3((1 - \theta - \theta^2 + \theta^3)\cos(3\omega_1 - \Omega_1) \\ &\quad + (1 + \theta - \theta^2 - \theta^3)\cos(3\omega_1 + \Omega_1)). \end{aligned} \tag{2.3}$$

To the first order in i, the evolution of e_1 and $\varpi_1 = \omega_1 + \Omega_1$ can be solved (we denote $\varpi_1 = \omega_1 + \Omega_1$ hereafter). Specifically, $\dot{e_1}$ and $\dot{\varpi}_1$ depend only on e_1 and ϖ_1:

$$\dot{e_1} = \frac{5}{8} J_1(3J_1^2 - 7)\epsilon \sin(\varpi_1), \tag{2.4}$$

$$\dot{\varpi}_1 = J_1\Big(2 + \frac{5(9J_1^2 - 13)\epsilon\cos(\varpi_1)}{\sqrt{1 - J_1^2}}\Big), \tag{2.5}$$

where $J_1 = \sqrt{1 - e_1^2}$. Combining the two differential equations, we can express $\cos\varpi_1$ as

a function of e_1:

$$\cos \varpi_1 = \frac{8e_1^2 - C}{e_1(20 + 15e_1^2)\epsilon}, \tag{2.6}$$

where C is an integration constant, which is the energy that corresponds to $i = 0$ and can be determined from the initial condition. Substituting $\cos(\varpi_1)$ in the differential equation of $\dot{e_1}$, we obtain a separable first order differential equation:

$$\dot{e_1} = -\frac{5}{8}(4 + 3e_1^2)\sqrt{(1 - e_1^2)\Big(1 - \frac{(C - 8e_1^2)^2}{25e_1^2(4 + e3_1^2)^2\epsilon^2}\Big)\epsilon}. \tag{2.7}$$

Integrating equation (2.7), we get e_1 as a function of time.

Figure 2.3 shows that the eccentricity increases steadily and the inclination oscillates in the low inclination scenario until the flip occurs. This behavior can also be seen in Figure 2.4. The steady change of e_1 can be explained by equation (2.4). Since

$$\frac{5}{8}J_1(3J_1^2 - 7)\epsilon < 0 (0 < J_1 < 1), \tag{2.8}$$

the sign of $\dot{e_1}$ depends on $\sin(\varpi_1)$, and e_1 reaches its extremum when $\sin(\varpi_1) = 0$. In addition, since ϖ_1 vanishes to the quadrupole order, the change of ϖ_1 is small. Thus, e_1 does not oscillate over the quadrupole timescale. Instead, e_1 increases or decreases monotonically to e_{min} or e_{max}.

Using the conservation of $F_{quad} + \epsilon F_{oct}$, we can estimate the evolution of the inner orbit in the low inclination case by calculating the constant energy curve in Figure 2.4 (pink dashed line). The total energy $F_{quad} + \epsilon F_{oct}$ depends on the four variables: e_1, i, ω_1 and Ω_1. To obtain the maximum inclination, i_{max} as a function of e_1 as shown in Figure 2.4, we need to express ω_1 and Ω_1 as a function of e_1 at $i = i_{max}$. From the equation of motion, $\dot{i} \propto \sin(2\omega_1)$, thus the maximum of inclination occurs at $\omega_1 = 0$. When $\omega_1 = 0$,

$\cos\varpi = \cos\Omega$, thus, substituting equation 2.6 in the conservation of $F_{quad} + \epsilon F_{oct}$, we get i_{max} as a function of e_1. The analytic expression is compared with the numerical trajectory in Figure 2.4, where the evolution of e_1 and i are obtained by integrating the equations of motion in the secular approximation.

Moreover, Figure 2.4 shows another major difference between the LeHi behavior and the HeLi case studied here. For the LeHi case, energy conservation of the quadrupole approximation, F_{quad}, can be used to find the maximum eccentricity and the minimum inclination. However, the octupole correction is non-negligible in the HeLi case.

The flip time can be estimated using equation (2.7). Since $\sin\varpi_1 < 1$, e_1 increases steadily before the flip, the flip time scale can be estimated as:

$$t_{flip} = \int_{e_{min}}^{e_{max}} \dot{e_1}^{-1}\, de\ . \tag{2.9}$$

.

The initial conditions of this configuration are $i \sim 0$, $e_{1,0} \to 1$, where the subscript "0" represents the initial condition. Since e_1 increases monotonically until the flip, we set the minimum eccentricity to be the initial eccentricity, i.e., $e_{min} = e_{1,0}$. Furthermore, the maximum eccentricity is simply $e_{max} = 1$.

On the other hand, when $\sin(\varpi) > 1$, e_1 decreases first before it increases. Since the flip always occurs at the maximum eccentricity, the flip time is simply:

$$t_{flip} = \int_{e_0}^{e_{min}} \dot{e_1}^{-1}\, de + \int_{e_{min}}^{e_{max}} \dot{e_1}^{-1}\, de\ . \tag{2.10}$$

We calculate e_{min} with equation (2.6) by setting $\cos(\varpi) = 1$ and estimate the flip time. As shown in Figure 2.5 the analytical flipping time, t_{flip}, agrees well with the numerical results.

It is straightforward now to derive the flip condition. Rearranging equation (2.6), we find

$$\epsilon \cos(\varpi_1) = \frac{8e_1^2 - C}{e_1(20 + 15e_1^2)} \ , \tag{2.11}$$

where C is the integration constant (energy at $i = 0$) introduced in equation (2.6). The difference on left hand side between the initial time and the flip time bound by $\epsilon(1 - \cos(\varpi_1))$. When the orbit flips, $e_1 \to 1$ and the difference on the right hand side is

$$\frac{8 - C}{35} - \frac{8e_1^2 - C}{e_1(20 + 15e_1^2)} \ . \tag{2.12}$$

Thus, a flip will happen when the following condition holds:

$$\epsilon(1 - \cos(\varpi_1)) > \frac{8 - C}{35} - \frac{8e_1^2 - C}{e_1(20 + 15e_1^2)} \ . \tag{2.13}$$

Substituting C from the initial condition, we obtain the flip criterion:

$$\epsilon > \frac{8}{5} \frac{1 - e_1^2}{7 - e_1(4 + 3e_1^2)\cos(\omega_1 + \Omega_1)} \ . \tag{2.14}$$

Figure 2.5 compares the analytical and the numerical results. The left panel focuses on the flip criterion, whereas the black line represents the analytical criterion, the green plus symbols represent the numerical runs that do not flip in $10^4 t_{Kozai}$, and the blue cross symbols represent the numerical runs that flip. The timescale t_{Kozai} is defined as:

$$t_{Kozai} = \frac{m_1}{m_2}\left(\frac{a_2}{a_1}\right)^3 (1 - e_2^2)^{3/2}(1 - e_1^2)^{1/2} P_{in}, \tag{2.15}$$

where P_{in} is the period of the inner orbit. We start the runs for different eccentricities and inclinations. The analytical criterion agrees well with the numerical results. In the right panel of Figure 2.5, we compare the flip timescale for three arbitrarily chosen eccentricities. The analytical results also agree well with the numerical results.

2.3 Systematic Study of 180° Flips

We explored the entire e_1 and i_0 parameters space that can produce flips. We scanned systematically the parameter space of the initial conditions e_1, i and a_2 and integrate for the secular evolution of the inner orbit in the test-particle limit. For systems that flipped within 1000 t_{Kozai} we recorded the time when the flip happens, where t_{Kozai} is defined in equation (2.15).

At low eccentricity, the critical inclination (above which the orbit flips) increases. This is consistent with the flip condition of the HiLe mechanism (Lithwick & Naoz 2011; Katz et al. 2011), where here we have extended Figure 8 of Lithwick & Naoz (2011) to larger initial e_1. However, unlike Lithwick & Naoz (2011) that scan the $e_1(\omega = 0)$ (i.e., the minimal eccentricity) and $i(\omega = 0)$, we determine the initial conditions that will lead to a flip. For the HeLi case, the result is also consistent with the analytical flip condition described in the §2. At moderate eccentricity, the behavior of the inner orbit is more complicated, and cannot be easily decried analytically. Figure 2.6 depicts the numerical results of the systematic exploration of the parameter space. The left panel of Figure 2.6 shows the flip condition for different initial inclinations and eccentricities, as a function of different ϵ. Not surprisingly, stronger perturbations (i.e., larger ϵ) can cause flips in larger regions of the parameter space. Consistent with Lithwick & Naoz (2011), we also find that the intermediate regime of $e_{1,0} \sim 0.4$ allows for flips.

The right panel of Figure 2.6 shows the flip time (similar to the right panel of Figure 2.5, but this time for different initial inclinations). We normalized the time by t_{Kozai}. Note that the flip time of the eccentric coplanar scenario is shorter than that of the HiLe mechanism (as also apparent in the example in Figure 2). In addition, when $e_1 > 0.5$,

the flip time is shorter as e_1 increases.

2.4 Application to Exoplanets and Tidal Disruption Events

The effect we discovered may have different interesting applications. We briefly mention two of them hereafter. As shown in Figure 2, during the evolution the eccentricity can reach very large values, which can result in a small pericenter distance and collisions between the inner two objects. In addition, if the objects do not collide, this allows for tidal dissipation to take place. Specifically, it shrinks and circularizes the orbit. If tide takes place after the orbit rolls over, a counter–orbiting inner orbit can be produced. This configuration is interesting as the inner orbit is almost coplanar with the outer orbit but goes in the opposite direction.

2.4.1 Counter Orbiting Hot Jupiters

Hot Jupiters – massive extrasolar planets in a very close proximity to their host star ($\sim 1-4$ day orbit) – are observed to exhibit interesting characteristics. The planet's projected orbital orientation ranges from almost perfectly aligned to almost perfectly anti-aligned with respect to the spin of the star (Albrecht et al. 2012). In other words, the sky projected angle between the stellar spin axis and the planetary orbit (the spin-orbit angle, otherwise known as obliquity) is observed to span the full range between 0° and 180°.

Formation theories that rely on a planet slowly spiraling in through angular momentum exchange with the protoplanetary disk produce low obliquities (Lin & Papaloizou (1986), but see Thies et al. (2011); Batygin (2012)). The highly misaligned configuration poses a unique challenge to planet formation and evolution models. It was suggested that secular perturbations due to a distant object (Fabrycky & Tremaine 2007; Veras & Ford 2010; Correia et al. 2011; Naoz et al. 2011, 2012), planet-planet scattering (Ford & Rasio 2008; Nagasawa & Ida 2011; Chatterjee et al. 2011; Boley et al. 2012) and secular chaos excursions (Wu & Lithwick 2011) can explain large obliquity, but cannot explain counter-orbiting configurations. Similar results can be achieved if the star and protoplanetary disk are initially in an aligned configuration for a fine tuned initial condition (see Batygin 2012). Furthermore, a test particle can be captured in a $2:1$ mean motion resonance and flip by $\sim 180^\circ$ as migration continues (Yu & Tremaine 2001), and test particles in a debris disk can be flipped due to the interaction of a closely separated planet (Tamayo 2013).

We note that while the EKL mechanism can produce retrograde orbits (both in the inclination and obliquity sense) (Naoz et al. 2011, 2012, 2013a), it cannot produce counter orbiting Hot Jupiters. This is because these studies initialized the inner planet with small eccentricity, which means that the initial inclination needed to produce large eccentricity oscillations is large $\sim 40^\circ - 140^\circ$. Furthermore, these initial conditions results in an inclination which are more likely to be confined in the same regime (Teyssandier et al. 2013). Thus, the final maximum hot Jupiters obliquity reached in these experiments and others (e.g. Fabrycky & Tremaine 2007; Naoz et al. 2012) is $\sim 150^\circ$. An obliquity of $\sim 180^\circ$ could be attributed to projection effects.

The coplanar $\sim 180^\circ$ flip may play a role in the obliquity evolution of many

exoplanetary systems. Coplanar configurations are naturally produced if the planet and the perturbing object (m_2, a star or a planet) are formed in the same disk, or if they are captured in the disk due to hydrodynamic drag. Eccentricity may be excited by planet-planet scattering or interactions with the protoplanetary disk (Ford & Rasio 2008; Nagasawa & Ida 2011). In addition, eccentric gas giant exoplanets are observed at distances larger than 0.1AU from their host star (Ford et al. 2000).

During the orbital flip, the orbit becomes radial ($e_1 \rightarrow 1$), which reduces the pericenter distance, and allows tide to operate. Tidal dissipation shrinks the orbit separation and circularizes it (Matsumura et al. 2010). If this happens after the orbital plane rolled over, a counter orbiting Hot Jupiter is formed.

We illustrate this behavior in Figure 2.7 where the orbit flips within 10Myr from $\sim 6^\circ$ to $\sim 170^\circ$ and the obliquity flips from 0° to $\sim 173^\circ$. This orbit reaches its equilibrium state in a circular counter-orbiting configuration with a small semi-major axis (0.032 AU). Such large obliquities may represent the observed retrograde hot Jupiter HAT-P-7 b and HAT-P-14 b, where the sky projected obliquities are $182^\circ.5 \pm 9^\circ.4$ and $189^\circ.1 \pm 5^\circ.119$, (Winn et al. 2011).

In Figure 2.7, we adopt the "equilibrium tidal" model (Hut 1981; Eggleton et al. 1998; Eggleton & Kiseleva-Eggleton 2001). Its complete set of equations of motion can be found in Fabrycky & Tremaine (2007). Specifically, this approach takes into account the rotation of the star, and the distortion of the planet due to rotation and the tide of the star. In addition, it assumes the viscous timescales of the planet and the star are constant and the tidal quality factor Q is proportional to the orbital period of inner orbit (Hansen 2010). In the example we show in Figure 2.7, we set the viscous timescale of

the star and the planet to 50 years and 0.94 years, respectively, which correspond to the quality factors of $Q \sim 10^6$ and 10^5 for a 10 day orbital period. In this calculation we also include General Relativity precession of the inner and outer body, following Naoz et al. (2013b).

The example shown in Figure 2.7 predicts that this counter-orbiting planet has an eccentric coplanar companion. We stress that this does not mean that one should expect a high abundance of counter orbiting planets, nor that even one exists. This mechanism can produce a large range of final inclinations depending on when tides start to dominate. The pericenter distance shrinks before and during the flips, and when tides become important their effect may effectively halt the orbital flip. In addition, this mechanism drives the inner orbit eccentricity to extremely high values and might result in the planet colliding with or tidally disrupted by the star. Calculating the fraction of systems that will result in a counter orbiting planet and the fraction of planets that will collide with the star is beyond the scope of this paper.

Related to the coplanar flips, we explain the behavior found by Fabrycky & Tremaine (2007), where the spin orbit angle flips in the test particle quadruple limit while the inclination does not flip. In this limit, one of the members of the inner orbit is a test particle and the outer orbit is circular, the z component of the angular momentum is conserved. If the orbit starts prograde $i < 90^\circ$ is will remain prograde. However, the obliquity can flip from prograde to retrograde, as shown in the top panel of Figure 2.8. This is a different kind of flip because the flips occur in the x-y plane (as discussed below).

In the limit at $i \sim 90^\circ$, dJ_1/dt is in the direction of J_1 and Ω_1 shifts by 180° (Katz

et al. 2011). Thus, J_1 moves in a straight line across the origin in the x-y plane and the orbit flips by 180° in the x-y plane. The orbital direction of the inner planet is reversed while the mutual inclination remains less than 90°.

This can be seen in the movies as well. The flip timescale is the quadrupole Kozai timescale. Because the flip of the orbit is abrupt, tides from the planet cannot respond fast enough to realign the stellar spin to the angular momentum of the inner orbit. As a consequence, the spin-orbit angle crosses 90° (Figure 2.8). The behavior also persists when the inclination is less than 90°, but in that case the shift of the longitude of ascending node and the change in obliquity are less than 180°.

Similar to the HeLi flip, the flip in the x-y plane can also produce $\sim$ 180° counter-orbiting planets with respect to the stellar spin, however, this requires the perturber's orbit to be nearly perpendicular to the inner orbit. The flip in the x-y plane may also be relevant for gravitational waves emitted by compact object binaries, where the orbital flip changes the polarization angle of the signal.

2.4.2 Tidal Disruption Events - Systematic Study

As mentioned above, the eccentric Kozai–Lidov mechanism (large and small inclination) drives the inner orbit eccentricity to very large values. This reduces the pericenter distance. When an object moves close to m_1, the tidal force of m_1 can get stronger than the object's self-gravity and hence tidally disrupt the object. For instance, stars may be tidally disrupted by supermassive black holes if they pass very close to the black holes. Tidal disruption of stars by black holes may produce luminous electromagnetic transients that have been observed (e.g. Bade et al. 1996; Komossa & Greiner 1999; Gezari et al.

2003, 2006, 2008b, 2009; van Velzen et al. 2011; Cenko et al. 2012; Gezari et al. 2012).

We show an example of an object passing the Roche limit in Figure 2.9. To mimick the case that produces a counter-orbiting exoplanet (e.g. Figure 2.7), we use the same initial parameters but with a different semi major axis ($a_1 = 39$ AU). In addition, this calculation includes both tidal dissipation and General Relativisty precession effects, similar to Figure 2.7. In this case, during the flip, the eccentricity increases, causes the pericenter to reach the Roche limit of the planet and disrupting the planet.

A very large eccentricity does not immediately imply a tidal dissipation event, since this depends on the initial separation of the orbit. We map the maximum eccentricity that can be reached during the evolution, which may then be useful to examine the likelihood of tidal disruption for specific systems.

Specifically, we study the maximum eccentricity reached during the evolution for $\epsilon = 0.03$. Since this depends on the time the integration stops, we record the respective maximum eccentricity of the inner orbit for integration times $3t_{Kozai}$, $5t_{Kozai}$, $10t_{Kozai}$ and 30 t_{Kozai}. As shown in Figure 2.10 the eccentricity of the inner orbit can be very close to one, with $1 - e_{1,max} \sim 10^{-4}$ during the first flip, and 10^{-6} over longer time periods.

This process is relevant for estimating the rates of planet-star collisions (Hellier et al. 2009; Bear et al. 2011), stellar tidal disruptions due to black hole binaries (Ivanov et al. 2005; Colpi & Dotti 2011; Chen et al. 2011; Wegg & Bode 2011; Bode & Wegg 2013; Stone & Loeb 2012; Li et al. in prep.), Type 1a supernovae (Katz & Dong 2012), and gravitational wave sources (O'Leary et al. 2009; Kocsis & Levin 2012).

To illustrate the percentage of systems that can avoid tidal disruptions and form

hot Jupiters, we perform a Monte Carlo simulation. We set $m_1 = 1\mathrm{M}_\odot$, $m_p = 0.001\mathrm{M}_\odot$, $m_2 = 0.03\mathrm{M}_\odot$, $a_2 = 500$ AU, $e_2 = 0.6$, a_1 to be uniformly distributed between $30 - 50$ AU, i_1 to be uniformly distributed between $0 - 10^\circ$, and e_1 to be uniformly distributed between unity and the minimum e_1 that can produce a 180° flip. The tidal model and its parameters are the same as those included in Figure 2.7. We include 500 runs. A small fraction of systems (90/500 systems) avoid collisions and form hot Jupiters (as shown in Figure 2.11). The final spin-orbit misalignment are typically lower than $\sim 150^\circ$ as shown in Figure 2.12. The percentage to form hot Jupiter is similar to the results by Naoz et al. (2012) and Petrovich (2015), who studied the effect of Kozai-Lidov mechanism in general. Note the spin-orbit misalignment does not reach 180° in this set of Monte Carlo simulation. Monte Carlo simulations including more runs are needed to estimate the fraction of systems that can produce a spin-orbit misalignment reaching 180°.

To require the hierarchical criterion to be valid, we set $\epsilon < 0.1$. When $\epsilon \gtrsim 0.1$, the planetary (inner) orbit can still be flipped by $\sim 180^\circ$. However, the non-hierarchical configuration leads to stronger interactions between the outer perturber and the inner orbit. This may cause instability, and the inner planet may be captured by the outer perturber. As shown in Figure 2.13, moving the outer perturber closer to 11 AU ($\epsilon = 0.125$), and keeping the other parameters the same as those in Figure 2.2, the inner orbit can still be flip by $\sim 180^\circ$. Nevertheless, the inner planet can be ejected from the system due to instability. Note that we ignore collisions or tidal disruptions of the planet to focus on the three-body point mass dynamics. Moving the outer perturber closer to $a_2 \sim 7$ AU, the inner planet can be captured by the outer perturber more easily. The inner planet exhibits chaotic orbital evolutions as it switches its host star between m_1 and m_2, and its inclination relative to the orbital plane of m_1 and m_2 varies chaotically

(see the movie on https://www.cfa.harvard.edu/~gli/images/case10.mp4, m_1 is placed at the center. The red line represents the planetary trajectory, and the blue line represents the perturber's orbit).

2.5 Conclusion

We have presented a new mechanism that flips an eccentric inner orbit by 180° starting with a coplanar configuration in a hierarchical three body system with an eccentric outer perturber. We use the secular approximation to study the dynamics, and show the agreement between the secular treatment and the N-body simulation in Figure 2.2.

The HeLi (high eccentricity low inclination) flip is a different mechanism from the LeHi flip discussed by Naoz et al. (2011, 2013a). The underlying resonances causing the large oscillation in the inclination and the flip are different: the LeHi flip is caused by both the quadrupole and the octupole interactions. However, in the HeLi case, only octupole resonances are in play (see for further discussion in Li et al. in prep). Moreover, for the low inclination case, the orbital evolution is regular, which admits a simple analytic flip criterion and timescale (which were shown to agree with the numerical results in Figure 2.5). In addition, the difference can be seen through the evolution of the orbit: the eccentricity increases monotonically and the inclination remains low before the flip, and the flip timescale of the coplanar case is shorter comparing with the high inclination case (see Figure 2.3 and movies[2]). Including both the high inclination and low inclination flip, we studied the flip condition for a wide range of parameter space for

[2] https://www.cfa.harvard.edu/~gli/images/lowi.mp4;
https://www.cfa.harvard.edu/~gli/images/lowi.mp4

the initial condition in Figure 2.6.

Observations of the sky-projected obliquity angle of Hot Jupiters shows that their orbital orientation ranges from almost perfectly aligned to almost perfectly anti-aligned with respect to the spin of the star (Albrecht et al. 2012). We showed in the hierarchal, nearly coplanar, three body framework, an initial eccentric inner orbit can flip its orientation by almost 180° in the presence of an eccentric companion (Figures 2.5 and 2.6). During the planet's evolution its eccentricity is increased monotonically, and thus tides are able to shrink and circularize the orbit. If the planet has flipped by $\sim 180°$ before tidal evolution dominates, a counter orbiting close-in planet can be formed.

Figure 2.7 demonstrated this behavior. Not only does the final planet inclination reach 180° with respect to the total angular momentum, but also the obliquity. This is because the timescale to torque the spin of the star is much longer than the orbital flip timescale, the spin-orbit angle is similar to the inclination at $\sim 180°$. Therefore, starting with an initially aligned spin orbit configuration, the mechanism presented here can produce counter orbiting close-in planets for a nearly coplanar system. The counter orbiting exoplanets with a 180° obliquity angle can be verified using the measured spin-orbit angle. The true spin-orbit angle can be obtained from the sky projected spin-orbit measurement using the Rossiter-McLaughlin method and the line of sight spin-orbit angle measurement using astroseismology.

We note that we do not expect an excess of counter orbiting planets, because this mechanism can drive the inner orbit to an extremely large eccentricity (see Figure 2.10) therefore the planet may often end up plunging into the star before circularizing due to tidal effects. A systematic survey of the likelihood of creating counter orbiting planets is

beyond the scope of this paper.

In addition to exo-planetary systems, this mechanism can be applied to many different astrophysical settings, which can tap into the parameter space of hierarchical three body system that has large initial eccentricities and low inclinations. As the eccentricity can be excited to $\sim 1 - 10^{-6}$ (Figure 2.10), this mechanism may result in an enhanced rate of collisions or tidal disruption events for planets, stars and compact objects with hierarchical three body configuration.

Acknowledgments

We thank Konstantin Batygin, Matt Holman, Josh Winn and Boaz Katz for useful remarks. SN is supported by NASA through a Einstein Post–doctoral Fellowship awarded by the Chandra X-ray Center, which is operated by the Smithsonian Astrophysical Observatory for NASA under contract PF2-130096. BK was supported in part by the W.M. Keck Foundation Fund of the Institute for Advanced Study and NASA grant NNX11AF29G. AL was supported in part by NSF grant AST-1312034.

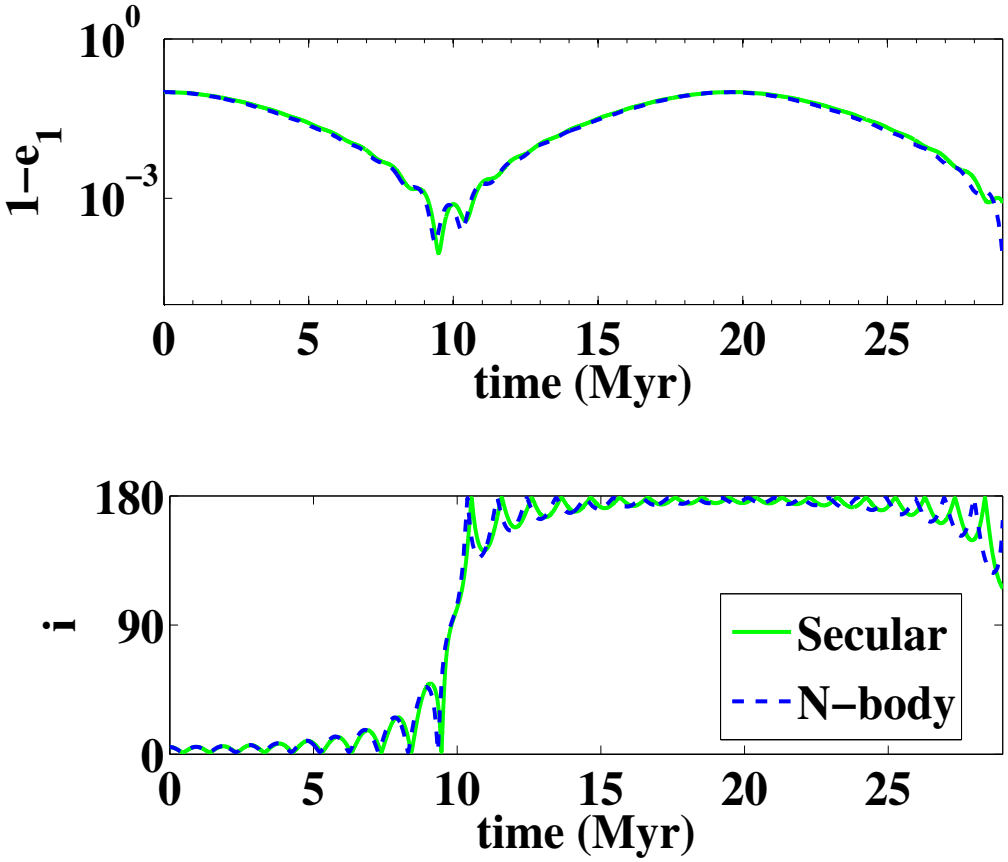

Figure 2.2: *The consistency and convergence of the numerical method for the point mass dynamical evolution of the inner orbit.* We set $m_1 = 1M_\odot$, $m_2 = 0.02M_\odot$, $m_P = 10^{-3}M_\odot$, $a_1 = 1$ AU, $a_2 = 50$ AU, $i = 5°$, $e_1 = 0.9$, $e_2 = 0.7$, $\omega_1 = \omega_2 = \Omega_2 = 0°$ and $\Omega_1 = 180°$. The green line represents the run integrated using the secular approximation, and the dashed blue line represents the results of the N-body simulation using the Mercury code. The results of the two methods agree. In both cases, the test particle exhibits an 180° flip in a coplanar configuration.

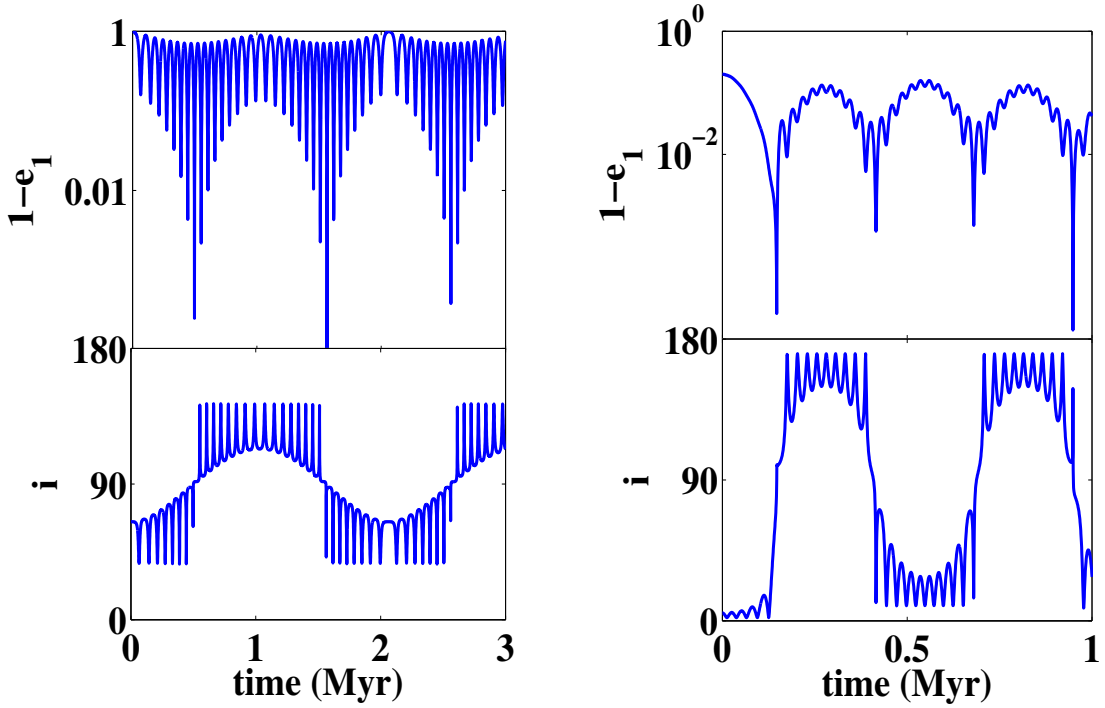

Figure 2.3: *The evolution of the inner orbit's eccentricity and mutual inclination.* We set the mass of m_1 and m_P to a solar and a Jupiter mass, and the mass of the outer perturber m_2 to $0.03M_\odot$, and $\omega_1 = 0°$, $\Omega_1 = 180°$, $e_2 = 0.6$, $a_1 = 4$ AU, $a_2 = 50$ AU. We use the secular approximation to calculate the dynamical evolution of point masses. The upper panel shows the standard Kozai cycles for comparison, ($e_1 = 0.01$, $i = 65°$), and the lower panel shows the eccentric coplanar scenario ($e_1 = 0.8$, $i = 5°$). For the former, both i and e_1 oscillate with large amplitudes, but in the eccentric coplanar case, e_1 increases steadily and i oscillates to maintain a coplanar configuration. The flip occurs much more rapidly in the eccentric coplanar case.

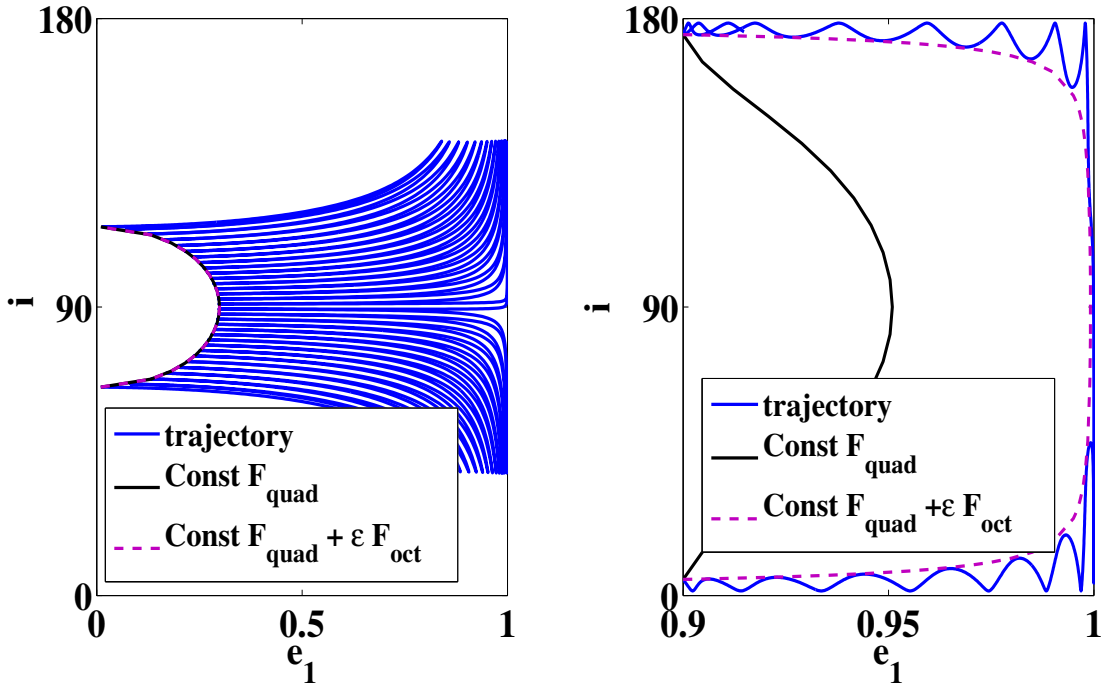

Figure 2.4: Left Panel: standard Kozai-Lidov scenario with initial conditions $e_1 = 0.01$, $i = 65°$, $m_1 = 0.3M_\odot$, $m_2 = 0.1M_\odot$, $a_1 = 1$ AU, $a_2 = 40$ AU, $\omega_1 = 0°$, $\Omega_1 = 180°$. Right Panel: the eccentric coplanar case, with initial conditions $e_1 = 0.9$, $i = 5°$, $m_1 = 0.3M_\odot$, $m_2 = 0.03M_\odot$, $a_1 = 1$ AU, $a_2 = 40$ AU, $\omega_1 = 0°$, $\Omega_1 = 180°$. The evolution tracks represent the change of Jz (Lithwick & Naoz 2011). The inclination i and e_1 oscillate for large initial inclinations, while in the low inclination case, i oscillates and e_1 increases steadily. The dashed line represents the constant $F_{quad} + \epsilon F_{oct}$ curve at $\omega_1 = 0°$, which sets the maximum or minimum inclination during a quadrupole cycle. The black solid line represents the constant F_{quad} curve. The maximum inclination in each quadrupole Kozai cycle follows the constant F_{quad} curve only in the HiLe mechanism.

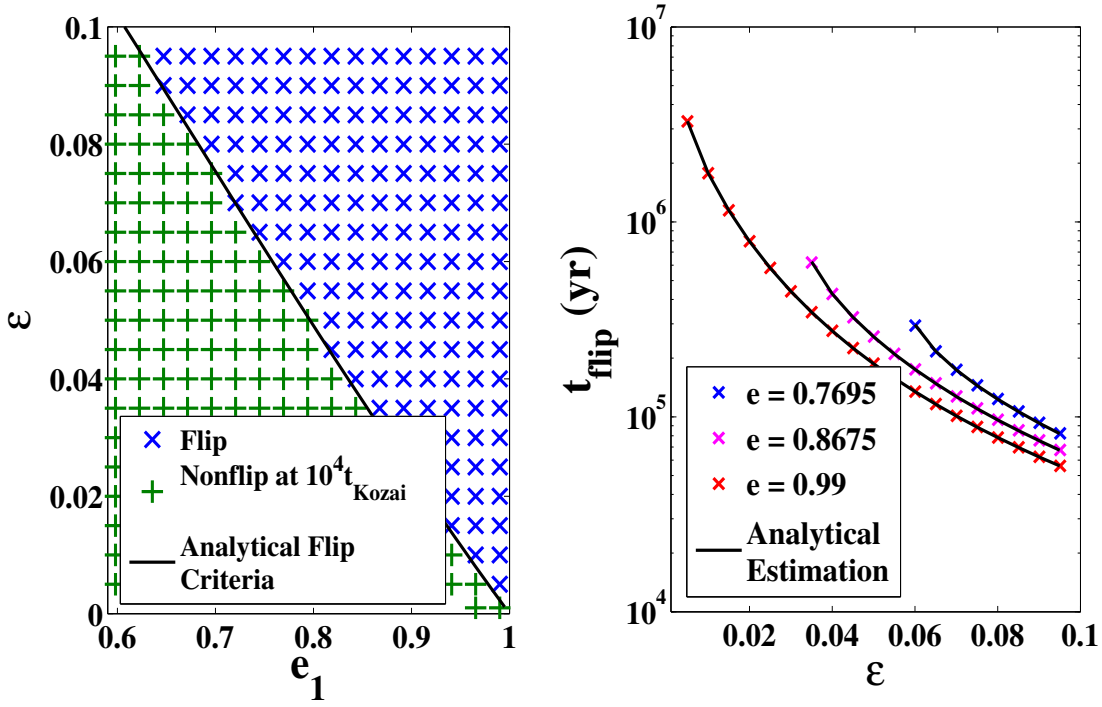

Figure 2.5: *Comparisons of the numerical results and the analytic expressions for the point mass dynamical evolutions.* The initial inclination is $i = 5°$. Left panel: the numerical results versus the analytic criterion for the flip condition (equation (2)). The black line indicates the analytic criterion. The numerical result is obtained from the secular integration, where the initial condition is: $m_1 = 1M_\odot$, $m_2 = 0.1M_\odot$, $a_1 = 1$AU, $a_2 = 45.7$AU, $\omega_1 = 0°$, $\Omega_1 = 180°$. The blue crosses represent the flipped runs and the green pluses represent the runs that do not flip in 10^4 t_{Kozai}, where t_{Kozai} is defined in equation 2.15. Right panel: the flip timescale for different initial eccentricity. The black line indicates the flip time calculated analytically, and the colored crosses are the flip time recorded in the numerical runs.

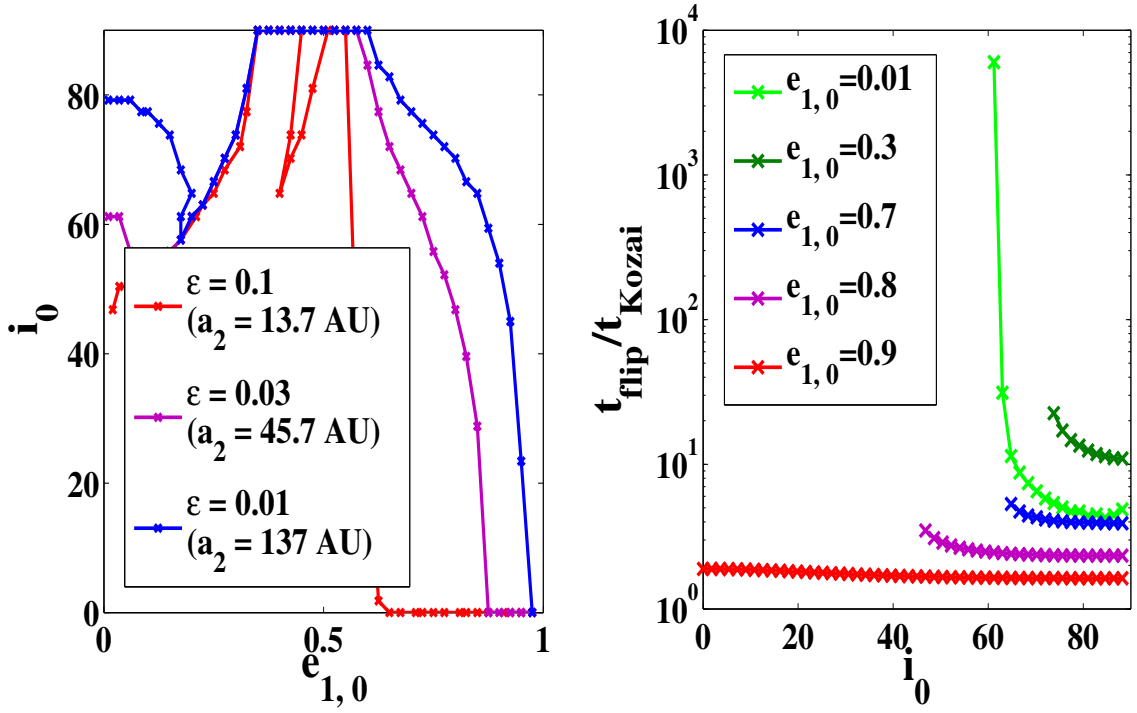

Figure 2.6: *The flip condition and the flip time.* Left panel: The flip condition for the whole parameter space of initial e_1 and i for three different outer semi-major axes, a_2. The initial condition for all the simulations are: $m_1 = 1M_\odot$, $m_2 = 0.1M_\odot$, $a_1 = 1$ AU, $\omega_1 = 0°$, $\Omega_1 = 180°$. a_2, e_1 and i are different for the runs. The simulations do not include the influence of tides. Initial conditions above the colored lines in the $e_1 - i$ plane exhibit an orbital flip. The red line represents the case when $a_2 = 13.7$ AU ($\epsilon = 0.1$), the purple line represents the case when $a_2 = 45.7$ AU ($\epsilon = 0.03$) and the blue line represents the case when $a_2 = 137.5$ AU ($\epsilon = 0.01$). The flip condition agrees well with our analytic estimates for the eccentric coplanar cases. The flip condition is more complicated at moderate e_1. Right panel: The flip time for $a_2 = 45.7$ AU. The flip time is shorter for the HeLi case. Note: when e_1 is higher, t_{Kozai} is shorter (see equation 2.15). Thus, the eccentric coplanar flip time is much shorter than the standard Kozai.

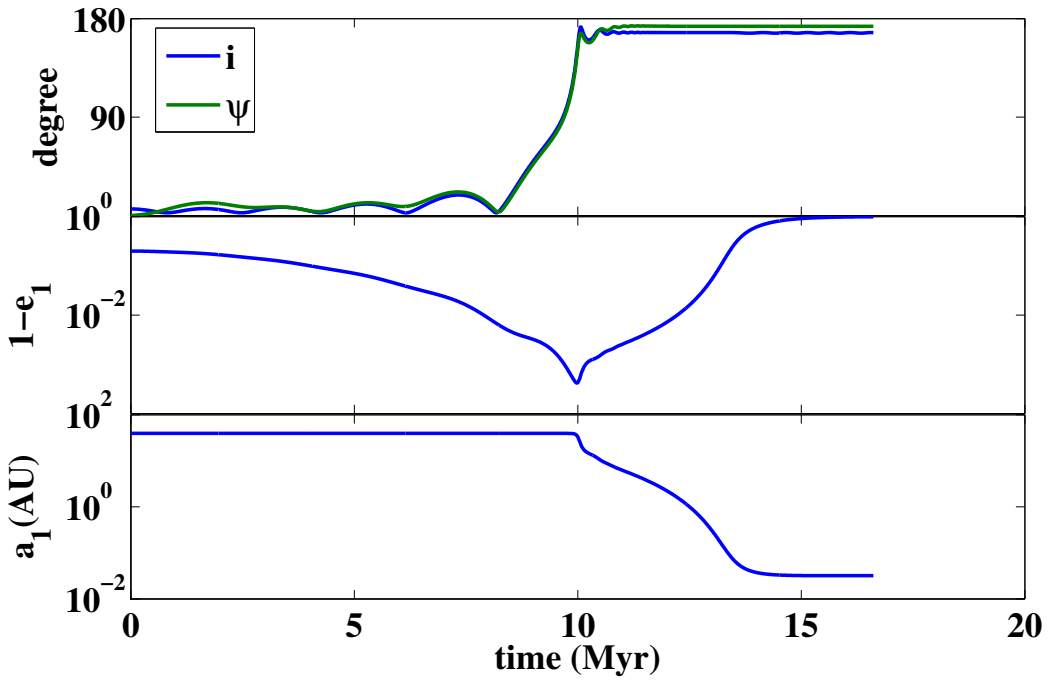

Figure 2.7: *The evolution of the inner orbit under gravitational and tidal forces.* The result is obtained by integrating the secular equation of motion. We set the mass and the radius of m_1 to be those of the Sun, and the mass and the radius of m_P to be those of Jupiter, and $m_2 = 0.03 M_\odot$. The initial obliquity angle (ψ) is set to be 0. We set $a_1 = 39.35$ AU, $a_2 = 500$ AU, $e_1 = 0.8$, $e_2 = 0.6$, $\omega_1 = 0°$, $\Omega_1 = 180°$, $i = 6°$ for the initial condition. For tides, we set the dissipation quality factor to be $Q_1 = 10^6$, $Q_J = 10^5$. The orbit flips after $\sim$ 10Myrs. During the flip, $e_1 \sim 1$ and the tidal dissipation forces the orbit to decay and circularize. The orbit reaches equilibrium with $\psi \sim 173°$, $a_1 \sim 0.032$ AU and $e_1 \sim 0$. General Relativity precession of the inner and outer body is included following Naoz et al. (2013b).

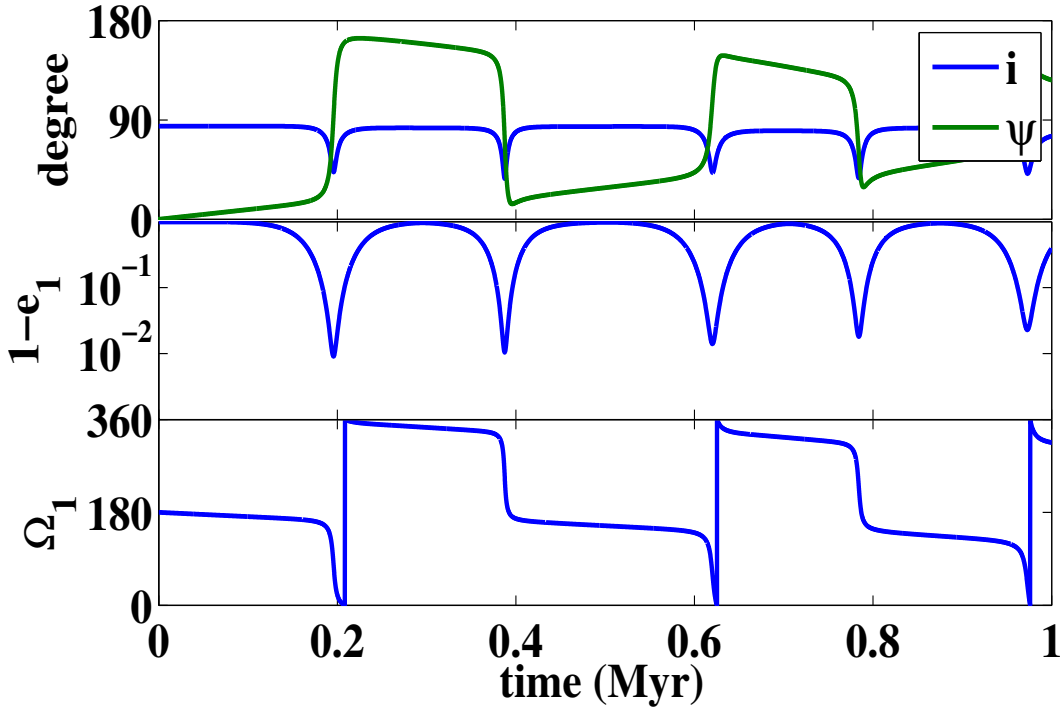

Figure 2.8: *The* $\sim 180°$ *flip of the spin-orbit angle when the mutual orbital inclination is slightly less than* $90°$. We set the mass and the radius of m_1 to be those of the Sun, and the mass and the radius of m_P to be those of Jupiter, and $m_2 = 0.03 M_\odot$. The initial spin-orbit angle (ψ) is set to be 0. We set $a_1 = 40$ AU, $a_2 = 500$ AU, $e_1 = 0.01$, $e_2 = 0.6$, $\omega_1 = 0°$, $\Omega_1 = 180°$, $i = 85°$ for the initial condition. The top panel shows the point mass dynamical evolution of the inclination and the spin orbit angle, and we can see that during each Kozai cycle and the inclination oscillates, the spin orbit angle flips. In the middle panel, e_1 is plotted as a function of time. In the bottom panel, we show that the longitude of the ascending node shifts by $\sim 180°$ abruptly at the end of each Kozai cycle. This indicates the rapid $\sim 180°$ flip of the orbit in the x-y plane.

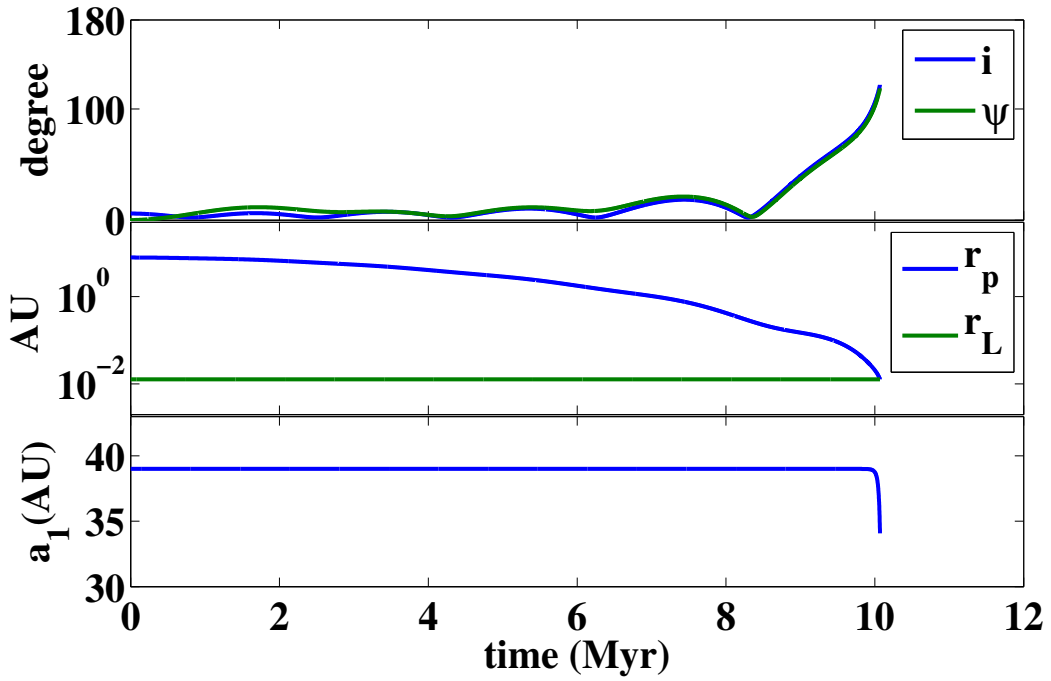

Figure 2.9: *An example illustrating a tidally disruption event.* The initial condition is the same as in Figure 2.7, except $a_1 = 39$ AU. Similar to Figure 2.7, both tidal dissipation and General Relativisty precession effects are included (see text). During the flip, $e_1 \sim 1$ and the tidal dissipation forces the orbit to decay (as shown in the bottom panel). However, the tidal circularization is outran by the eccentricity excitation during the flip, and the object is disrupted before reaching 180° when $r_p < r_L$, where r_L is the Roche limit of the object to m_1.

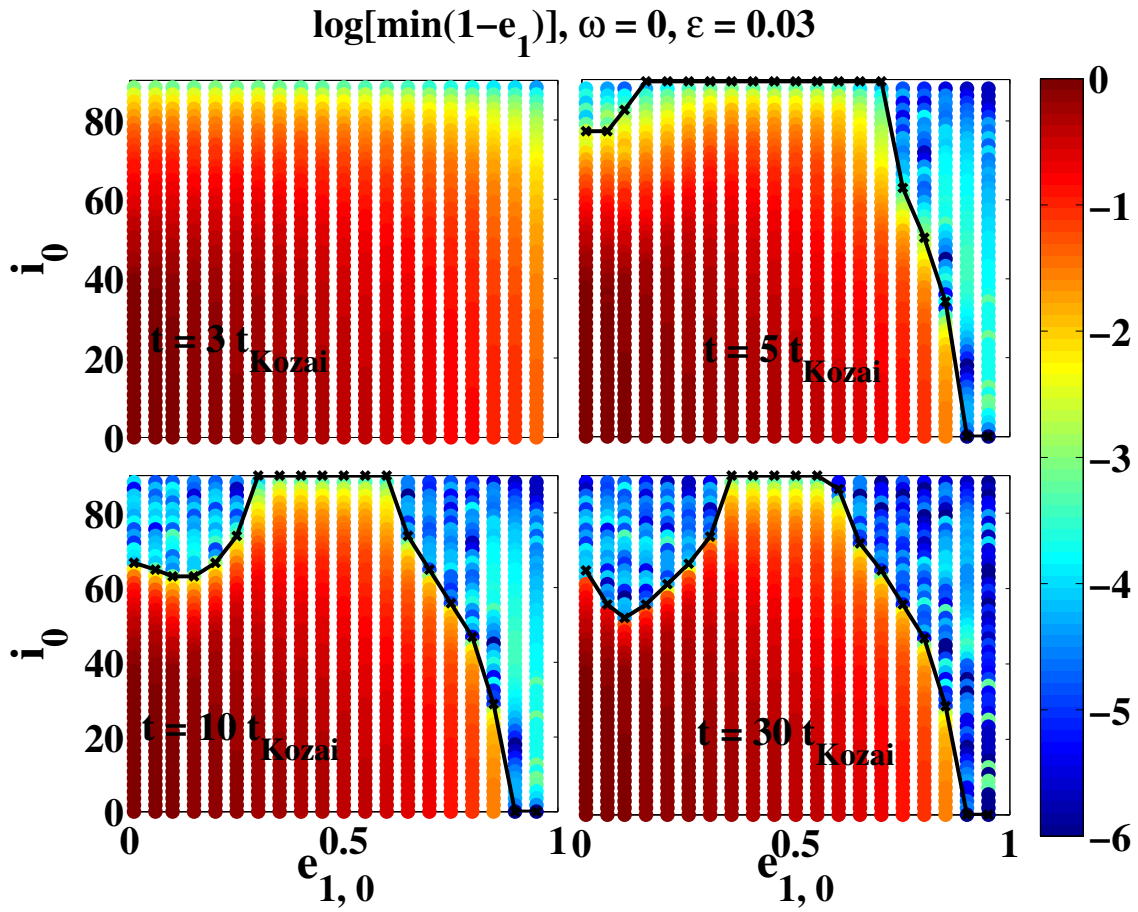

Figure 2.10: *The maximum eccentricity.* The maximum eccentricity reached during the secular evolution in time $3t_{Kozai}$ (upper left panel), $5t_{Kozai}$ (upper right panel), $10t_{Kozai}$ (lower left panel) and $30t_{Kozai}$ (lower right panel) as a function of the initial eccentricity (horizontal axis) and inclination (vertical axis). Tides are not included in the simulation. The initial condition of the runs are $m_1 = 1M_\odot$, $m_2 = 0.1M_\odot$, $a_1 = 1$ AU, $a_2 = 45.7$ AU, $e_2 = 0.7$, $\omega_1 = 0°$, $\Omega_1 = 180°$. The typical eccentricity reached at the first flip is $\sim 1 - 10^{-4}$, and the eccentricity may increase to $\sim 1 - 10^{-6}$ after several flips. The HiLe case reaches the maximum eccentricity later than the LiHe case. The inner orbit flips above the black solid lines.

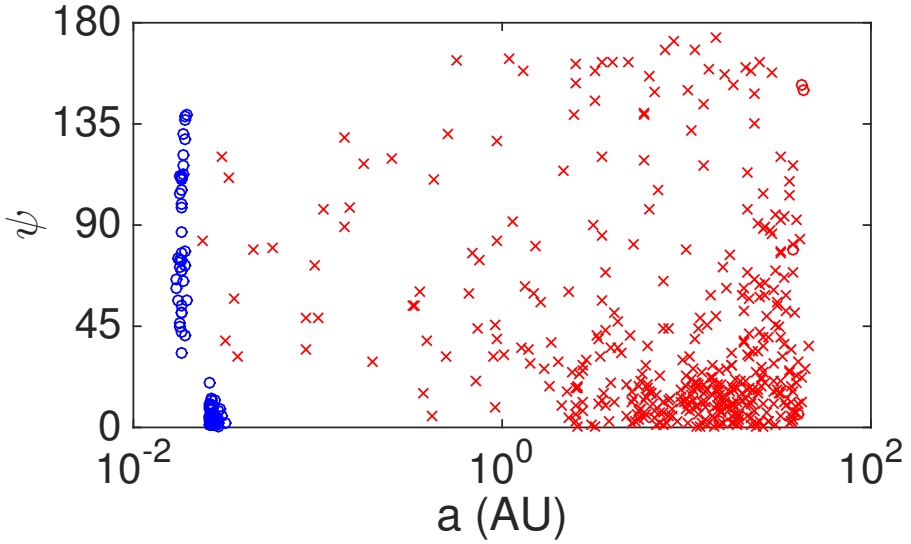

Figure 2.11: The spin orbit misalignment v.s. the final a_1 in 100 Myr produced by the Monte Carlo simulations. The systems where the planets can be tidally disrupted are marked by crosses. 90 out of 500 systems avoid collisions and form hot Jupiters.

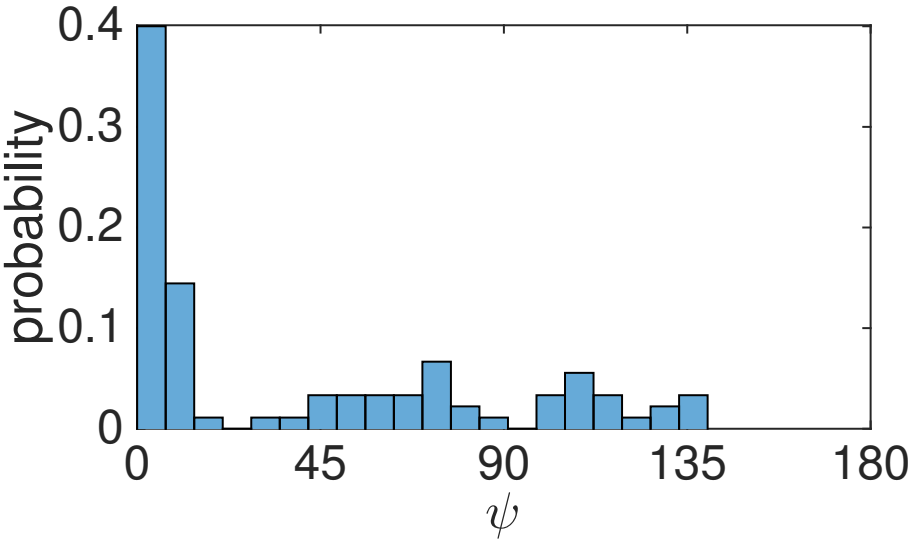

Figure 2.12: The histogram of spin orbit misalignment of the hot Jupiters produced in the Monte Carlo simulations.

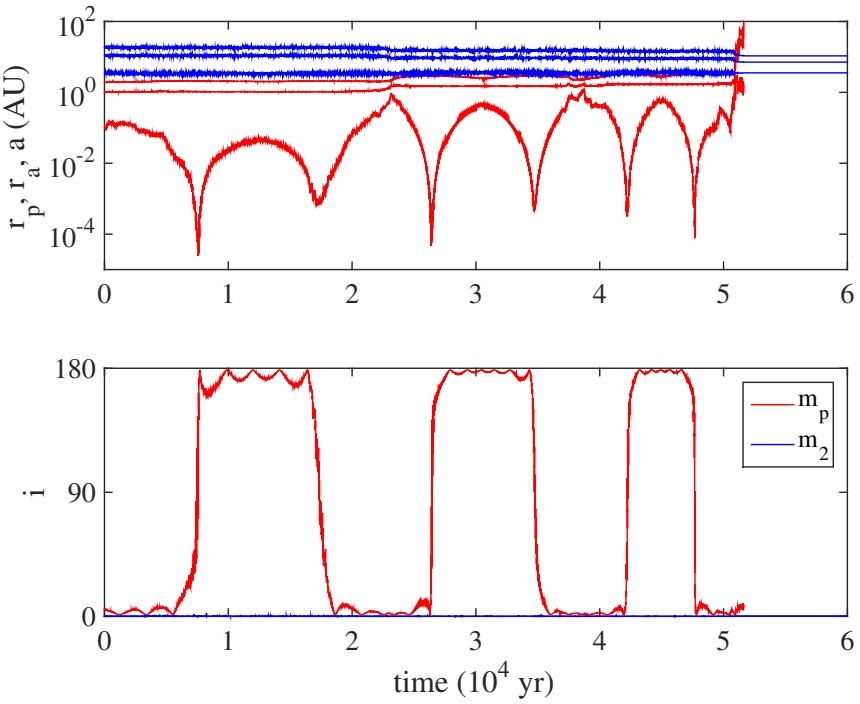

Figure 2.13: The orbital evolution of the inner planet at $\epsilon = 0.125$. The system configuration is the same as that in figure 2.2, except that the outer perturber is moved to $a_2 = 11$ AU. The inner planet can still flip. a_1 is increased at $\sim 2.5 \times 10^4$ yr, and the inner planet is eventually ejected at $\sim 5 \times 10^4$ yr.

Chapter 3

Chaos in the Test Particle Eccentric Kozai-Lidov Mechanism

This thesis chapter originally appeared in the literature as

Li, G., Naoz, S., Holman, M. & Loeb, A. Chaos in the Test Particle Eccentric Kozai-Lidov Mechanism, *The Astrophysical Journal*, 791, 86, 2014

Abstract

The Kozai-Lidov mechanism can be applied to a vast variety of astrophysical systems involving hierarchical three-body systems. Here, we study the Kozai-Lidov mechanism systematically in the test particle limit at the octupole level of approximation. We investigate the chaotic and quasiperiodic orbital evolution by studying surfaces of section and the Lyapunov exponents. We find that the resonances introduced by the octupole

level of approximation cause orbits to flip from prograde to retrograde and back as well as cause significant eccentricity excitation, and the chaotic behaviors occur when the mutual inclination between the inner and the outer binary is high. We characterize the parameter space that allows large amplitude oscillations in eccentricity and inclination.

3.1 Introduction

The Kozai-Lidov mechanism (Kozai 1962; Lidov 1962) has proven very useful for interpreting numerous astrophysical systems. For example, it has been shown that it can play a major role in exoplanet configurations and obliquities (e.g. Holman et al. 1997; Wu & Murray 2003; Fabrycky & Tremaine 2007; Veras & Ford 2010; Correia et al. 2011; Naoz et al. 2011, 2012). In addition, close stellar binaries with two compact objects are likely produced through triple evolution, and the Kozai-Lidov mechanism may play a key role in these systems (e.g. Harrington 1969; Mazeh & Shaham 1979; Soderhjelm 1982; Kiseleva et al. 1998; Ford et al. 2000; Eggleton & Kiseleva-Eggleton 2001; Fabrycky & Tremaine 2007; Perets & Fabrycky 2009; Thompson 2011; Katz & Dong 2012; Shappee & Thompson 2013; Naoz et al. 2013a; Naoz & Fabrycky submitted). Furthermore, the Kozai-Lidov mechanism has been proposed as an important element in the growth of black holes at the centers of dense star clusters, the formation of short-period binaries black hole (Blaes et al. 2002; Miller & Hamilton 2002; Wen 2003; Ivanova et al. 2010), and tidal disruption events (Chen et al. (2009, 2011); Wegg & Bode (2011); Bode & Wegg (2013), Li et al., in prep).

The Kozai-Lidov mechanism focuses on hierarchical three-body systems, which can be treated as the interaction between two elliptical wires by orbit averaging: the inner

wire is composed of the inner two objects, and the outer wire is composed of the outer companion orbiting around the center mass of the inner two objects. The total angular momentum of this system, the vector sum of the inner orbit's and the outer orbit's angular momenta, is conserved.

Kozai (1962) and Lidov (1962) first studied this mechanism by expanding the gravitational potential in a power series of the semi-major axis ratio and considered applications when one of the inner object is massless (the test particle limit) and the outer orbit is circular. Kozai (1962) considered the secular (long term) evolution of asteroids under the perturbation of Jupiter, and Lidov (1962) studied the secular evolution of satellites under the perturbation of the Moon. In those cases, the gravitation potential of the inner orbit is axisymmetric, which renders the $\hat{z}$ component of the inner orbit's angular momentum (J_z) constant, where $\hat{z}$ is the direction of the total angular momentum of the system. The quadrupole order of approximation ($O\big((a_1/a_2)^2\big)$) sufficiently describes the orbital evolution of such systems, and the eccentricity and the inclination undergo large amplitude oscillations due to the "Kozai resonance" when $i > 39.2°$.

Recently, Naoz et al. (2011) considered the case when none of the inner objects is a test-particle, and pointed out that J_z is no longer conserved. In addition, the eccentric Kozai-Lidov Mechanism (hereafter EKL) applies to cases when the outer orbit is non-circular, where the $\hat{z}$ component of the angular momentum of the inner orbit is also not conserved (Naoz et al. 2011). In this situation, the octupole terms in the potential ($O\big((a_1/a_2)^3\big)$) need to be taken into account to describe the orbital evolution, where the eccentricity of the inner orbit can be excited to unity, and the inner orbit may flip from prograde to retrograde or vice versa (Naoz et al. 2011; Lithwick & Naoz 2011;

Katz et al. 2011; Naoz et al. 2013a). As the eccentricity increases, the pericenter distance decreases, and causes an enhanced tidal disruption rate (Li et al., in prep). Furthermore, including the octupole effects, the oscillation in the eccentricity and the inclination of the inner orbit may still exist when $i < 39.2°$, and the inner orbit may undergo a coplanar flip from $\sim 0°$ to $\sim 180°$ (Li et al. 2014a).

Here, we probe the test particle limit, which simplifies the analysis due to its smaller number of degrees of freedom. This approximation was proven to be very useful in a large range of astrophysical settings (Lithwick & Naoz (2011); Katz et al. (2011); Naoz et al. (2012); Li et al. (2014a), Naoz & Silk in prep, Li, et al., in prep). Importantly, probing this limit can help us gain some basic understanding of the EKL mechanism. The test particle limit has been studied in the literature before to obtain an analytical understanding on the flip of the orbit (Lithwick & Naoz 2011; Katz et al. 2011). Nevertheless, a systematic study on the chaotic behavior and the identification of the underlying resonances are necessary but are uncovered in the literature. We identify the resonances, and characterize the chaotic regions and the initial conditions where high eccentricity and the flips may occur in the parameter space. This can help predict the dynamical evolution of systems without doing a large amount of simulations.

This paper is organized as follows. In §2, we give a brief overview of the Kozai-Lidov mechanism. In §3, we investigate the surface of section systematically for a large range of orbital parameters. In §4, we characterize the initial condition which allows large amplitude oscillations in eccentricity and inclination. Finally in §5, we characterize the chaotic regions.

3.2 Overview of the Eccentric Kozai-Lidov Mechanism in the Test-particle Limit

As mentioned in the introduction, the Kozai-Lidov mechanism describes the dynamical behavior of hierarchical three-body systems (see Figure 8.1). The inner two objects (m_1 and m_t) form an inner orbit, and the outer orbit is formed by the outer object (m_2) orbiting around the center mass of the inner two objects. The eccentric Kozai-Lidov mechanism describes the dynamics when the outer orbit is eccentric, and the test-particle limit requires one of the closely separated objects to be a test particle $m_t \to 0$.

In the hierarchical configuration, we average over the mean motion of the two orbits and treat the evolution of the system as the interaction of two elliptical wires. This reduces this system from six degrees of freedom to four degrees of freedom. In addition, in the test-particle limit, the outer orbit is stationary, and reduces the system to two degrees of freedom (Harrington 1968, 1969; Ford et al. 2000). Expanding the Hamiltonian of the interaction energy between the two ellipses in a power series of a_1/a_2, the Hamiltonian can be expressed as the following at the second (quadrupole) and the third (octupole) order (Lithwick & Naoz 2011):

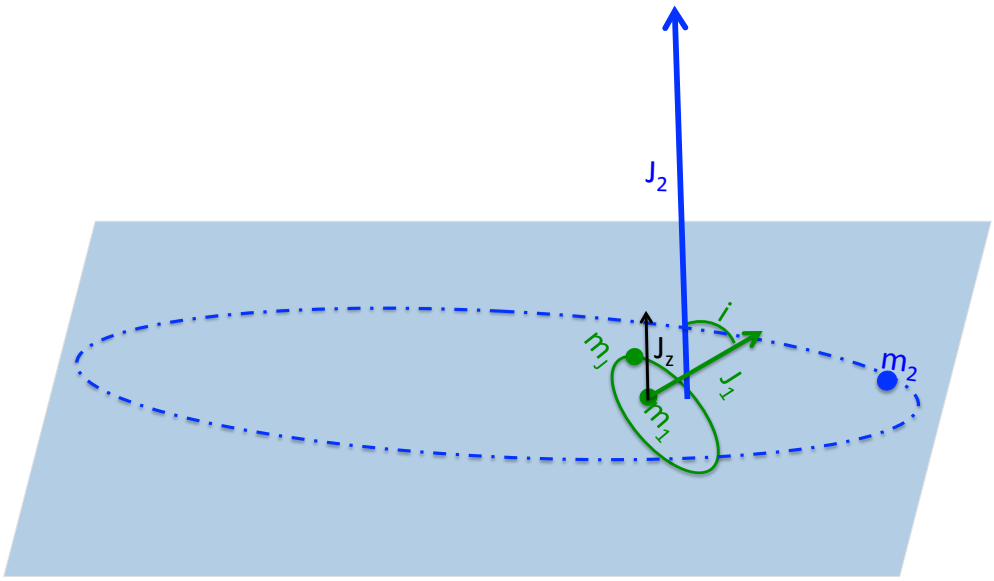

Figure 3.1: The system configuration. A test particle m_t orbits around an object m_1 and forms the inner binary. The outer binary consists of the object (m_2) and m_1 (in the test particle limit). J_o represents the angular momentum of the outer binary, J represents that of the inner binary, and J_z represents the $\hat{z}$ component of J, where $\hat{z}$ is in the direction of J_o. In the test particle limit $J \ll J_o$ and the outer orbit is stationary.

$$F_{quad}(J,\omega,J_z,\Omega) = \frac{1}{2}(-1+J^2) + \frac{J_z^2}{J^2} + \frac{3(1-J^2)J_z^2}{2J^2} + \frac{5}{2}(1-J^2)(1-J_z^2/J^2)\cos(2\omega) \tag{3.1}$$

$$\begin{aligned} F_{oct}(J,\omega,J_z,\Omega) = {} & \frac{5}{16}(\sqrt{1-J^2} + \frac{3}{4}(1-J^2)^{3/2}) \\ & \Big[(1 - \frac{11J_z}{J} - \frac{5J_z^2}{J^2} + \frac{15J_z^3}{J^3})\cos(\omega-\Omega) \\ & + (1 + \frac{11J_z}{J} - \frac{5J_z^2}{J^2} - \frac{15J_z^3}{J^3})\cos(\omega+\Omega)\Big] \\ & - \frac{175}{64}(1-J^2)^{3/2} \\ & \Big[(1 - \frac{J_z}{J} - \frac{J_z^2}{J^2} + \frac{J_z^3}{J^3})\cos(3\omega-\Omega) \\ & + (1 + \frac{J_z}{J} - \frac{J_z^2}{J^2} - \frac{J_z^3}{J^3})\cos(3\omega+\Omega)\Big], \end{aligned} \tag{3.2}$$

where $H_{quad} = -F_{quad}$ and $H_{oct} = -F_{quad} - \epsilon F_{oct}$, and

$$\epsilon = \frac{a_1}{a_2}\frac{e_2}{1-e_2^2}. \tag{3.3}$$

ϵ characterizes the importance of the octupole order. The Hamiltonian is scaled with $m_t\sqrt{Gm_1a_1}t_K$, where

$$t_K = \frac{8}{3}P_{in}\frac{m_1}{m_2}\Big(\frac{a_2}{a_1}\Big)^3(1-e_2^2)^{3/2} \tag{3.4}$$

(Lithwick & Naoz 2011). $J = \sqrt{1-e_1^2}$ is the angular momentum of the inner orbit, ω is the argument of periapsis of the inner orbit, $J_z = \sqrt{1-e_1^2}\cos i_1$ is the $\hat{z}$ component of the inner orbit's angular momentum J, and Ω is the longitude of the ascending node of the inner orbit. Specifically, J, ω and J_z, Ω are conjugate momentum and coordinate pairs. We denote e_1 as the eccentricity of the inner orbit, and i_1 as the inclination of the inner orbit to the total angular momentum of the system. In the test particle limit, $i_1 = i$ is the mutual inclination between the two orbits.

In the quadrupole limit, the Hamiltonian is independent of Ω, so J_z is constant, and the system is integrable. In addition, the angle $\omega = \varpi - \Omega$ is the resonant angle of the system, where ϖ is the longitude of the periapsis. When $i > 39.2°$, the solution admits a resonant region and e_1 and i exhibit large amplitude oscillations. Particularly, e_1 may be excited to high values starting from $e_1 \sim 0$ (e.g. Morbidelli 2002).

As mentioned in the introduction, the octupole order adds variations in J_z which allows the inner orbit to flip from prograde to retrograde, and the eccentricity to be excited very close to 1 (Lithwick & Naoz 2011; Katz et al. 2011; Naoz et al. 2011, 2012, 2013a). We work with the Hamiltonian at the octupole level of approximation to analyze the surface of section and the chaotic behaviors in the next sections.

3.3 Surfaces of Section

For a two degree of freedom system, the surface of section projects a 4-dimensional trajectory on a 2-dimensional surface. Specifically, we plot points on a 2-dimensional surface composed of one canonically conjugate pair (e.g. $J - \omega$ or $J_z - \Omega$) whenever the other angle (Ω or ω) reaches a fixed value and moves in a fixed direction (see the left panel in Figure 3.2). The collection of the points form the surface of section.

There are three distinct regions in the surface of section: "resonant regions", "circulation regions", and "chaotic regions" (right panel in Figure 3.2). The resonant regions are formed by points where the momenta and coordinates (the angles) undergo bounded oscillations. The trajectories in this region are quasiperiodic, where the system is in the *libration* mode. The *circulation* region represents trajectories where the

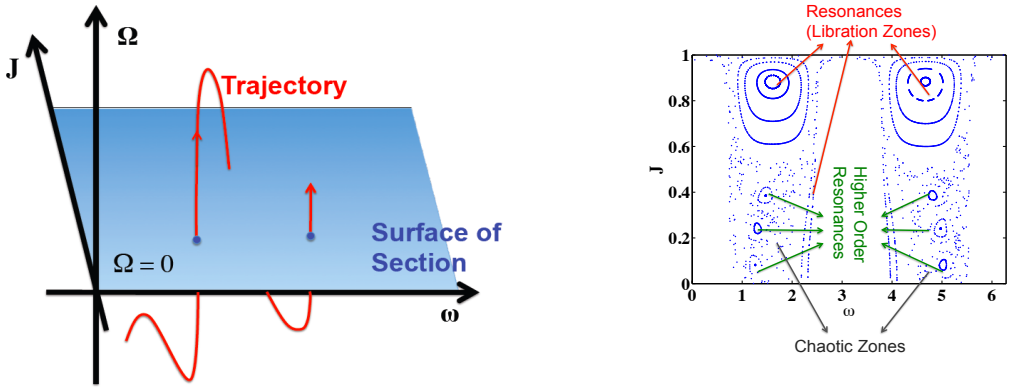

Figure 3.2: Upper panel: Illustration of the "surface section" for the $J-\omega$ plane. By recording the point in the trajectory every time $\Omega = 0$, $\dot{\Omega} > 0$, the trajectory can be represented by a 2 dimensional graph, as shown in the left panel. This set of points form the "surface of section". Lower panel: Illustration of the resonant and chaotic regions in surface of section. We set $H = -0.1$, $\epsilon = 0.1$ in this plot. The resonant and higher order resonant zones are marked by the red and the green arrow. The chaotic zones are indicated by the grey arrow. In the resonant region, the angle ω is constrained in a small region and the trajectories are quasiperiodic. In the chaotic region, the position of the points are not regular and the trajectories are chaotic.

coordinates are not constrained to a specific interval. Both resonant and circulatory trajectories map onto a 1D manifold on the surface of section. On the contrary, chaotic trajectories map onto a 2D manifold. In other words, while quasi-periodic trajectories form lines on the section, chaotic trajectories are area-filling. Embedded in the chaotic region, the small islands correspond to the second order resonances, which are caused by the interaction between the primary resonances. The trajectories in the second order resonant regions are also quasiperiodic.

We now consider the surface of section in the $J-\omega$ plane (setting $\Omega = 0$ and $d\Omega/dt > 0$). When e_1 is excited to large values, $J \to 0$. When Ω is set, for each point in the $J-\omega$ plane, J_z $(-J \leqslant J_z \leqslant J)$ is unequivocally defined by the conservation of H. There is a finite range of H that the system can take on, because both actions must have

zero imaginary components. Since we plot the sections with constant H values, we first explore the range of energy H it can achieve in the $J-\omega$ plane. This way, we can select the range in H that we explore below.

We notice that the maximum and minimum energy it can reach in the $J-\omega$ plane when $\Omega = 0$ is ~ 3 and ~ -2.4 (see Appendix Figures 3.8 and 3.9, which show the maximum and the minimum H in the $J-\omega$ plane). Thus, we plot six surfaces of section for H ranging from $H = -2$ to $H = 1.2$, since when $H > 1.2$, the behavior is similar to that of $H = 1.2$. Note that the H admits positive values for this bounded system, because it is the interaction energy between the test particle (m_t) and the outer companion (m_2), i.e. the disturbing function of this system to the Kepler Hamiltonian of the inner and outer orbits. To investigate the role of the octupole effects, we plot the surface section for two extreme values of ϵ: $\epsilon = 0.001$ and $\epsilon = 0.1$. When $\epsilon < 0.001$, the octupole effects are negligible. On the other hand, $\epsilon = 0.1$ represents the maximal octupole effects, where when $\epsilon > 0.1$, the hierarchical condition may break down and the system may become unstable.

The sections are shown in Figure 3.3. The empty region (bounded by the black curves) do not have physical solutions. The comparison between the two rows in Figure 3.3 shows the difference between the octupole and the quadrupole resonances: $\epsilon = 0.001$ is dominated by the quadrupole effect and $\epsilon = 0.1$ is dominated by both the quadrupole and the octupole effects. For the former, where the quadrupole dominates, there are two resonant regions with fixed points at $\omega = \pi/2$ and $3\pi/2$ when H is high (as shown in Figure 3.3 at $\epsilon = 0.001$, $H = -0.5, -0.1, 0.5$ and 1.2). For the latter when the octupole plays an important role (i.e., $\epsilon = 0.1$), we find different resonant regions for different energy levels, and the location of the resonant regions vary according to the energy levels.

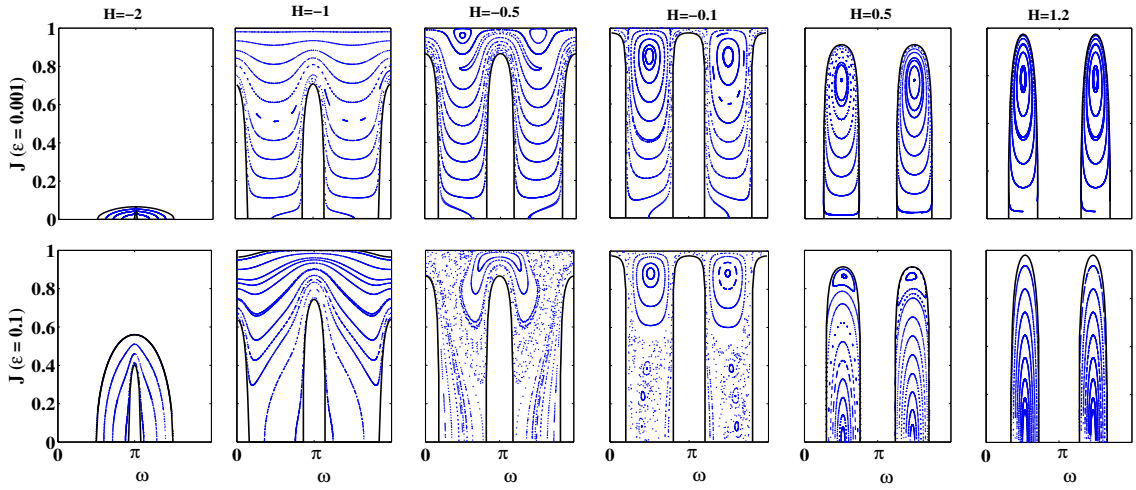

Figure 3.3: The surface of section in the $J - \omega$ plane. In the first row, $\epsilon = 0.001$ and in the second row, $\epsilon = 0.1$. The octupole terms are important when ϵ is bigger. H varies from $-2 \sim 1$. The corresponding e_1 and i in this plane is shown in Figure 3.10 and 3.11. There are chaotic regions at $H = -0.5$ and $H = -0.1$.

The resonant regions are associated with fixed points at $\omega = \pi$, $\omega = \pi/2$ and $\omega = 3\pi/2$ depending on the energy level. These resonant zones result from the interaction of the resonances associated with the "harmonics" in the octupole level Hamiltonian, i.e. 2ω, $\omega \pm \Omega$, and $3\omega \pm \Omega$. Moreover, chaotic regions can only be seen for high ϵ at $H = -0.5$ and $H = -0.1$, where the chaotic zones are a result of the overlap of the resonances between the quadrupole and the octupole resonances. Embedded in the chaotic region, higher order resonances can be found at $H = -0.1$, where the trajectories are quasi-periodic and the eccentricity cannot be excited.

On the other hand, the comparison between the different energy levels shows the orbital evolution corresponds to different orbital parameters. The corresponding e_1 and i are shown in Figure 3.10 and Figure 3.11 in the appendix. Accordingly, the low H corresponds to the low inclination ($i \sim 0 - 30°$) and high eccentricity ($e_1 \gtrsim 0.6$) case,

the higher H corresponds to the high inclination ($i \sim 30^\circ - 60^\circ$) and low eccentricity ($e_1 \lesssim 0.6$) case, and $H > 0$ corresponds to high inclination ($i \sim 60 - 90^\circ$) and low eccentricity case ($e_1 \lesssim 0.3$). When H is low ($H \sim -2$), the evolution is only affected by the octupole resonances, while when H is higher, octupole and quadrupole resonances both contribute and may overlap to cause the chaotic region as mentioned above. We find that e_1 can be excited to high values ($J \to 0$) for almost all energy levels but is only excited very close to unity for higher ϵ. This emphasizes that the octupole level of approximation causes large eccentricity excitation, since larger ϵ implies that the octupole level is important.

Next, we study the surface section in the plane of $J_z - \Omega$ (Figure 3.4). These sections clearly show the flip of the orbit when J_z changes sign. The maximum and minimum energy that can be reached in the $J_z - \Omega$ (with $\omega = 0$) plane is ~ 0 and ~ -2.4. Thus, we plot the surface of section ranging from $H = -2$ to $H = -0.1$ for two values of $\epsilon = 0.001$ and 0.1. At the quadrupole level, J_z is constant, and there's no resonances in the $J_z - \Omega$ plane. Thus, all the resonances originated from the octupole level of approximation, and the fixed points are at $\Omega = \pi$ and $\Omega = 0$. In addition, similar to the surface section on the $J - \omega$ plane, we see higher order resonances for $\epsilon = 0.1$ at $H = -0.3$ and $H = -0.1$ embedded in the chaotic region, and the chaotic region is confined to $H = -0.5$ and $H = -0.1$. Since J_z changes sign in all energy levels, the orbit may flip for all energy levels, and the flip parameter space is larger for higher ϵ. The corresponding e_1 and i on the surface are shown in Figure 3.12 and Figure 3.13.

To summarize, the surfaces of section show that flips and the excitation of e_1 can occur for both regular regions and chaotic regions for a wide range of H, and they depend sensitively on the initial condition. In addition, the trajectories are chaotic only when

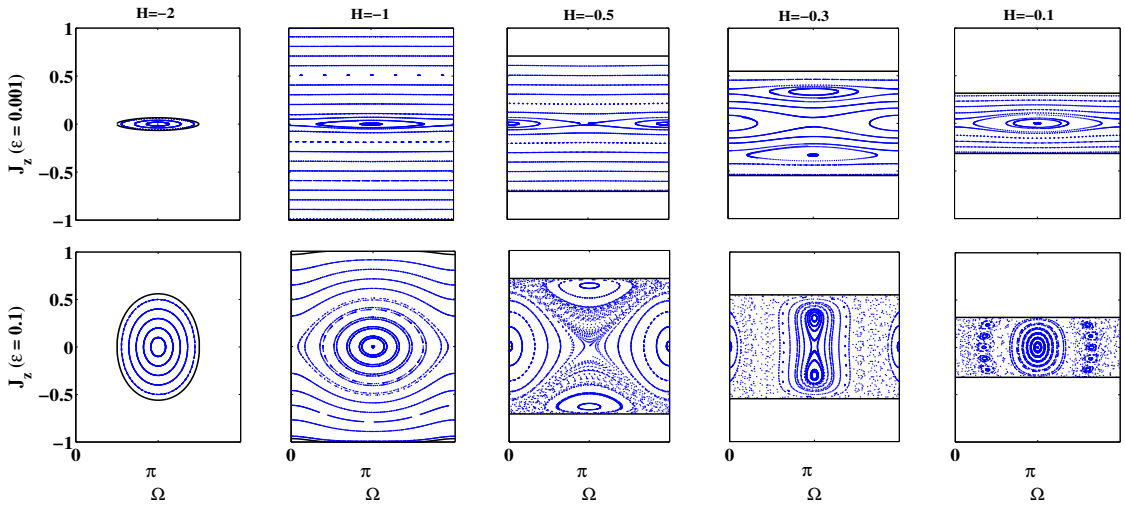

Figure 3.4: The surface of section in the $J_z - \Omega$ plane. In the first row, $\epsilon = 0.001$ and in the second row, $\epsilon = 0.1$. H varies from $-2 \sim 0$. There are chaotic regions at $H = -0.5$, $H = -0.3$ and $H = -0.1$. All the features are due to the octupole order, as the J_z is constant in the quadrupole order. The corresponding e_1 and i are shown in Figure 3.12 and 3.13.

$H \lesssim 0$, corresponding to high mutual inclination low eccentricity cases. Furthermore, it is the octupole resonances that cause the flip of the orbit and the excitation of eccentricity very close to unity.

3.4 The Maximum Eccentricity and the Flip Condition

To apply this mechanism to astrophysical systems with different initial conditions, we investigate the parameter regions which exhibit interesting dynamical behaviors. We create a finer grid of H and ϵ than those presented in Figure 3.3 and 3.4, and we monitor the trajectories that start with the selected initial condition in the $J - \omega$ or the $J_z - \Omega$

plane. Of course, some behaviors which do not pass through the selected initial condition will be missed, but this exploration gives a general idea of the behavior of the system as a whole.

We start with the exploration in the $J-\omega$ plane. To systematically estimate the range in J that the trajectories may reach, we start at the maximum energy boundary of J for a given H and ϵ, which corresponds to the minimum eccentricity. Accordingly, for $H<-1$, ω starts at π, and for $H>-1$, ω starts at $\pi/2$. The maximum e_1 is recorded after monitoring for $t=500t_K$ (we define t_K in equation (3.4)), which is much longer than the Lyapunov timescale (see below).

In Figure 3.5, we plot $1-e_{1,max}$ as a function of ϵ, where each curve represents a fixed H ($H\in[-2,2]$), and ϵ ranges from 0.001 to 0.1. In addition, we use the symbol "x" to mark the ϵ higher than which the orbit flips. It shows that there are roughly five dynamical regions in H: when $H\lesssim-1.5$, $-0.5\lesssim H\lesssim 0$ and $H\gtrsim 0.5$, the orbit may flip and e_1 can be excited very close to unity; when $-1.5\lesssim H\lesssim -0.5$ and $0\lesssim H\lesssim 0.5$, starting with the minimum e_1, e_1 cannot be excited to unity. Reading from the surface of section in Figure 3.3, the lack of e_1 excitation at $0\lesssim H\lesssim 0.5$ and high ϵ is due to the quadrupole resonances, which traps the trajectory at low e_1.

Particularly, e_1 may be excited and the orbit may flip in three scenarios: when the inner orbit is eccentric and coplanar, when the inner orbit is circular and with high inclination, or when the inner orbit is moderately eccentric and with very high inclination $\sim 80-90^\circ$ (see Figure 3.14). In addition, the maximum change in ΔJ can be well fit by a power law from $H<-1$:

$$\Delta J = e^{-2.77H-3.62}\epsilon^{0.051H+1.08}. \tag{3.5}$$

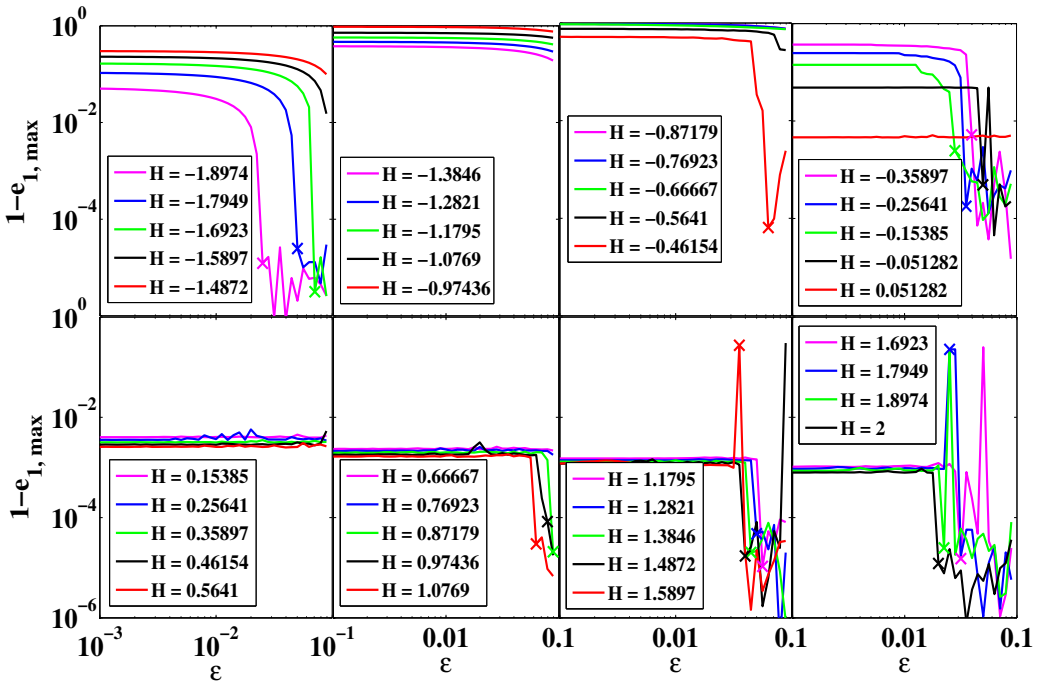

Figure 3.5: The maximum e_1 for different H and ϵ. We set the initial condition at the top of the energy boundary condition of the $J-\omega$ plane, and we record the maximum e_1 reached in $t = 500t_K$. Each line represents a different H, and the cross marks the ϵ bigger than which the inner orbit may flip (i cross over 90°). We find that e_1 may be excited and the orbit may flip when$H \lesssim -1.5$, $-0.5 \lesssim H \lesssim 0$ and $H \gtrsim 0.5$. The first case corresponds to the coplanar flip (i flips from $\sim 0°$ to $\sim 180°$ or vise versa), and the latter two correspond to the high inclination flip.

Next, we explore the $J_z - \Omega$ plane. We start the trajectories at the lower energy boundary of J_z at $\Omega = \pi$ for the given H and ϵ, and we record the maximum change in J_z after $t = 500t_K$. Figure 3.6 shows ΔJ_z as a function of ϵ, where each curve represents a different H. ϵ ranges from 0.001 to 0.1, and H ranges from -2 to 0, since the maximum H is zero for $\omega = 0$. Similarly to the $J-\omega$ plane, we use the symbol "x" to mark the ϵ higher than which the orbit flips. As expected, it shows that the orbit may flip when $-2 < H < -1.5$ and $-0.5 < H < 0$, where $-2 < H < -1.5$ corresponds to an eccentric

and coplanar inner orbit, and $-0.5 < H < 0$ corresponds to a circular inner orbit with a high inclination. Moreover, ΔJ_z can be fit by a power law of H and ϵ:

$$\Delta J_z = \begin{cases} e^{-2.21}\epsilon^{1.06} & (H < -0.5) \\ e^{10.7H+4.23}\epsilon^{0.48H+1.31} & (H > 0.5)\ , \end{cases} \tag{3.6}$$

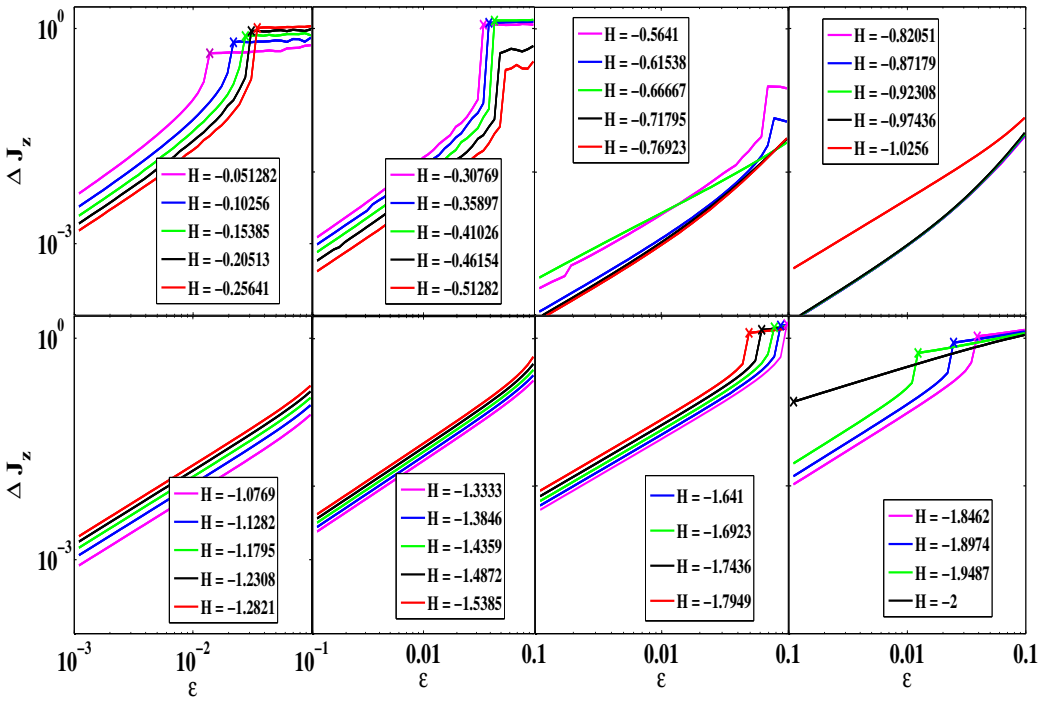

Figure 3.6: The maximum change in J_z for different H and ϵ. We set the initial point at $\Omega = \pi$, where J_z is on the lower energy boundary. We record the maximum change in J_z for $t = 500t_K$. The crosses represent the ϵ bigger than which the inner orbit may flip (J_z changes sign). We find the orbit may flip at $-2 < H < -1.5$ and $-0.5 < H < 0$. The former corresponds to the coplanar flip and the latter corresponds to the high inclination flip.

3.5 Chaotic Regions

The surfaces of section show that the system is chaotic when $H \lesssim 0$ (Figure 3.3 and 3.4). To better characterize the chaotic regions, we first calculate the percentage of area that is chaotic in each surface in Figure 3.3. Specifically, we divide each surface into equally spaced grids in J and ω, and count the fraction of grids that has chaotic trajectories. We use the Lyapunov exponent (λ) to determine whether the trajectories are chaotic, where λ indicates how quickly two closely separated trajectories diverge from each other,

$$\lambda = \lim_{t\to\infty} \frac{1}{t} \ln \frac{\delta_{traj}(t)}{\delta_{traj}(0)}. \tag{3.7}$$

We integrate the tangent of the trajectories for $1000t_K$ to compute λ, and we find that there are chaotic trajectories only when $\epsilon = 0.1$, $H = -0.5$ or -0.1. Specifically, 85 out of 276 ($\sim 31\%$) grid cells have chaotic trajectories when $\epsilon = 0.1$ and $H = -0.5$, and 109 out of 242 ($\sim 45\%$) grid cells have chaotic trajectories when $\epsilon = 0.1$ and $H = -0.1$. It shows even when $H \lesssim 0$, a large range of orbital parameters would still yield regular trajectories.

Next, we characterize the chaotic region in the parameter space of H and ϵ. We arbitrarily select the trajectories starting with $\Omega = 0$, $\omega = \pi/2$ and the maximum J for the given H and ϵ, where the associated e_1 and i of the initial condition are shown in Figure 3.14. Similarly, we integrate the tangent of the trajectories for $1000t_K$ to compute λ, and we plot λ as a function of H and ϵ in the left panel of Figure 3.7. The larger λ corresponds to the more chaotic systems. A large region in the parameter space is regular, and the system is chaotic only when $-0.6 < H < 0$ for larger ϵ. The Lyapunov timescale is $\sim 6t_K$ when $\epsilon \gtrsim 0.01$ and $-0.6 < H < 0$ (low e_1 and $i \gtrsim 40°$).

To justify that the regions with smaller λ are regular, we increase the run time to $4000t_K$, and we find that the Lyapunov exponents for the regular region decrease, while the Lyapunov exponents in the chaotic region remain at $\sim 6t_K$. Moreover, to avoid missing chaotic regions due to the specific choice of the initial condition, we vary the initial condition and make several contour plots of λ in the plane of H and ϵ. The right panel of Figure 3.7 shows the case for ω starts at 0, where the trajectories are also chaotic when $-0.6 < H < 0$.

3.6 Conclusion

The hierarchical three-body system in the test particle limit is common in a large range of astrophysical settings. The dynamical behavior of such systems may lead to retrograde objects, an enhanced rate for tidal disruption, and merger or collision events (e.g. Holman et al. (1997); Fabrycky & Tremaine (2007); Naoz et al. (2011, 2012); Chen et al. (2011); Bode & Wegg (2013), Naoz & Silk, in prep, Li et al., in prep). Here, we used a large range of the initial condition to systematically study the dynamics, including the underlying resonances, and the chaotic characteristics of the system.

First, we plotted the surface of section on the $J - \omega$ plane for a large range of energy H and two different ϵ to identify the underlying resonances (Figure 3.3). In the quadrupole level, the resonances occur at high H center around fixed points at $\omega = \pi/2$ and $3\pi/2$. On the other hand, the octupole level resonances center at $\omega = 0$, $\pi/2$, π, or $3\pi/2$ depending on the different energy levels, and we can identify resonances in all these energy levels. The octupole resonances cause the excitation of the e_1 in the high eccentricity coplanar case (corresponds to low H), shown in Li et al. (2014a). The overlap

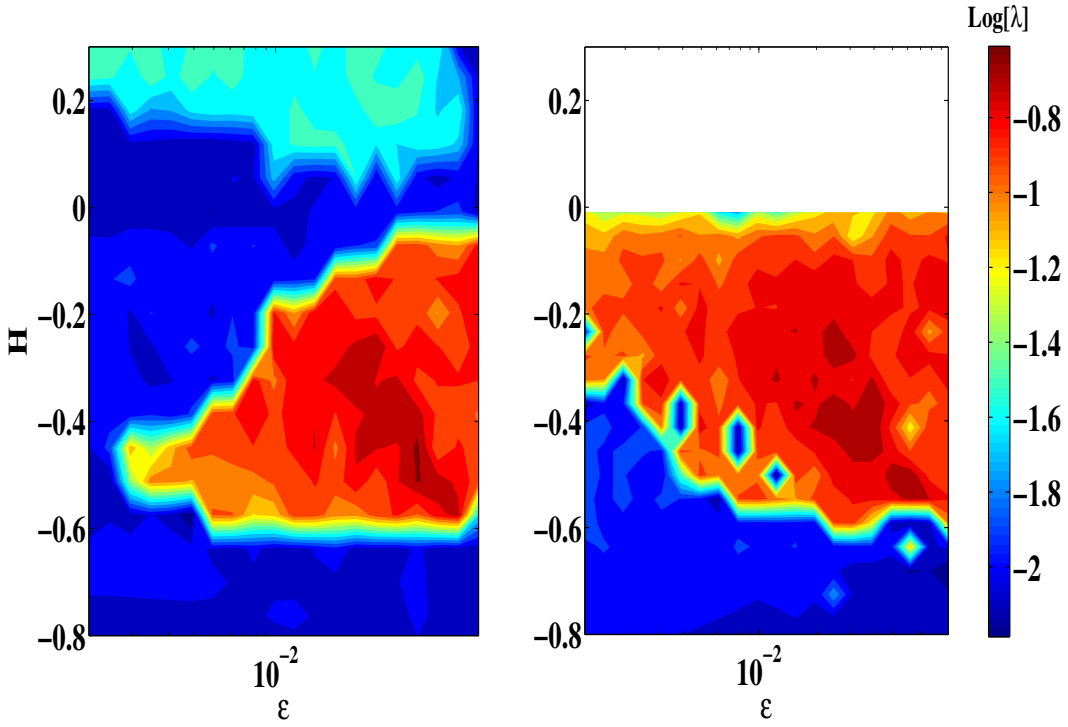

Figure 3.7: Lyapunov exponents with different H and ϵ. Run time $t = 1000$. Left Panel: we consider the following initial condition: $\omega_0 = \pi/2$, $\Omega_0 = 0$, $J_0 = 1$ or the maximum J at the energy boundary and $-0.8 < H < 0.3$. Right Panel: we consider the following initial condition: $\omega_0 = \Omega_0 = 0$, $J_0 = 1$ and $-0.6 < H < 0$. Note that for this choice of initial conditions no physical solution exists for $H > 0$. The colormap represents the value of the Lyapunov exponents λ. The yellow and red colors correspond to big Lyapunov exponents, which are associated with chaotic regions, and cyan and blue colors represent the regular regions.

of the quadrupole and octupole resonances causes the chaos for the low eccentricity and high inclination case (corresponds to higher H), (e.g. Naoz et al. (2011)).

The surfaces of section in the $J_z - \Omega$ plane not only show the octupole resonances but the condition when the orbit flips as J_z changes sign (Figure 3.4). At the quadrupole level, J_z is a constant, and there is no resonant zones in the $J_z - \Omega$ plane. However, at the octupole level, the resonant zones exist and lead to the flip of the orbit. As expected, similarly to the $J - \omega$ plane, it also shows that chaotic behavior exist when $H \lesssim 0$ for high ϵ.

Finally, we calculated the Lyapunov exponent for different H and ϵ to characterize the region where the evolution is chaotic. Consistently with the surface of section, we have found that the orbital evolution is chaotic when $H \lesssim 0$ (low e_1 high i cases). Specifically, the Lyapunov timescale $\sim 6t_K$.

By monitoring the trajectories, we find that the inner eccentricity may be excited and the orbit may flip for a circular high inclination orbit or for an eccentric and nearly coplanar orbit. This agrees with previous discussions in the literature for the flips with high inclination (Naoz et al. 2011; Lithwick & Naoz 2011; Katz et al. 2011), and the coplanar flips (Li et al. 2014a). In addition, we note that the flips with high inclination are chaotic and the coplanar flips are regular. This analysis can be applied to observed systems. Knowing roughly the orbital elements, one can identify the type of trajectories in the surface of section. Then, one can study the evolution features of the system without doing a large number of simulation for different initial condition. Moreover, our analysis could help predict the enhancement in the rate of tidal disruption events due to eccentricity excitation (Li, et al., in prep).

3.7 Acknowledgments

We thank Konstantin Batygin for helpful remarks. This work was supported in part by NSF grant AST-1312034 (for A.L.).

3.8 Appendix

First, we explore the range of H it can reach for the surface of section in the $J-\omega$ plane with $\Omega = 0$ and in the $J_z - \Omega$ plane with $\omega = 0$. We contour plot the maximum and minimum of H as a function of J and ω while setting $\Omega = 0$ in Figure 3.8, which depicts that the range of H is ~ -2.4 to ~ 3. Similarly, we plot the maximum and minimum of H for different J_z and Ω with $\omega = 0$ in Figure 3.9. It shows that H ranges from ~ -2.4 to 0. Accordingly, we plot the surface of section for $-2 < H < 1.2$ in Figure 3.3, since when $H > 1.2$ the section are similar to that when $H =\sim 1.2$, and we set $-2 < H < 0$ for the surface of section in Figure 3.4.

Next, we show the associated eccentricity and the inclination for the surface of section (Figure 3.3, 3.4) and the initial condition in Figure 3.5 and 3.6. This helps to connect the resulting dynamical behavior to the parameters in e_1 and i, that can be obtained more directly for observations.

In Figure 3.10 and 3.11, we plot the initial condition in the $J-\omega$ plane corresponding to the surfaces of section in Figure 3.3. e_1 can be calculated from the J value directly as $e_1 = \sqrt{1 - J^2}$, so higher J associates with lower e_1. On the other hand, i is lower for larger J when $H = -2, -1, -0.5$, and i is higher for larger J when $H = -0.1, 0.5, 1.2$.

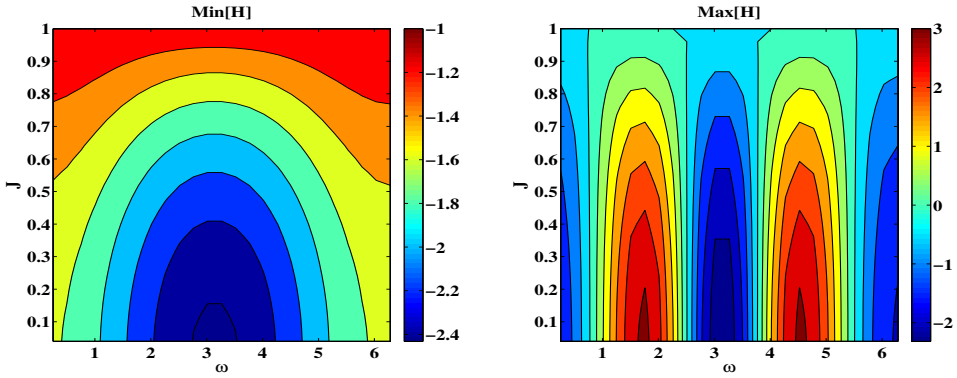

Figure 3.8: The maximum and minimum H it can reach for different $J-\omega$ with $\Omega = 0$. In this plot, we set $\epsilon = 0.1$. The energy range is about $-2.5 \sim 3$ in the $J-\omega$ plane. In addition, this explains the shape of the empty region (where there are no solution) in the surface of section plot.

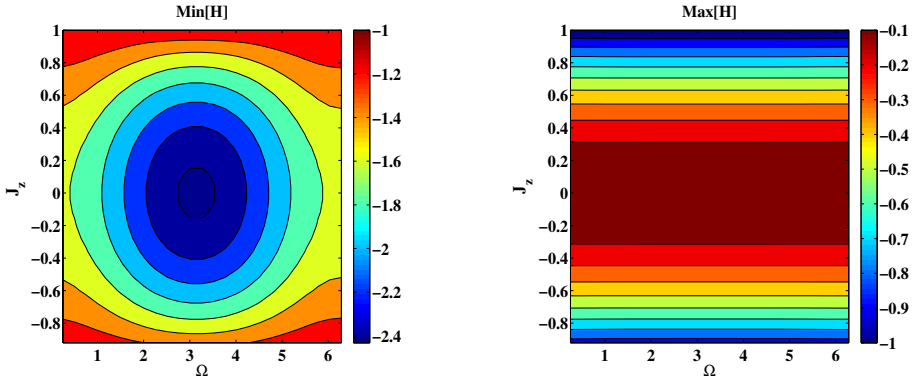

Figure 3.9: The maximum and minimum H it can reach for different $J_z-\Omega$ with $\omega = 0$. In this plot, we set $\epsilon = 0.1$. The energy range is about $-2.5 \sim 0$ in the $J_z-\Omega$ plane. In addition, this explains the shape of the empty region (where there are no solution) in the surface of section plot.

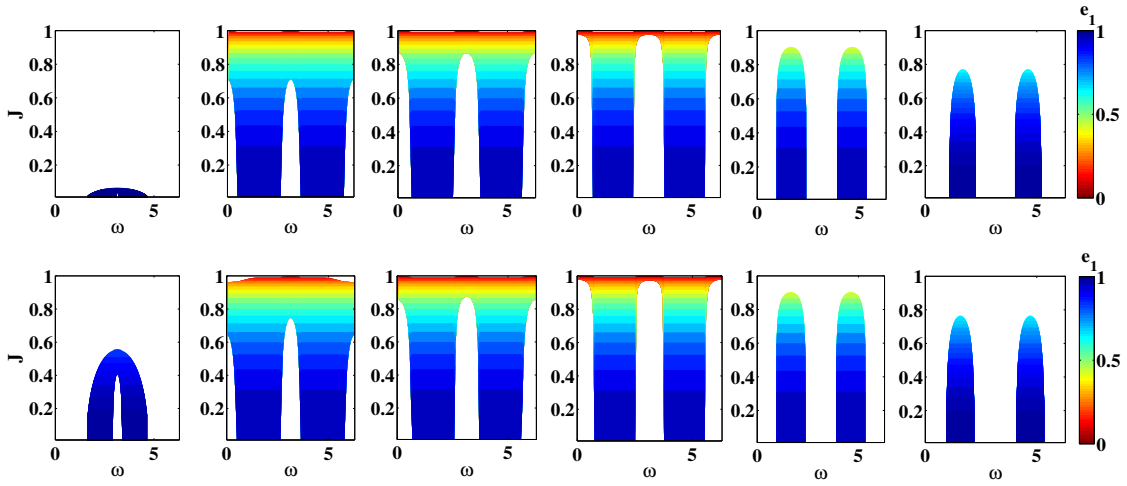

Figure 3.10: The eccentricities in the $J-\omega$ plane ($\Omega = 0$). Note that these are not the initial conditions, but directly the values of e_1 in the $J-\omega$ surface at fixed $\Omega = 0$ for the given H and ϵ. Similar to Figure 3.3, in the first row, $\epsilon = 0.001$ and in the second row, $\epsilon = 0.1$. The octupole terms are more dominant when ϵ is bigger.

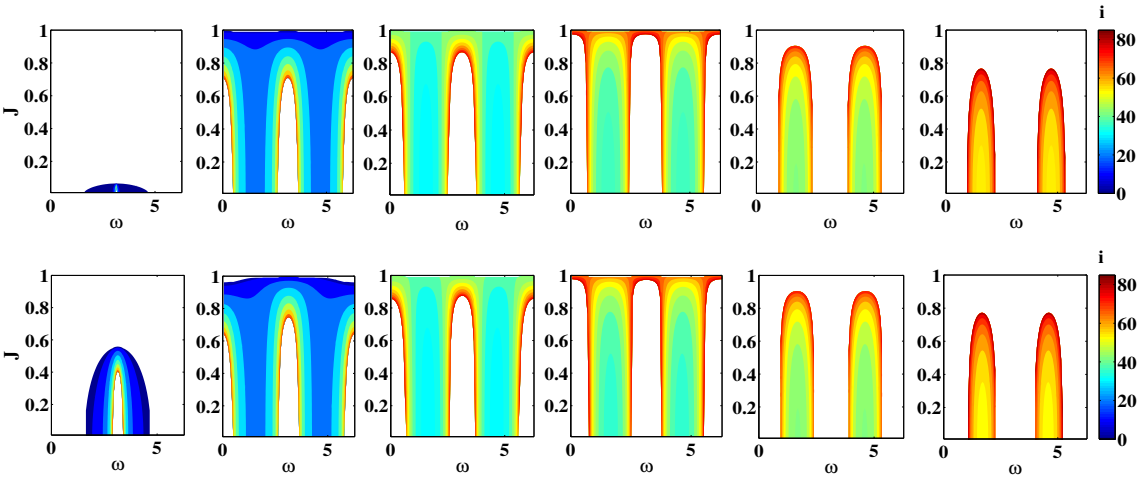

Figure 3.11: The inclinations in the $J-\omega$ plane ($\Omega = 0$). Note that these are not the initial conditions, but directly the values of i in the $J-\omega$ surface at fixed $\Omega = 0$ for the given H and ϵ. Similar to Figure 3.3, in the first row, $\epsilon = 0.001$ and in the second row, $\epsilon = 0.1$. The octupole terms are more dominant when ϵ is bigger.

Next, in Figure 3.12 and 3.13, we plot e_1 and i in the $J_z - \Omega$ plane, corresponding to the surface section in the $J_z - \Omega$ plane with $\omega = 0$ in Figure 3.4. When $i > 90°$, $J_z > 0$, and when $i < 90°$, $J_z < 0$. We find that e_1 is higher for lower H, and i is closer to $90°$ for higher H.

Furthermore, we plot the initial condition for the trajectories we selected to investigate the maximum e_1 in Figure 3.14. It shows that for the maximum e_1 plot (Figure 3.5), when $H \lesssim -1.2$, we monitor the trajectories that start with high eccentricity and low inclination. In this case, when $H \lesssim -1.7$, the orbit may flip at high ϵ and the maximum e_1 may reach $\sim 1 - 10^{-6}$ for high ϵ. When $-1.2 \lesssim H \lesssim 0$, we monitor trajectories that start with low eccentricity and high inclination. In this case, not much variations are seen unless $H \lesssim 0$. When $H > 0$, we monitor trajectories starting with high inclination $i \sim 80 - 90°$.

In the end, we plot the initial condition for the trajectories that are monitored for J_z or the flip of the orbit in Figure 3.15. When $H \lesssim -1$, we start the trajectories with high e_1 and low i; when $H \gtrsim -1$, we start the trajectories with low e_1 and high i. The orbit may flip with $-0.4 \lesssim H \lesssim 0$ at high ϵ for trajectories starting with low e_1 and high i, and the orbit may flip with $H \lesssim -1.5$ when the trajectories start with high e_1 and low i.

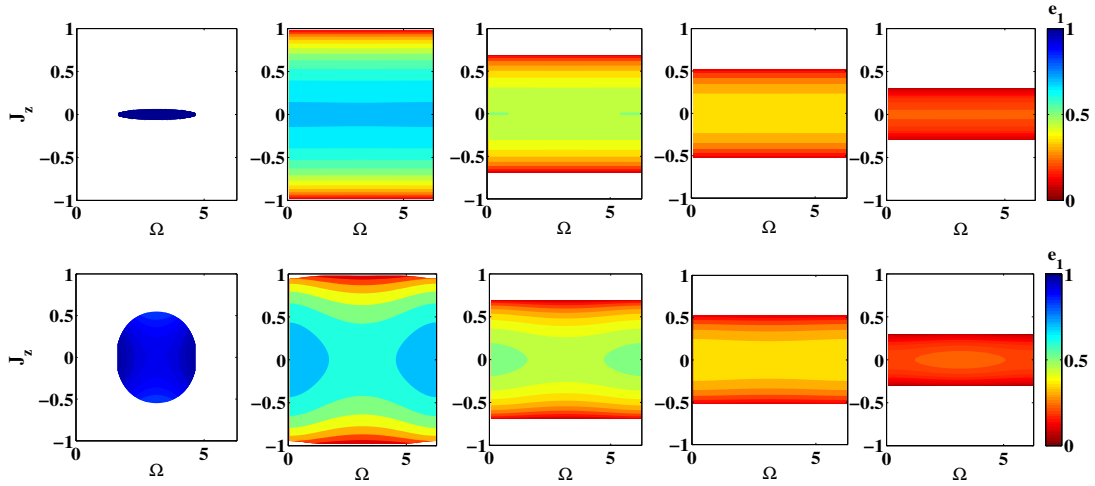

Figure 3.12: The eccentricities on the $J_z - \Omega$ plane ($\omega = 0$). Note that these are not the initial conditions, but directly the values of e_1 in the $J_z - \Omega$ surface at fixed $\omega = 0$ for the given H and ϵ. Similar to Figure 3.4, in the first row, $\epsilon = 0.001$ and in the second row, $\epsilon = 0.1$. The octupole terms are more dominant when ϵ is bigger.

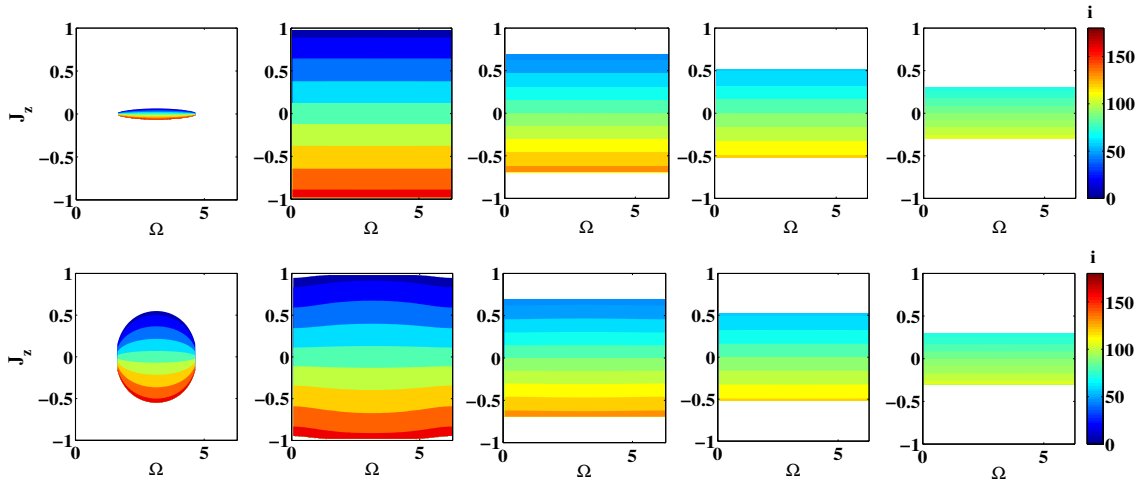

Figure 3.13: The inclinations in the $J_z - \Omega$ plane ($\omega = 0$). Note that these are not the initial conditions, but directly the values of i in the $J_z - \Omega$ surface at fixed $\omega = 0$ for the given H and ϵ. Similar to Figure 3.4, in the first row, $\epsilon = 0.001$ and in the second row, $\epsilon = 0.1$. The octupole terms are more dominant when ϵ is bigger.

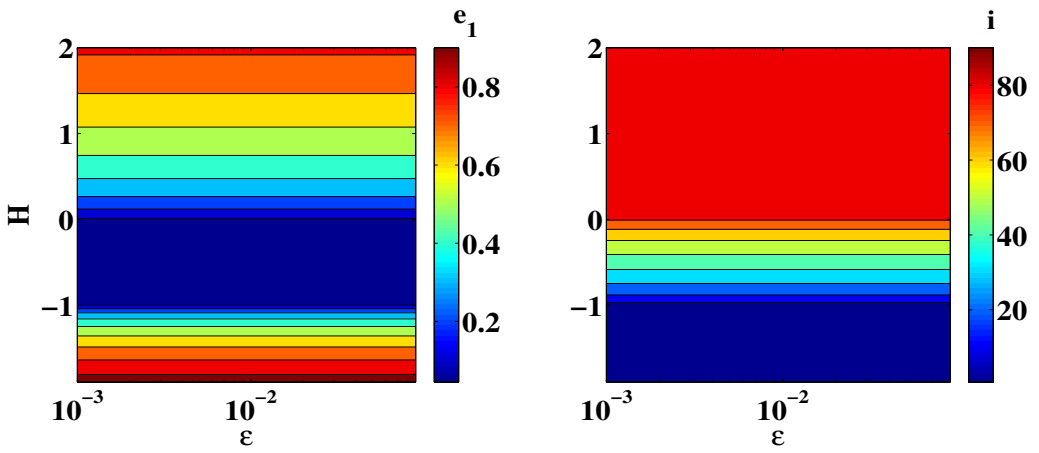

Figure 3.14: e_1 and i with $\omega_0 = \pi$ ($H < -1$), $\omega_0 = \pi/2$ ($H > -1$), $\Omega = 0$ and J at the upper energy boundary. This is associated with the initial condition for Figure 3.5, i.e. the initial e_1 and i_1 for each run at fixed ϵ and H.

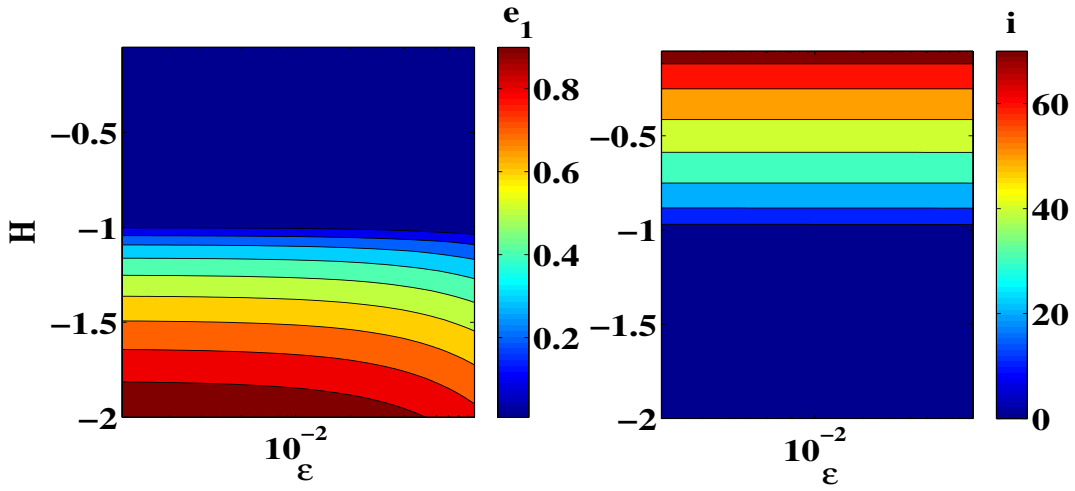

Figure 3.15: e_1 and i_1 with $\Omega = \pi$, $\omega = 0$ and J_z are at lower energy boundary for different H and ϵ. This is associated with the initial condition in Figure 3.6, i.e. the initial e_1 and i_1 for each run at fixed ϵ and H.

Chapter 4

The Dynamics of the Multi-planet System Orbiting Kepler-56

This thesis chapter originally appeared in the literature as

Li, G., Naoz, S., Valsecchi, F., Johnson, J. & Rasio, F. The Dynamics of the Multi-planet System Orbiting Kepler-56, *The Astrophysical Journal*, 794, 131, 2014

Abstract

Kepler-56 is a multi-planet system containing two coplanar inner planets that are in orbits misaligned with respect to the spin axis of the host star, and an outer planet. Various mechanisms have been proposed to explain the broad distribution of spin-orbit angles among exoplanets, and these theories fall under two broad categories. The first is based on dynamical interactions in a multi-body system, while the other assumes that

disk migration is the driving mechanism in planetary configuration and that the star (or disk) is titled with respect to the planetary plane. Here we show that the large observed obliquity of Kepler 56 system is consistent with a dynamical origin. In addition, we use observations by Huber et al. (2013) to derive the obliquity's probability distribution function, thus improving the constrained lower limit. The outer planet may be the cause of the inner planets' large obliquities, and we give the probability distribution function of its inclination, which depends on the initial orbital configuration of the planetary system. We show that even in the presence of precise measurement of the true obliquity, one cannot distinguish the initial configurations. Finally we consider the fate of the system as the star continues to evolve beyond the main sequence, and we find that the obliquity of the system will not undergo major variations as the star climbs the red giant branch. We follow the evolution of the system and find that the innermost planet will be engulfed in ~ 129 Myr. Furthermore we put an upper limit of ~ 155 Myr for the engulfment of the second planet. This corresponds to $\sim 3\%$ of the current age of the star.

4.1 Introduction

Over the past few years, measurements of the sky-projected obliquity of exoplanets have found that large obliquities and even retrograde systems are common among hot Jupiters (e.g. Fabrycky & Winn 2009; Triaud et al. 2010; Morton & Johnson 2011; Moutou et al. 2011; Albrecht et al. 2012; Hébrard et al. 2013). Recently, Hirano et al. (2012), Sanchis-Ojeda et al. (2012), Albrecht et al. (2013), Chaplin et al. (2013) and Van Eylen et al. (2014) have measured the obliquity of six transiting multi-planet systems discovered by the NASA *Kepler* mission, and found they all have low obliquities.

However, Huber et al. (2013), using asteroseismology, showed that large obliquities are not confined to Hot Jupiter systems. In fact Kepler-56 has two, low mass, inner planets whose orbit normal is tilted with respect to the stellar spin axis.

Several mechanisms have been suggested to explain the formation of misaligned planets. These theories can be divided into two categories. The first is based on tilting the orientation of an inner planet compared to the stellar spin axis. This category includes scattering and secular dynamical effects between a planet and a companion, or other planets in the system that can produce large obliquities (e.g., Fabrycky & Tremaine 2007; Chatterjee et al. 2008; Nagasawa et al. 2008; Naoz et al. 2011, 2012, 2013a; Wu & Lithwick 2011; Li et al. 2014a; Li et al. 2014b; Valsecchi & Rasio 2014a,b). These mechanisms predict that an inner planet with a large obliquity has an outer perturber which is inclined with respect to the plane of the inner planet, the perturber can be either a stellar companion or a planet, or even multiple planets. In the second category, planets move inward from their birthplaces beyond the snow line by migrating inward through the protoplanetary disk (e.g. Lin & Papaloizou 1986; Masset & Papaloizou 2003). Large obliquities can then be produced either by tilting the stellar spin axis with respect to the orbital angular momentum (e.g. Winn et al. 2010; Lai et al. 2010; Rogers et al. 2012, 2013; Spalding & Batygin 2014), or by tilting the protoplanetary disk (Bate et al. 2010; Batygin 2012). This second category of models predicts that the various planets in a system should lie roughly in the same plane since they were confined to the same flattened disk.

Here we focus on the dynamical mechanism that produced the large obliquities in the Kepler-56 planetary system. Most of the theoretical studies investigating large obliquities focused on Hot Jupiters, mainly because these were observed to have large

obliquities. The underlining physics of producing a misalignment in the presence of a perturber is very similar. Thus, such studies are relevant for investigating the Kepler-56 system (as we will show below).

Kepler multiple systems are typically packed, small sized ($\sim 1-10$ $R_\oplus$ e.g. Lissauer et al. 2011; Swift et al. 2013) and close–in ($\sim 1-100$ d, e.g., Steffen & Farr 2013) systems. At face value these configurations may indicate that dynamical and secular processes are suppressed, since these systems better resemble the theoretical outcome of planet migration in the protoplanetary disk, given their low mutual inclinations (Lissauer et al. 2011; Fang & Margot 2012). Therefore, a large obliquity in a multi-planet system may be used as a laboratory to test the two categories of models summarized above. In other words, since it seems that these planets form in a disk, a tilt of the protoplanetary disk or of the star, will cause the multiple planets to show the same obliquity.

Kepler-56 is an evolved star at the base of the red giant branch in the HR diagram with $m_\star = 1.32$ $M_\odot$ $R_\star = 4.23$ $R_\odot$ and an age of 3.5 Gyr (Huber et al. 2013). Furthermore, Huber et al. (2013) showed that the innermost planet ($m_b = 0.07$ M_J, $R_b = 0.65$ R_J, hereafter planet "b") has a period of 10.5 d, and a period of 21.4 d for the other planet ($m_c = 0.57$ M_J, $R_c = 0.92$ R_J, hereafter planet "c"). The mutual inclination between these two planets is measured to be $< 5°$. Kepler-56 is an interesting system as it raises many questions regarding its formation and future evolution. Most importantly, Huber et al. (2013), measured the obliquity of the system using asteroseismology and placed a lower limit on the true obliquity of the two inner planets of $\psi > 37°$. The dynamical analysis of Huber et al. (2013) favors the scattering and later torquing scenario.

Here we use Kepler-56's current observations to compute the probability distribution for its obliquity. (Huber et al. (2013) reported observations already give enough information to calculate such distribution.) This enables us to also put strong constrains on the probability distribution of the outer planet's inclination with respect to the innermost two. Furthermore, we estimate that the two inner planets will be engulfed in $\sim$ 129 Myr and $\lesssim$ 155 Myr, respectively. The engulfment of the inner planets is consistent with the the deficit in short period planets around retired A stars (e.g. Johnson et al. 2007; Sato et al. 2008; Bowler et al. 2010; Schlaufman & Winn 2013).

The paper is structured as follows. We calculate the obliquity distribution function from observations, and show that the current observations give more information than just a lower limit (Section 4.2). We then discuss the current obliquity precession as a function of the system initial conditions (Section 4.3.2) and show that combining the physical understanding and the observed distribution, we can infer the outer most planet orbital inclination with respect to the innermost two as a function of the initial configuration (Section 4.3.3). We also calculate the orbit and obliquity future evolution as the star further ascends the giant branch (Section 4.4). We finally offer our discussion (Section 4.5).

4.2 The Obliquity Distribution Function

Huber et al. (2013) analyzed the stellar oscillations observed in the *Kepler* photometry and used the splitting of the observed oscillation frequencies to measure the inclination between the stellar spin axis and the line of sight, finding $i_{ls}^{\star} = 47^{\circ} \pm 6$. With the transit photometry, Huber et al. also measured the inclination of the inner planet's orbit with

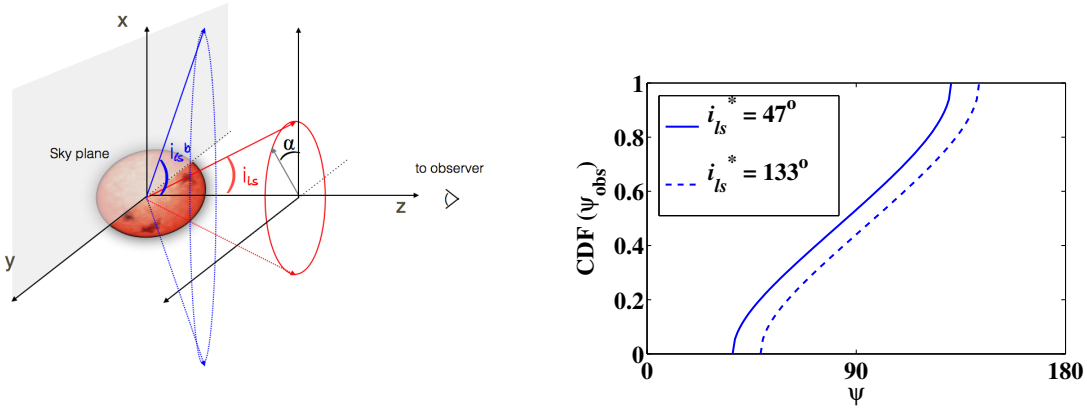

Figure 4.1: *The cumulative distribution function of ψ.* This calculation is based on the observed parameters from Huber et al. (2013). We assume that the angle between the stellar spin axis ($\mathbf{n}_s$) and the normal to the innermost orbit ($\mathbf{n}_{in}$) in the azimuthal direction around the line of sight (i.e., α in the schematic to the left) is random (taken from a uniform distribution). This enable us to produce a distribution function and not only a lower limit, see text for more details. We show a schematic of the geometry in the right panel. The solid curve corresponds to $i^{\star}_{ls} = 47^{\circ} \pm 6$, and the dashed curve corresponds to $i^{\star}_{ls} = 133^{\circ} \pm 6$ (due to the degeneracy in the asteroseismology measurements).

respect to the line of sight, finding $i^{b}_{ls} = 83.84^{\circ}{}^{+0.26}_{-0.25}$. Together, these angles place a lower limit on the three-dimensional angle between the stellar spin axis and planetary orbital plane of $\psi > 37^{\circ}$.

The angle between the normal of the orbit and the stellar spin is not simply $i^{b}_{ls} + i^{\star}_{ls}$ since, for example, the angle, i^{b}_{ls} can have different values on the sky plane (different values of α as shown in Figure 4.1). In this simple geometrical configuration (see Figure 4.1, left panel) and defining $\mathbf{L}_{in}$ and $\mathbf{S}$ as the angular momentum of the innermost orbit and stellar spin, respectively, the obliquity is defined by the scalar product between the three dimensional spin axis unit vector $\mathbf{n}_s = \mathbf{S}/S = (\sin i^{\star}_{ls}, 0, \cos i^{\star}_{ls})$ and the three dimensional normal to the innermost orbit $\mathbf{n}_{in} = \mathbf{L}_{in}/L = (\sin i^{b}_{ls}, 0, \cos i^{b}_{ls})$, in random orientation with each other:

$$\cos\psi = \mathbf{n}_s \cdot \mathbf{R}_{ls}\mathbf{n}_{in} \ . \tag{4.1}$$

Here

$$\mathbf{R_{ls}}(\alpha) = \begin{pmatrix} \cos\alpha & -\sin\alpha & 0 \\ \sin\alpha & \cos\alpha & 0 \\ 0 & 0 & 1 \end{pmatrix} \tag{4.2}$$

is the rotation matrix in the azimuthal direction around the line of sight. We assume that α, the angle between the stellar spin and the orbital angular momentum in the azimuthal direction around the line of sight, is uniformly distributed. It is sufficient to multiply only once by the rotation matrix, with the random angle. Therefore, from Equation (4.1) we can estimate the cumulative distribution function of ψ. As shown in the right panel of Figure 4.1, the lower limit on ψ is of course the same one found by Huber et al. (2013), i.e,. $\psi > 37°$, but an upper limit of 131° also exists and both these values have the same probability, which is larger than the probability of the angles in the range of $37° < \psi < 131°$. We use ψ_{obs} to denote the observationally constrained value of ψ. Note that due to the degeneracy in the asteroseismology measurements, $i^{\star}_{ls}$ could also be $133° \pm 6$. Setting $i^{\star}_{ls} = 133°$, ψ_{obs} is in the range of $49° < \psi < 143°$ (see the dashed line in Figure 4.1). Therefore, adding these two pieces together, the distribution of ψ_{obs} is symmetric over $37° < \psi < 143°$. This distorts ψ_{obs} only slightly, because i^{b}_{ls} is almost 90°. Accordingly, we adopt $i^{\star}_{ls} = 47° \pm 6$, and have ψ_{obs} constrained in the range of $37° < \psi < 131°$ for the following discussion.

4.3 Obliquity and Inclination Evolution in the Presence of an Outer Perturber

4.3.1 Overview of the System Architecture

In a sufficiently packed multi–planet system the planets' apsidal precessions are dictated by both the outer orbital companion and gravitational interactions between the two inner planets. In our case, the inner two planets are packed very close together, which suppresses eccentricity excitations that may arise due to the gravitational perturbations induced by the perturber (planet "d"). If this perturber is inclined with respect to the orbital plane of the inner planets, then the plane will precess (e.g., Innanen et al. 1997; Takeda et al. 2008; Mardling 2010; Kaib et al. 2011; Boué & Fabrycky 2014). However the exact evolution of the obliquity and its current value are highly sensitive to the initial configuration of the system and, specifically, to the inclination of the outer orbit with respect to the inner one.

We first evolve the system with direct N-body integration using `Mercury` software package (Chambers & Migliorini 1997) and then use our numerical results to evaluate the spin-orbit evolution (§ 4.3.2). The latter is being set by the point mass dynamics (see below for more details). The system orbital parameters are set initially to $a_b = 0.1028$ AU, $a_c = 0.1652$ AU (based on the orbital solution provided by Huber et al. 2013). Since the properties of the outer body are yet unknown, we set $a_d = 2$ AU as an illustrative example following the dynamical simulation of Kepler 56 in Huber et al. (2013). We work in the invariable plane where the z axis is parallel to the total angular momentum, $\mathbf{L_{tot}}$. Therefore, the inclinations of the orbits are defined with respect to the total angular

momentum. In this frame, we set for simplicity $\omega_b = \omega_c = \omega_d = \Omega_b = \Omega_c = \Omega_d = 0$, where ω_j (Ω_j) is the argument of perihelion (longitude of ascending nodes) of the planet j. In addition, we simplify the system by imposing zero mutual inclination between the two inner planets and by setting the eccentricity of the two inner planets to zero (which is consistent with Huber et al. 2013, estimate). Following Huber et al. (2013), we also take the mean anomalies to be $f_b = 57°$, $f_c = 182°$ and $f_d = 256°$. The outer orbit eccentricity (e_d) does not affect the evolution of the system significantly, thus we only show results for $e_d = 0$. The parameter that sets the system evolution is the mutual inclination between the outer planet's orbit and the inner plane, $i_{\rm mut}$, which we discuss in details below. Given the observed obliquity distribution (Figure 4.1) we calculate next the probability distribution of the inclination of the system as a function of the system initial conditions.

4.3.2 Dynamics of Kepler 56

In the presence of a tilted outer orbit with inclination $i_{\rm mut}$, the two inner planets will precess around the total angular momentum vector. Note that the precession of the orbit due to the oblateness of the star is negligible in this case. The torque felt by planet "b" due to stellar oblateness[1] is more than two orders of magnitude smaller than the torque due to planet "c" (see Tremaine et al. 2009 and Tamayo et al. 2013). Therefore, the orbital evolution is not affected by the torque due to the stellar oblateness, and the system is in the "pure orbital regime" (Boué & Fabrycky 2014). We thus obtain the

[1]The J_2 coefficient, which approximates the non-spherical shape by the star level of oblateness, was calculated following Eggleton et al. (1998).

orbital evolution from an N-body simulation.

The obliquity angle is defined with respect to the innermost planet's orbital angular momentum, $\mathbf{L}_b$. Thus, a natural coordinate choice for the spin is the Laplace–Runge–Lenz $(\hat{\mathbf{q}}_b, \hat{\mathbf{h}}_b, \hat{\mathbf{e}}_b)$. Here, $\hat{\mathbf{e}}_b$ is the eccentricity vector (whose direction is toward the pericenter of planet "b" orbit), $\hat{\mathbf{h}}_b$ is the unit vector parallel to the orbital angular momentum of planet "b" (the vector $\mathbf{h}_b$ is the specific angular momentum vector, i.e., $\mathbf{L}_b = m_\star m_b/(m_\star + m_b)\mathbf{h}_b$), and $\hat{\mathbf{q}}_b$ completes the right-hand triad of unit vectors. In this notation the precession of the stellar spin, $\mathbf{S} = (S_e, S_q, S_h)$, due to one planet is simply (Eggleton et al. 1998)

$$\frac{d\mathbf{S}}{dt}_{prec,a} = \mathbf{S} \times \mathbf{K}_b + \frac{m_\star m_b}{m_\star + m_b} h_b / I_2 (-\tilde{Y}_b \hat{\mathbf{e}}_b + \tilde{X}_b \hat{\mathbf{q}}_b + \tilde{W}_b \hat{\mathbf{h}}_b) \ , \tag{4.3}$$

where $h_b = [G(m_\star + m_b) a_b (1+e_b^2)]^{1/2}$, G is the gravitational constant, and $\mathbf{K}_b = (X_b, Y_b, Z_b)$ represents the precession due to the orbital evolution:

$$X_b = \frac{di_b}{dt} \cos\omega_b + \frac{d\Omega_b}{dt} \sin\omega_b \sin i_b \ , \tag{4.4}$$

$$Y_b = -\frac{di_b}{dt} \sin\omega_b + \frac{d\Omega_b}{dt} \cos\omega_b \sin i_b \ , \tag{4.5}$$

$$Z_b = \frac{d\omega_b}{dt} + \frac{d\Omega_b}{dt} \cos i_b \ , \tag{4.6}$$

and $\tilde{X}_b$, $\tilde{Y}_b$ and $\tilde{W}_b$ represent the torque due to the stellar oblateness and the tidal

dissipation:

$$\tilde{X}_b = -\frac{m_b k_\star R_\star^5}{\mu \dot{l} a_b^5} \frac{S_h S_e}{(1-e_b^2)^2} - \frac{S_q}{2\dot{l} t_{F\star}} \frac{1+(9/2)e_b^2+(5/8)e_b^4}{(1-e_b^2)^5} , \tag{4.7}$$

$$\tilde{Y}_b = -\frac{m_b k_\star R_\star^5}{\mu \dot{l} a_b^5} \frac{S_h S_q}{(1-e_b^2)^2} - \frac{S_e}{2\dot{l} t_{F\star}} \frac{1+(9/2)e_b^2+(5/8)e_b^4}{(1-e_b^2)^5} , \tag{4.8}$$

$$\tilde{W}_b = \frac{1}{t_{F\star}} \Big[\frac{1+(15/2)e_b^2+(45/8)e_b^4+(5/16)e_b^6}{(1-e_b^2)^{13/2}} - \frac{S_h}{\dot{l}} \frac{1+3e_b^2+(3/8)e_b^4}{(1-e^2)^5} \Big] , \tag{4.9}$$

where $\dot{l} = \sqrt{G m_\star / a_b^3}$, and

$$t_{F\star} = \frac{t_{V\star}}{9} \frac{m_\star^2}{(m_\star + m_b) m_b} \left(\frac{a_b}{R_\star} \right)^8 \frac{1}{(1+2k_2)^2} , \tag{4.10}$$

To calculate the orbital evolution due to the orbital precession (the $\mathbf{K}_b$ term), we take the time evolution of ω, Ω and i of planets "b" directly from the N-body integration. This dominates the obliquity variation. The tidal effects are negligible until planet b is almost engulfed (see discussion on the future evolution of Kepler-56 in §4.4). The timescale for the evolution of planet b's orbital separation due tidal dissipation in the star is defined in terms of the stellar viscous timescale $t_{V\star}$. $t_{V\star}$ is set to be 50 yr and kept constant, where $t_{V\star}$ corresponds to $Q \sim 10^6$ for a 10 day orbit. The parameter k_2 is the apsidal precession constant, which is related to the Love parameter k_L via $k_2 = 2k_L$ (a similar equation exists for planet "b" and "c"). Note that the effects of tides in the planets are negligible. In fact, assuming a viscous timescale corresponding to $Q = 12$ and 10^5 for planet "b" and "c" (Murray & Dermott 1999), respectively, the small planets radii yield much longer tidal timescales [see equation (4.10)]. In any case,

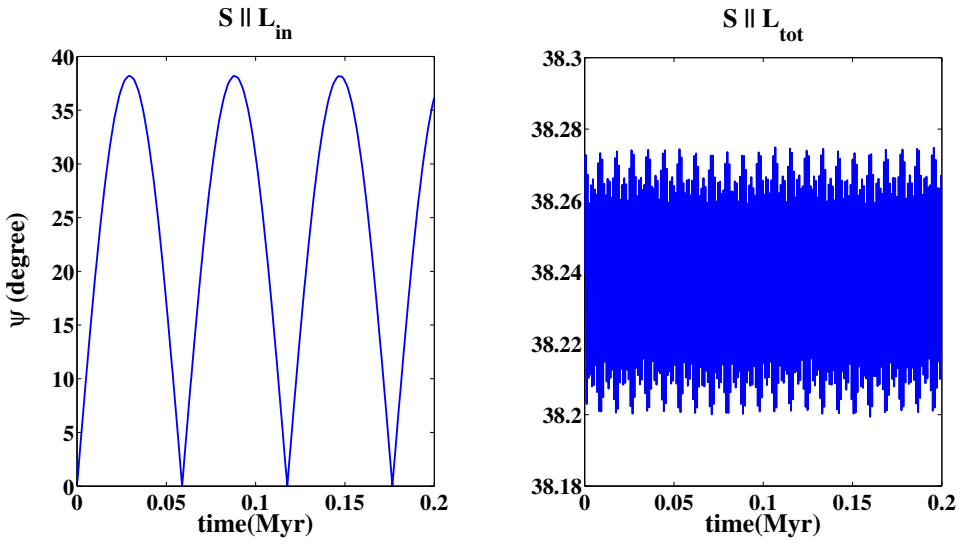

Figure 4.2: **Short time scale obliquity evolution for the two scenarios.** The left panel shows the evolution in the $\mathbf{S}||\mathbf{L_{in}}$ with an initial $i_{\rm mut} = 20°$ scenario while the right panel is for the $\mathbf{S}||\mathbf{L_{tot}}$ with an initial $i_{\rm mut} = 40°$. The orbital evolution was done using direct N-body integration.

the unconstrained nature of exoplanets makes it difficult to conclude how their tidal coefficients evolve.

Equations (4.3)–(4.10) imply that the time evolution of $i_{\rm mut}$ (and thus ψ) depends on the initial system's configuration. This can be constrained from the observed obliquity distribution. In Figure 4.2 we show the evolution of ψ assuming two possible initial configurations: $\mathbf{S}$ parallel to $\mathbf{L_{in}}$ and $i_{\rm mut} = 20°$ (left, hereafter "$\mathbf{S}||\mathbf{L_{in}}$" scenario), and $\mathbf{S}$ parallel to $\mathbf{L_{tot}}$ and $i_{\rm mut} = 40°$ (right, hereafter "$\mathbf{S}||\mathbf{L_{tot}}$" scenario), where $\mathbf{L_{in}}$ and $\mathbf{L_{tot}}$ are the orbital angular momentum of the *inner* two planets and the *total* orbital angular momentum, respectively. We show below that these values for $i_{\rm mut}$ give a misalignment of at least 37° during the evolution (the minimum value constrained observationally).

In the $\mathbf{S}||\mathbf{L_{in}}$ scenario, ψ oscillates between well-aligned ($\psi = 0°$) and $\sim 2 \times i_{\rm mut}$

($\sim 38.2°$). In this case, we postulate that the system formed initially in a disk and planet "d" was perhaps scattered to large inclinations (e.g., Rasio & Ford 1996), causing the obliquity angle to precess between 0° and $\sim 2 \times i_{\rm mut}$. Another possible case for this configuration is accretion of material onto the protoplanetry disk, which can tilt the outer parts of the disk and the total angular momentum (Bate et al. 2010; Tremaine 2011; Thies et al. 2011). Therefore, in the $\mathbf{S}||\mathbf{L_{in}}$ scenario, $\psi \sim 40°$ can be produced by an initial inclination $i_{\rm mut} > 20$. Note that a retrograde configuration with $i_{\rm mut} = 160°$ can also produce $\psi \sim 40°$.

In the $\mathbf{S}||\mathbf{L_{tot}}$ scenario, ψ remains close to the initial value. This configuration could have occurred if the inner parts of the disk were warped perhaps due to magnetic interactions with the inner disk edge (e.g., Lai et al. 2010). Therefore in the $\mathbf{S}||\mathbf{L_{tot}}$ scenario, $\psi \sim 40°$ can be produced by an initial $i_{\rm mut} = 40°$.

We show below that for the $\mathbf{S}||\mathbf{L_{in}}$ scenario ψ is more likely to be detected in the maximum (at $\sim 38.2°$) where the derivative is closer to zero. For each possible obliquity value $\tilde{\psi} \in (0°, 180°)$, we derived a cumulative distribution function of the mutual inclination, where $\mathrm{CDF}(\tilde{\psi}|i_{\rm mut}) = \Delta t(\psi < \tilde{\psi}|i_{\rm mut})/t$, where Δt is the time interval. This quantity will be used below to estimate the probability distribution of the system configuration for the actual observations. We run 35 N-body runs, for an array of initial inclinations $i_{\rm mut}$ between 5° and 175°, and calculate the cumulative probability for the two scenarios.

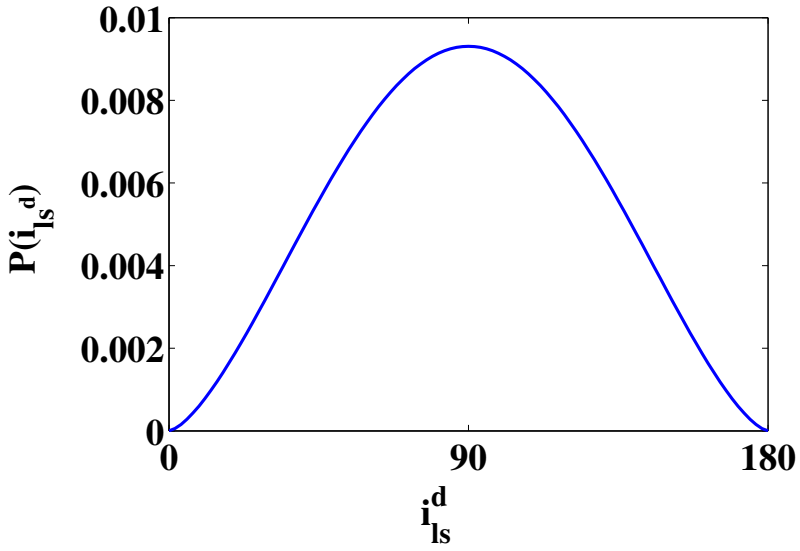

Figure 4.3: **The probability distribution of** i_{ls}^{d}. We calculate this probability assuming m_d follows the mass function of Cumming et al. (2008).

4.3.3 Inferring the Inclination Distribution Function from Observations

When the spin-orbit misalignment is due to the dynamical interaction between the planets, the obliquity distribution function derived from observations (Section 4.2, Figure 4.1) can be used to place strong constrains on the mutual inclination between the inner planets and planet "d", i.e., $i_{\rm mut}$. We calculate the conditional probability distribution of $i_{\rm mut}$ given the observed distribution ψ_{obs}, i.e., $p(i_{\rm mut}|\psi_{obs})$. This posterior probability can be written as

$$p(i_{\rm mut}|\psi_{obs}) = \frac{p(\psi_{obs}|i_{\rm mut})p(i_{\rm mut})}{p(\psi_{obs})} \ , \tag{4.11}$$

where $p(\psi_{obs})$ is a normalization term, which we disregard because the shape of the distribution is of larger significance than the absolute probability here, and the absolute probability is out of the scope of this paper.

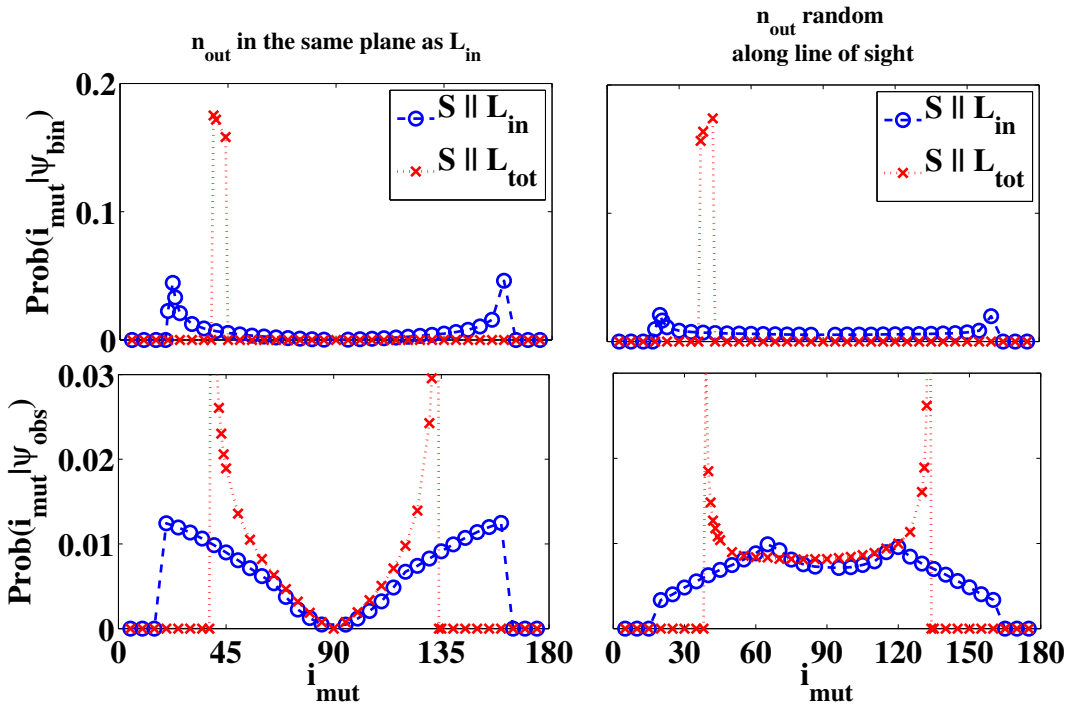

Figure 4.4: **The probability distribution of the mutual inclination inferred from observations.** We consider the two scenarios $\mathbf{S}||\mathbf{L_{in}}$ (blue circle) $\mathbf{S}||\mathbf{L_{tot}}$ (red lines), and two possible probability distribution on $p(i_{\rm mut})$. The *left panels* are for $\mathbf{n}_d$ lying in the plane defined by $\mathbf{n}_{in}$ and the line of sight, i.e., $i_{\rm mut} = i^b_{ls} - i^d_{ls}$, while in the *right panels* we assume random orientation (see text). The *top panels* show a specific example for the advantage in having a more precise observation $\psi_{bin} = 37 - 43^\circ$, and the *bottom panels* show the results form the observed cumulative distribution (Figure 4.1).

Furthermore, we use the distribution function of planet "d" line of sight inclination, i^d_{ls}, to estimate the prior probability, $p(i_{\rm mut})$. Note, that the actual value of $m_d \sin i^d_{ls}$ only affect the normalization of the probability, but since we care about the shape of the probability we can ignore this. Note that if we assume the outer orbit to be isotropically distributed, the probability density function for i^d_{ls} takes the form of $\sin i^d_{ls}$. This suggests that the most probable value for i^d_{ls} is 90°.

Following Ho & Turner (2011) we calculate the probability $p(i^d_{ls})$ assuming Cumming

et al. (2008) mass function for m_d (see Figure 4.3). Note that the distribution in Cumming et al. (2008) is for $m \sin i$, not m. However, since the power law index is large, we use this power law for the mass distribution according to Ho & Turner (2011). The angle we are actually interested in is the angle between the normal to the outer orbit $\mathbf{n}_{out}$ and the normal to the inner orbit $\mathbf{n}_{in}$. While i_{ls}^b has been measured to be 83.84°, (Huber et al. 2013) we have no information about the orientation of these two vectors on the plane of the sky. Consider first the case where the three dimensional normal to the outer orbit, $\mathbf{n}_d$ lies in the plane defined by $\mathbf{n}_{in}$ and the line of sight. This yields a simple relation between the different angles, i.e., $i_{\rm mut} = i_{ls}^b - i_{ls}^d$. Therefore, $p(i_{\rm mut}) = p(i_{ls}^b - i_{ls}^d)$, where the latter is calculated from $p(\sin i_{ls}^d)$ following Ho & Turner (2011). Their mass distribution function yields small m_d (compared to the measured $m_d \sin i_{ls}^d$), thus $\sin i_{ls}^d$ is more likely to be close to its maximum of 1. This suggests angles near 90 degrees for i_{ls}^d, which implies that $i_{\rm mut} = i_{ls}^b - i_{ls}^d$ is more likely to have a small value.

However, another possible prior is that $\mathbf{n}_d$ has a random orientation (similar to the configuration depicted in the left side of Figure 4.1). Thus, as in Section 4.2, we multiply the normal to the orbit with the rotation matrix in Eq. (4.2) assuming a random azimuthal angle α, i.e.,

$$\cos i_{\rm mut} = \mathbf{n}_{out}(i_{ls}^d) \cdot \mathbf{R}_{ls}(\alpha) \mathbf{n}_{in}(i_{ls}^b) \ , \tag{4.12}$$

where $\mathbf{n}_{out}(i_{ls}^d)$ is chosen with $p(\sin i_{ls}^d)$ distribution, which gives $p(i_{\rm mut})$. This prior also gives a high probability for large values of $i_{\rm mut}$, as this case covers large parts of the parameter space. Below we consider these two cases.

The probability of ψ_{obs} for a given $i_{\rm mut}$, i.e., $p(\psi_{obs}|i_{\rm mut})$ can be calculated from

$$p(\psi_{obs}|i_{\rm mut}) = \int_0^\infty p(\tilde{\psi}|i_{\rm mut}) p_{obs}(\tilde{\psi}) d\tilde{\psi} \ , \tag{4.13}$$

where $p_{obs}(\psi)$ was computed in Section 4.2, Figure 4.1. The probability $p(\psi|i_{\rm mut})$ is calculated from theory for the two different cases, i.e., $\mathbf{S}||\mathbf{L_{tot}}$ and $\mathbf{S}||\mathbf{L_{in}}$. In the discrete description we calculate the probability distribution of $i_{\rm mut}$ for each ψ. This can be easily derived from the cumulative distribution function calculated in Section 4.2, Figure 4.1.

Using Equations (4.11) − (4.13) we can find the mutual inclination probability function given the observed obliquity distribution. This is depicted in Figure 4.4, *bottom panels*. We consider the two initial configurations scenarios, i.e., $\mathbf{S}||\mathbf{L_{tot}}$ and $\mathbf{S}||\mathbf{L_{in}}$, and the two $p(i_{ls}^{d})$ cases, i.e., $\mathbf{n}_{out}$ random along line of sight (*right panels*) and $\mathbf{n}_{out}$ in the same plane as $\mathbf{n}_{in}$ (*left panels*). Since the obliquity distribution function derived from observations has two high probability peaks, ($\psi = 37^{\circ}$ and $\psi = 131^{\circ}$), the possible $i_{\rm mut}$ values that can produce such distribution function also have two peaks. In the case of $\mathbf{S}||\mathbf{L_{in}}$, the double peak distribution is also probable since the precession of a retrograde orbit can as well produce this configuration. Note that if we also consider the case when $i_{ls}^{\star} = 133^{\circ} \pm 6$ (due to the degeneracy in the asteroseismology measurements), ψ_{obs} is symmetric, and $p(i_{\rm mut}|\psi_{obs})$ would also be symmetric.

Interestingly, better observations may help constraining $i_{\rm mut}$ but will not disentangle the degeneracy between the $\mathbf{S}||\mathbf{L_{tot}}$ and $\mathbf{S}||\mathbf{L_{in}}$ cases. We show this in the top panels of Figure 4.4, where we consider an example of $\psi = 40 \pm 3^{\circ}$. In the $\mathbf{S}||\mathbf{L_{tot}}$ scenario, the symmetry is broken, since, there is a direct link between the obliquity and $i_{\rm mut}$ in this case, as seen from the right panel of Figure 2. Note that the two different $p(i_{\rm mut})$ cases produce slight differences in the probability peak. Assuming that $\mathbf{n}_{out}$ and $\mathbf{n}_{in}$ are coplanar produces a decreasing probability toward $i_{\rm mut} \sim 45^{\circ}$, as in this case near polar configurations are less likely. On the other hand, assuming a random orientation for $\mathbf{n}_{out}$ produces an increasing probability toward the larger $i_{\rm mut}$ values. In fact, as mentioned

above, this case yields a larger parameter space for near polar configurations. Having a precise observation also improves the $i_{\rm mut}$ estimation for the $\mathbf{S}||\mathbf{L_{in}}$ but the double peak probability remains, because the same obliquity can be reached in a prograde and retrograde configurations. The degeneracy can be broken only for the case where $\mathbf{S}||\mathbf{L_{tot}}$, a more precise measurement of ψ will be available. This can be seen in the top panels of Figure 4.4, where ψ_{bin} represents $37^\circ < \psi < 43^\circ$.

So far, we have assumed two possible priors for $p(i_{\rm mut})$. These represent two extreme possibilities, one which favors low mutual inclinations and one which favors large values. The truth may lay in between. Thus, we have tested the possibility that $\mathbf{n}_d$ is randomly oriented within a small interval as a prior (see the left side of Figure 4.1, where α, is now confined to a certain interval). In this case, differently from what figure 3 shows, we assumed an initial tilt of 37° between the stellar spin axis and the angular momentum of the inner orbit. This way, we consider the possibility that the source of the obliquity is not dynamical. We find that for $\alpha >\sim 10^\circ$ equation (4.11) and the observed obliquity distribution favors large mutual inclinations. In other words, the three planets will be aligned, and the observations will be consistent with tilt of the star or the disk in the migration scenario, if the random angle $\alpha < 10^\circ$

4.4 Tidal and Stellar Evolution

Here we focus on the fate of the innermost planet and the future evolution of the obliquity as a result of tidal dissipation in the star and stellar evolution. We compute a detailed model of the host star with the publicly available stellar evolution code `MESA` (version 4798 Paxton et al. 2011, 2013). Specifically, we follow Huber et al. (2013) and consider

a star with an initial mass and metallicity of 1.32 $M_\odot$ and $Z = 0.032$, respectively. We evolve the stellar model with the same physical assumptions adopted in Valsecchi & Rasio (2014b). Briefly, we account for stellar wind mass loss following the test suite example provided with `MESA` for the evolution of a 1 $M_\odot$ star, and we set the mixing length α_{MLT} parameter to 1.92, following the `MESA` star Standard Solar Model (Paxton et al. 2011, Table 10). Note that the mass loss is negligible in this case, since the star is only slightly evolved (as shown in Figure 4.5). This negligible mass loss explains why the planets' orbits are significantly expanding, differently from the case of the Earth when the Sun evolves into a red giant. The model agrees with the observationally inferred stellar mass, radius, and effective temperature (within $1\,\sigma$) at 4.418 Gyr. The latter is consistent with the age quoted by Huber et al. (2013) within 1σ (3.5 ± 1.3 Gyr).

The advanced evolutionary stage of the host star (which is off its Main Sequence) poses the interesting possibility that, if Kepler-56 is similar to other Kepler multi-planet systems, it may have had planets that were engulfed as the star expanded (such possibilities have been investigated in the literature, Bear & Soker 2011a, 2012). If this is the case, the observed small stellar rotation rate suggests that the host star in Kepler-56 did not engulf a large planet. In fact, to increase the stellar spin by more than 10%, the engulfed planet should have had a mass larger than 0.6 M_J (neglecting the possibility of core-envelope decoupling, see, e.g., Teitler & Königl 2014). However, we note that magnetic braking, stellar winds, and the expansion of the star as a result of natural stellar evolution might all contribute to spin down after engulfment. Nevertheless, it also seems unlikely (but not impossible) that a very massive planet could have migrated to the innermost configuration, with two lighter planets outside (planets "b" and "c") which also supports the notion that no inner planet was engulfed.

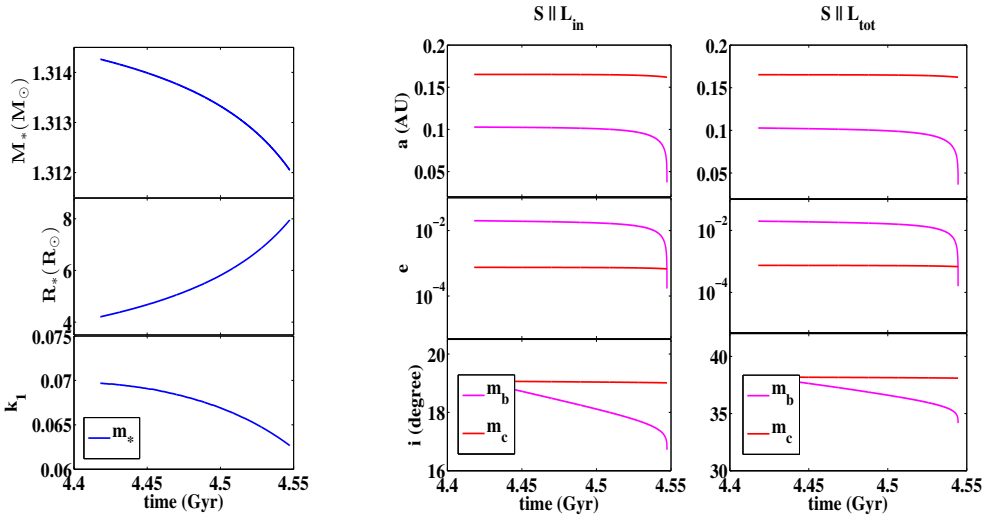

Figure 4.5: **Future evolution of the star and the innermost planets.** *Left column (from top to bottom):* evolution of the stellar mass, radius and the apsidal precession constant (k_2) computed with MESA (Paxton et al. 2011, 2013). *Middle and right columns (from top to bottom)*: evolution of the semi-major axis, eccentricity, and inclination with respect to the invariable plane for planet "b" (magenta lines) and planet "c" (red lines). In the middle panels we consider the $\mathbf{S||L_{in}}$ scenario with an initial $i_{\rm mut} = 20°$, while in the right panels we consider the $\mathbf{S||L_{tot}}$ scenario with an initial $i_{\rm mut} = 40°$. We start the calculation at the present time and we stop it when the innermost planet is engulfed ($a_b = R_\star$). The evolution depicted is due to tidal interactions between the evolving star and the two inner planets, also accounting for the point mass dynamics via direct N-body integrations.

The inner planets' orbital evolution is affected by tides, whose efficiency changes as the star evolves. In the left panels of Fig. 4.5 we show the forward evolution of the stellar mass, radius, and Love parameter. The latter was computed following Valsecchi et al. (2012).

Both the specific angular momentum (h_b) and the eccentricity undergo tidal dissipation, which leads to circularization and orbital shrinking. Following Eggleton et al. (1998) we have

$$\frac{de_b}{dt} = -\tilde{V}_b e_b \ , \tag{4.14}$$

$$\frac{dh_b}{dt} = -\tilde{W}_b h_b \ . \tag{4.15}$$

The parameters $\tilde{W}_b$ and $\tilde{V}_b$ are the dissipation coefficients (see Eggleton et al. 1998), where $\tilde{W}_b$ is given by equation (4.9), and $\tilde{V}_b$ is defined as:

$$\tilde{V}_b = \frac{9}{t_{F\star}}\Big[\frac{1+(15/4)e_b^2+(15/8)e_b^4+(5/64)e_b^6}{(1-e_b^2)^{13/2}} - \frac{11 S_h}{18\dot{l}}\frac{1+(3/2)e_b^2+(1/8)e_b^4}{(1-e^2)^5}\Big] \ . \tag{4.16}$$

We compute the evolution of the orbital separation, eccentricity, and inclination, using the extrapolated orbital parameters from the initial direct N-body integration, together with the equations mentioned above. We stop the integration when the innermost planet is engulfed ($a_b = R_\star$) and neglect possible mass transfer events between the planet and the star (e.g., Trilling et al. 1998), for simplicity. The evolution is shown in the right two panels of Figure 4.5. During the first ~ 0.1 Gyr of evolution, the star loses about 0.1% of its mass and its radius expands by about 40%. After this stage tidal effects become increasingly important and planet "b" is quickly engulfed. We note that the tidal treatment adopted here does not fully account for how the evolution of the

star affects the efficiency of tides (i.e. the stellar viscous timescale $t_{V\star}$ is kept fixed). However, a more consistent orbital evolution calculation with the method adopted in Valsecchi & Rasio (2014a,b), but only accounting for the evolution of the innermost planet, yields similar results. Note also that the precession due to the stellar oblateness affects the final stages of the evolution (very close to the final engulfment of planet "b"). This occurs because tidal dissipation dominates the dynamics only towards the end of the evolution right before the engulfment, and thus, it does not change the overall orbital dynamics. Moreover, we find that the final semimajor axis of the planet is ~ 0.03 AU during the engulfment, which is within twice the Roche limit (the Roche limit is 0.016 AU according to the prescription of Paczyński (1971)). This suggests that the planet may be tidally distorted during the engulfment and that the accumulated heat due to tidal dissipation as the planet orbits the star multiple times may increase the chance of tidal disruption (Li & Loeb 2013). Past studies have investigated the engulfment of planets by their host stars (Nordhaus et al. 2010; Bear & Soker 2011a; Kaib et al. 2011; Kratter & Perets 2012; Veras et al. 2013; Lillo-Box et al. 2014). Figure 4.5 shows that the innermost planet will be engulfed in ~ 129 Myr. Similarly, the second planet (Kepler 56c) will be engulfed in less than ~ 155 Myr.

The tidal evolution of the inner planets affects the stellar spin evolution (equation (4.3)). The same equation holds for planet "c" (substituting subscript "b" with "c"). The stellar spin evolves due to the precession of planets "b" and "c", and their tidal torque. We extrapolate the evolution of their precession directly from the N-body calculation. The evolution of the stellar spin direction and magnitude is shown in Figure 4.6. In particular, we show the evolution of the obliquity ψ and the angle between the stellar spin and the total angular momentum (ϕ). The magnitude of the spin

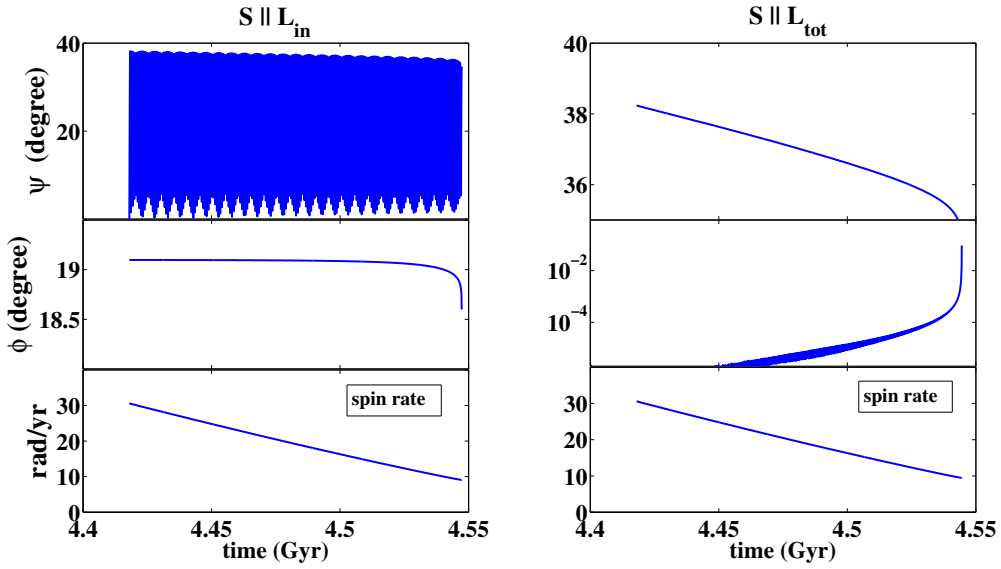

Figure 4.6: **The evolution of the stellar spin**. *Top:* obliquity; *middle:* angle between the stellar spin and the total angular momentum; *bottom:* spin magnitude $|\mathbf{S}|$ in units of rad yr^{-1}. The initial spin period is 75 d, which translates to a spin rate of ~ 30 rad yr^{-1}. The left panel shows the evolution in the $\mathbf{S}||\mathbf{L_{in}}$ scenario with an initial $i_{\rm mut} = 20°$, while the right panel is for the $\mathbf{S}||\mathbf{L_{tot}}$ scenario with an initial $i_{\rm mut} = 40°$.

decreases due to the mass lost and the expansion of the stellar radius (irrespective of the scenario considered). This exercise reveals that the obliquity behavior for the two cases does not vary much as the star evolves. In the $\mathbf{S}||\mathbf{L_{in}}$ scenario with an initial $i_{\rm mut} = 20^\circ$, the obliquity oscillates between zero and $\sim 40^\circ$, the amplitude slightly decreases, and additional modulations due to tides appears. In the $\mathbf{S}||\mathbf{L_{tot}}$ scenario with an initial $i_{\rm mut} = 40^\circ$, the obliquity monotonically decreases.

4.5 Discussion

We studied the configuration and obliquity of Kepler-56, a multi planet system with two coplanar inner planets that are misaligned with respect to their host star. Two main scenarios were proposed in the literature to explain the large obliquities observed for close-in exoplanets. The first model involves dynamical evolution between multi planetary members or stellar companion (e.g., Winn et al. 2010; Fabrycky & Tremaine 2007; Chatterjee et al. 2008; Nagasawa et al. 2008; Naoz et al. 2011, 2012, 2013a; Wu & Lithwick 2011; Li et al. 2014a). The second model proposes disk migration as the main mechanism which controls the planetary configuration, while the star spin axis is tilted with respect to the planets by other mechanisms (e.g. Winn et al. 2010; Lai et al. 2010; Rogers et al. 2012, 2013; Spalding & Batygin 2014). The two scenarios lead to different configurations for the configuration of the planets with respect to each other and the star. The dynamical scenario predicts that large obliquities are associated with an inclined perturber, while the disk-migration scenario predicts aligned planetary systems. We showed that the large obliquity observed in Kepler-56 is consistent with a dynamical nature.

We showed that we can improve the Huber et al. (2013) lower limit on the obliquity ($\psi > 37°$). Specifically, using the Huber et al. (2013) current observations, we found the probability distribution of the observed true obliquity (see Figure 4.1). This probability has a large range with two main peaks at $\psi = 37°$ and $\psi = 131°$. Furthermore, using this probability distribution we gave the probability distribution of the inclination of the third planet with respect to the inner two ($i_{\rm mut}$). This is highly dependent on the system's initial conditions. For this reason, we explored two scenarios: $\mathbf{S}||\mathbf{L_{in}}$ and $\mathbf{S}||\mathbf{L_{tot}}$. In the former, the initial spin axis of the star was set along the orbital angular momentum of the inner two planets. A possible origin for this configuration is that the system formed initially in a disk and the third Jupiter-like planet was perhaps scattered to a large inclination. Instead, in the $\mathbf{S}||\mathbf{L_{tot}}$ scenario, the initial stellar spin was set parallel to the *total* orbital angular momentum. This initial condition may be ad hoc, and possibly caused by, e.g., magnetic interactions Lai et al. (e.g., 2010) warping the inner parts of the disk. For these two scenarios, we found the mutual inclination probability function for the observed obliquity distribution (see Figure 4.4 *bottom panels*). Both configurations have a double peak distributions, with zero probability of having aligned configuration between the two orbits. The degeneracy between the two probability peaks may be broken only for the $\mathbf{S}||\mathbf{L_{tot}}$ case, with a more precise measurement of ψ. However, a precise measurement of ψ would not disentangle between the $\mathbf{S}||\mathbf{L_{tot}}$ and $\mathbf{S}||\mathbf{L_{in}}$ cases, as shown in the top panels of Figure 4.4.

We finally considered the effect of the stellar evolution on the system's parameters and, specifically, the obliquity. We evolved the host star using `MESA` (Paxton et al. 2011, 2013) and extrapolated the planets orbital evolution calculated with direct N-body integration (since the latter is rather regular and periodic). We have also included the

spin precession and tidal evolution. This exercise revealed that the obliquity behavior for the two cases does not vary significantly as the star evolves. It also shows that planet "b" will be engulfed in ~ 129 Myr.

4.6 Acknowledgments

SN is supported by NASA through an Einstein Post–doctoral Fellowship awarded by the Chandra X-ray Center, which is operated by the Smithsonian Astrophysical Observatory for NASA under contract PF2-130096. This work was also supported by NASA Grant NNX12AI86G at Northwestern University. JAJ gratefully acknowledges funding from the Alfred P. Sloan and David & Lucile Packard foundations.

Chapter 5

Cross Sections for Planetary Systems Interacting with Passing Stars and Binaries

This thesis chapter originally appeared in the literature as

Li, G., Adams F. Cross Sections for Planetary Systems Interacting with Passing Stars and Binaries, *Monthly Notices of the Royal Astronomical Society*, 448, 344, 2015

It is presented here with minor modifications.

Abstract

Most planetary systems are formed within stellar clusters, and these environments can shape their properties. This paper considers scattering encounters between solar systems

and passing cluster members, and calculates the corresponding interaction cross sections. The target solar systems are generally assumed to have four giant planets, with a variety of starting states, including circular orbits with the semimajor axes of our planets, a more compact configuration, an ultra-compact state with multiple mean motion resonances, and systems with massive planets. We then consider the effects of varying the cluster velocity dispersion, the relative importance of binaries versus single stars, different stellar host masses, and finite starting eccentricities of the planetary orbits. For each state of the initial system, we perform an ensemble of numerical scattering experiments and determine the cross sections for eccentricity increase, inclination angle increase, planet ejection, and capture. This paper reports results from over 2 million individual scattering simulations. Using supporting analytic considerations, and fitting functions to the numerical results, we find a universal formula that gives the cross sections as a function of stellar host mass, cluster velocity dispersion, starting planetary orbital radius, and final eccentricity. The resulting cross sections can be used in a wide variety of applications. As one example, we revisit constraints on the birth aggregate of our Solar System due to dynamical scattering and find $N \lesssim 10^4$ (consistent with previous estimates).

5.1 Introduction

A large fraction of planetary systems form within stellar clusters (Lada & Lada 2003; Porras et al. 2003) and these birth environments can influence their resulting properties (e.g., see the reviews of Adams 2010; Pfalzner 2013). One potentially important process occurs when binary systems — and single stars — fly past solar systems and disrupt the

orbits of their constituent planets. This type of scattering interaction has been studied in the field (Laughlin & Adams 2000), and within young embedded clusters (e.g., Adams et al. 2006; Malmberg et al. 2007, 2011; Boley et al. 2012; Dukes & Krumholz 2012; Chatterjee et al. 2012; Hao et al. 2013; Pacucci et al. 2013), where the latter results can be used to provide constraints on the possible birth environment of our own solar system (e.g., Adams & Laughlin 2001; Hester et al. 2004; Williams & Gaidos 2007; Spurzem et al. 2009; Portegies Zwart 2009; Adams 2010; Williams 2010; Pfalzner 2013). We stress that the dynamical constraints derived for the birth aggegate of the solar system depend on many variables, including assumptions made about the cluster properties, any other constraints imposed on the problem, and the interaction cross sections.

This present study focuses on the cross sections themselves, and expands previous work to include a much wider range of parameter space; the implications for the solar birth environment are then briefly considered at the end of the paper. For studies concerning our solar system, most previous work has calculated the cross sections for this mode of disruption by considering the initial orbits of the giant planets to have their present-day values of semimajor axis. However, some recent work suggests that our solar system may have begun in a more compact configuration (Gomes et al. 2005; Tsiganis et al. 2005), and the planets may not have reached their present-day orbits until the solar system reached an age of hundreds of millions of years. One motivation for this present study is thus to determine cross sections for solar system disruption for more compact configurations. Note that the sign of the effect is not obvious *a priori*: The geometrical cross section of the compact solar system is smaller, and hence implies a smaller interaction cross section. However, the decreased relative separations of the planets allow for increased planet-planet interactions, which could result in more

disruption from the passing stars; in addition, the close spacing in compact solar systems allows for orbit crossing to occur for smaller values of eccentricity.

In some compact configurations of the solar system, the giant planets can be at or near mean motion resonance. This possibility leads to interesting dynamics: Mean motion resonances can protect planetary systems from disruption, and could thus lead to greater stability and smaller interaction cross sections. On the other hand, the mean motion resonances themselves are more easily compromised than planetary orbits — the potential energy corresponding to the resonance angle being in a bound state is much less than the gravitational potential energy of the planetary orbit. An important related question is thus to find the cross sections for passing stars (including binaries) to disrupt mean motion resonances. Planetary systems with disrupted resonances will usually retain their planets in the near term, although they could be subject to orbit instabilities over longer spans of time.

In addition to compact solar system architectures, this paper considers a wider range of parameter space than previous studies. Part of this expanded scope is possible due to increased computational capabilities. This present study includes results from more than 2 million individual numerical experiments that simulate a solar system interacting with a passing binary (or single star). For each choice of solar system architecture and each choice of the background parameters for the encounters, we run a large ensemble of $\mathcal{N}_E$ simulations (where $\mathcal{N}_E = 80{,}000$ for most cases, but can be larger). The variations that we consider for the target solar systems include compact configurations (described above), more massive planets, nonzero initial orbital eccentricities, and a range of masses for the central stars. Regarding variations in the background environment, this paper considers two main issues: We determine the effects of varying the velocity dispersion of

the cluster stars, and we compare the relative sizes of the scattering cross sections for single stars versus binaries as they interact with planetary systems.

This paper is organized as follows. We formulate our approach to calculating the interaction cross sections in Section 5.2. The resulting cross sections are then given in Section 5.3, which provides $\langle \sigma \rangle$ for increases in eccentricity, increases in the spread of inclination angles, planet ejection, planet capture, and changes in semimajor axes. Results are also presented for increasing orbital eccentricities up to orbit-crossing configurations and compares the efficacy of passing single and binary stars. These results are given as a function of solar system architecture, velocity dispersion of the cluster, and mass of the host star. Over much of the parameter space of interest, the cross sections display a nearly self-similar form. Section 5.4 presents a scaling analysis that shows how the results scale with velocity disperion, stellar mass, and starting semimajor axis. As an application, Section 5.5 revisits the possibile dynamical constraints on the birth cluster of the solar system. In order to assess the level of disruption, one also needs the rate of close encounters in young stellar clusters. These rates have already been calculated for a wide range of cluster properties (Adams et al. 2006; Proszkow & Adams 2009) and are used herein. The paper concludes, in Section 5.6, with a summary of our results and a discussion of their implications.

5.2 Formulation of the Problem

One useful way to specify the effects that passing stars can have on planetary systems is to define cross sections of interaction. For example, the scattering interactions could eject a planet, increase the eccentricity, change the semimajor axis, and/or perturb the

inclination angle of the orbit. For a given type of disruption, a solar system presents an effective target area for being disrupted by passing stars. With this definition, the effective interaction rate Γ for disruption is then given by the usual formula

$$\Gamma = n_* \langle \sigma \rangle \langle v \rangle \, , \tag{5.1}$$

where n_* is the mean density of stars in the environment, $\langle v \rangle$ is the mean relative velocity between systems, and $\langle \sigma \rangle$ is the cross section for the given mode of disruption. We note that the background environment determines the stellar density n_* and the distribution of relative velocities. As outlined below, the relative velocities follow a Maxwellian distribution characterized by the expectation value $\langle v \rangle$. The interaction cross section depends on this velocity distribution, so that we actually calculate the quantity $\langle \sigma \rangle_v \equiv \langle \sigma v \rangle / \langle v \rangle$, where the subscript denotes that the cross section depends on the velocity expectation values $\langle v \rangle$. For ease of notation, however, we drop the subscript for the remainder of the paper. In young embedded clusters, we expect $n_* \sim 100$ pc^{-3} and $\langle v \rangle \sim 1 - 2$ km/s; in the field (in the solar neighborhood) these quantities have typical values $n_* \sim 1$ pc^{-3} and $\langle v \rangle \sim 30 - 40$ km/s. Because of the velocity dependence of the cross sections, solar systems in the field (with high fly-by speeds) are, on average, less affected by passing stars.

To calculate the cross sections for interactions, we adopt the following approach. First we must specify the configuration of the solar system that will be targetted for disruption (for example, we can use the current set of four giant planets in our solar system, with their current masses and semimajor axes, all in orbit about a solar mass star). Next we must specify the background environment, which determines the distribution of relative velocities. For most of this work, we focus on the case where the

target solar system encounters binaries. We then perform a large ensemble of numerical simulations, where the input parameters are specified according to a Monte Carlo scheme. The results are then used to calculate the probability of various outcomes and the corresponding cross sections (for further detail, see Laughlin & Adams 2000; Adams & Laughlin 2001; Adams et al. 2006).

In principle, the Monte Carlo sampling scheme should sample all possible encounters between binaries and the target solar system, including those with large impact parameters. In practice, however, only sufficiently close encounters have a non-negligible chance of affecting the planetary orbits. In order to conserve computer time, we thus make the following limitation. We treat the semimajor axes a of the binaries on a different footing than the others: The values of a are sampled uniformly out to $a_{\max} =$ 1000 AU (more than 30 times the size of Neptune's orbit in our solar system). For a given value of a, we then limit the possible range of impact parameters to fall within an area given by $A_0 = B\pi a^2$. With this sampling scheme, the cross section of interaction, for a given type of disruption event, is given by

$$\langle \sigma \rangle = \int_0^{a_{\max}} p(a) da \, f_D(a) \, \left(B\pi a^2 \right) \, , \tag{5.2}$$

where $p(a)$ is the probability distribution for binaries having a semimajor axis a. The factor $f_D(a)$ represents the fraction of all encounters (within the pre-determined area $A_0 = B\pi a^2$) that results in the outcome of interest. Note that the maximum allowed value of the impact parameter varies with a and is given by $\varpi_{max} = \sqrt{B}a$.

The formulation of equation (5.2) can be understood as follows: Consider a given outcome of interest, say, the ejection of Neptune. We only consider fly-bys that take place within the area $A_0 = B\pi a^2$, where a is sampled uniformly. If every encounter within this

area leads to the ejection of Neptune, and all encounters outside this area (which are not computed) have no effect, then $f_D = 1$; the probability factor $p(a)$ corrects for the actual distribution of binary semimajor axis, and one can see that equation (5.2) provides the correct effective cross section. In practice, of course, only a small fraction of encounters lead to the ejection of Neptune so that $f_D \ll 1$. As long as we choose the factor B large enough, we are ignoring only distant encounters that have little contribution to the cross section. Nonetheless, since B is finite, this procedure leads to a lower limit on the cross section. We have run convergence tests with ever-increasing values of B and find that $B = 100$ is large enough to include essentially all relevant encounters. In most of this work we thus use $B = 100$, which provides a good compromise between computational speed and accuracy. For comparison, our previous work (Laughlin & Adams 2000; Adams & Laughlin 2001) used the smaller value $B = 4$, so that the reported cross sections (again presented as lower limits) were smaller than those obtained here by a factor of ~ 2. This present treatment thus provides a more complete accounting for wide binaries and results in a greater lower bound on the true cross sections.

The distribution $p(a)$ is determined by the observed binary period distribution, which is nearly uniform in the quantity $\log a$, but has a broad peak centered at period $P = 10^5$ days, which implies $a \approx 42$ AU for solar type stars (Duquennoy & Mayor 1991).

Within the scheme outlined above, encounters between a given solar system and a passing binary are specified by a large number of input parameters: We must specify the properties of the binary, including its semimajor axis a, orbital eccentricity $e_{\rm b}$, the masses of the two stars M_{1*} and M_{2*}, and finally the phase of the binary orbit $\theta_{\rm b}$ at the start of the encounter. The orbital elements $(a, e_{\rm b})$ are sampled from their observed distributions (Duquennoy & Mayor 1991). Similarly, the stellar masses are sampled from

a log-normal form of the stellar initial mass function (consistent with that advocated by Adams & Fatuzzo 1996 and Chabrier 2003). Both members of the binary are sampled independently from the distribution and the stellar masses are limited to the range $M_* = 0.07 - 10 M_\odot$. As a result, we exclude brown dwarfs and the very largest stars (which are both rare and tend to reside at cluster centers). The phase angle $\theta_{\rm b}$ of the orbit is sampled uniformly over $[0, 2\pi]$. Next we must specify the incoming velocity v_∞ of the solar system with respect to the binary center of mass; this speed is sampled from a Maxwellian distribution with a velocity dispersion $v_{\rm b}/2$ that characterizes the background environment (e.g., a cluster). The remaining variables are the three angles (θ, ψ, ϕ) necessary to specify the direction and orientation of the encounter, and finally the impact parameter ϖ. The impact parameter is chosen randomly within a circle of radius $10a$ centered on the binary center of mass (corresponding to the choice $B = 100$ in equation [5.2]).

Using a Monte Carlo scheme to select the input parameters according to the distributions described above, we carry out a large ensemble of scattering simulations. For most cases we find that the number of simulations $\mathcal{N}_E = 80,000$ is large enough to provide good statistics. The outcomes of these numerical experiments are then used to compute the fraction f_D of disruptive encounters for a given type of outcome. The resulting errors due to incomplete sampling are typically 5 percent or less, but can be larger for rare events (e.g,. for planet ejections, the sampling errors are ~ 10 percent).

Each simulation is thus an N-body problem. For most cases, $N = 7$, where the target system consists of four giant planets orbiting a host star and interacts with a binary. The equations of motion are integrated using a Bulirsch-Stoer method (Press et al. 1986), which allows for rapid integrations and high accuracy. Because we are

interested in the planetary orbits, which only contain a small fraction of the total energy of the N-body system, the simulations must conserve the total energy to high accuracy in order to determine the final orbital elements. For example, the energy contained in the orbit of Neptune, the least bound planet, is typically 10^4 times smaller than the binding energy of a binary, or the initial gravitational potential energy between the binary and the solar system. In practice, our individual simulations have an accumulated error of only one part in 10^8, so that orbital changes are safely resolved.

5.3 Results for the Cross Sections

Using the formulation described in the previous section, we have performed several large ensembles of numerical scattering simulations. Unless stated otherwise, we consider the solar systems to have four giant planets and to interact with passing binary stars. We then consider a number of different solar system architectures for the starting states, as outlined below (see Table 1). To obtain reasonable statistics within the Monte Carlo scheme, the number of individual numerical experiments for each solar system architecture must typically be of order $\mathcal{N}_E \approx 80,000$. This choice produces relative errors (due to incomplete sampling) of order 5 percent or smaller.

In the first set of simulations, we consider the target system to be an analog of our present-day solar system. In this case, we place the four giant planets in orbit about a solar mass star and give the planets their current masses and semimajor axes. The eccentricities are all set to zero, however, so that we can measure the eccentricity increases produced by the scattering encounters. From the results of these experiments, we compute the cross sections for orbital disruption of each of the four planets (as

outlined in the previous section). The results are shown as the solid blue curves in Figure 5.1, which also presents the cross sections for a more compact starting configuration (described below). The error bars (not shown) due to incomplete Monte Carlo sampling correspond to relative errors with a root-mean-square (RMS) value of $\sim$4.4%.

In Figure 5.1, and throughout this paper, the cross sections for increasing the eccentricity to $e = 1$ incorporate all of the ways that the planet can be removed from its solar system. These channels include [1] actually increasing the eccentricity to $e \geq 1$, which includes both hyperbolic orbits and planetary orbits that intersect the host star, [2] ejection from the solar system by increasing the kinetic energy so that the orbit is unbound, and [3] capture by one of the (two) passing stars. These channels are not mutually exclusive, but the simulations are stopped after one of these events takes place. However, these channels only include ejection processes that happen during or immediately after the encounter (we denote these processes as prompt ejections). In other cases, the planets are scattered into high eccentricity orbits, so that the orbits cross each other. With these configurations, in the absence of resonance, the planets will eventually experience close encounters, which in turn lead to ejections or collisions (we denote this process as delayed ejection). The cross sections for delayed ejections will be considered later.

For comparison, we also present the results from a series of numerical experiments using a more compact orbital architecture (shown as the red dashed curves in Figure 5.1), which is motivated by the Nice model of solar system formation (Gomes et al. 2005). Although the Nice model has a number of variations, one feature is that the giant planets could have formed with a more compact configuration than that of the present day. For this case, we fix the orbit of Jupiter at $a_J = 5.2$ AU, and then let each successive

planet have a semimajor axis that is larger than the previous one by a factor of 5/3. This evenly-spaced solar system thus extends out to only 24 AU. The results, shown in Figure 5.1, indicate that the cross sections for the compact configuration are somewhat smaller than those obtained with the current semimajor axes. For this compact solar system, the RMS errors (not shown) due to incomplete sampling are $\sim$4.6%.

Next we consider an even more compact orbital configuration, again motivated by the Nice model, where the four giant planets are in mutual mean motion resonance (MMR). In this case, we choose the starting semimajor axes to have values of $a = 5.88$ AU (Jupiter), 7.89 AU (Saturn), 10.38 AU (Uranus), and 12.01 AU (Neptune). With these semimajor axes, Jupiter and Saturn are in a 3:2 MMR, Saturn and Uranus are in a 3:2 MMR, while Uranus and Neptune are in a 5:4 MMR (for further discussion of this initial state, and others, see Batygin & Brown 2010; Nesvorný & Morbidelli 2012; Li & Batygin 2014b). Note that the semimajor axis ratios do not imply period ratios with exact integer values (although they are close). All of the orbital elements must be chosen properly to put the system in mutual MMR, and this requirement displaces the period ratios somewhat. Nonetheless, the resonance angles of the system (for all three planet pairs) are librating in the initial state, as required for MMR. With this initial state, the solar system is much more compact than at the present epoch, and the cross sections for interactions are smaller. This trend is illustrated in Figure 5.2, which compares the cross sections with those obtained for solar systems with the standard starting configuration. To leading order, the smaller cross sections obtained for the resonant architecture are a direct consequence of the smaller geometrical size. However, closer inspection of the results suggests that the cross sections are larger than the smaller size would imply (see the analysis of the following section). For example, the cross sections for changing the

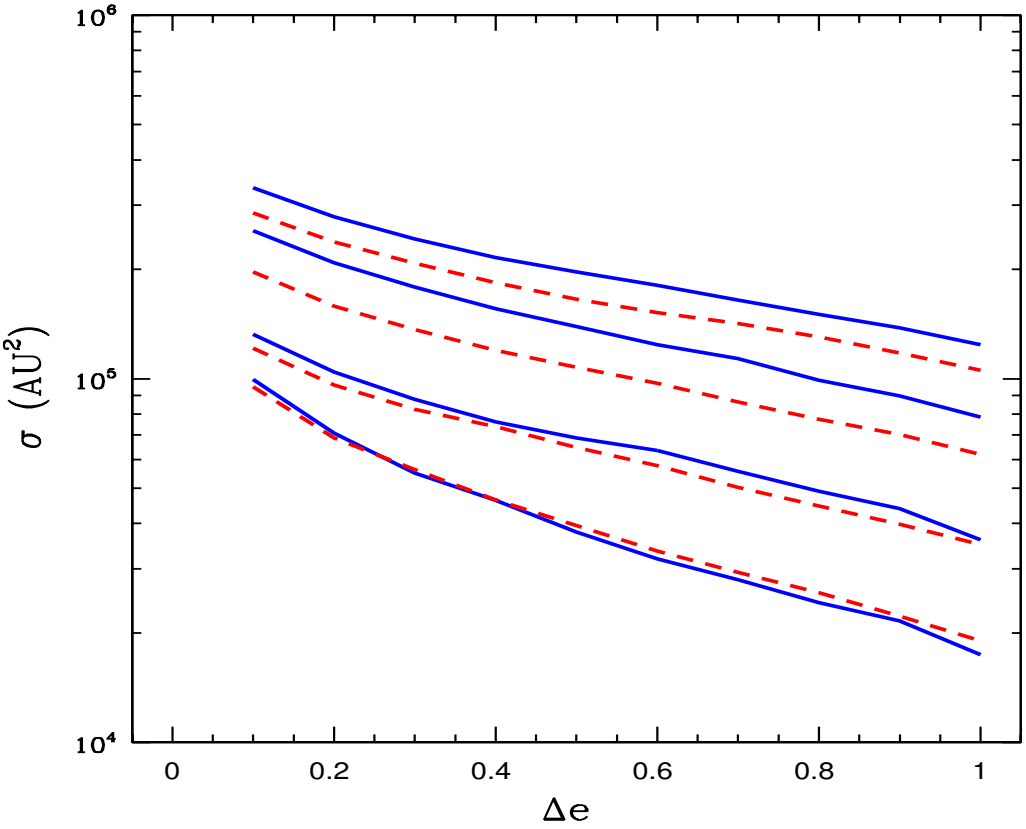

Figure 5.1: Cross sections for eccentricity increase for the current solar system architecture and for a more compact configuration movitated by the Nice model. For the current solar system (solid blue curves), the four giant planets are started with their current semimajor axes and zero eccentricity. For the compact configuration (dashed red curves), the planets are started with semimajor axes having a fixed ratio $a_{j+1}/a_j = 5/3$, where Jupiter ($j = 1$) is started at its present location $a_J = 5.2$ AU. For both sets of cross sections, the curves, from top to bottom, correspond to Jupiter (bottom), Saturn, Uranus, and Neptune (top). Since the orbits start with zero eccentricity, the eccentricity increase $\Delta e = e$, where e is the post encounter eccentricity.

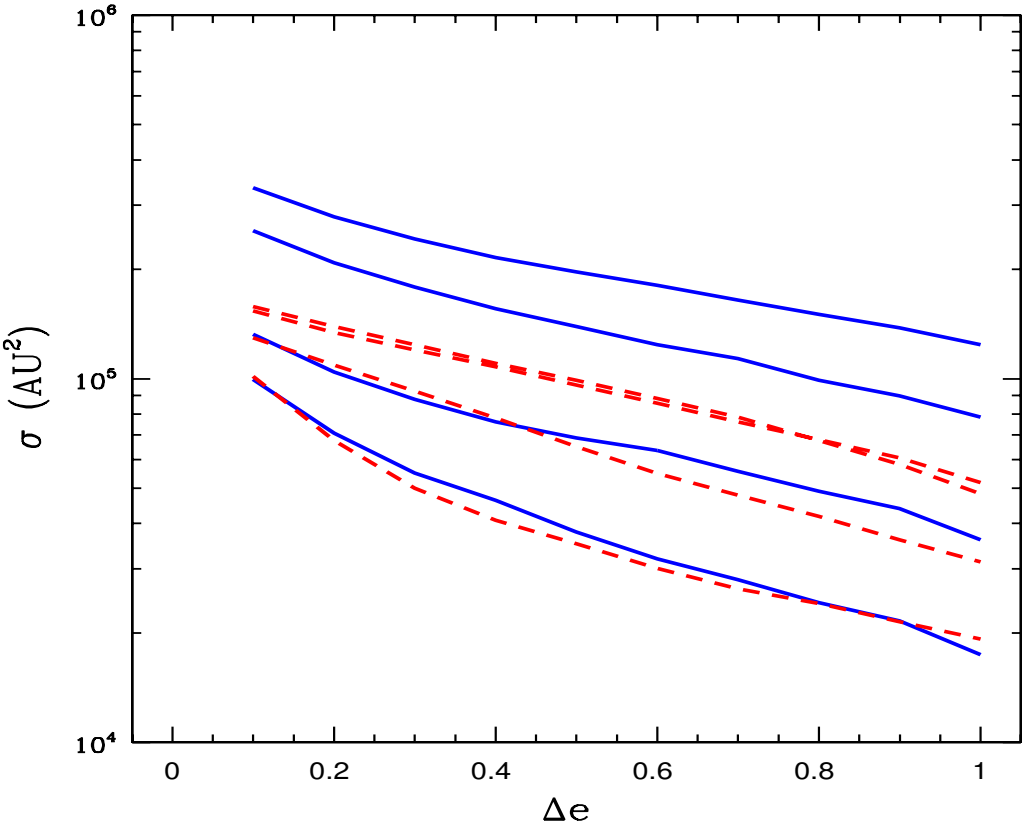

Figure 5.2: Cross sections for eccentricity increase for the current solar system architecture and for a resonant configuration movitated by the Nice model. For the current solar system (solid blue curves), the four giant planets are started with their current semimajor axes and zero eccentricity. For the resonant configuration (dashed red curves), the planets are started with semimajor axes $a = 5.88$, 7.89, 10.38, and 12.01 AU (for the analogs of Jupiter to Neptune). For both sets of cross sections, the curves, from top to bottom, correspond to Jupiter (bottom), Saturn, Uranus, and Neptune (top). Since the orbits start with zero eccentricity, the eccentricity increase $\Delta e = e$, where e is the post encounter eccentricity.

eccentricity of Uranus and Neptune are comparable. In this compact state, planet-planet interactions can be important and act to increase the the cross sections of Uranus (and Saturn) beyond the values obtained for more widely separated orbits.

In addition to changes in the orbital elements of the individual planets, as shown in Figure 5.2, scattering interactions can remove solar systems from their resonant states. The energy required to remove a planetary system from resonance is much less than that required to eject a planet, or even to substantially change its orbital elements. To address this issue, we have run an additional series of numerical simulations to determine the fraction of systems that are removed from their initial resonant state due to passing binaries. As before, the ensemble size $\mathcal{N}_E \approx 80{,}000$, although the simulations take longer because the resonance angles must be monitored for several libration times after the encounters. The result of this set of experiments is the cross section for removing the solar system from its initial resonant state, namely

$$\langle \sigma \rangle_{\rm res} \approx (2,280,000 \pm 20,800)\,{\rm AU}^2\,. \tag{5.3}$$

This cross section is about 20 times larger than that required to eject Neptune from the solar system in its normal state, and nearly 40 times larger than the cross section to eject Neptune from the compact, multi-resonant state. If the removal of the system from resonance results in orbital instability over longer time intervals, then the multi-resonant state could be more sensitive to disruption from passing stars than the standard solar system architecture. We have carried out 70 longer-term integrations for post-encounter systems and find that all but one are stable on time scales of ~ 1 Myr. Other authors (Batygin & Brown 2010; Nesvorný & Morbidelli 2012) also find that multi-resonant states can be unstable due to perturbations (generally due to a planetesimal disk), and

can eject planets, but more follow-up integrations are required to assess the probability of significant instability.

The results reported thus far have all been calculated for cases where $v_{\rm b} = 1$ km/s, a typical value for an embedded cluster environment (Lada & Lada 2003; Porras et al. 2003). Now we generalize the treatment by considering the dependence of the cross section on the velocity dispersion of the background environment. As is well known, interaction cross sections for high speed encounters, such as in the field (Laughlin & Adams 2000), are much lower than those in clusters (Adams et al. 2006), and the velocity dependence is relatively steep (Adams & Spergel 2005; Dukes & Krumholz 2012). To study this dependence, we consider ensembles of numerical simulations with different values of velocity dispersion $v_{\rm b}$. More specifically, we consider solar system starting with the current value of semimajor axes, and $v_{\rm b}$ in the range from 1 km/s to 32 km/s, varied by factors of $\sqrt{2}$ (so they are evenly spaced in a logarithmic sense). For the low end of this range of $v_{\rm b}$, we can use the usual number $\mathcal{N}_E = 80{,}000$ of trials in the ensemble for each value of $v_{\rm b}$. For the larger values of $v_{\rm b}$, however, the cross sections are lower, and disruptive events are rare, so that we need larger values of $\mathcal{N}_E$ to obtain good statistics (we find that the choice $\mathcal{N}_E \approx 200,000$ is usually large enough).

The interaction cross sections produced by this study are shown in Figure 5.3, where each panel corresponds to the results for one of the giant planets. The cross sections are plotted as a function of the post-encounter eccentricity e, for each choice of $v_{\rm b}$. Figure 5.3 shows that the cross sections are almost evenly spaced in a logarithmic sense, with the lowest (highest) velocity dispersions producing the largest (smallest) largest cross sections. This finding suggests that the cross sections — to leading order — display a power-law dependence on the $v_{\rm b}$. This claim is verified in the following section.

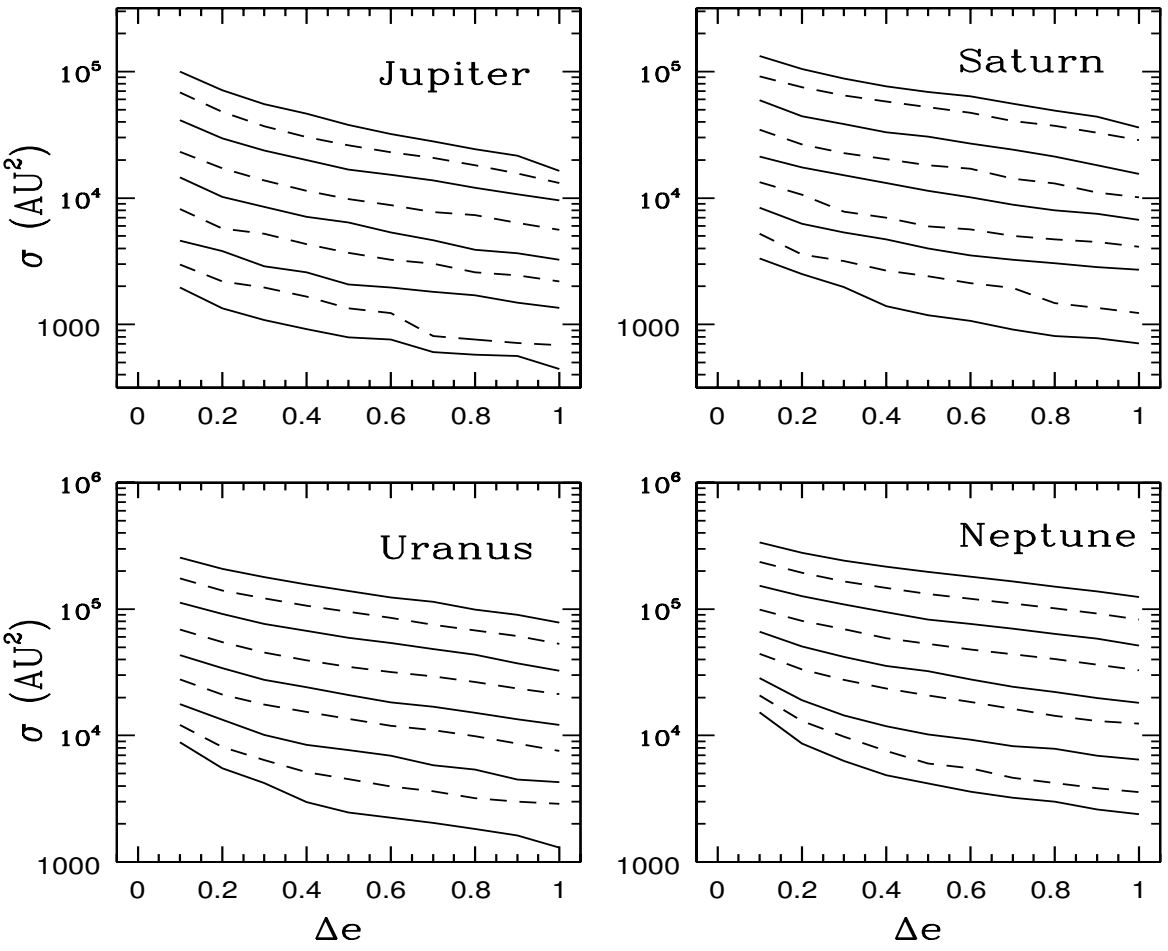

Figure 5.3: Cross sections for eccentricity increase for the current solar system architecture over a wide range of velocity dispersions in the background cluster. The four giant planets of the solar system are started with their current semimajor axes and zero eccentricitiy. Each panel shows the cross sections to increase orbital eccentricity for Jupiter (upper left), Saturn (upper right), Uranus (lower left), and Neptune (lower right). $v_{\rm b}$ fall in the range from 1 km/s (uppermost curves in each panel) to 16 km/s (lower curves), and are equally spaced logarithmically (by factors of $\sqrt{2}$).

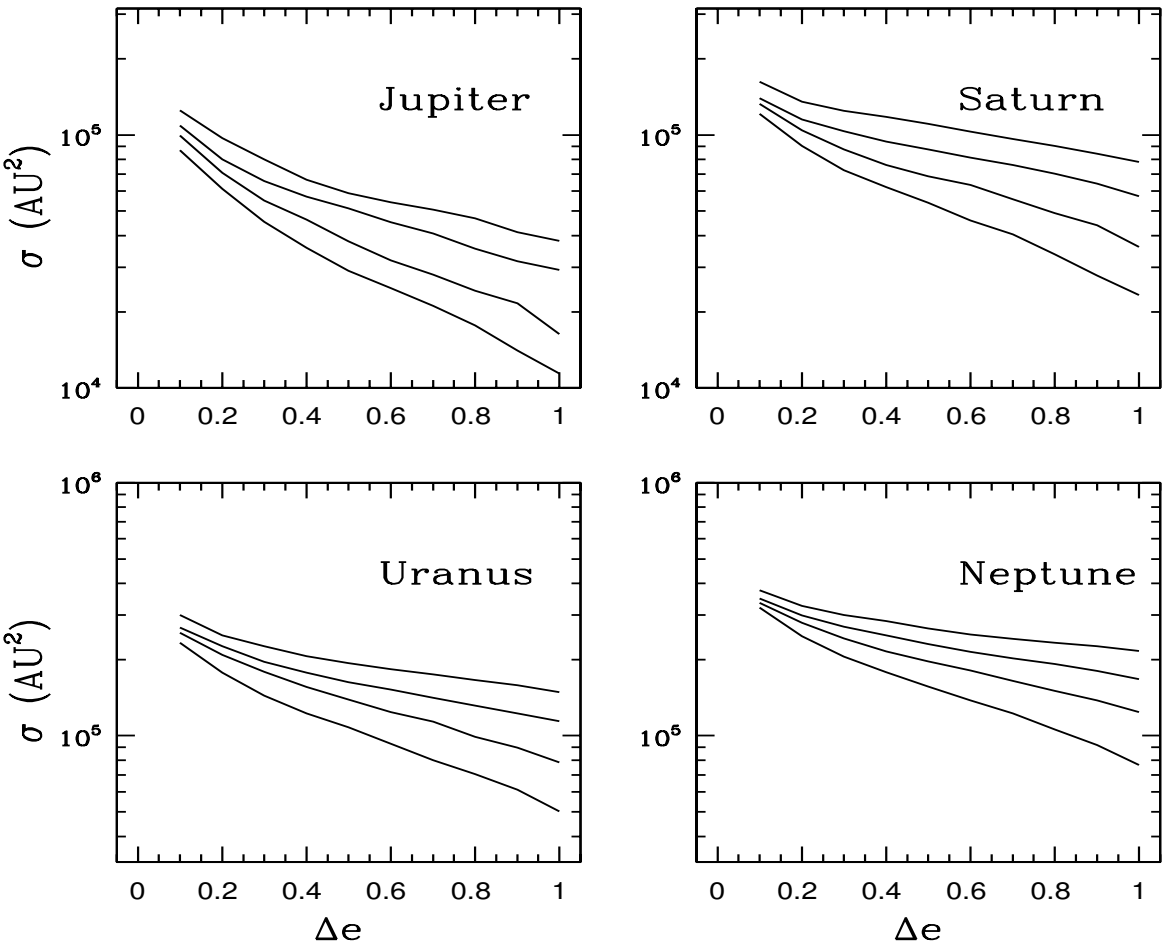

Figure 5.4: Cross sections for a range of masses of the host star. Each case uses analogs of the four giant planets of our solar system, where the planets start with the current semimajor axes and zero eccentricitiy. Each panel shows the cross sections to increase orbital eccentricity for the analog Jupiter (upper left), Saturn (upper right), Uranus (lower left), and Neptune (lower right). The four curves in each panel correspond to four stellar masses, $M_* = 0.25$, 0.5, 1.0, and 2.0 $M_\odot$, from top to bottom.

Next we consider the effect of changing the mass M_* of the host star. Figure 5.4 shows the cross sections for systems with the current solar system architecture and varying stellar masses, from $M_* = 0.25 - 2.0 M_\odot$. For these numerical experiments, the solar systems are all started with four planets that have the same masses and semimajor axes of the giant planets of our solar system. These analogs are labeled as 'Jupiter' through 'Neptune', although the host star can have a mass that differs from the Sun. As expected, the cross sections shown in Figure 5.4 decrease as the stellar masses increases. Unlike the case of varying the velocity dispersion, however, the cross sections, considered as a function of eccentricity increase, do not display as much self-similarity: The cross sections decrease more steeply with eccentricity as the mass of the host star increases. Nonetheless, for a given value of eccentricity increase, cross sections for the four planets (with their four values of a) all show the nearly same (power-law) scaling with stellar mass.

Notice that changing the stellar mass is (in one sense) akin to changing the planetary masses, because the mass ratios are the most important variables. However, this association is not an equivalence: The masses of the passing binaries also enter into the problem, and their mass distribution is kept invariant. In addition, if the masses of the planets are increased to the point where the planet-planet interactions play a role, then self-excitation of eccentricity can produce larger cross sections. This issue is addressed below where we consider solar systems with larger planets. We expect interactions to be important in the regime where the angular momentum exchange time scale between planets is comparable to the encounter timescale. The exchange time scale can be determined, but the calculation is different for widely separated planets where the secular approximation is valid and for the resonant case (for further discussion, see

Batygin & Morbidelli 2013).

For the starting configurations used thus far, the initial orbital eccentricities of the planets have been taken to be zero. Given this choice, the resulting cross sections represent the cross sections for increasing eccentricity (which cannot decrease from its initial value). However, for the related problem of single stars interacting with binaries, an important difference arises between starting states where the binary has zero eccentricity and states where the binary has small but finite eccentricity (Heggie & Rasio 1996). One might worry that the cross sections calculated herein could be affected by introducing small starting eccentricities for the planetary orbits. We have explored this possibility by using two additional starting configurations for the solar system. In one case, the planetary orbits are started with their currently observed eccentricities, e = 0.049, 0.057, 0.045, and 0.011 for Jupiter, Saturn, Uranus, and Neptune, respectively. In the second case, the planetary orbits are all started with a larger value of eccentricity $e = 0.10$. The resulting cross sections are shown in Figure 5.5, along with our previous results with zero starting eccentricity. As shown in the Figure, all of the cross sections converge to the same values as long as the final eccentricity is moderately larger than the starting values. The difference between results obtained starting with zero eccentricity and those where the orbits have their current eccentricity is modest. For the larger starting values $e = 0.10$, the cross sections for reaching $e = 0.10$ are enormous of course, much larger than the limits of the plot (and hence are not shown). Even for this starting state, however, the cross sections have almost converged to their "natural" values for $e \gtrsim 0.20$, except for the case of Uranus; for this planet, the cross sections for eccentricity excitation only converge for $e \gtrsim 0.35$.

The results illustrated in Figure 5.5 indicate that the problem of solar systems

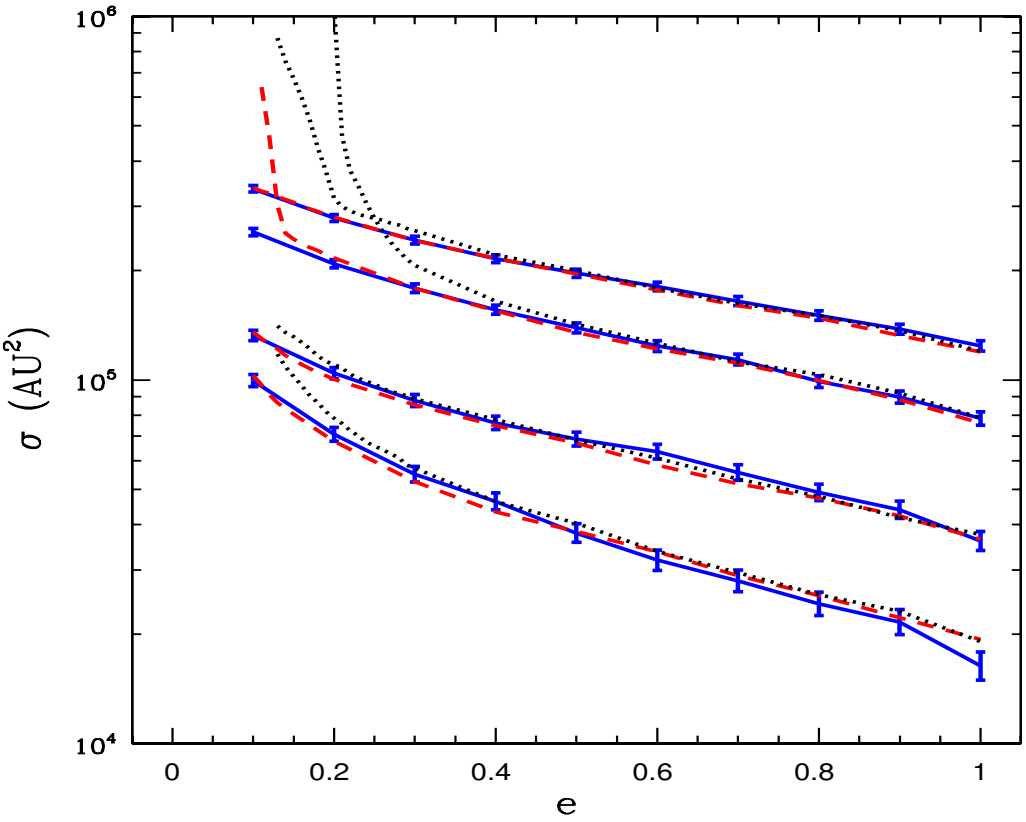

Figure 5.5: Cross sections for the solar system planets and varying initial eccentricities of the planetary orbits. For all cases, the four giant planets of our solar system are started with their current semimajor axes. The solid blue curves show the results for zero initial eccentricitiy; the dashed red curves show the results where the planets start with their current orbital eccentricities ($e = 0.049$, 0.057, 0.045, and 0.011); the black dotted curves show the results where the starting orbits all have $e = 0.10$. Cross sections are given for Jupiter (bottom curves), Saturn, Uranus, and Neptune (top curves), all given as a function of the post-encounter value e of the eccentricity.

interacting with passing binaries is somewhat different than that of single stars interacting with binaries (Heggie & Rasio 1996). Starting with zero eccentricities has a larger effect in the binary-single-star setting. One difference between the two cases is that of symmetry: For a single star passing by a binary with zero eccentricity, the incoming trajectory is the same as the outgoing trajectory provided that the encounter is distant (so that the binary orbit can be considered as a ring of mass); this symmetry cancels some of the forcing. However, this symmetry is absent for solar system scattering, even when the planetary orbits are circular. The binaries that impinge upon the solar systems are themselves eccentric, where e is drawn from the observed binary eccentricity distribution (which favors high e). In addition, the solar systems have four planets, with different orbital phases, and this property also breaks the symmetry (albeit to a lesser degree). Another difference between the two scattering problems is that the cross sections of this paper are averaged over an ensemble of different binary properties and different encounter parameters. The binary scattering results (Heggie & Rasio 1996) show that the the difference between finite eccentricity and circular orbits is largest for distant encounters, but the effect (the change in eccentricity) is largest for close encounters (see their Figure 2). The cross sections of this paper include both regimes, but the cross section is dominated by the close encounters where the results for $e = 0$ and $e \neq 0$ are similar. As a result, starting the planetary orbits with non-zero eccentricity has only a modest effect on the cross sections considered in this paper (provided that one considers post-encounter eccentricities sufficiently larger than the starting values).

Next we consider the effects of planetary mass on the scattering cross sections. The results are shown in Figure 5.6 for the usual Solar System parameters and for an analog solar system where all of the giant planets have the mass of Jupiter ($m_P = 1 m_J$). Both

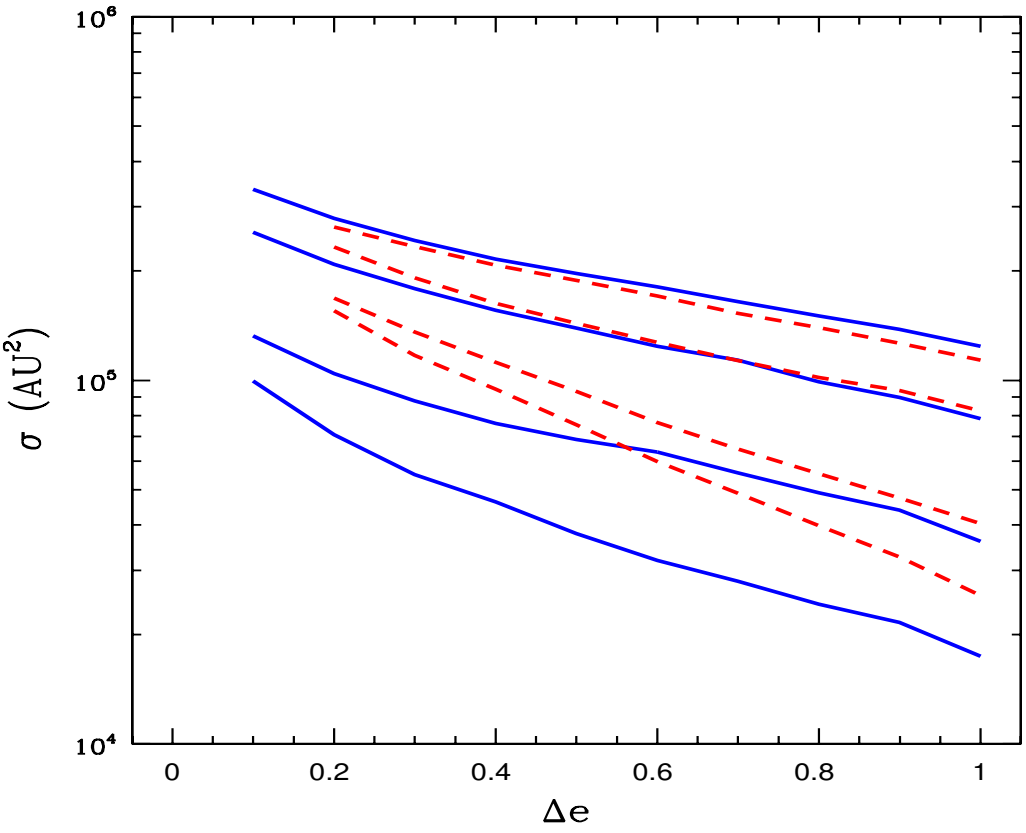

Figure 5.6: Cross sections for eccentricity increase in systems where the giant planets all have mass $m_P = 1m_J$ (dashed red curves). The cross sections for the current solar system architecture are shown for comparison (solid blue curves). In both cases, the planets are started with the current semimajor axes of the giant planets in our Solar System and with zero eccentricity. Cross sections are shown for analogs of Jupiter (bottom curves), Saturn, Uranus, and Neptune (top curves).

classes of systems start with the same semimajor axes (the present-day values in our system) and zero eccentricity. The figure shows that the cross sections for increasing the eccentricities of Neptune and Uranus are largely unaffected by the increase in planetary mass, but the cross sections for Jupiter and Saturn are somewhat larger. Note that the cross sections are plotted only for eccentricity values $e \geq 0.20$. Within such a massive planetary system, small eccentricities ($e \sim 0.10$) are easily excited by planet-planet interactions; as a result, the cross sections for eccentricity increase — as determined through our numerical scheme — are extremely large and are not plotted in the figure.

The numerical results for the cross sections can be understood as follows: To leading order, we often expect the planets to act as test particles, so that the cross sections should not be sensitive to the planetary masses. For sufficiently massive planets, however, an increase in the eccentricity of one planet can lead to significant perturbations acting on the other planets, thereby leading to increased eccentricity excitation. By increasing the mass of all of the planets to that of Jupiter, the resulting solar systems are more excitable. The largest increase in the cross sections, which occurs for Jupiter and for low eccentricties, is only a factor of ~ 2; most cross sections experience smaller changes. These results are generally consistent with the idea that our Solar System is "full", i.e., no additional planets and little additional mass can be added to the extant planets without rendering the system unstable. In fact, even the current solar system is unstable on sufficiently long time scales (Batygin & Laughlin 2008; Laskar & Gastineau 2009).

Another way in which planetary orbits can be altered by scattering encounters is by changing their inclination angles. For all of the simulations, we start the four giant planets in the same plane (so that $i_J = i_S = i_U = i_N = 0$). After the encounters, the inclination angles of the four planets are, in general, nonzero. We define the

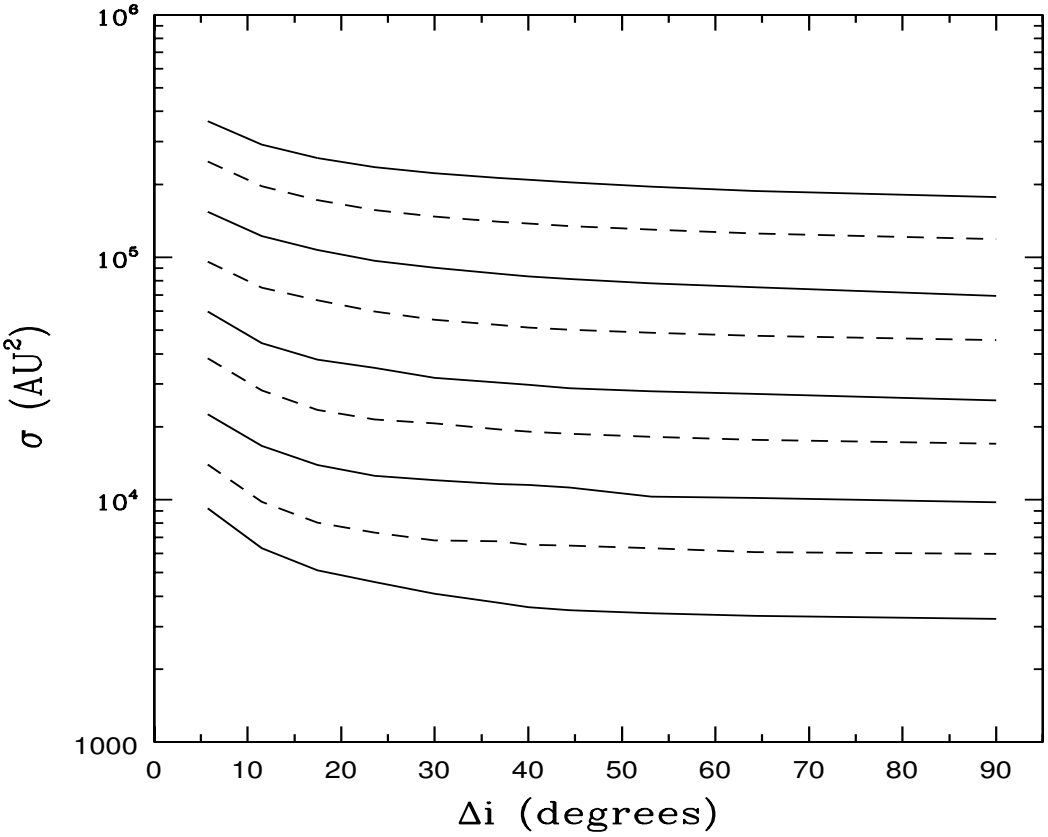

Figure 5.7: Cross sections for increasing the spread of inclination angles of the planetary orbits. All of the giant planets are started in the same plane; the quantity Δi is the total range of inclination angles of the four orbits after the encounters. Cross sections are shown for a variety of $v_{\rm b}$, from $v_{\rm b} = 1$ km/s (top curve) to $v_{\rm b} = 16$ km/s (bottom curve), where the values are evenly spaced logarithmically (by factors of $\sqrt{2}$).

post-encounter spread Δi of the inclination angles according to the expression

$$\Delta i \equiv \max \left\{ \cos^{-1} \left[\frac{\mathbf{J}_j \cdot \mathbf{J}_k}{J_j J_k} \right] \right\} , \tag{5.4}$$

where the $\mathbf{J}_i$ are the angular momentum vectors of the planetary orbits and where the indices run through all four of the giant planets. The resulting cross sections for increasing the spread of inclination angles is shown in Figure 5.7. The Figure shows the cross sections for a range of velocity dispersions of the background cluster, from $v_{\rm b} = 1$ km/s to $v_{\rm b} = 16$ km/s, where the values are spaced by factors of $\sqrt{2}$. The cross sections are almost evenly spaced in the semi-logarithmic plot and have nearly the same shape as a function of Δi. These properties indicate that the cross section has a power-law dependence on $v_{\rm b}$ (see Section 5.4).

In general, increases in the inclination angles are positively correlated with increases in eccentricity. This result is not unexpected, as changes in both orbital elements correspond to disruption of the initial states. To illustrate this trend, in Figure 5.8 we plot the increases in the spread of inclination angle Δi versus the change in eccentricity (equivalently, the post-encounter eccentricity since $\Delta e = e$). The two variables are in fact well correlated, but the range of possible Δi values for a given eccentricity $e = \Delta e$ is large. As a result, in the figure we plot the mean values of Δi averaged over a bin in Δe with a width of $\delta = 0.05$. The data show a well-defined correlation; for this choice of binning, the spread in the inclination angles grows to about 80° as the eccentricity grows to unity. The four curves shown in Figure 5.8 correspond to the four giant planets. Note that the orbits of all four planets show the same general trend.

The cross sections discussed thus far correspond to the immediate, post-encounter properties of the solar systems. In addition to immediate ejection, however, the solar

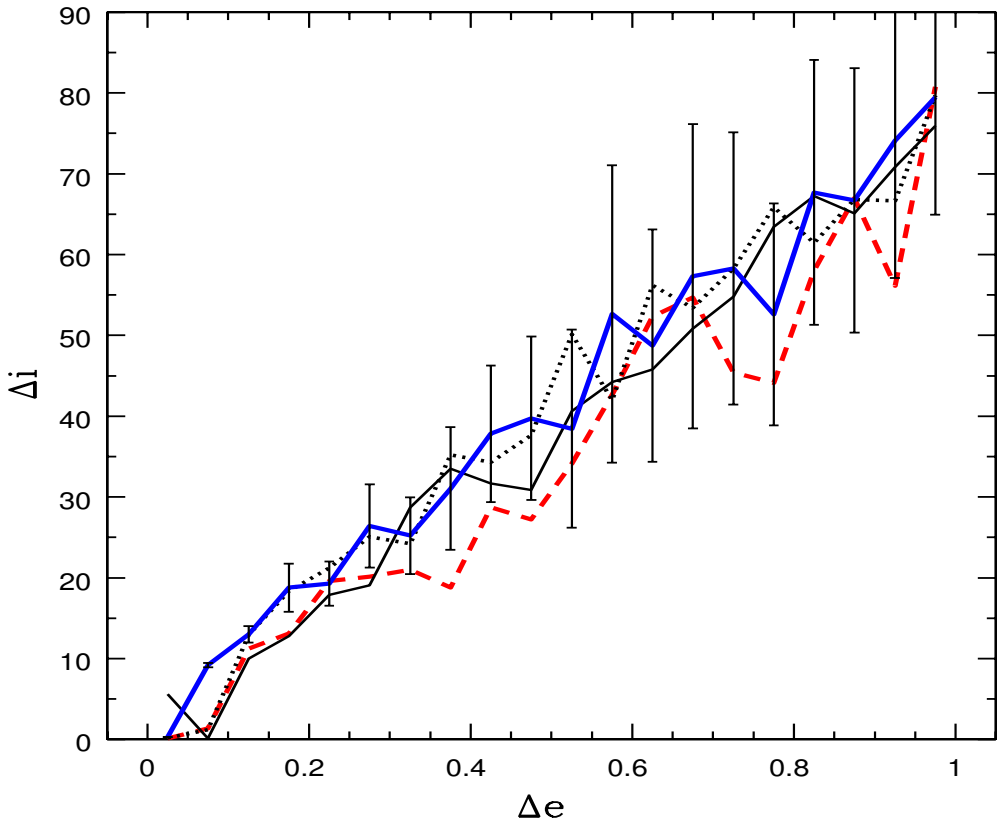

Figure 5.8: Correlation between eccentricity increases and increases in the spread of inclination angles of the planetary orbits. All of the giant planets are started in the same plane with circular orbits; the quantity Δi is the total range of inclination angles of the four orbits after the encounters. Correlations are shown for the orbital elements changes of Jupiter (heavy dashed red curve), Saturn (black solid curve), Uranus (black dotted curve), and Neptune (heavy blue solid curve). For each planet, the inclination angle increases are binned over a range in Δe of width $\delta = 0.05$. Although the correlation is well-defined, the range of Δi for a given value of Δe is relatively large. The error bars (shown for the Neptune curve only) depict the standard deviations.

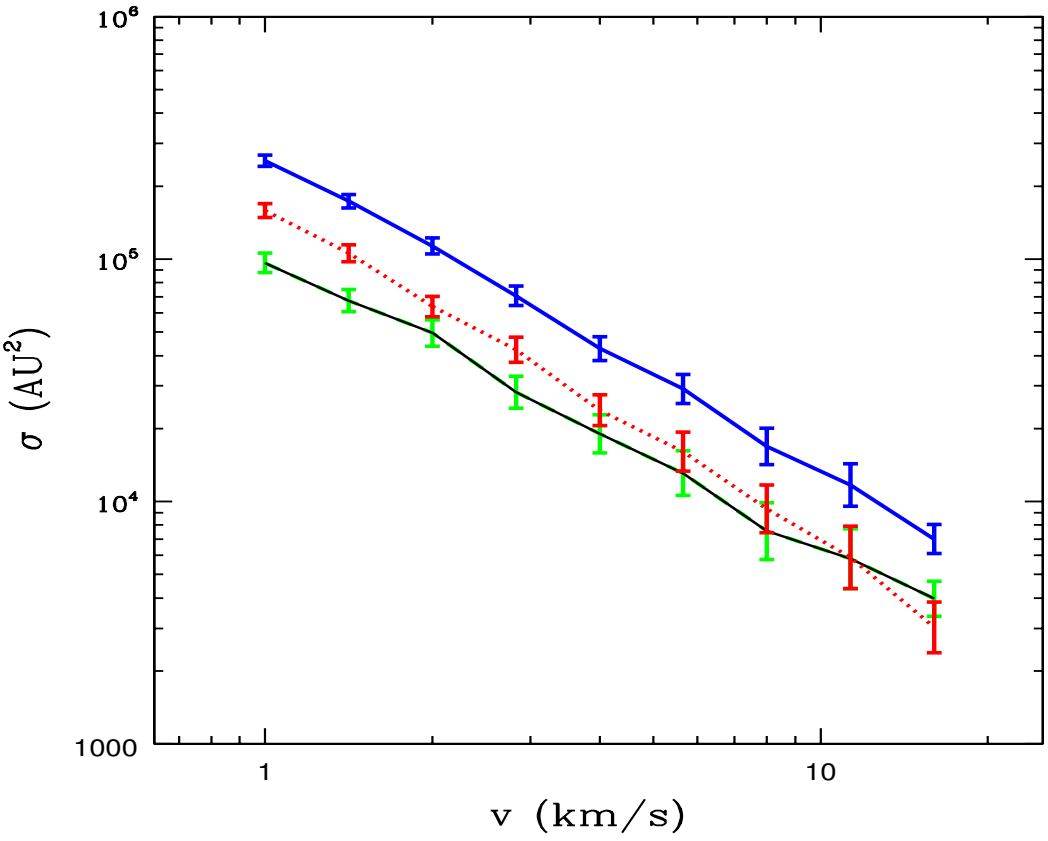

Figure 5.9: Cross sections for the ejection of at least one planet as a function of v_b in the cluster. The target systems have four giant planets with the masses and semimajor axes of our solar system bodies. Cross sections are shown for three cases: increases in eccentricity large enough to produce orbit crossing (solid dark curve marked by green error bars), direct ejection of a planet (dotted red curve), either channel of ejection (solid blue curve).

systems can be rendered sufficiently unstable so that they eject planets long after the scattering encounters are over. These longer term ejection events can be divided into (at least) two types. In the first — and most unstable — case, the scattering encounters leave the planetary orbits with high enough eccentricity so that adjacent orbits cross. Most orbiting-crossing systems will eventually eject one of their planets, provided that the system is not in a mean motion resonance; furthermore, perturbations due to stellar encounters are unlikely to place a planetary system in resonance. We address the effects of this type of instability by finding the cross sections for producing orbit-crossing planetary systems (see below). In the second case, systems with more modest eccentricities can be unstable over long spans of time. In order to assess the effects of this latter class of outcomes, the post-encounter systems must be integrated over typical stellar ages (billions of years). This task is beyond the scope of this present work, but provides an interesting problem for the future.

Using the results of our numerical experiments, we can calculate the cross sections for the scattering interactions to leave any two orbits with high enough eccentricities to cross. For the case of the analog solar system, where the four giant planets have their current masses and semimajor axes, the resulting cross sections are shown in Figure 5.9. Three sets of cross sections are shown as a function of $v_{\rm b}$ of the background cluster. The cross sections for the post-encounter system to have an orbit-crossing configuration are shown as the lower, green solid curve in the figure. For the calculation of this cross section, only systems where all of the planets are retained by the host star are included. The cross sections for the system to eject any planet (including those planets captured by the passing stars) are shown as the red dotted curve. Finally, the total cross sections for ejection, including both direct ejection of a planet and/or crossing orbits, are shown

as the blue solid curve in the figure. The error bars depict the uncertainties in the cross sections due to incomplete Monte Carlo sampling. Note that the cross sections for orbit crossing and the cross sections for direct ejection are roughly comparable, with the latter slightly larger (except at high velocity dispersion, where they are the same within the sampling uncertainties). The total cross section for ejection is thus larger than that for direct ejection by a factor of ~ 2. This statement holds only for the current solar system architecture, but remains valid over the range of velocity dispersion shown here ($v_{\rm b} = 1 - 16$ km/s).

We can now compare the results for the standard solar system architecture with that of the more compact configuration motivated by the Nice model. Here we consider only the most compact version where the planets are in multiple mean motion resonances (see Figure 5.2). The compact configuration is expected to have lower cross sections for direct ejection. But the orbits are closer together, so that less eccentricity excitation is required to produce crossing orbits. On the other hand, the semimajor axes are smaller, which lowers the cross sections for eccentricity increase. We find here that the cross sections for orbit crossing are comparable, $\langle \sigma \rangle = 96,500 \pm 3750$ AU^2 for the standard configuration versus $\langle \sigma \rangle = 92,200 \pm 3710$ AU^2 for the compact multi-resonant case. However, the cross section for direct ejection is larger for the standard solar system by a factor of 1.5, so that the total ejection cross section remains larger by a factor of ~ 1.25.

Although the semimajor axes of planetary orbits are altered less dramatically than the eccentricities and inclination angles during scattering encounters, the values of a are nonetheless affected. The possible variations are quantified in Figure 5.10, which shows the cross sections for producing relative changes $(\Delta a)/a$ in the semimajor axes of the four giant planets. This ensemble of numerical simulations uses the standard solar

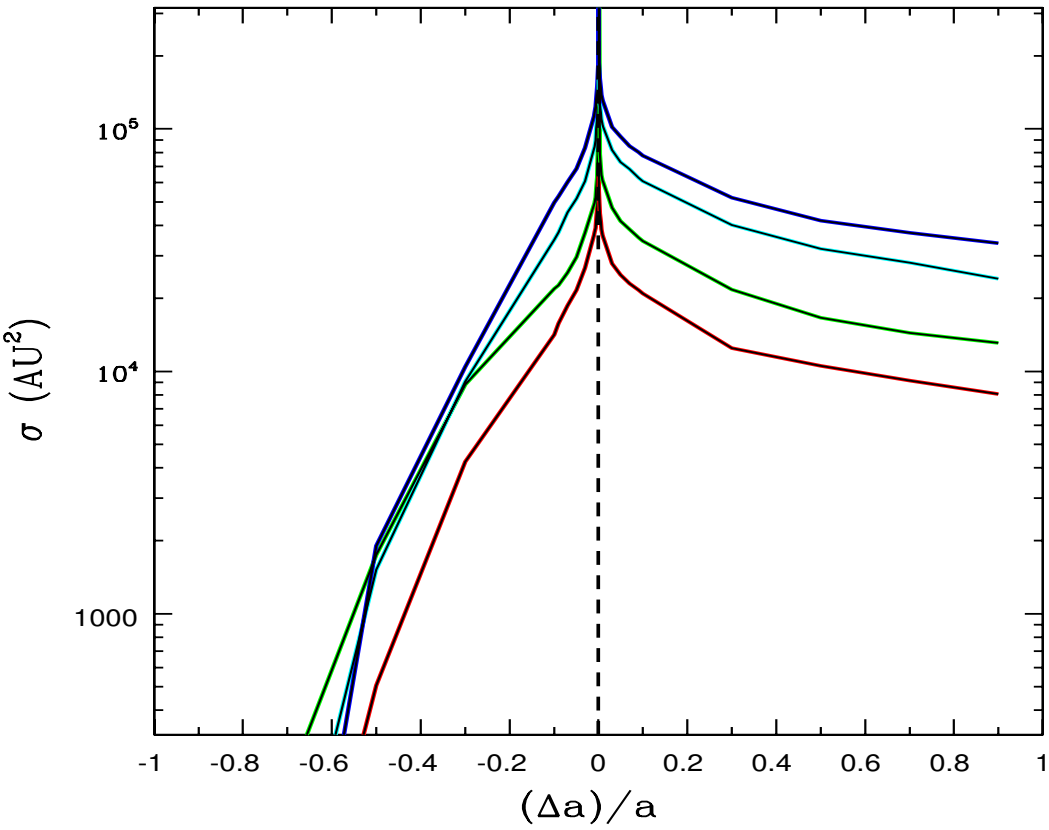

Figure 5.10: Cross sections for changes in the semimajor axis of the planetary orbits due to scattering encounters. The target systems are analogs of our Solar System, with the four giant planets initially in circular orbits with the current values of their semimajor axes. The plots shows the cross sections for relative changes $(\Delta a)/a$ in the semimajor axis for the orbits of Jupiter (lower red curve), Saturn (green curve), Uranus (cyan curve), and Neptune (upper blue curve).

system architecture as initial conditions, where the planets have their current masses and semimajor axes. The velocity dispersion of the background cluster is taken to be $v_{\rm b}/2 = 0.5$ km/s. As expected, the cross sections are largest for Neptune (top blue curve) and smallest for Jupiter (bottom red curve). As a crude approximation, the cross sections are proportional to the starting semimajor axes of the planets (although closer inspection shows the scaling is somewhat less steep than linear).

Scattering encounters can cause the semimajor axes to become either smaller or larger, corresponding to the loss or gain of orbital energy. However, Figure 5.10 shows that the process is highly asymmetric, where the orbits are much more likely to become larger (gain energy) than to move inward (lose energy). The scattering encounters rarely reduce the semimajor axes by more than a factor of two. Moreover, the magnitude of the cross sections are relatively small. More specifically, the cross sections for changing the initial semimajor axes by 10% are roughly comparable to — but somewhat smaller than — the cross sections for ejecting a planet (compare Figures 5.1 and 5.10). One might think that cross sections for moderate changes Δa would be larger than those for ejection. However, the cross sections for changes in semimajor axis do not include the ejections themselves, i.e., they are the cross sections for changing the semimajor axis with the planet remaining bound to its host star. For large changes in a, there is not much parameter space where a is increased but the planet remains bound (thereby leading to the values shown in Figure 5.10). Notice also that the figure does not show cross sections for overly small values of $(\Delta a)/a$; the cross sections become singular in the limit $(\Delta a)/a \to 0$, as marked by the vertical dashed line.

The cross sections considered thus far correspond to interactions between solar systems and passing binaries. On the other hand, roughly half of the stellar population

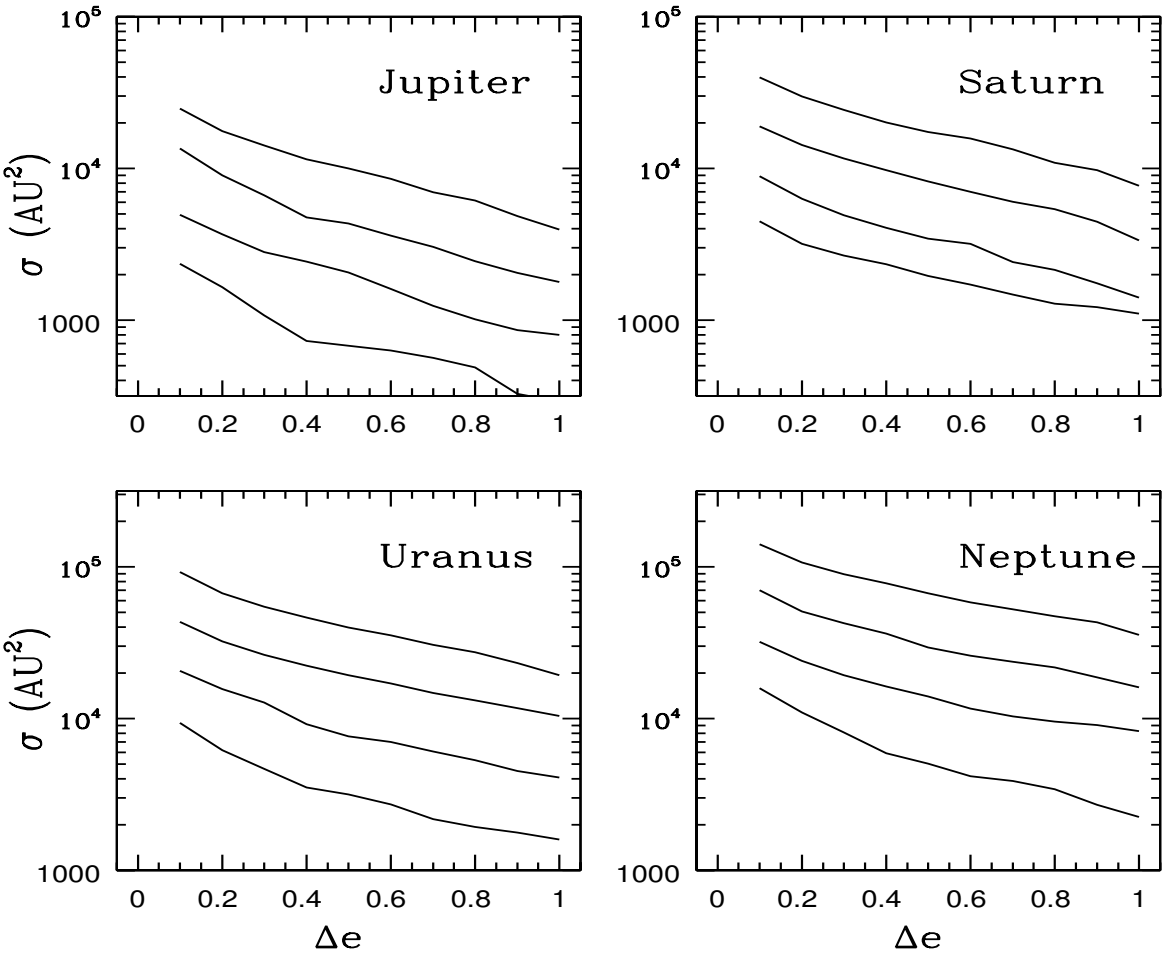

Figure 5.11: Cross sections for eccentricity increase due to encounters with passing single stars. The target systems are analogs of our Solar System, with the four giant planets in circular orbits with their current values of semimajor axis. Each panel shows the cross sections for a given planet, as labeled, where the curves correspond to varying velocity dispersions of the background cluster: $v_{\rm b} = 1$, 2, 4, and 8 km/s (from top to bottom).

consists of single stars, so that the corresponding cross sections for singles must also be determined. Since we are primarily interested in a comparison between the cross sections for single stars and binaries, it is crucial to use the same sampling for all of the parameters in the problem. Toward this end, we use exactly the same procedure as before (outlined in Section 5.2), but let the mass of the second star go to zero. In this limit, the other, single star automatically resides at the center of mass of the system (and the value of the binary eccentricity becomes irrelevant). The resulting cross sections for single stars interacting with solar system analogs are shown in Figure 5.11. As before, the initial solar systems consist of four giant planets with the masses and semimajor axes of the present day Solar System (but with zero starting eccentricity). Each panel shows the interaction cross sections for eccentricity increases for a given planet (as labeled). Results are shown for four values of the velocity dispersion of the background cluster, i.e., $v_{\rm b}$ = 1, 2, 4, and 8 km/s (ordered from top to bottom in each panel).

Next we make a rough comparison of the cross sections for single star interactions (Figure 5.11) with those obtained earlier for binaries (e.g., Figure 5.3). The single star cross sections are smaller by *more than a factor of two*. Note that the binary systems are, on average, somewhat wider than the size of the solar systems. As a result, as a pair of stars passes by a solar system, it consists mostly of empty space but still provides (roughly) twice the opportunity for interaction as a single star. One thus expects at least a factor of two reduction in the cross sections for passing singles. The fact that the reduction is larger than a factor of two is thus significant and indicates that the dynamics of the binaries themselves must contribute. Further, as discussed in the following section, the cross sections for single stars exhibit a different dependence on the background velocity dispersion and a slightly steeper dependence on post-encounter eccentricity.

For convenience, Table 2 collects the cross sections for the ejection and capture of all four planets. For each solar system configuration considered in this paper, the table lists two sets of cross sections, where the first line corresponds to planetary ejection and the second line corresponds to planetary capture. The Standard Model (the first configuration in the table) represents the case where the four giant planets have the masses and semimajor axes of our current Solar System, the host star has mass $M_* = 1.0 M_\odot$, the velocity dispersion of the cluster $v_\mathrm{b} = 1$ km/s, and the interacting stars are binary. The first column in the table labels the solar system configuration by the variable that differs from its standard value. The error bars in the table are those due to incomplete Monte Carlo sampling. One way to assess statistical significance is through the ratio of the cross section to its sampling error. For the ejection cross sections, the mean value (averaged over the entire table) of this signal to noise ratio is ~ 14, so that the ejection cross sections are well-determined. Capture events are much more rare. For the capture cross sections, the mean value of the signal to noise ratio is only ~ 4. For the rarest events, captures with high cluster velocity dispersion, the cross sections are only defined at the factor of two level.

5.4 Analysis and Scaling Laws

The cross sections found in the previous section display relatively simple dependences on the underlying variables of the problem: For example, for each type of solar system, the cross sections, when considered as functions of the post-encounter planetary eccentricity e, all display the same general shape. As a result, the functions $\langle\sigma\rangle(e)$ can (almost) be rescaled to find a universal functional form, where scaling factors take into account the

initial semimajor axis a of the planet, the velocity dispersion $v_{\rm b}/2$ of the background environment, the stellar mass M_*, and so on. The goal of this section is to understand the general scaling properties of the cross sections and to determine the extent to which they are self-similar. In general, self-similarity arises when physical scales are either missing from a problem or do not contribute to the results (Barenblatt 2003); we return to this issue at the end of the section.

Even in the reduced case where we consider one planet at at time, the interactions considered in this paper involve four bodies (the host star, the planet, and two binary members). Unfortunately, four-body interactions are rather difficult to describe analytically to any reasonable degree of approximation. As a result, the goal of this section is relatively modest: Instead of building complicated analytical models for 4-body (and higher N-body) dynamics, we consider here basic physical principles that can be used as motivation for scaling laws. We then combine these heuristic results with our detailed numerical determinations of the cross sections. The result is physically motivated fitting formula that characterize the cross sections over the parameter space of interest $(a, v_{\rm b}, M_*, e)$.

To start the discussion, consider the simplest case where the the cross section for interactions is the geometrical cross section πa^2 provided by a planet in its initial orbit. Further, we consider the planets to be independent of each other during the encounters. This cross section will be enhanced by gravitational focusing, so we can write down an heuristic expression for the cross section in the form

$$\langle\sigma\rangle_0 \approx \alpha\pi a^2 \left(1 + \frac{v_{esc}^2}{v_\infty^2}\right) , \tag{5.5}$$

where v_{esc} is the escape speed from the target system (at the location of the planet), and

v_∞ is the asymptotic relative speed between the two systems. In order to pass within this cross sectional area, the interacting star (binary) must be about the same distance from the planet as its host star, so that the planet has a chance of being ejected from its original solar system. This expression thus represents the escape cross section. The parameter α is a dimensionless constant of order unity and is included to encapsulate the uncertainties inherent in this approximation. After inserting the expression for the escape speed, we obtain

$$\langle\sigma\rangle_0 = \alpha\pi a^2 \left(1 + \frac{GM_*}{av_\mathrm{b}^2}\right) \rightarrow \alpha\pi\ell a\,, \tag{5.6}$$

where we have replaced the asymptotic speed v_∞ with v_b of the cluster (or other background stellar system) and we have defined the corresponding length scale $\ell \equiv GM_*/v_\mathrm{b}^2$ (where $\ell \sim 890$ AU for $v_\mathrm{b} = 1$ km/s). The final expression represents the limiting form, which is applicable when gravitational focusing dominates, and implies a linear dependence of the cross section on a. Given this form, the cross section requires another length scale. In this problem, the orbit speed of the binary, the asymptotic speed v_∞ of the encounter, the orbit speed of the planet, and v_b are all roughly comparable (1 – 10 km/s). For example, the orbit of Neptune in our solar system has an escape speed of ~ 5.5 km/s, whereas the orbit speed of a binary at the peak of the period distribution is also ~ 5 km/s. If we only have a single velocity V, then dimensional analysis implies that the relevant length scale must be $\ell = GM_*/V^2$, as given in equation (5.6); additional uncertainties can be absorbed into the dimensionless parameter α. Finally we note that for a velocity dispersion $v_\mathrm{b} = 1$ km/s, the gravitational focusing term dominates by a factor of 30.

The limiting form of equation (5.6) is linear in the starting semimajor axis a of

the planet. To see how well this expression works, we plot the ejection cross sections of the planets versus semimajor axis in Figure 5.12. As expected, the ejection cross section is a nearly linear function of the semimajor axis. This trend holds for solar systems starting with the present-day semimajor axes (star symbols) and the more compact configuration where the semimajor axes are spaced by factors of 5/3 (open triangles). We also plot results for ultra-compact solar systems in multiple mean motion resonance (open squares). In order to isolate the dependence of the cross sections on initial semimajor axis from planet-planet scattering effects, this latter case uses smaller planet masses (by a factor of 10), so they act more like test masses; to explore a wider range in a, we also take this compact system to be smaller by a factor of 1.35 compared to that considered in the previous section. The error bars delineate the uncertainty due to incomplete Monte Carlo sampling. Not only do the cross sections show nearly linear dependence on a, but the slope of the curve is predicted by the above analysis. The red solid (blue dashed) curve in Figure 5.12 shows the cross section predicted by equation (5.6) for the limiting case (full form); for both cases, the characteristic length scale $\ell =$ 890 AU and the dimensionless parameter $\alpha = 7/5$.*

Next we consider the dependence of the cross sections on the post-encounter eccentricity e (which is equivalent to Δe because the orbits start with zero eccentricity). For all four planets in all three types of solar system, the e-dependence is similar. Since the ejection cross sections scale linearly with semimajor axis a (see Figure 5.12), we scale the cross sections by dividing out one power of a. The resulting scaled cross sections are

*In order to set the value for this dimensionless parameter, and others specified in this section, we generally search in increments of 10^{-2}, find the value that gives the minimum RMS error, and then choose the nearest round number (ratio of relatively small integers).

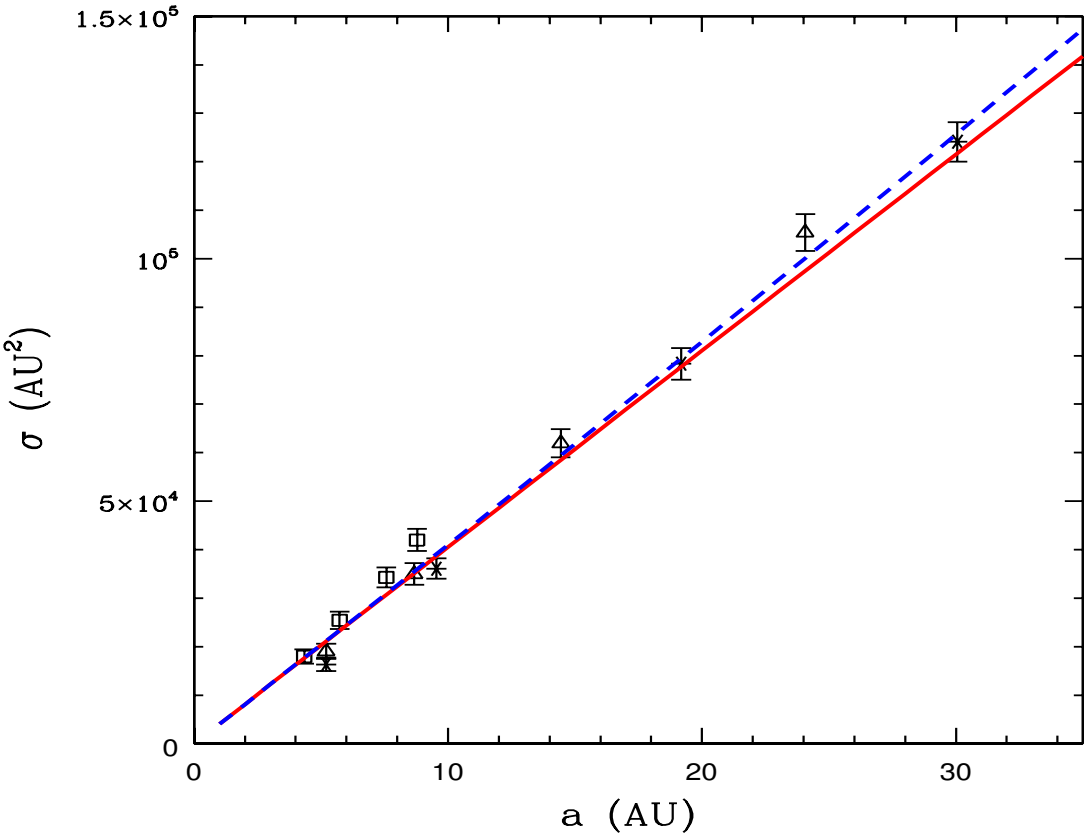

Figure 5.12: Cross sections for planetary escape versus the starting semimajor axis. The 12 points on the plot correspond to the four giant planets in each of three versions of the initial solar system architecture. The symbols represent different starting states, including the semimajor axes of the present-day solar system (stars), a compact configuration with 5/3 semimajor axis ratios (open triangles), and an ultra-compact solar system starting in multiple mean motion resonances (open squares). The red solid line shows the cross section indicated by the limiting form of equation (5.6); the blue dashed curve shows the full form.

shown in Figure 5.13 as a function of eccentricity e. In addition to the individual cases (shown as the light dotted curves), the average is shown as the heavy blue curve, where the error bars depict the standard deviation. This latter quantity provides a measure of the spread in the values of the cross section over the various cases. The standard deviation varies from about 17% of the cross section at low eccentricity $e = 0.10$ to only about 9% at $e = 1.0$.

The curves in Figure 5.13 are nearly straight lines on the semi-logarithmic plot, so that the dependence of the cross sections on eccentricity is nearly exponential. For purposes of illustration, we use an exponential fitting function of the form

$$\frac{\langle\sigma\rangle_e}{a} = \alpha\pi\ell \exp[\, b\,(1-e)\,]\,, \tag{5.7}$$

where the first factor enforces consistency with the ejection cross sections considered above. For the value $b = 4/3$, we obtain a good fit to the calculated, scaled cross sections, as shown by the heavy red line in Figure 5.13. Except for first point ($e = 0.1$), the exponential fit (straight red line) agrees with the average values (solid blue curve) to within about 3%, i.e., the difference is much less than the width of the distributions as measured by the standard deviations. Another measure of the quality of the fit is provided the relative differences between the numerically determined cross sections used in constructing Figure 5.13 and the exponential form given by equation (5.7); the RMS of these relative errors is $\sim 12\%$.

Next we consider the effects of the velocity dispersion of the background cluster environment. As shown in Figure 5.3 in the previous section, the cross sections vary with the post-encounter eccentricity with approximately the same functional form over a wide range of v_b. Only the leading cofficient changes. Moreover, the uniform spacing of the

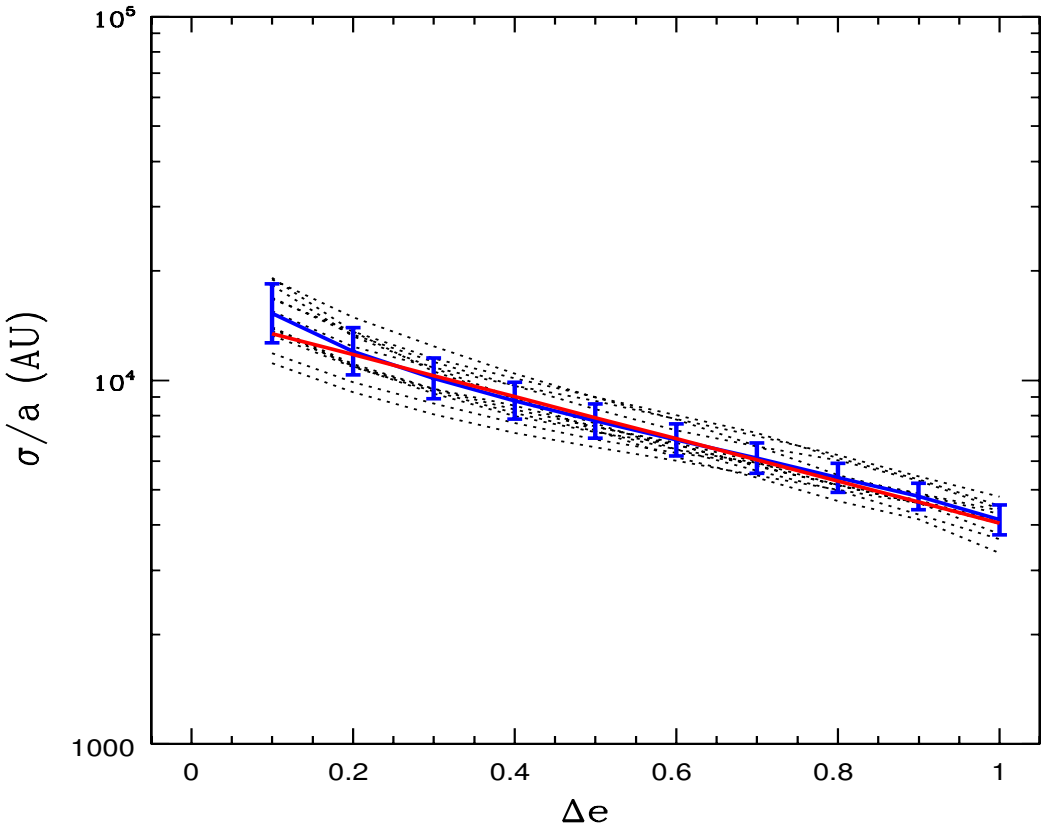

Figure 5.13: Scaled cross sections versus eccentricity increase Δe (equivalently, the post-encounter eccentricity e) for the four giant planets in each of the starting architectures for the solar system. The individual cases are shown as light dotted curves. The heavy solid blue curve depicts the average, where the error bars depict the standard deviation. The straight red line shows the result for cross sections with a purely exponential dependence on eccentricity.

curves in Figure 5.3 indicates that the cross sections must have a power-law dependence on $v_{\rm b}$ (to leading order). We have explored scalings with velocity dependence of the form $\langle\sigma\rangle \propto v_{\rm b}^{-\gamma}$ and find that the best fit occurs for $\gamma \approx 7/5$. Using this choice of power-law index, we plot the scaled cross sections versus post-encounter eccentricity in Figure 5.14, where we include the linear a-dependence found previously (i.e., $\langle\sigma\rangle v_{\rm b}^{7/5}/a$). Each light dotted curve in the figure shows the result for one planet and one choice of velocity dispersion. The heavy blue curve shows the average over all of the curves, where the error bars depict one standard deviation. The heavy straight red line represents the same exponential dependence given in equation (5.7) and used in Figure 5.13. The RMS of the relative differences between the numerically determined cross sections and the curve given by equation (5.7) is $\sim 13\%$. The cross section curves are thus self-similar to this level of accuracy. Furthermore, the dependence of the cross sections on velocity dispersion is nearly independent of the dependence on starting semimajor axis a of the planet.

The dependence of the interaction cross sections on the mass of the host star is somewhat more complicated than for the other variables, as illustrated in Figure 5.4. As the mass M_* of the star increases, the cross sections, considered as functions of eccentricity, become steeper. The spacing of the curves in Figure 5.4 (for different stellar masses) grows with e, so that the curves are not self-similar. In spite of this complication, we can still fit the cross sections with a power-law function of stellar mass, although the accuracy of the approximation is not expected to be as high as in the previous cases. We thus consider a scaling of the form $\langle\sigma\rangle \propto M_*^{-\mu}$, and vary the index μ to find the best fit. The choice $\mu = 1/3$ provides the lowest RMS of the relative error. Figure 5.15 shows the result by plotting the scaled cross sections $\langle\sigma\rangle M_*^{1/3}/a$ (again including the

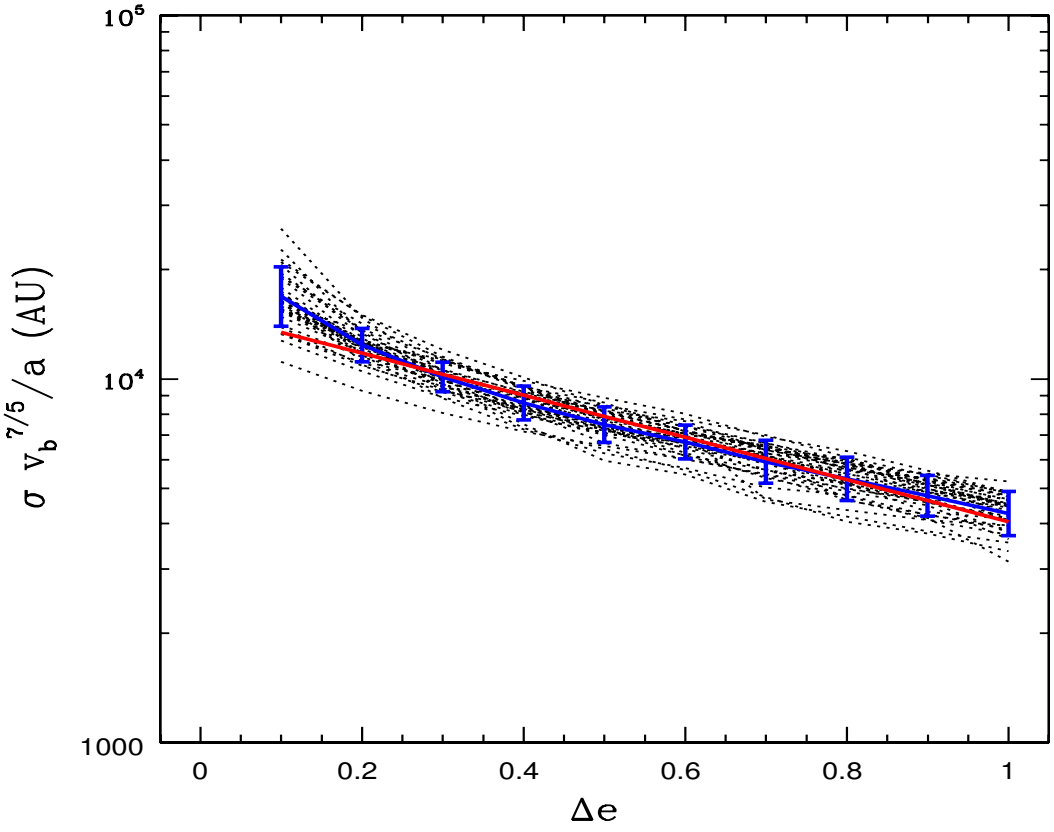

Figure 5.14: Scaled cross sections versus eccentricity increase Δe (equivalently, post-encounter eccentricity e) for a collection of different velocity dispersions for the background. The starting state is taken to have four giant planets with the current semimajor axes. Cross sections are scaled by $v_{\rm b}^{7/5}/a$ (see text). The individual cases are shown as light dotted curves, with include curves for each of the planets for $v_{\rm b} = 1$ – 16 km/s, equally spaced logarithmically (by factors of $\sqrt{2}$). The heavy solid blue curve depicts the average, where the error bars depict the standard deviation. The red striaght line shows the result for cross sections with a purely exponential dependence on eccentricity.

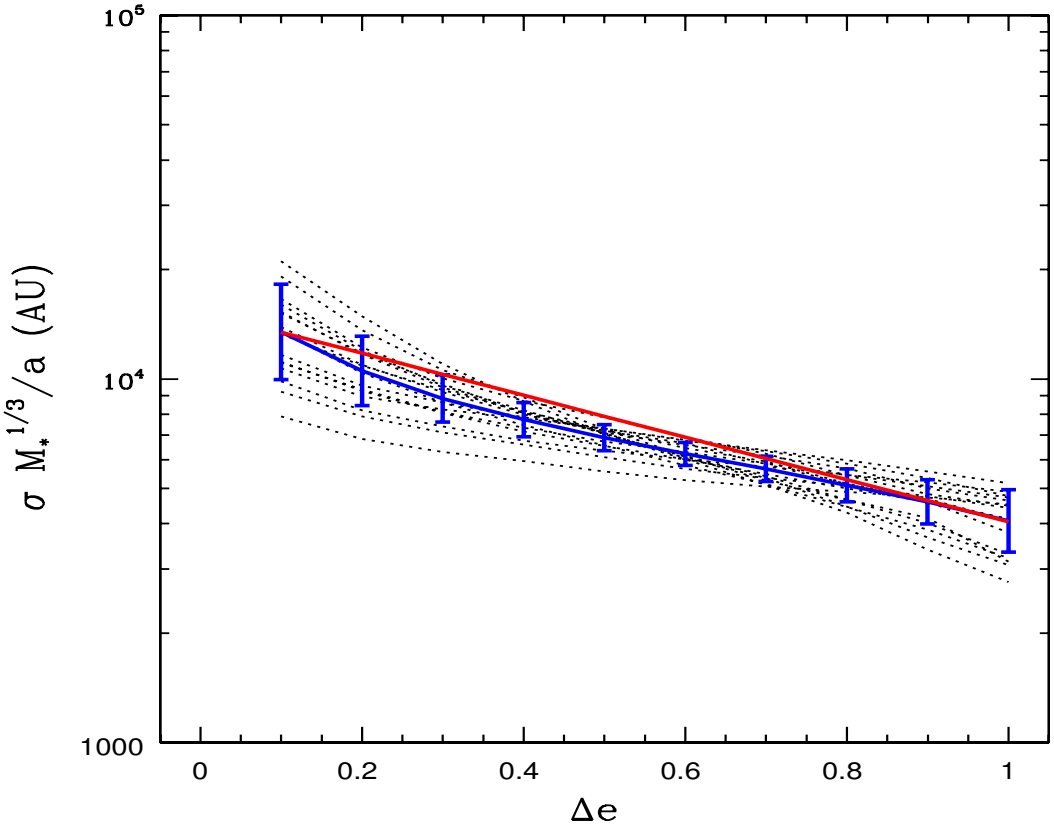

Figure 5.15: Scaled cross sections versus eccentricity increase Δe (equivalently, post-encounter eccentricity e) for solar systems with different stellar masses. The starting state is taken to have four giant planets with the current masses and semimajor axes. Cross sections are scaled by $M_*^{1/3}/a$ (see text). The individual cases are shown as light dotted curves, with include curves for each of the four planets for four choices of stellar mass $M_* = 0.25 - 2.0\ M_\odot$ (spaced by factors of 2). The heavy solid blue curve depicts the average, where the error bars depict the standard deviation. The red striaght line shows the result for cross sections with a purely exponential dependence on eccentricity.

linear dependence on semimajor axis a) as a function of post-encounter eccentricity. The light dotted lines show the individual (scaled) cross sections and the heavy blue curve shows the average. The error bars depict the corresponding standard deviation, which is larger than for the cases considered previously (compare Figure 5.15 with Figures 5.13 and 5.14). The heavy red staight line shows the same result as before (from equation [5.7]). The RMS error between the exponential line and the numerically determined cross sections is about 20%. This larger error measure results from fitting the cross sections with a power-law form, even though the results depart somewhat more from self-similarity.

The cross sections for increasing the spread of inclination angles, considered over a range of velocity dispersions, also show a nearly self-similar form (see Figure 5.7). This finding indicates that the cross section should scale with a nearly power-law dependence so that $\langle\sigma\rangle \propto v_{\rm b}^{-\eta}$. Over the range $v_{\rm b} = 1 - 16$ km/s, we find that the best fit occurs for $\eta \approx 7/5$. To illustrate how well this scaling law works, we plot the scaled cross sections $\langle\sigma\rangle v_{\rm b}^{7/5}$ as a function of $\sin(\Delta i)$ in Figure 5.16. Each light dotted curve in the figure corresponds to the result of one choice of velocity dispersion. The heavy blue curve shows the average of the scaled cross sections, where the error bars depict the standard deviations. The mean size of the error bars corresponds to relative differences of $\sim 6\%$, so that the curves are self-similar to this degree of accuracy. Notice that the scaling exponent $\eta \approx 7/5$ for inclination angle increases as a function of $v_{\rm b}$ is the same as the corresponding index for eccentricity increases.

After the velocity dependence has been scaled out, the cross section for increasing the spread of inclination angles is a slowly varying monotonic function of Δi (see Figure 5.16). If we consider $x = \sin\Delta i$ as the independent variable (instead of Δi itself), the

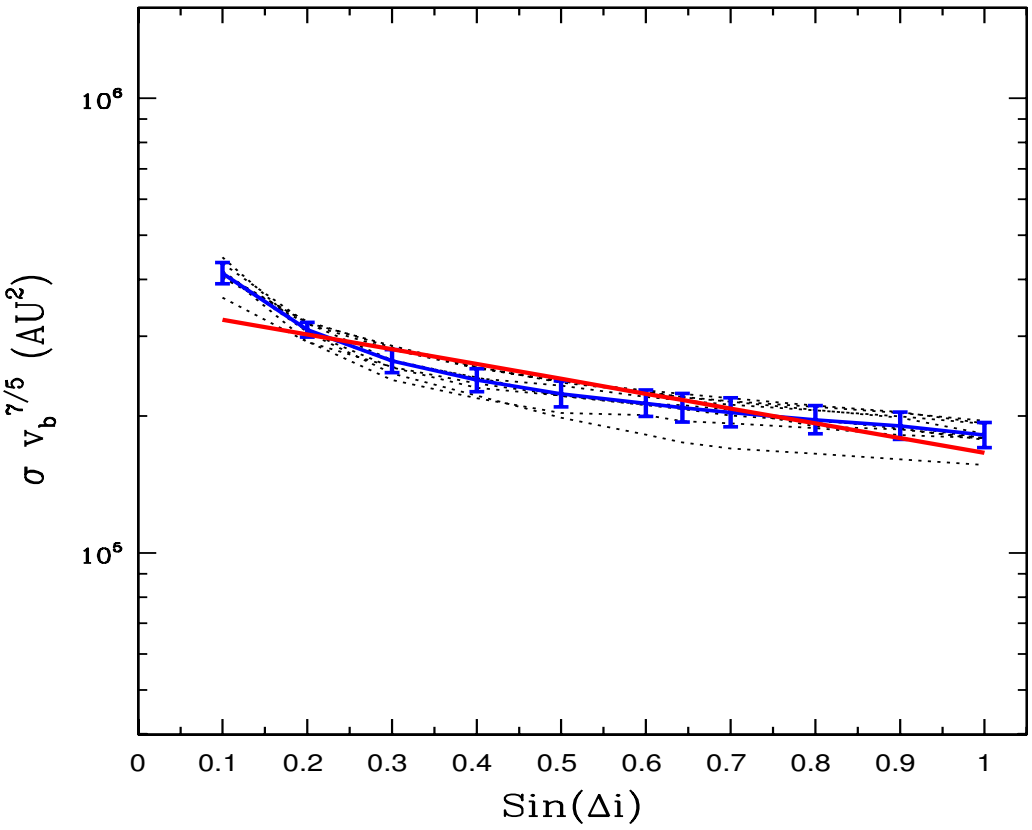

Figure 5.16: Scaled cross sections for increasing the post-encounter spread Δi of the inclination angles of the planetary orbits. The starting states have the four giant planets orbiting in the same plane ($\Delta i = 0$). The cross sections are scaled by the velocity dispersion of the cluster with the relation $\langle\sigma\rangle v_{\rm b}^{7/5}$. The individual cases are shown as light dotted curves. The heavy solid blue curve depicts the average, whereas the error bars depict the standard deviation. The heavy red curve shows the fitting function described in the text.

cross section can be fit with an exponential function which is analogous to that used to describe the eccentricity dependence. More specifically, if we use the functional form

$$\langle\sigma\rangle_i = \langle\sigma\rangle_0 \exp\left[b_0\left(1 - \sin\Delta i\right)\right] , \tag{5.8}$$

then the cross section for increasing Δi can be fit using the parameters $b \approx 3/4$ and $\sigma_0 \approx 166,000$ AU^2. Note that the value of the index b used here somewhat smaller than that needed to fit the dependence of the cross sections on (post-encounter) eccentricity (compare with equation [5.7]). The fitting function from equation (5.8) is shown in Figure 5.16 as the solid red curve. The quality of the fit is reasonably good: The fitting curve falls within one standard deviation (marked by errorbars in the figure) of the mean for all of the range except the first point ($x = \sin\Delta i = 0.1$); alternately, the RMS of the relative error between the two curves is $\sim 8\%$. However, the mean of the numerical results (blue curve) shows more curvature than the exponential fit (red curve), especially at small values of x.

Although we could find a more complicated fitting function that has smaller RMS relative error, we use equation (5.8) in order to compare changes in the spread of inclination angle with changes orbital eccentricity. If we equate the variable $x = \sin\Delta i$ with e, then equations (5.7) and (5.8) have the same general form. We can then compare the leading coefficients, which have values $\langle\sigma\rangle_0 \approx$ 166,000 AU^2 for Δi-dependence and $\alpha\pi\ell a \approx$ 120,000 AU^2 for e-dependence, where we have used $a = 30$ AU to evaluate the latter expression. The cross sections for eccentricity increase and spread of the inclination angles thus display similar behavior. The leading coefficients agree to within $\sim 28\%$ and we can make the following inexact analogy: An increase in Neptune's eccentricity of Δe = 0.1 corresponds to changing the spread of the inclination angles (of all four planets)

so that $\sin \Delta i$ increases by 0.1. We can also make a rough association between increasing the spread of inclination angles to $\Delta i \geq 90$ degrees and the ejection of a planet ($e \geq 1$). Both of these events have (approximately) the same cross section and both involve order unity changes to the angular momenta of the planetary orbits. In addition, the cross sections for inclination angle increase and eccentricity increase scale with the $v_{\rm b}$ in the same manner ($\propto v_{\rm b}^{7/5}$).

The association between changes in the variables $\sin \Delta i$ and e provides an intriguing topic for additional work. To leading order, the canonical actions written in terms of the orbital elements have the forms

$$\Gamma \propto \frac{1}{2} e^2 \qquad \text{and} \qquad Z \propto \sin^2(i/2) \,. \tag{5.9}$$

The apparent relation between the two variables (as observed in the simulation results) could thus be evidence of an equipartition-like mixing of the actions (see Lichtenberg & Lieberman 1992). Although beyond the scope of the present paper, this issue should be explored further.

We can extract a potentially important cross section from these results. The scattering interactions considered here can readily increase the spread of inclination angles of outer bodies in a solar system. On the other hand, the scattering events themselves have little effect on planets in tight orbits, such as the multi-planet systems observed by the *Kepler* mission (Batalha et al. 2013). However, the bodies in the outer solar system can have important long-term effects on the inner bodies provided that they are scattered into orbits with sufficiently high inclination angles. More specifically, if the inclination angles of the outer orbits are larger than 39.2°, then the Kozai effect can operate (Kozai 1962; Lidov 1962), and the inner portions of the solar system can be

excited over the age of the systems. Combining this requirement with the results of our numerical simulations, we find that the cross section for scattering a solar system into a state where the Kozai effect can operate is given by

$$\langle\sigma\rangle_{\rm Kozai62} \approx 210,000\,{\rm AU}^2 \left(\frac{a_{\rm out}}{30\,{\rm AU}}\right)\left(\frac{v_{\rm b}}{1\,{\rm km/s}}\right)^{-7/5}, \tag{5.10}$$

where $a_{\rm out}$ is the semimajor axis of the outermost planet of the system. Note that the requirement of large mutual inclination is necessary but not sufficient for the Kozai effect to play a role. The Kozai effect is a highly fragile type of interaction because it involves libration of the argument of periastron, and this quantity can be subject to many other sources of precession (for further discussion, see Batygin et al. 2011). We also note that this form for the cross section (equation [5.10]) involves some extrapolation: The numerical simulations were carried out primarily for the architecture of the current solar system. Nonetheless, the outermost planet is always the most affected by fly-by interactions, and the cross sections scale linearly with semimajor axis to a good approximation.

Next we consider the scaling behavior of the cross sections for interactions with passing single stars. As for the case of binary systems, we expect the cross sections to scale nearly linearly with the semimajor axis a of a given planet. In addition, the nearly equal spacing on the logarithmic plot of Figure 5.11 indicates that the cross sections should display power-law dependence on the velocity dispersion, such that $\langle\sigma\rangle \propto v_{\rm b}^{-\gamma_s}$. The velocity dependence for these single star cross sections is moderately less steep than those found earlier for binaries; the optimal value of the index $\gamma_s \approx 6/5$, which is somewhat smaller than the value for binary cross sections $\gamma \approx 7/5$. After scaling out the semimajor axis and velocity dispersion, the reduced cross sections are shown in Figure

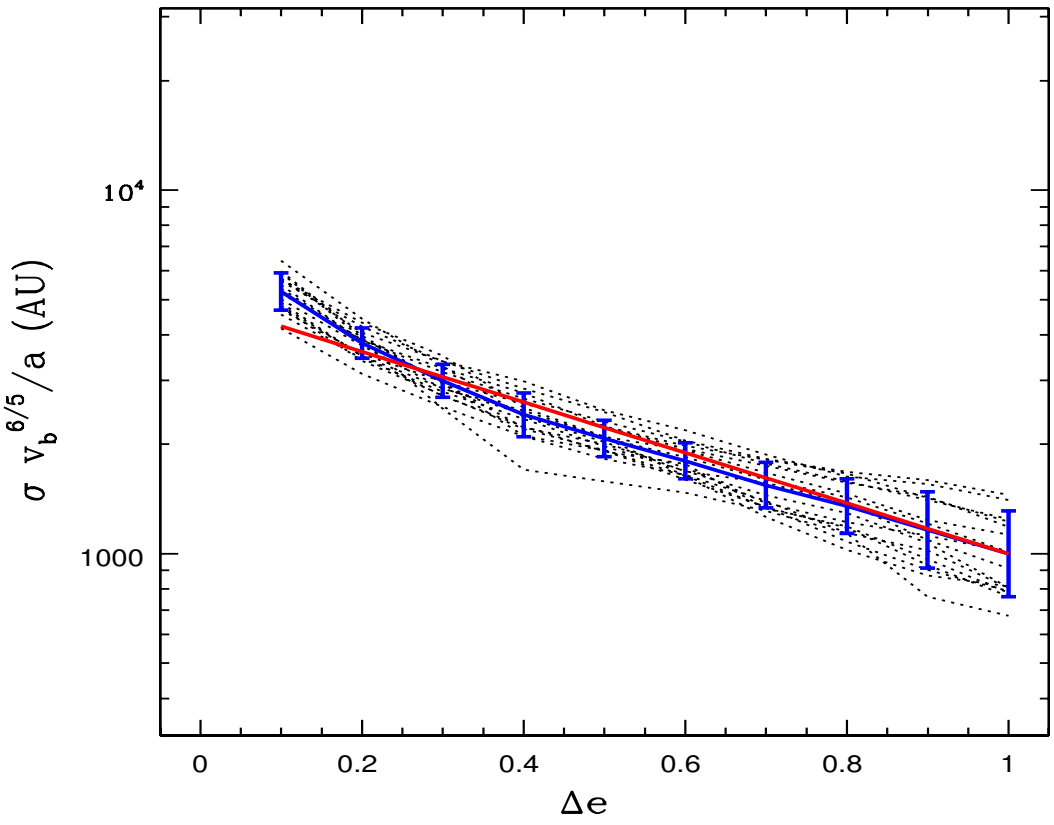

Figure 5.17: Scaled cross sections versus eccentricity increase Δe (equivalently, post-encounter eccentricity e) for solar systems interacting with single stars. The starting states have four giant planets with the current masses and semimajor axes of our Solar System. Cross sections are scaled by the factor $v_{\rm b}^{6/5}/a$. The individual cases are shown as light dotted curves, which include the four giant planets and four values of velocity dispersion of the background cluster: $v_{\rm b} = 1$, 2, 4, and 8 km/s. The heavy solid blue curve depicts the average, where the error bars depict the standard deviation. The red striaght line shows the result for cross sections with an exponential dependence on eccentricity.

5.17. The light dotted curves show the scaled values for given planets and values of $v_{\rm b}$ (which lie in the range 1 – 8 km/s). The heavy blue curve shows the mean over the entire collection and the error bars denote the standard deviations. These error bars correspond to an average relative error of $\sim 15\%$, which is comparable to, but somewhat larger than that found for the binary cross sections.

The scaled cross sections shown in Figure 5.17 for single star interactions show a nearly exponential dependence on the post-encounter eccentricity. Although this behavior is analogous to that found for the binary cross sections, the slope of the exponential is somewhat steeper. Here we consider a fitting function of the form

$$\langle\sigma\rangle_{\rm single} = \langle\sigma\rangle_0 \left(\frac{a}{\rm AU}\right) \left(\frac{v_{\rm b}}{1\,{\rm km/s}}\right)^{6/5} \exp\left[b_s(1-e)\right], \tag{5.11}$$

where we obtain a good fit for $\langle\sigma\rangle_0 = 1000$ AU^2 and $b_s = 8/5$. The resulting fit is shown as the red straight line in Figure 5.17. The RMS difference between the expression of equation (5.11) and the numerically determined, scaled cross sections for single stars is only $\sim 8\%$.

Now we can compare the cross sections for single stars with those for binaries. The comparison is complicated by the different scalings of the two cases with velocity dispersion and the different exponential laws for the eccentricity dependence. To fix ideas, consider the benchmark case where $v_{\rm b} = 1$ km/s for the background cluster. Here, the cross sections for binary star interactions are ~ 4.2 times larger than those for single stars at the high end of the eccentricity range $e = 1$. Similarly, the binary cross sections are ~ 3.2 times larger at the low end of the eccentricity range where $e = 0.10$. Averaged over the span of eccentricity considered here, the binary cross sections are larger by a factor of ~ 3.6. This factor decreases with increasing velocity dispersion, however,

because the binary cross sections fall according to the relation $\langle\sigma\rangle \propto v_{\rm b}^{-7/5}$, whereas the single star cross sections fall as $\langle\sigma\rangle \propto v_{\rm b}^{-6/5}$. With these scaling laws, the cross sections for binaries are only a factor of 2 larger (than those for single stars) when the $v_{\rm b}$ is increased to $v_{\rm b} \approx 20$ km/s.

These results can be interpreted as follows: At high asymptotic speeds, which occur for $v_{\rm b} \gtrsim 20$ km/s, the two members of a binary pass by the solar system quickly enough so that binary motion and planetary motion play only a minor role in the interaction (this speed is much larger than the mean orbital speed of either the binary or the outer planet). As a result, the two stars interact with the solar system in an almost independent manner, and the cross sections for binary interactions should be a factor of ~ 2 larger than those for single stars (for large $v_{\rm b}$). On the other hand, lower impact speeds can be comparable to the binary orbital speed and/or the planetary orbital speeds. In this regime, the motion of the binary stars relative to one another during the encounter can increase their chances of interacting with the planets, thereby leading to larger cross sections. In extreme cases, resonant interactions can occur when the velocity scales of the problem are all comparable (see also Laughlin & Adams 2000), and these long-lived events can greatly increase the chances of disruption of planetary orbits during the encounters. To be consistent with this picture, the ratio of the single-star cross section to the binary cross section must decrease less steeply with $v_{\rm b}$, as found here.

Before leaving this section, we briefly address the issue of how self-similarity can arise in the context of solar system scattering. In its full form, this problem has six velocities (four planetary orbits, one binary orbit, and the encounter velocity) and seven masses (four planets and three stars). One expects self-similarity only when most of these scales do not contribute (Barenblatt 2003). We can construct an argument to reduce the

number of relevant scales as follows: To leading order — and only during the encounter itself — planetary interactions with the binary are independent of interactions with other planets. As a result, we can (often) treat the encounters as single-planet systems scattering with binaries. The planet itself is usually small enough to be considered as a test mass, so that we are left with "only" three masses and three velocities. The binary masses are always drawn from the same IMF, and the cross sections are determined through many samples of that IMF ($\mathcal{N}_E \gtrsim 80,000$), thereby leaving the ratio $M_*/(M_{1*} + M_{2*})$ as the most important mass variable. In the regime of interest, the cross sections have values in the range $\langle\sigma\rangle \sim 10^4 - few \times 10^5$ AU^2, which implies that the length scales that characterize the interactions $\ell_{\rm c} \equiv \langle\sigma\rangle^{1/2} \approx 100 - 500$ AU. This size scale is larger than that of both the planetary orbits ($a = 5 - 30$ AU) and most binary orbits (where the peak of the period distributions corresponds to $a_{\rm b} \approx 42$ AU). If the orbital speeds of the planets and the binary are fast enough, then their orbits can be replaced by rings of mass with the same semimajor axis and eccentricity (Murray & Dermott 1999). This averaging effectively eliminates the orbital velocities from the problem and leaves $v_{\rm b}$ as the most important velocity variable. Indeed, we find that the cross sections depend most sensitively on the stellar host mass M_* (equivalently, the mass ratio $M_*/(M_{1*} + M_{2*})$) and the velocity dispersion $v_{\rm b}$. This argument is not exact, however, and the additional scales (e.g., orbits speeds) do play some role. These complications are responsible for the spread in the scaled cross sections shown in Figures 5.12 – 5.16.

We can also compare these scaling results to analytic results found in previous studies (see, e.g., Heggie & Rasio 1996; Spurzem et al. 2009), although the system parameters are not exactly the same. The latter study finds a scaling relation $\langle\sigma\rangle \propto a^{3/2} v_{\rm b}^{-1}$ in the

impulsive regime (where $v_\infty \sim v_\mathrm{b}$ is much greater than the orbital speed of the planet) and $\langle\sigma\rangle \propto a v_\mathrm{b}^{-2}$ for non-impulsive encounters. Our results (see Figures 5.14 and 5.17) are intermediate between these two scaling laws, since the encounters are rarely fully in the impulsive or the non-impulsive regime. In addition, this current study includes binaries, and the binary orbital speed is generally comparable to the planetary orbital speed. The binary motion can either add to or subtract from the relative velocity of the encounter (depending on the timing and geometry of the encounters), so that the scattering interactions have a wide range of relative velocities, even for a given v_b. As a result, our parameter space does not fall fully in any of the limiting regimes considered by previous analytic estimates.

We note that we took into account the flux of the incoming stars after obtaining the scattering cross section. It is more accurate to consider the flux while calculating the cross section. An additional velocity dependence on the cross section due to the flux can slightly reduce the cross section, because higher velocity stars (weaker perturber) are more likely to encounter the planetary system. Figure 5.18 shows the cross section versus the final eccentricity for Neptune when $v_b = 1$ km/s, comparing with the original velocity distribution. The reduction in the cross section is similar for the other planets.

We further note that the expression of gravitational focusing also provides a scaling law for the dependence of the cross sections on v_b. However, the cross section cannot be fit well by this simple expression. The dependence on the incoming velocity is more complicated, and the cross section can be fit better with a power law expression as shown in Figure 5.19.

Table 5.1:: Solar System Architectures

Configuration	Jupiter	Saturn	Uranus	Neptune
Standard	$e = 0$	$e = 0$	$e = 0$	$e = 0$
Compact	$a = 5.20$ AU	$a = 8.67$ AU	$a = 14.4$ AU	$a = 24.1$ AU
Resonant	$a = 5.88$ AU	$a = 7.89$ AU	$a = 10.38$ AU	$a = 12.01$ AU
Eccentric # 1	$e = 0.049$	$e = 0.057$	$e = 0.045$	$e = 0.011$
Eccentric # 2	$e = 0.10$	$e = 0.10$	$e = 0.10$	$e = 0.10$
Massive	$m_P = 1m_J$	$m_P = 1m_J$	$m_P = 1m_J$	$m_P = 1m_J$

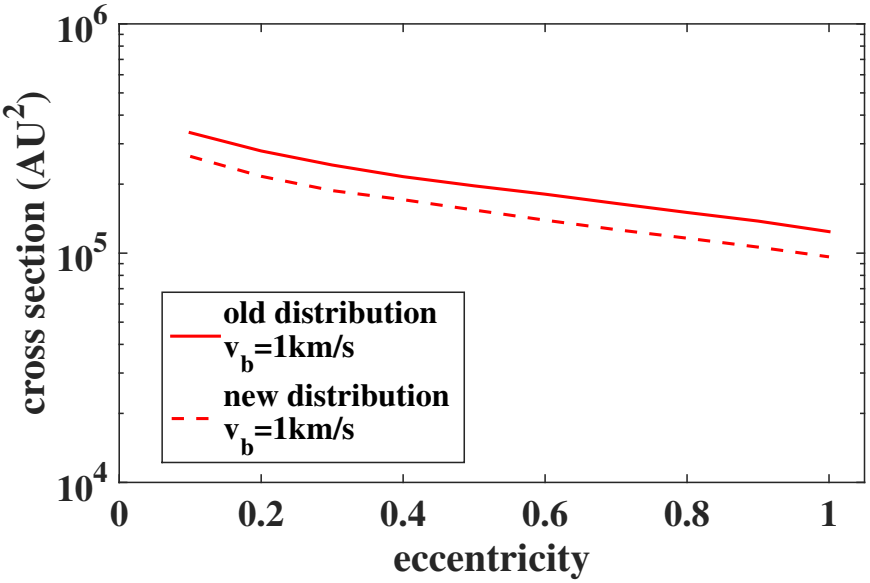

Figure 5.18: The cross section of Neptune when $v_{\rm b} = 1$ km/s, comparing with the distribution taken into account the flux. The cross section taking into account the flux is slightly smaller than the original case.

Table 5.2:: Cross Sections for Ejection and Capture

Configuration	Jupiter	Saturn	Uranus	Neptune
Standard model	15500 ± 1360	34000 ± 2050	72300 ± 3100	113000 ± 3860
	812 ± 306	2140 ± 531	6040 ± 994	11400 ± 1280
Compact model	18100 ± 1510	32700 ± 2130	57500 ± 2790	93900 ± 3570
	915 ± 379	2280 ± 607	4380 ± 817	11500 ± 1320
Resonant model	23900 ± 1810	40200 ± 2440	61100 ± 2990	60100 ± 2900
	1240 ± 467	2150 ± 569	3430 ± 701	3620 ± 738
Massive planets	24100 ± 1890	38300 ± 2390	77700 ± 3360	105000 ± 3880
	1530 ± 579	2170 ± 637	4810 ± 932	8480 ± 1190
$v_{\rm b} = 2$ km/s	9170 ± 947	14800 ± 1250	29800 ± 1770	45200 ± 2240
	391 ± 136	635 ± 173	2600 ± 487	6370 ± 903
$v_{\rm b} = 4$ km/s	2980 ± 454	6090 ± 776	10600 ± 918	15700 ± 1140
	270 ± 173	607 ± 230	1580 ± 486	2430 ± 569
$v_{\rm b} = 8$ km/s	1220 ± 258	2580 ± 403	4060 ± 506	5830 ± 698
	130 ± 85	134 ± 75	239 ± 88	624 ± 228
$v_{\rm b} = 16$ km/s	181 ± 39	607 ± 113	1220 ± 182	2140 ± 252
	82 ± 52	53 ± 39	214 ± 83	169 ± 69
$M_* = 0.25 M_\odot$	37400 ± 2195	74800 ± 3170	138000 ± 4350	196000 ± 5130
	766 ± 330	3510 ± 742	10300 ± 1240	19500 ± 1720
$M_* = 0.5 M_\odot$	27600 ± 1830	54000 ± 2630	107000 ± 3740	152000 ± 4460
	1730 ± 560	3310 ± 755	7470 ± 1060	15100 ± 1490
$M_* = 2.0 M_\odot$	11000 ± 1170	21700 ± 1720	45700 ± 2420	69300 ± 2980
	458 ± 234	1590 ± 467	4420 ± 844	7410 ± 1110
Single, $v_{\rm b} = 1$ km/s	3840 ± 651	7100 ± 856	17300 ± 1430	30600 ± 1980
	135 ± 80	587 ± 210	2080 ± 480	5090 ± 871
Single, $v_{\rm b} = 2$ km/s	1620 ± 324	3110 ± 429	9030 ± 926	13200 ± 1090
	168 ± 86	236 ± 106	1370 ± 423	2810 ± 641
Single, $v_{\rm b} = 4$ km/s	685 ± 177	1300 ± 244	3740 ± 531	6790 ± 793
	116 ± 94	117 ± 51	360 ± 117	1480 ± 411
Single, $v_{\rm b} = 8$ km/s	269 ± 103	1090 ± 322	1440 ± 286	1880 ± 266
	21 ± 14	23 ± 14	157 ± 53	374 ± 202

5.5 The Solar Birth Aggregate

Given that most stars are born within clusters, it is likely that the birth environment of our own Solar System was a cluster of some type. The argument for a substantial birth cluster is bolstered by evidence for short-lived radionuclides in meteorites, which suggests that the early solar nebula was enriched by a nearby supernova (Cameron & Truran 1977; see the review of Dauphas & Chaussidon 2011). A number of previous papers have considered how dynamical scattering encounters in this putative birth cluster can provide constraints on the cluster properties (see the discussion of Section 5.1). Unfortunately, however, no consensus has been reached. This section briefly revisits the issue in light of the updated cross sections determined above.

The basic problem posed by the solar birth aggregate involves a number of ingredients: [I] Direct supernova enrichment of the early solar nebula requires a nearby massive star, which is more likely to form in a larger stellar system. Further, significant nuclear enrichment requires close proximity (distances $d = 0.1 - 0.3$ pc), which implies that the supernova progenitor lives within the same cluster. Acting in the opposite direction, larger clusters can potentially disrupt planetary systems through the action of both [II] dynamical scattering (with the cross sections determined here) and through [III] intense radiation fields which can evaporate gaseous disks. In order for the solar system to reach its present-day state, however, the orbits of the giant planets cannot be greatly perturbed and the early solar nebula could not be too severely evaporated. On the other hand, [IV] the classical Kuiper belt has an apparent edge at ~ 50 AU, and [V] the dwarf planet Sedna has an unusual orbit; both of these solar system properties could be explained by *requiring* a close encounter with another member of the cluster. The

challenge is to find a birth scenario for the solar system that successfully negotiates the compromises required to simultaneously explain all five of these constraints. Supernova enrichment, the edge of the Kuiper belt, and the orbit of Sedna all argue in favor a large and long-lived cluster; disruption via both scattering and radiation argue in the opposite direction.

Existing work has considered a variety of approaches to this issue. Several authors advocate solar birth clusters with stellar membership size in the range $N = 10^3 - 10^4$ (e.g., Adams & Laughlin 2001; Portegies Zwart 2009; Adams 2010; Pfalzner 2013). These studies find that cluster systems in this decade of N lead to moderate dynamical disruption of their constituent planetary systems. Additional work focuses on even larger, longer-lived clusters and find that they can instigate substantial changes to planteary orbits, including frequent ejections (Malmberg et al. 2007, 2011; Spurzem et al. 2009; Parker & Quanz 2012; Hao et al. 2013). On the other hand, competing work suggests that the solar birth cluster does not produce significant disruption of planetary orbits (Williams & Gaidos 2007; Dukes & Krumholz 2012; Craig & Krumholz 2013; see also Williams 2010).

The aforementioned papers thus reach different conclusions about the importance of dynamical scattering of planetary systems in clusters. These differences arise because of varying assumptions about cluster properties and varying assumptions about how to enforce the five constraints on solar system properties outlined above. Although a full review of this topic is beyond the scope of this work, we provide a brief overview below (for additional detail, see the reviews of Adams 2010; Dauphas & Chaussidon 2011; Pfalzner 2013).

For a given type of disruption, with cross section $\langle\sigma\rangle$, the interaction rate is given by $\Gamma = n_*\langle\sigma\rangle v$ (from equation [5.1]). The total expected number $N_{\rm dis}$ of disruption events, per solar system, integrated over the lifetime τ of the cluster is then given by

$$N_{\rm dis} = \int_0^\tau \Gamma dt = \int_0^\tau n_*\langle\sigma\rangle v dt\,. \tag{5.12}$$

The number of disruptive interactions thus depends on the speed v at which a given solar system encounters passing binaries, their number density n_*, and the total time τ spent within the cluster.

We first consider the speed v. Recall that the interaction cross section $\langle\sigma\rangle$ varies with the velocity dispersion of the cluster according to the relation $\langle\sigma\rangle \propto \langle\sigma\rangle_0 v_{\rm b}^{-7/5}$. If we identify the speed v with the velocity dispersion $v_{\rm b}$ of the cluster, then the product $\langle\sigma\rangle v \propto v_{\rm b}^{-2/5}$. As a result, most of the velocity dependence of the cross section is compensated by that of the interaction rate, so that the number of disruption events depends only weakly on the velocity dispersion. As an example, consider the Orion Nebula Cluster (ONC), an intermediate-sized young stellar system with velocity dispersion $v_{\rm b} \sim 2$ km/s (Hillenbrand & Hartmann 1998). Provided that it stays intact, the ONC is likely to evolve into an open cluster resembling the Pleiades (Kroupa et al. 2001); over the coming ~ 100 Myr, the velocity dispersion of the cluster will slowly decrease to $v_{\rm b} \sim 1$ km/s. Over this span of time, the quantity $v_{\rm b}^{-2/5}$ that defines the velocity dependence of the interaction rate varies by only about 32%.

For setting the number of disruption events, one important quantity is the time τ over which clusters remain intact as dynamical systems. In the simplest terms, although most stars are formed in clusters, these astronomical entities come in (at least) two distinctly different flavors. Only about 10 percent of the stellar population is born within

clusters that are sufficently robust to become open clusters (Roberts 1957; Battinelli & Capuzzo-Dolcetta 1991), which are relatively long-lived (τ = 100 Myr – 1 Gyr). The remaining 90 percent of the stellar population is born within embedded clusters (e.g., Allen et al. 2007), which have much shorter lifetimes ($\tau \sim 10$ Myr). As shown below, solar systems that are born within long-lived clusters can have an appreciable chance of dynamical disruption; short-lived clusters lead to significant disruption with greatly reduced probability.

Another important quantity is the density of the cluster. For clusters found in the solar neighborhood, the cluster radius $R \propto N^{1/2}$ (Lada & Lada 2003), so that the clusters display nearly constant surface density (Adams et al. 2006). With this relation, clusters with larger stellar membership sizes N have lower mean densities. However, the clusters in the sample are relatively small (with $N < 2500$), and this trend does not continue up to the largest clusters with $N = 10^4 - 10^6$ (Whitmore et al. 2007), or to the subpopulation of systems that become globular clusters. The largest clusters can thus have larger densities.

To assess the effects of scattering encounters, we need to specify the rate Γ at which solar systems encounter passing binaries (and single stars). As shown previously (Adams et al. 2006; Proszkow & Adams 2009), the rate of close encounters in a cluster can be written in the convenient form

$$\Gamma = \Gamma_0 \left(\frac{b}{b_0} \right)^\gamma , \tag{5.13}$$

where b_0 is a fiducial distance (taken here to be $b_0 = 1000$ AU), and where the fiducial rate Γ_0 and index γ depend on the cluster properties. The index γ falls in the range $1 \leq \gamma \leq 2$, where the extreme of the range correspond to perfect gravitational focusing

($\gamma \to 1$) and the full geometrical cross section ($\gamma \to 2$). In these systems, encounters beyond ~ 1000 AU are little affected by gravitational focusing. Since the cross sections calculated in this paper include gravitational focusing, we can write the interaction rate in the form

$$\Gamma = \Gamma_0 \frac{\langle \sigma \rangle}{\pi b_0^2} \,. \tag{5.14}$$

The benchmark interaction rate Γ_0 has a typical value of about 0.1 interactions per target star per Myr. However, given the wide range of possible cluster properties, it can vary over a wide range, from an order of magnitude lower to an order of magnitude larger than this fiducial value (see Figures 6 and 7, and Tables 8 – 13 in Proszkow & Adams 2009). Note that the benchmark rate is, in general, larger than the simple estimate $\Gamma_0 \sim \langle n_* \rangle v_\mathrm{b} \pi b_0^2$, where $\langle n_* \rangle$ is the mean density of the cluster. The stellar density that defines the interaction rate is not the mean over the cluster, but rather the weighted mean over the integrated orbits of the ensemble of cluster members. The cluster members generally do not stay at a given cluster radius, and the cluster density is centrally concentrated, so that solar systems sample the higher stellar densities of the cluster core. This effect is amplified by the starting conditions for clusters, which start with subvirial initial conditions; as a result, the orbits are more radial than isotropic, resulting in more excursions through the dense central core (see Adams et al. 2006; Proszkow & Adams 2009 for further discussion).

Collecting the results outlined above, we can write the number of disruption events (from equation [5.12]) in the form

$$N_\mathrm{dis} \approx \frac{\langle \sigma \rangle_0}{\pi b_0^2} \int_0^\tau \Gamma_0 \left(\frac{v_\mathrm{b}}{1 \,\mathrm{km/s}} \right)^{-2/5} dt \,. \tag{5.15}$$

The cross section for moderate solar system disruption can be taken as $\langle \sigma \rangle_0 \approx 2.5 \times 10^5$

AU^2, which corresponds to events producing eccentricity increases $\Delta e = 0.1$ and/or increases in the spread of inclination angles $\Delta i = 10^\circ$ (e.g., see Figures 5.1 and 5.7). To obtain this value, we use a linear combination of the binary and single-star cross section (see Figure 5.11), and an assumed binary faction of 2/3. Although these changes to the orbital elements are not devastating, they are large enough to distinguish a disrupted solar system from our own. Note that this value can be written $\langle \sigma \rangle_0 \approx (500\,\mathrm{AU})^2$, which is somewhat larger than the previous estimate of $\sim (400\,\mathrm{AU})^2$ (from Adams & Laughlin 2001).[†] The leading factor in equation (5.15) is thus of order 1/10. Since the benchmark interaction rate $\Gamma_0 \sim 0.1$ Myr^{-1}, the cluster lifetime must be relatively long, $\tau \sim 100$ Myr, in order for disruption to take place with high probability. In other words, most solar systems residing in long-lived clusters can experience moderate disruption.

The cross sections for planet ejection are smaller than the values used above by a factor of ~ 3. As a result, only a fraction ($\sim 1/3$) of the solar systems in long-lived clusters are expected to lose planets with Neptune-like orbits (with even smaller fractions for closer planets). Keep in mind, however, that the benchmark interaction rates Γ_0 can vary by a factor of ~ 10 in both directions.

The above considerations resolve some of the differences found in the literature concerning the disruption rates for planetary systems in clusters. In order for disruption to occur with high probability, clusters must live for relatively long times $\tau \gtrsim 100$ Myr. Indeed, the studies that find low disruption rates consider the clusters to have relatively

[†]The difference arises because the present study increases the target area in equation (5.2) from $B = 4$ to $B = 100$, thereby including more distant events. Note that the original work (Adams & Laughlin 2001) correctly introduced the cross sections as lower limits. The present cross sections are also lower limits, although they are much closer to their greatest lower bounds.

short lifetimes $\tau \sim 10$ Myr (e.g., Williams & Gaidos 2007; Dukes & Krumholz 2012).

How long are clusters expected to stay together? As outlined above, the cluster population has at least two branches. Some clusters disperse over relatively short time scales of only ~ 10 Myr. The robust clusters that survive to become open clusters have empirically determined lifetimes τ_{em} that can fit with a function of the form

$$\tau_{em} = 2.3\mathrm{Myr}\left(\frac{M_c}{1M_\odot}\right)^{0.6}, \tag{5.16}$$

where M_c is the cluster mass (Lamers et al. 2005). With this relation, clusters with initial masses larger than $\sim 550M_\odot$ live longer than 100 Myr and can potentially disrupt their constituent solar systems. More specicifally, we can write the dynamical constraint in the form

$$N_{\mathrm{dis}} \approx \frac{\langle\sigma\rangle_0}{\pi b_0^2}\langle\Gamma_0\rangle 2.3(\Upsilon N)^{3/5}\langle(v_{\mathrm{b}}/1\,\mathrm{km/s})^{-2/5}\rangle \lesssim 1\,, \tag{5.17}$$

where Υ ($\approx 1/2\ M_\odot$/star) is the mass-to-number ratio (the conversion factor between cluster mass M_c and cluster membership size N), and where we include the time average of the velocity dispersion of the cluster (raised to the proper power). After some rearrangement and the specification of typical numbers, this constraint can be written in the form

$$N \lesssim 5000\Big[\left(\frac{\langle\sigma\rangle_0}{2.5\times10^5\mathrm{AU}^2}\right)\left(\frac{\langle\Gamma_0\rangle}{0.05\mathrm{Myr}^{-1}}\right) \times\left\langle\left(\frac{v_{\mathrm{b}}}{1\,\mathrm{km/s}}\right)^{-2/5}\right\rangle\Big]^{-5/3} \lesssim 10^4\,. \tag{5.18}$$

Note that the disruption cross section is determined more precisely than either the expected age of the cluster (from equation [5.16]) or the benchmark interaction rate Γ_0. This latter quantity can be determined to high accuracy for a given set of cluster properties and initial conditions, but its value varies appreciably from cluster to cluster

(Proszkow & Adams 2009). Equation (5.18) uses a value near the low end of the range in order to provide an upper limit on N. In light of these uncertainties, a reasonable order-of-magntidue estimate for the dynamical constraint is $N \lesssim 10^4$, as given by the final inequality. This result is roughly consistent with previous estimates (Adams & Laughlin 2001; Portegies Zwart 2009; Adams 2010; Pfalzner 2013). Nonetheless, the full probability distribution for the survival (or disruption) of planetary systems as a function of cluster size N should be constructed.

The constraint given by equation (5.18) assumes that the solar birth cluster is relatively long-lived. If the solar system formed within a cluster that disperses in only ~ 10 Myr, the corresponding dynamical constraint would be considerably weaker. The motivation for considering a long-lived cluster comes from constraints jointly implied by the five solar system properties outlined at the beginning of this section. Direct supernova enrichment [I] favors a long-lived cluster, so that the progenitor star has enough time to live, evolve, and explode. An even stonger argument comes from the need for a scattering event to produce the edge of the classical Kuiper belt [IV] and to produce the orbit of Sedna [V]. If these solar system properties arise from dynamical interactions in the birth cluster, then a long-lived stellar system is strongly indicated. It remains possible for these features of the solar system to be explained in other ways. Nonetheless, any self-consistent set of constraints on the solar birth environment must explain all three of these properties, and must simultaneously account for the corresponding constraints due to dynamical scattering encounters [II] and radiation fields [III] (e.g., see Fatuzzo & Adams 2008; Thompson 2013).

For completeness, we also consider possible constraints on the solar birth cluster for the scenario where the solar system spends much of its early life in the ultra-compact

multi-resonant configuration (see Section 5.3, Figure 5.2). The cross section for removing the solar system from its resonant state is then given by equation (5.3), which is more than nine times larger than that used above. If, in addition, the removal of the solar system from resonance *always* led to significant disruption over longer times, then the maximum size of the solar birth cluster would be ~ 40 times smaller than that of equation (5.18). In practice, however, the solar system, after being removed from resonance, will not always be significantly disrupted (for example by ejecting a planet) before it evolves and spreads out (as advocated by the Nice model; Gomes et al. 2005; Tsiganis et al. 2005). To assess the risk of disruption in this case, one must also know the probability of the non-resonant (but still compact) solar system experiencing disruption on sufficiently short time scales. This calculation involves a large ensemble of long-term (~ 100 Myr) solar system integrations and is beyond the scope of this present work. Nonetheless, direct application of equations (5.3) and (5.18) suggests that the constraint could be tighter than that derived for the solar system in its usual configuration.

Finally, we note that another class of observational constraints on the solar birth environment might become available. Given that the birth cluster is expected to have $N \approx 10^3 - 10^4$ stars with similar chemical composition, it is possible in principle to find other members of our solar birth aggregate. Although billions of years have passed and the cluster has long since dispersed, perhaps ~ 20 of these solar siblings could reside within 100 pc of the Sun (Portegies Zwart 2009). By focusing on the chemical species that show the most variation from cluster to cluster, it is possible to observationally distinguish these siblings from other stars (Ramírez et al. 2014). The discovery of even a few such stars would provide strong constraints on the properties of the solar birth cluster and its location within the Galaxy. On the other hand, the Solar System could

have had a more complicated dynamical history including large radial migration in the Galaxy (Kaib et al. 2011), which could reduce the chances of finding solar siblings.

5.6 Conclusion

5.6.1 Summary of Results

Using results from more than 2 million individual numerical scattering experiments, this paper has found cross sections for the disruption of planetary orbits in solar systems interacting with passing stars and binaries. Our specific results can be summarized as follows:

[1] More compact solar systems have smaller interaction cross sections (Figures 5.1 and 5.2). To leading order, the cross section for a given disruption event (e.g., planet ejection or eccentricity increase) scales linearly with the semimajor axis of the initial orbit, i.e., $\langle\sigma\rangle \propto a$ (see Figure 5.12).

[2] For most solar systems, the cross section for a given planetary orbit to be disrupted during a scattering encounter is almost independent of the other planets. This feature of the interactions allows for the scaling analysis presented in Section 5.4. Of course, after the encounter, solar systems that suffer moderate disruption can subsequently experience orbital instability, and this latter effect does depend (quite sensitively) on the other planets in the system. In addition, for highly self-interacting solar systems, those with sufficiently massive planets and/or close orbits, interactions among the planets themselves can lead to effectively higher cross sections (e.g., see

Figures 5.2 and 5.6).

[3] The dependence of the cross sections $\langle\sigma\rangle$ on the post-encounter eccentricity e has a nearly exponential form (see Figures 5.1 – 5.5). As a result, the cross sections can be written $\langle\sigma\rangle \propto \exp[-be]$, where $b \approx 4/3$ provides a good fit across the range of parameter space considered in this work (Figures 5.13, 5.14, and 5.15).

[4] The cross sections depend sensitively on the velocity dispersion $v_{\rm b}$ of the background environment, where the dependence displays a nearly power-law form. Moreover, the shape of the cross section curves, as a function of eccentricity, are nearly the same across the parameter space considered here (Figures 5.3 and 5.14). The cross sections can thus be written as $\langle\sigma\rangle \propto v_{\rm b}^{-\gamma} \exp[-be]$, where $\gamma = 7/5$ and $b = 4/3$ provide a good fit over range of interest.

[5] The cross sections depend on the mass M_* of the host star, where the dependence has the approximate form $\langle\sigma\rangle \propto M_*^{-1/3}$. The mass dependence is somewhat more complicated, however, as the cross sections are not fully self-similar (see Figures 5.4 and 5.15). For more disruptive encounters (where $e \to 1$ and planets are ejected), the scaling with mass is somewhat steeper and the form $\langle\sigma\rangle \propto M_*^{-1/2}$ provides a better fit (consistent with previous results from Adams et al. 2006).

[6] Most of this work considers planetary orbits with vanishing initial eccentricity e. Nonetheless, for solar systems starting with $e \neq 0$, the interaction cross sections for eccentricity increase are nearly the same (Figure 5.5), provided that one considers post-encounter eccentricities sufficiently larger than the starting values (roughly, by the increment $\delta e \sim 0.1$). This finding stands in contrast to the related problem of single stars interacting with binaries, where the cross sections for binaries with $e = 0$ and $e \neq 0$

are significantly different (Heggie & Rasio 1996).

[7] The above results can be combined to write the cross section for eccentricity increase for solar systems interacting with binaries in the general form

$$\langle \sigma \rangle = 4050 \text{ (AU)}^2 \left(\frac{a}{\text{AU}}\right) \left(\frac{M_*}{M_\odot}\right)^{-1/3} \times \left(\frac{v_\text{b}}{1\text{km/s}}\right)^{-7/5} \exp\left[\frac{4}{3}(1-e)\right] . \tag{5.19}$$

This result holds over the ranges of parameters given by 5 AU $\leq a \leq$ 50 AU, $0.25 M_\odot \leq M_* \leq 2 M_\odot$, 1 km/s $\leq v_\text{b} \leq$ 16 km/s, and $0.1 \leq e \leq 1$. Equation (5.19) is in good agreement with the numerically obtained results: For fixed stellar mass, the RMS relative error for the range of starting semimajor axis, velocity dispersion, and post-encounter eccentricity is less than about 12 percent (see Figures 5.13 and 5.14). Including variations in the stellar mass, the RMS error is less than about 20 percent (Figure 5.15). Over the same regime of parameter space, the cross section itself varies by more than a factor of ~ 1000. Equation (5.19) provides the total ejection cross sections (including capture events) in the limit $e \to 1$; the cross sections for ejection and capture are listed separately in Table 5.1.

[8] The cross sections for increasing the spread of inclination angles Δi are comparable to those for increasing eccentricity (Figure 5.7). The cross sections for Δi also show a nearly self-similar form, and scale with velocity dispersion of the background cluster according to $\langle \sigma \rangle \propto v_\text{b}^{-7/5}$ (Figure 5.16). This scaling exponent is the same as that found for eccentricity increases. The cross sections can be fit with an exponential dependence on the variable $x = \sin \Delta i$. Although inexact, one can identify increases in inclination with increases in eccentricity such that $\Delta x \sim \Delta e$. In general, increases in the spread of inclination angles and orbital eccentricity are well-correlated (Figure 5.8),

although the Δi values for a given Δe display a wide range. We have also determined the cross sections for increasing the inclination angles beyond 39.2°, the benchmark value required for the Kozai effect to operate (equation [5.10]).

[9] In addition to the ejection of planets during the scattering encounters, orbital eccentricites can be increased so that planetary orbits will cross each other. Most solar systems in such states will eject — or perhaps accrete — planets on relatively short time scales. For systems with the architecture of the current solar system, the cross section for this channel of secondary ejection is comparable to that of direction ejection, so that the total cross section for ejection is effectively doubled (Figure 5.9). For the ultra-compact configuration of the solar system (in or near multiple mean motion resonances), the cross section for ejection due to orbit crossing is comparable to that of the standard solar system, but the cross section for direct ejection is smaller.

[10] The cross sections for changing the semimajor axes of the planetary orbits are smaller than those for increasing eccentricity and/or inclination angle (Figure 5.10). Equivalently, the semimajor axes change much less than the other orbital elements during scattering encounters. In rough terms, 10% changes in the semimajor axis — for planets that remain bound — have approximately the same cross sections as planetary ejection.

[11] The cross sections for solar systems interacting with single stars are smaller than those for binary encounters (Figure 5.11). The single-star cross sections are nearly self-similar (Figure 5.17), and scale with the semimajor axis of the planet and cluster velocity dispersion according to $\langle \sigma \rangle \propto a\ v_{\rm b}^{6/5}$. The scaling exponent for velocity is somewhat smaller than that for binaries and the dependence of the cross sections on

the post-encounter eccentricity is steeper. On average, the single-star cross sections are smaller than the binary cross sections by a factor of ~ 3.6 for small velocity dispersions ($v_{\rm b} = 1$ km/s). This factor falls to only ~ 2 for larger values $v_{\rm b} \sim 20$ km/s; for higher speeds we expect the binary components to act as two separate stars during the encounters (except for close binaries). In general, the effective cross section is a linear combination of the single and binary star cross sections,

$$\langle \sigma \rangle = f_b \langle \sigma \rangle_{\rm binary} + (1 - f_b) \langle \sigma \rangle_{\rm single} \, , \tag{5.20}$$

where f_b is the binary fraction.

[12] We have briefly revisited the dynamical constraint that can be placed on the birth aggregate of our solar system due to scattering encounters (Section 5.5). The strength of this constraint depends crucially on whether one assumes that the solar system forms in a robust, long-lived cluster (with $\tau \gtrsim 100$ Myr, like those that become open clusters) or in a short-lived cluster that dissipates within $\tau \sim 10$ Myr. For long-lived clusters, the requirement that the solar system is not disrupted implies an order of magnitude upper limit on the solar birth aggregate of $N \lesssim 10^4$ (see equation [5.18]). In practice, one should construct the probability distribution for solar system survival/disruption as a function of N (using the cross sections determined herein), and combine it with the other constraints on the birth cluster (see Figure 7 in Adams 2010; see also Portegies Zwart 2009 and Pfalzner 2013).

[13] The cross section for removing a solar system from mean motion resonance is much higher than that required to disrupt the planetary orbits. For the ultra-compact multi-resonant configuration advocated by some versions of the Nice model, this cross section (see equation [5.3]) is ~ 9 times larger than the disruption cross section for

the usual solar system architecture. If removal from resonance leads to longer-term instability, then constraints on the solar birth aggregate would be tighter for systems in the multi-resonant configuration.

5.6.2 Discussion

The cross sections reported in this paper are subject to three different types of uncertainties, and the distinctions among these quantities should be kept in mind. [1] First, the Monte Carlo procedure used to determine specific cross sections (as outlined in Section 5.2) results in uncertainties due to incomplete sampling. These uncertainties decrease with increasing size of the ensemble of simulations and are proportional to $\mathcal{N}_E^{-1/2}$. Over most of the parameter space, we run sufficient numbers $\mathcal{N}_E$ of scattering experiments so that the sampling errors are less than $\sim 5\%$ and usually even smaller. These sampling errors are present in all of the cross sections presented in Section 5.3, although they are usually not included on the plots (however, see Figure 5.5). [2] Next, in Section 5.4, we explore scaling laws to collapse the cross sections for varying velocity dispersion $v_{\rm b}$, host mass M_*, and planet semimajor axis a into nearly self-similar forms. The range of the resulting scaled functions is thus characterized by the error bars shown in Figures 5.13, 5.14, 5.15, 5.16, and 5.17. These error bars represent a measure of the degree to which the cross sections depart from self-similarity. The size of these error bars falls in the range 10 – 15%, except for the scaling with the mass of the host star (where the error bars correspond to 20% departures). [3] Finally, the mean of the scaled cross sections are described by fitted functions with simple forms. The differences between these functions and the mean scaled cross sections are of order 5 – 10%, smaller than

the standard deviations of the different sets of cross sections used to construct the mean forms.

In addition to the uncertainties outlined above, the cross sections calculated herein depend on the features of the stellar population that provides the perturbations. As described in Section 5.2, the cross sections sample the distributions of stellar masses, binary periods, binary mass ratios, binary orbital eccentricities, etc. Different choices for these distributions will lead to corresponding variations in the cross sections. Although we use observations to specify the distributions, they are nonetheless subject to both measurement error and possible variations from region to region.

The numerical simulations carried out for this paper determine the immediate changes in the orbital elements of the solar systems due to passing stars. However, additional changes in the orbital elements can occur over longer time scales. As one example, after an encounter, a planetary system often has larger eccentricities, which can lead to orbital instability over longer spans of time. But the timescales for such instabilities can have a wide range. For systems where the eccentricities are increased so much that planetary orbits cross, one expects instability and (usually) planet ejection on a relatively short time. The cross sections for orbit crossing are thus of great interest and are given in Figure 5.9. For systems with smaller eccenticity increases, however, orbital instability can take much longer. For compact multi-resonant solar systems, modest changes in the orbital elements and/or the removal of the system from its resonant state can lead to instabilities over millions of years (Batygin & Brown 2010). For systems with more widely separated orbits, instabilities can take even longer than the current age of the universe (Batygin & Laughlin 2008; Laskar & Gastineau 2009). To study this issue, the post-encounter solar systems must be integrated over long time scales (up to billions

of years) to fully determine the effects of the encounters. This task is left for future work. On another front, the orbits could also damped after the scattering encounters, thereby moving the orbits back towards smaller eccentricities (Levison & Morbidelli 2007; Picogna & Marzari 2014). This effect should also be considered in follow-up studies, especially on time scales of 1 – 100 Myr when solar systems are expected to retain a significant population of planetesimals.

The scattering encounters considered herein can be effective in sculpting giant planet orbits and the Kuiper Belt of our Solar System (e.g., Kenyon & Bromley 2004). On the other hand, the Oort cloud is too large to be produced within a young embedded cluster (e.g., see Brasser et al. 2012 for further discussion). More specifically, the Oort cloud extends out to $\sim 50,000$ AU (Oort 1950; Jewitt 2001), more than 1000 times the size of the solar systems considered in this paper. With this enormous size, the Oort cloud would be decimated by passing stars within the cluster. As a result, the cloud must be produced later, after the solar system leaves its birth cluster, or perhaps during its exit. Any viable scenario for the solar birth environment must simultaneously account for the Oort cloud, the giant planet orbits, Kuiper Belt properties, radioactive enrichment, Sedna's orbit, and survival of the solar nebula gas reservoir; these coupled constraints thus pose an interesting and challenging opimization problem for further study.

Acknowledgments: We would like to thank Konstantin Batygin, Greg Laughlin, Fred Rasio, and Maxwell Tsai both for early motivation and subsequent useful discussions. This collaboration was initiated through the 2014 International Summer Institute for Modeling in Astrophysics (ISIMA), which focused on gravitational dynamics, and was hosted by the Canadian Institute for Theoretical Astrophyics (CITA). The numerical

calculations were performed at the Harvard Smithsonian Center for Astrophysics (CfA), on a cluster supported by the Institute for Theory and Computation (ITC). We are grateful for the hospitality and resources of CfA, CITA, ISIMA, ITC, and Univ. Michigan.

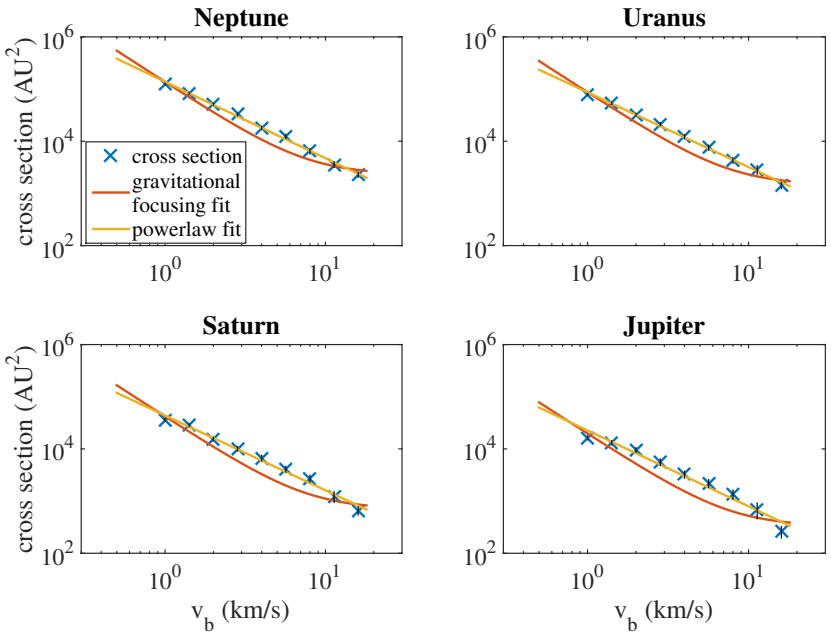

Figure 5.19: The ejection ($e = 1$) cross section of the planets versus v_b. The cross sections cannot be fit well by a simple expression based on gravitational focusing.

Chapter 6

On the Spin-axis Dynamics of a Moonless Earth

This thesis chapter originally appeared in the literature as

Li, G. & Batygin, K. On the Spin-axis Dynamics of a Moonless Earth, *The Astrophysical Journal*, 790, 69, 2014

Abstract

The variation of a planet's obliquity is influenced by the existence of satellites with a high mass ratio. For instance, the Earth's obliquity is stabilized by the Moon, and would undergo chaotic variations in the Moon's absence. In turn, such variations can lead to large-scale changes in the atmospheric circulation, rendering spin-axis dynamics a central issue for understanding climate. The relevant quantity for dynamically-forced climate change is the rate of chaotic diffusion. Accordingly, here we reexamine the spin-axis

evolution of a Moonless Earth within the context of a simplified perturbative framework. We present analytical estimates of the characteristic Lyapunov coefficient as well as the chaotic diffusion rate and demonstrate that even in absence of the Moon, the stochastic change in the Earth's obliquity is sufficiently slow to not preclude long-term habitability. Our calculations are consistent with published numerical experiments and illustrate the putative system's underlying dynamical structure in a simple and intuitive manner.

6.1 Introduction

With the exception of Venus and Mercury, all planets in our solar system have satellites. However, satellites that comprise a high mass ratio are apparently not very common. In the solar system, the Earth-Moon system is the only planet (not counting Pluto-Charon) where $m_M/m_\oplus$ is not negligible. Moreover, no compelling evidence has been found for exomoons around the observed exoplanets (Kipping et al. 2013a,b).

The existence of satellites with high mass ratios may play a significant role in stabilizing the planet's obliquity. For instance, the Earth's obliquity is currently stable. However, if the Moon were removed, the Earth's obliquity would undergo chaotic variations (Laskar et al. 1993; Neron de Surgy & Laskar 1997; Lissauer et al. 2012). Mars's satellites comprise a negligible fraction of Mars' mass, and Martian obliquity is thought to have been chaotic throughout the solar system's lifetime (Ward 1973; Touma & Wisdom 1993; Laskar & Robutel 1993).

The stability of the obliquity is very important for climate variations, as obliquity changes affect the latitudinal distribution of solar radiation. For the case of Mars (an

ocean-free atmosphere-ice-regolith system), the obliquity changes apparently result in drastic variations of atmospheric pressure by runaway sublimation of CO_2 ice (Toon et al. 1980; Fanale et al. 1982; Pollack & Toon 1982; Francois et al. 1990; Nakamura & Tajika 2003; Soto et al. 2012). For Earth-like planets (planets partially covered by oceans) the change of climate depends on the specific land-sea distribution and on the position within the habitable zone around the star. In other words, while it is debatable whether the variation in obliquity truly renders a planet inhabitable, it is clear that the climate can change drastically as the obliquity varies (Williams & Kasting 1997; Chandler & Sohl 2000; Jenkins 2000; Spiegel et al. 2009).

Although spin-axis chaos for a Moon-less Earth is well established, the rate of chaotic diffusion appears to be inhomogeneous in the chaotic layer. To this end, Laskar et al. (1993) used frequency map analysis and noted that Earth obliquity may exhibit large variations (ranging from 0 degree to about 85 degree), if there were no Moon. However, recently Lissauer et al. (2012) used direct integration and showed that the obliquity of a moonless Earth remains within a constrained range between -2 Gyr to 2 Gyr, and concluded that the chaotic variations of the Earth's obliquity and the associated climatic variations are not catastrophic. This finding is in fact consistent with the frequency map analysis of Laskar et al. (1993). Moreover, even prior to the direct numerical integration, Neron de Surgy & Laskar (1997) has already pointed out that rapid chaotic variation have a restricted range. Interestingly, a similar analysis applies to the obliquity evolution of Mars (Laskar et al. 2004). Stated more simply, it is not only important to understand if the obliquity undergoes chaotic variations but also to understand how rapidly such variations occur, to obtain a handle on the climatic changes that govern the habitability of a given planet. Our goal here is to describe a framework

for such an analysis. We adopt a perturbative approach to the problem, and calculate the characteristic Lyapunov timescale and the diffusion coefficient of the obliquity. With the Lyapunov timescale and the diffusion coefficient, one can estimate the range of the obliquity the planet may reach in a given time, and inform the climate change of the planet.

Our paper is structured as follows. In section 2, we delineate the perturbative model and lay out the inherent assumptions. In section 3, we calculate the diffusive properties of the system and compare our analytical estimates to numerical simulations. We conclude and discuss the implications of our results in section 4.

6.2 A Simplified Perturbative Model

As the primary goal of this work is to obtain analytical estimates of the relevant timescales for chaotic diffusion, we begin by considering a simplified description of the system.

Without the Moon, the Earth's obliquity is found to be chaotic in the range $0 - 85^o$, where there are two large chaotic regions: $0^o - 45^o$ & $65^o - 85^o$. There also exists a moderately chaotic bridge that connects the two regions: $45^o - 65^o$ (Laskar et al. 1993; Morbidelli 2002). The dynamical analysis is simpler in the large chaotic regions. Thus, we treat them first.

6.2.1 Large Chaotic Regions: $0^\circ - 45^\circ$ & $65^\circ - 85^\circ$

The Hamiltonian describing the evolution of planetary obliquity is well documented in the literature (e.g. Colombo (1966); Laskar & Robutel (1993); Touma & Wisdom (1993); Neron de Surgy & Laskar (1997)):

$$H(\chi, \psi, t) = \frac{1}{2}\alpha\chi^2 + \sqrt{1-\chi^2} \times (A(t)\sin\psi + B(t)\cos\psi)), \tag{6.1}$$

where ψ is the longitude of the spin-axis, $\chi = \cos\varepsilon$, ε is the obliquity, and α is an approximately constant parameter. Specifically,

$$\alpha = \frac{3G}{2\omega}\Big[\frac{m_\odot}{(a_\odot\sqrt{1-e_\odot^2})^3} + \frac{m_M}{(a_M\sqrt{1-e_M^2})^3}(1 - \frac{3}{2}\sin^2 i_M)\Big]E_d, \tag{6.2}$$

where $m_\odot$ is the mass of the Sun, $a_\odot$ and $e_\odot$ are the semi major axis and the eccentricity of the Earth's orbit, m_M is the mass of the moon, a_M, e_M and i_M are the semi major axis, eccentricity and inclination of the Moon's orbit around the Earth, E_d is the dynamical ellipticity of Earth, and ω is the spin of the Earth. α characterizes the intrinsic precession of the Earth's spin axis, and is obtained by averaging the torques from the Sun and Moon over their respective orbits. For a moonless Earth, $\alpha = 0.0001\text{yr}^{-1}$ (Neron de Surgy & Laskar 1997). In addition,

$$A(t) = 2(\dot{q} + p(q\dot{p} - p\dot{q}))/\sqrt{1-p^2-q^2}, \tag{6.3}$$

$$B(t) = 2(\dot{p} - q(q\dot{p} - p\dot{q}))/\sqrt{1-p^2-q^2}, \tag{6.4}$$

where $p = \sin i/2\ \sin\Omega$ and $q = \sin i/2\ \cos\Omega$, i is the inclination of the Earth with respect to the fixed ecliptic and Ω is the longitude of the node.

The inclination and the longitude of node of the Earth change as the other planets in the solar system perturb the Earth's orbit. The evolution of i and Ω can be obtained

by direct numerical integration or in the low-e,i regime via perturbative methods such as the Lagrange-Laplace secular theory. Specifically, within the context of the latter, a periodic solution represented by a superposition of linear modes can be obtained.

$$i \cos \Omega = \sum i_k \cos (s_k t + \gamma_k), \tag{6.5}$$

$$i \sin \Omega = \sum i_k \sin (s_k t + \gamma_k). \tag{6.6}$$

The amplitudes and the frequencies of the modes have been computed in classic works (Le Verrier 1855; Brouwer & van Woerkom 1950). We use the latest update of these values from Laskar (1990).

In adopting equations (6.5) and (6.6) as a description of the Earths inclination dynamics, we force the disturbing function in Hamiltonian (1) to be strictly periodic. In fact, it is well known that the orbital evolution of the terrestrial planets is chaotic with a characteristic Lyapunov time of $\sim$ 5Myr (Laskar 1989; Sussman & Wisdom 1992). Consequently, our model does not account for the stochastic forcing of the obliquity by the diffusion of the Earths inclination vector (see Laskar et al. 1993). Such a simplification is only appropriate for systems where the intrinsic Chirikov diffusion is faster than that associated with the disturbing function. As will be shown below, the assumption holds for the system at hand.

As already mentioned above, in absence of the Moon, rapid chaos spans two well-separated regions, which are joined by a weakly chaotic bridge (Laskar et al. 1993). In each of the highly chaotic regions, irregularity arises from overlap of a distinct pair of secular resonances (see Chirikov (1979)). As shown in Figure (6.1), the overlap of s_1

and s_2 causes the chaotic region in $\varepsilon \sim 65^o - 85^o$ ("C2") and the overlap of s_3 and s_4 causes the chaotic region in $\varepsilon \sim 0^o - 45^o$ ("C1"). Including only the terms associated with these four frequencies in Hamiltonian (7.2), the chaotic region of $\varepsilon \sim 0^o - 85^o$ can be well reproduced (Morbidelli 2002). Accordingly in the following analysis, we retain only the four essential modes to analyze the two chaotic regions and the "bridge" that connects them sequentially.

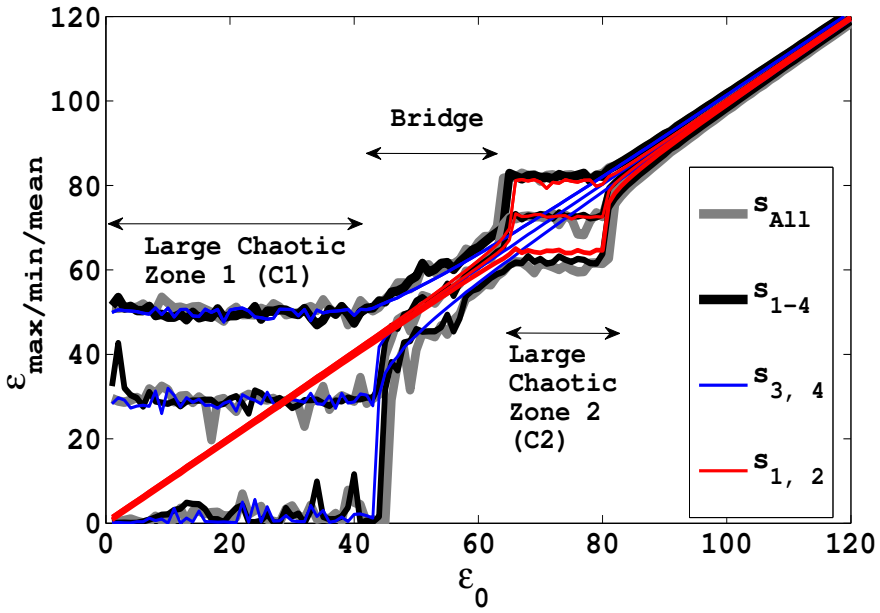

Figure 6.1: The minimum/mean/maximum of the obliquity reached in 18Myr as a function of the initial obliquity. The grey lines represent the results including all the frequencies, the black lines represent the results including s_1, s_2, s_3 and s_4, the red lines represent the results including s_1 and s_2, and the blue lines represent the results including s_3 and s_4. The four frequencies reproduces the results including all the frequencies. Between $\varepsilon_0 \sim 65^o - 85^o$ and $\sim 0^o - 45^o$, the chaotic behavior of obliquity is caused by s_1 and s_2, and s_3 and s_4 separately. Between $45^o - 65^o$, the evolution of the obliquity is also not regular, and is caused by a nonlinear coupling among the resonant doublets ($s_{1,2}$ and $s_{3,4}$).

Substituting the expansion for $i\cos\Omega$ and $i\sin\Omega$ and keeping only the four

frequencies (s_{1-4}), we can rewrite the Hamiltonian as

$$H_{C1,2}(\chi,\psi,t) = \frac{\alpha}{2}\chi^2 + \epsilon\sqrt{1-\chi^2} \times \sum_{k=1}^{4} a_k \cos(s_k t + \delta_k + \psi), \tag{6.7}$$

where $\epsilon = 10^{-7}$, $\alpha = 0.0001\text{yr}^{-1}$. The other parameters are included in table (6.1). An identical derivation is followed in Laskar (1996).

Within "C1" and "C2", the chaotic variations are not sufficiently large to induce overwhelming variations in $\sqrt{1-\chi^2}$. To leading order, it can be assumed to be constant, and we evaluate it at the center of the chaotic regions (specifically $\chi_{0,1} = 20^\circ$ for "C1" and $\chi_{0,2} = 70^\circ$ for "C2"). In doing so, we deform the topology of the domain inherent to Hamiltonian (7) from a sphere to a cylinder. While not appropriate in general, such an operation is justified for the system at hand because both "C1" and "C2" individually occupy a limited obliquity range (see Appendix for additional discussion). Then, the Hamiltonian obtains a simple pendulum like structure, characterized by four forced resonances. Keeping one resonance at a time, we can plot the separatrixes associated with each harmonic (Figure (6.2)). As noted before, the two large chaotic zones can be understood to be the interaction of the resonant doublets s_1 & s_2, and s_3 & s_4 separately. The region in the bridge is dominated by the secondary resonances

Table 6.1:: Parameters for the simplified Hamiltonian (6.7).

	a (yr^{-1})	s ($\times 10^{-5}\text{yr}^{-1}$)	δ
k = 1	2.47638	-2.72353	-2.56678
k = 2	2.93982	-3.43236	-1.70626
k = 3	15.5794	-9.1393	1.1179
k = 4	5.46755	-8.6046	2.4804

which will be described in the next section. We also note that by setting $\sqrt{1-\chi^2}$ to a constant, the "C1" region extends to $\chi = \cos\varepsilon > 1$. Because here we only focus on the qualitative dynamical behavior, the extension to the unphysical regions can be neglected. Furthermore, we notice that there is a gap between the second order resonances and the "C2" region. This gap is likely also an artifact that arises from setting $\sqrt{1-\chi^2} = const.$, as this assumption leads to a deformation of the resonant structure. Since the dynamical behavior in the bridge is well characterized by a second-order truncation of the averaged Hamiltonian, we do not extend our analysis to the higher orders.

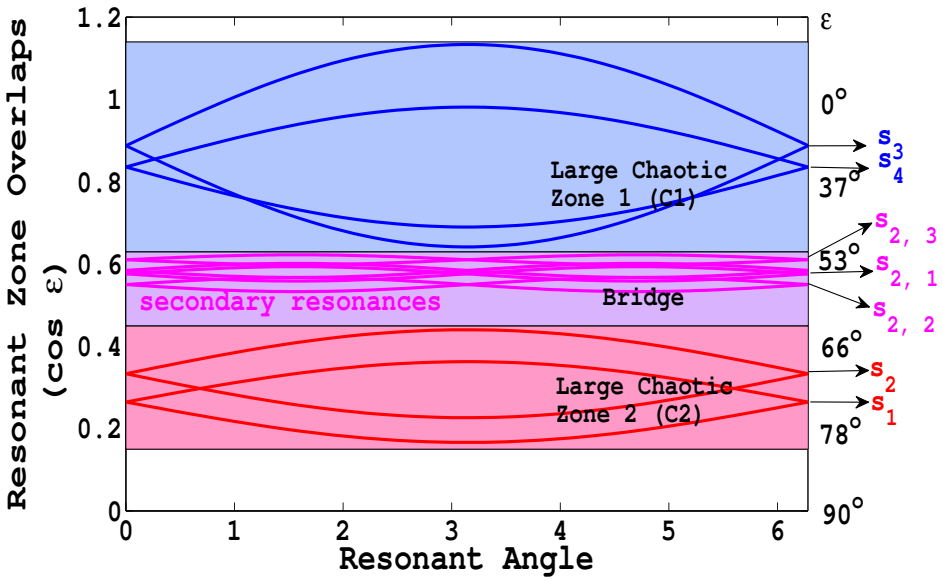

Figure 6.2: The overlap of primary and secondary resonances. The red lines represent the resonances of s_1 and s_2, while the blue lines represent the resonances of s_3 and s_4. The purple lines represent the second order resonances in the bridge.

Keeping $s_{3,4}$ or $s_{1,2}$ only, we can adequately reproduce the large chaotic regions "C1" and "C2". Thus, we obtain simplified Hamiltonians for "C1" and "C2" separately.

$$\begin{aligned} H_{C1}(\chi,\psi,t) &= \frac{\alpha}{2}\chi^2 + \epsilon\sqrt{1-\chi_{0,1}^2} \\ &\times \ (a_3\cos(s_3t+\delta_3+\psi) + a_4\cos(s_4t+\delta_4+\psi)), \end{aligned} \tag{6.8}$$

$$\begin{aligned} H_{C2}(\chi,\psi,t) &= \frac{\alpha}{2}\chi^2 + \epsilon\sqrt{1-\chi_{0,2}^2} \\ &\times \ (a_1\cos(s_1t+\delta_1+\psi) + a_2\cos(s_2t+\delta_2+\psi)), \end{aligned} \tag{6.9}$$

where the parameters can be found in table (6.1).

6.2.2 Bridge Region: $45^\circ - 65^\circ$

In case of the Earth, if the obliquity were to be confined to either large chaotic domain, the climatic variability could in principle be relatively small. However, the analysis of Laskar et al. (1993) shows that transport between the two regions is possible. To understand the migration between the two chaotic zones, one needs to understand the dynamics in the bridge zone between $45^o - 65^o$. As the bridge zone is a region between the two doublet resonant domains, it is likely that the diffusion is driven by secondary, rather than primary resonances. In this section, we present the simplified Hamiltonian governing the dynamical behavior in the bridge.

In order to obtain an analytical description of the resonant harmonics in the bridge, we must generate them by averaging over the primary harmonics. In particular, here we do so by utilizing the Poincare-Von Ziepel perturbation method (Goldstein 1950; Lichtenberg & Lieberman 1983). Consider a canonical transformation that arises from

a type-2 generation function $G(\Phi, \psi, t)$, $\Phi = \chi - \epsilon\frac{\partial G}{\partial \psi}$, $\phi = \psi + \epsilon\frac{\partial G}{\partial \Phi}$. Upon direct substitution, we obtain:

$$H_B(\Phi, \phi, t) = \frac{\alpha}{2}\Phi^2 + \epsilon^2\Big[\frac{\alpha}{2}\Big(\frac{\partial G}{\partial \psi}\Big)^2 + \sum_{i=1}^{4}\sin(s_i t + \phi)\frac{\partial G}{\partial \Phi}\Big] + O(\epsilon^3), \tag{6.10}$$

where

$$\begin{aligned} G(\Phi, \psi, t) &= \frac{\sqrt{1-\Phi^2}}{\prod_{k=1}^{4}(\alpha\Phi + s_k)}\Big(\\ &- \sum_{i=1}^{4}\alpha^3\Phi^3\sin(\psi + s_i t + \delta_i)a_i - \sum_{j\neq i}\alpha^2\Phi^2\sin(\psi + s_i t + \delta_i)a_i s_j \\ &- \sum_{j,l\neq i}\alpha\Phi\sin(\psi + s_i t + \delta_i)a_i s_j s_l - \sum_{j,l,m\neq i}\sin(\psi + s_i t + \delta_i)a_i s_j s_l s_m\Big). \end{aligned} \tag{6.11}$$

As before, we set Φ to a constant (at $\Phi = \cos(50^o)$) in the second term and rewrite the Hamiltonian as:

$$H_B(\Phi, \phi, t) = \frac{\alpha}{2}\Phi^2 + \epsilon^2\Big(\sum_{k} b_k\cos\left(s_{2,k}t + \delta_{2,k} + 2\phi\right)\Big), \tag{6.12}$$

where $s_{2,k}$ is the sum of any two of the first order resonance frequencies s_{1-4}. Note that because the bridge region is even more tightly confined in obliquity than either "C1" or "C2", it is sensible to ignore the variations in Φ in the second term.

Considering each resonant term in isolation, the Hamiltonian resembles that of a simple pendulum. Plotting the separatrix of the Hamiltonian for each term, we find that there are four second order resonances in the bridge region (as shown in Figure (6.2)). Two of the resonances reside in extreme proximity to each-other and only give rise to modulational diffusion that is much slower than that arising from marginally overlapped harmonics (Lichtenberg & Lieberman 1983). Consequently, we can approximate the

Hamiltonian in the bridge by three overlapping resonances. Thus, the simplified Hamiltonian for the bridge is:

$$H_B(\Phi, \phi, t) = \frac{\alpha}{2}\Phi^2 + \epsilon^2 \sum_{k=1}^{3} b_k \cos\left(s_{2,k}t + \delta_{2,k} + 2\phi\right), \tag{6.13}$$

where the parameters can be found the table (6.2).

Table 6.2:: Parameters for the simplified Hamiltonian (6.13).

	b (yr^{-1})	s (yr^{-1})	δ
k=1	789482.	$s_1 + s_3 = -0.000118628$	-1.69271
k=2	755727.	$s_1 + s_4 = -0.000113281$	-3.05521
k=3	364558.	$s_2 + s_3 = -0.000125717$	-2.55324

6.3 Results

6.3.1 Analytical Estimates

With simplified expressions for the Hamiltonians in each charscteristic region delineated, we can estimate quantities relevant to the extent of the motion's irregularity (specifically, the Lyapunov exponent and the action-diffusion coefficient) following Chirikov (1979), with the method discussed in the Appendix.

Briefly, for a simple asymmetrically modulated pendulum:

$$H_D(p, q, t) = \frac{\beta}{2}p^2 + c(\cos q + \cos(q + \omega_B t)), \tag{6.14}$$

where there are two resonant regions separated by ω_B/β in action. The libration frequency associated with the stable equilibria of either resonance is $\omega_L = \sqrt{c\beta}$, which is

identical (in magnitude) to the unstable eigenvalue of the separatrix. Moreover, the half width of the resonance, Δ, can be calculated as $\Delta = 2\sqrt{c/\beta}$.

When the resonances are closely overlapped (e.g. in region "C1", "C2"), the Lyapunov exponent (λ) is roughly the breathing frequency: $\nu_B = \omega_B/(2\pi)$. Meanwhile, in the marginally overlapped case ("bridge"), it amounts to roughly $2\nu_L = 2\omega_L/(2\pi)$. In other words,

$$\lambda \sim \frac{1}{K}\frac{\omega_L}{2\pi} \sim \begin{cases} \nu_B & (\omega_B/\beta < \Delta) \\ 2\nu_L & (\omega_B/\beta \sim 2\Delta), \end{cases} \tag{6.15}$$

where $K = \frac{\Delta}{\omega_B/\beta} = 2\frac{\omega_L}{\omega_B}$ is a stochasticity parameter, which characterizes the extent of resonance overlap. Note that when $\omega_B < \Delta$, $\frac{1}{K}\frac{\omega_L}{2\pi} = \nu_B/2$. We adopt $\lambda \sim \nu_B$ based on the results from the Appendix in the following calculation. The empirical factor of 2 does not affect our results on the qualitative behavior of the system.

Accordingly, the quasi-linear diffusion coefficient (D) can be estimated as $\Delta^2\nu_B$ when the resonances are closely overlapped, and as $\Delta^2\nu_L$ when the resonances are farther apart (Murray et al. 1985), although better estimates can be obtained in adiabatic systems (Cary et al. 1986; Bruhwiler & Cary 1989; Henrard & Morbidelli 1993):

$$D \sim \Delta^2\lambda \sim \begin{cases} \Delta^2\nu_B & (\omega_B/\beta < \Delta) \\ \Delta^2\nu_L & (\omega_B/\beta \sim 2\Delta). \end{cases} \tag{6.16}$$

Taking the simplified Hamiltonian (6.8) and following Murray & Holman (1997), we approximate the two resonances as having the same widths (which quantitatively amount to the average width). Upon making this approximation, we get:

$$\tilde{H}_{C1}(\chi, \psi, t) = \frac{\alpha}{2}\chi^2 + \epsilon\tilde{a}_2(\cos(s_3 t + \delta_3 + \psi) + \cos(s_4 t + \delta_4 + \psi)). \tag{6.17}$$

As noted earlier, $\epsilon = 10^{-7}$, $\alpha = 0.0001\text{yr}^{-1}$, $s_4 - s_3 = 5 \times 10^{-6}\text{yr}^{-1}$, $\tilde{a}_1 = 3.6\text{yr}^{-1}$.

Because the two resonances are closely overlapped (as shown in Figure (6.2)), the Lyapunov exponent can be estimated as the breathing frequency: $\nu_B = (s_4 - s_3)/2/\pi \sim 10^{-6}\text{yr}^{-1}$. Accordingly, the diffusion coefficient (D) is $\Delta^2\nu_B \sim 10^{-8}\text{yr}^{-1}$, where $\Delta = 2\sqrt{\epsilon\tilde{a}/\alpha}$ is the half width of the resonant region. With the diffusion coefficient, we can estimate the time needed to cross the two chaotic zones and the bridge: $t \sim \delta\chi^2/D$. Specifically, taking $\delta\chi = \cos 0^o - \cos 45^o$, $t_{C1} \sim 7.5$ Myr.

Next, we consider zone "C2" (equation (6.9)). After approximating the two resonances as having the same width, we rewrite the Hamiltonian as

$$\tilde{H}_{C2}(\chi, \psi, t) = \frac{\alpha}{2}\chi^2 + \epsilon\tilde{a}_2(\cos(s_1 t + \delta_1 + \psi) + \cos(s_2 t + \delta_2 + \psi)), \tag{6.18}$$

where $\alpha = 0.0001\text{yr}^{-1}$, $\epsilon = 10^{-7}$, $\tilde{a}_2 = 2.5\text{yr}^{-1}$, $s_1 - s_2 = 7 \times 10^{-6}\text{yr}^{-1}$.

Similarly to zone "C1", the Lyapunov exponent can be estimated as $\nu_B \sim 10^{-6}\text{yr}^{-1}$, because the two resonance are closely overlapped. The diffusion coefficient thus evaluates to $D = \Delta^2\nu_B \sim 10^{-8}\text{yr}^{-1}$. Finally, the time to cross "C2" can be estimated as $t_{C2} \sim \delta\chi^2/D \sim 10$ Myr.

Finally, for the bridge zone, we can approximate the simplified Hamiltonian in equation (6.13) as a resonance triplet with the same width:

$$\begin{aligned} \tilde{H}_B(\Phi, \phi, t) &= \frac{\alpha}{2}\Phi^2 \\ &+ \epsilon^2\tilde{a}_3(\cos(s_{2,1}t + \delta_{2,1} + 2\phi) + \cos(s_{2,2}t + \delta_{2,2} + 2\phi) + \cos(s_{2,3}t + \delta_{2,3} + 2\phi)), \end{aligned} \tag{6.19}$$

where $\alpha = 0.0001\text{yr}^{-1}$, $\epsilon = 10^{-7}$, $\tilde{a}_3 = 664633\text{yr}^{-1}$, $\delta_s = 6.21769 \times 10^{-6}$.

Because the resonances are not closely overlapped as shown in Figure (6.2), the Lyapunov exponent can be estimated as $2\omega_L/(2\pi)$, where the libration frequency is

$\omega_L = \sqrt{2\alpha(\epsilon^2\tilde{a})}$ (the angle is 2ϕ instead of ϕ). Thus, the Lyapunov exponent is roughly $\sim 3.7\times10^{-7}\mathrm{yr}^{-1}$. Then the diffusion coefficient can be estimated as $\Delta^2\nu_L \sim 5\times10^{-11}\mathrm{yr}^{-1}$, and $t_{bridge} \sim 2$ Gyr.

The stark differences in the estimates of the crossing times obtained above place the results of Lissauer et al. (2012) into a broader context. That is, our calculations explicate the fact that the long-term confinement of the obliquity to either the "C1" or the "C2" regions observed in direct numerical simulations arises from the distinction in the underlying resonances that drive chaotic evolution. Because the diffusion in the bridge is facilitated by secondary resonances, it is considerably slower, allowing the stochastic variation in obliquity to remain limited.

6.3.2 Numerical Results

To validate the analytical results, we numerically estimate the Lyapunov exponent. We follow the method discussed in Ch. 5 of Morbidelli (2002). Specifically, we linearize the Hamiltonian and evolve the difference ($\delta_{traj}(t)$) of two initially nearby trajectories in phase space. The initial separation is set to 10^{-6}. The Lyapunov exponent is calculated as:

$$\lambda = \lim_{t\to\infty} \frac{1}{t} \ln \frac{\delta_{traj}(t)}{\delta_{traj}(0)}. \tag{6.20}$$

We start our runs with different initial obliquity to probe the different chaotic/regular regions. We check the convergence of our results using two different running times ($t = 500$ Myr and $t = 1$ Gyr). In the regular regions, the Lyapunov exponent approaches zero, and is limited only by the integration time. As shown in Figure (6.3), the Lyapunov

exponents in the two large chaotic zones are $\lambda_{C1} \sim \lambda_{C2} \sim 10^{-6}\text{yr}^{-1}$ and the Lyapunov exponents in the bridge zone is $\lambda_{bridge} \sim 5 \times 10^{-7}\text{yr}^{-1}$.

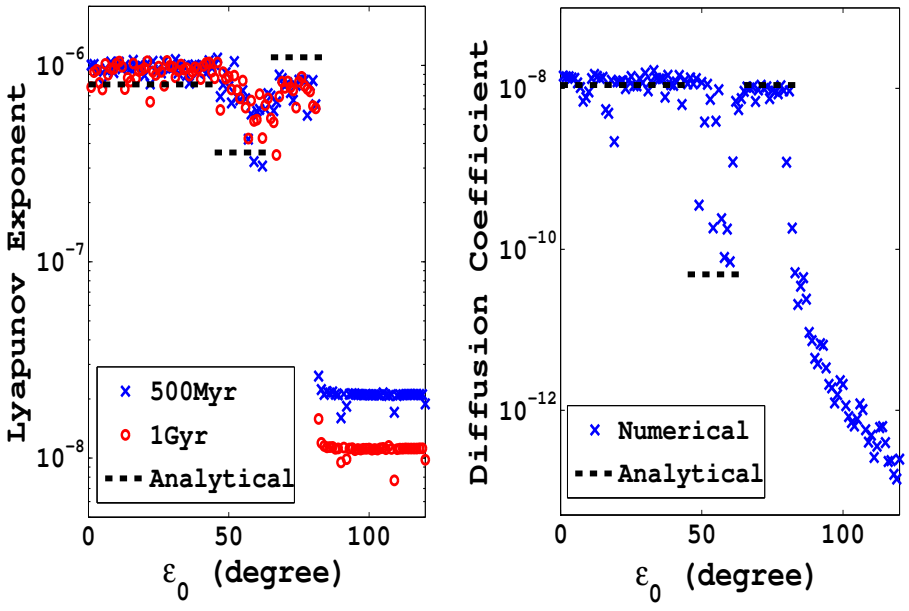

Figure 6.3: The numerical result of the Lyapunov exponent and the diffusion coefficient with different initial obliquity. Left panel: the Lyapunov exponent. The red circles represent the Lyapunov exponent calculated for $t = 500$ Myr, and the blue crosses represent that calculated for $t = 1$ Gyr. The Lyapunov exponent converges in the chaotic region for the different running times and in the regular region the Lyapunov exponent approaches zero as the running time increases. Right panel: the diffusion coefficient estimated by taking averages over bins of 0.5 Myr before taking the difference in χ. The diffusion coefficient in the bridge is much smaller than that in the chaotic zones. The dashed lines in the two panels are the results using the analytical method.

Then, we follow the numerical method discussed in Chirikov (1979) to calculate the diffusion coefficient. Specifically, to eliminate the oscillations caused by the libration of the resonances, we average χ in bins with the same bin size δt. Then, we take the difference ($\delta\chi$) between neighboring bins. The diffusion coefficient is estimated by averaging $\delta\chi^2/\delta t$. The bin size δt needs to be bigger than the libration period of the

resonances but smaller than the saturation timescale in the chaotic zone and the bridge. Here, we set $\delta t = 0.5$ Myr, and run the simulation for 500 Myr. The results are plotted in the right panel of Figure (6.3). Unsurprisingly, the diffusion coefficient is much smaller in the bridge than that in the chaotic zones.

We compare the analytical results with the numerical estimation. In Figure (6.3), the analytical results are represented by black dashed lines. Roughly, the analytical results are consistent with the numerical results. To further elucidate the qualitative agreement, we integrated the full Hamiltonian (equation (7.2)) and the resulting evolutionary sequences are shown in Figure (6.4).

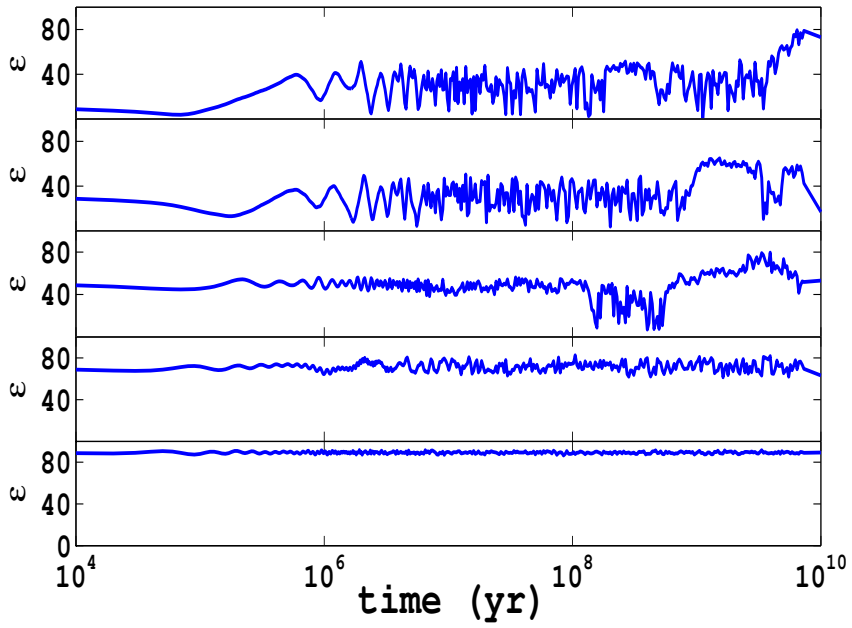

Figure 6.4: The evolution of the obliquity as a function of time by integrating the full secular Hamiltonian numerically (equation (7.2)). The different panels represent different initial obliquities: from top to bottom: $\varepsilon_0 = 10^o$, $\varepsilon_0 = 30^o$, $\varepsilon_0 = 50^o$, $\varepsilon_0 = 70^o$. $\varepsilon_0 = 90^o$. $\psi_0 = 0$ for all the panels.

Note that the time to cross "C1" and "C2" are about ∼few Myr, and the time to

cross the bridge is much longer: $\gtrsim$ Gyr. This is fully consistent with our analytical arguments. Furthermore, as already mentioned above our results are consistent with Lissauer et al. (2012), who noticed that the Earth's obliquity is constrained in "C1" within -2 Gyr to 2 Gyr. Although the diffusion time we calculated for the bridge is ~ 2 Gyr, the diffusion time only roughly characterizes the timescale it takes to cross the bridge, and the exact crossing time depends on the specific initial condition. Thus, as 2 Gyr is on the similar timescale of the integration time used in Lissauer et al. (2012), it is probable that the obliquity would reach "C2" if the integration time in their simulations were to be increased.

6.4 Conclusion

Without the Moon, Earth's obliquity is chaotic, however, the rate at which the system explores the irregular phase space is not evident a-priori (Laskar et al. 1993; Lissauer et al. 2012). In other words, the characteristic range over which the obliquity varies in a given time-frame depends sensitively on the exact architecture of the underlying resonances that drive chaotic motion. Here, we utilized canonical perturbation theory to estimate the Lyapunov exponent and the diffusion coefficient which characterize the chaotic rate of the change of the obliquity. Our calculations were performed within the context of a perturbative approach which yields a simple model, which in turn illuminates the underlying structure of the dynamics in a direct and intuitive way.

In order to obtain a qualitatively tractable description of the system, we simplified the Hamiltonian to a restricted sum of single pendulums, and followed Chirikov (1979) to estimate the characteristic timescales. Subsequently, we validated the analytical

results by calculating the Lyapunov exponent and diffusion coefficient numerically and by integrating the full Hamiltonian in the secular approximation. We found broad agreement between the analytical and numerical results. Particularly, there are three distinct regions where the obliquity exhibits chaotic variations. Rapid chaos is observed between $0 - 45^o$ and $65 - 85^o$, while a mildly chaotic bridge connects the two regions. Our estimates suggest that the time to cross the "bridge" is ~ 2 Gyr, much longer than the time to cross the two large chaotic zones. This is consistent with the findings of Lissauer et al. (2012).

With the envelope of the exoplanetary detection edging ever closer to the discovery of numerous Earth-like planets*, the spin-axis dynamics of a Moonless Earth presents itself as an important paradigm for the assessment of the potential climate variations on such objects. Indeed, it is tempting to apply a framework such as that outlined in this work to an array of multi-transiting planetary systems, for which the masses and orbital parameters are well established. Unfortunately, results stemming from such an exercise would be under-informed by a lack of observational constraints on the physical properties of the individual planets such as spin rates and dynamical ellipticities. Consequently, endeavors of this sort must await substantial breakthroughs in observational characterization. Nevertheless, the implications of the present study for the emerging extrasolar planetary aggregate are clear: an absence of a high-mass ratio Moon should not be viewed as suggestive of extreme climate variations. That is, even for a Moonless Earth-like planet, residing in a stochastic spin-axis state, the characteristic chaotic diffusion rate may sufficiently slow to not limit long-term habitability.

*To date, the recently completed Kepler mission has detected four super-Earths (namely Keper-22b,62e,62f,69c) in the habitable zone (Borucki et al. 2012, 2013; Barclay et al. 2013).

6.5 Acknowledgments

We thank Jacques Laskar for helpful comments.

References

Albrecht, S. et al. 2012, ApJ, 757, 18, 1206.6105

Bade, N., Komossa, S., & Dahlem, M. 1996, A&A, 309, L35

Batygin, K. 2012, Nature, 491, 418

Bear, E., Kashi, A., & Soker, N. 2011, MNRAS, 416, 1965, 1104.4106

Blaes, O., Lee, M. H., & Socrates, A. 2002, ApJ, 578, 775, astro-ph/0203370

Bode, N., & Wegg, C. 2013, ArXiv e-prints, 1310.5745

Boley, A. C., Payne, M. J., & Ford, E. B. 2012, ApJ, 754, 57, 1204.5187

Cenko, S. B. et al. 2012, ApJ, 753, 77, 1107.5307

Chatterjee, S., Ford, E. B., & Rasio, F. A. 2011, in IAU Symposium, Vol. 276, IAU Symposium, ed. A. Sozzetti, M. G. Lattanzi, & A. P. Boss, 225–229, 1012.0584

Chen, X., Madau, P., Sesana, A., & Liu, F. K. 2009, ApJ, 697, L149, 0904.4481

Chen, X., Sesana, A., Madau, P., & Liu, F. K. 2011, ApJ, 729, 13, 1012.4466

Colpi, M., & Dotti, M. 2011, Advanced Science Letters, 4, 181

Correia, A. C. M., Laskar, J., Farago, F., & Boué, G. 2011, Celestial Mechanics and Dynamical Astronomy, 111, 105, 1107.0736

Eggleton, P. P., Kiseleva, L. G., & Hut, P. 1998, ApJ, 499, 853, astro-ph/9801246

Eggleton, P. P., & Kiseleva-Eggleton, L. 2001, ApJ, 562, 1012, astro-ph/0104126

Fabrycky, D., & Tremaine, S. 2007, ApJ, 669, 1298, 0705.4285

Ford, E. B., Kozinsky, B., & Rasio, F. A. 2000, ApJ, 535, 385

Ford, E. B., & Rasio, F. A. 2008, ApJ, 686, 621, astro-ph/0703163

Gezari, S. et al. 2012, Nature, 485, 217, 1205.0252

——. 2008, ApJ, 683, L131, 0804.1123

Gezari, S., Halpern, J. P., Komossa, S., Grupe, D., & Leighly, K. M. 2003, ApJ, 592, 42

Gezari, S. et al. 2009, ApJ, 698, 1367, 0904.1596

——. 2006, ApJ, 653, L25, astro-ph/0612069

Hansen, B. M. S. 2010, ApJ, 723, 285, 1009.3027

Harrington, R. S. 1968, AJ, 73, 190

——. 1969, Celestial Mechanics, 1, 200

Hellier, C. et al. 2009, Nature, 460, 1098

Holman, M., Touma, J., & Tremaine, S. 1997, Nature, 386, 254

Hut, P. 1981, A&A, 99, 126

Ivanov, P. B., Polnarev, A. G., & Saha, P. 2005, MNRAS, 358, 1361, astro-ph/0410610

Katz, B., & Dong, S. 2012, ArXiv e-prints, 1211.4584

Katz, B., Dong, S., & Malhotra, R. 2011, Physical Review Letters, 107, 181101, 1106.3340

Kiseleva, L. G., Eggleton, P. P., & Mikkola, S. 1998, MNRAS, 300, 292

Kocsis, B., & Levin, J. 2012, Phys. Rev. D, 85, 123005, 1109.4170

Komossa, S., & Greiner, J. 1999, A&A, 349, L45, astro-ph/9908216

Kozai, Y. 1962, AJ, 67, 591

Lee, M. H., & Peale, S. J. 2003, ApJ, 592, 1201, astro-ph/0304454

Li, G., Naoz, S., Kocsis, B., & Loeb, A. 2013, ArXiv e-prints, 1310.6044

Lidov, M. L. 1962, Planet. Space Sci., 9, 719

Lidov, M. L., & Ziglin, S. L. 1974, Celestial Mechanics, 9, 151

Lin, D. N. C., & Papaloizou, J. 1986, ApJ, 309, 846

Lithwick, Y., & Naoz, S. 2011, ApJ, 742, 94, 1106.3329

Matsumura, S., Peale, S. J., & Rasio, F. A. 2010, ApJ, 725, 1995, 1007.4785

Mazeh, T., & Shaham, J. 1979, A&A, 77, 145

Miller, M. C., & Hamilton, D. P. 2002, ApJ, 576, 894, astro-ph/0202298

Morbidelli, A. 2002, Modern celestial mechanics : aspects of solar system dynamics

Nagasawa, M., & Ida, S. 2011, ApJ, 742, 72

Naoz, S., Farr, W. M., Lithwick, Y., Rasio, F. A., & Teyssandier, J. 2011, Nature, 473, 187, 1011.2501

——. 2013a, MNRAS, 431, 2155, 1107.2414

Naoz, S., Farr, W. M., & Rasio, F. A. 2012, ApJ, 754, L36, 1206.3529

Naoz, S., Kocsis, B., Loeb, A., & Yunes, N. 2013b, ApJ, 773, 187, 1206.4316

O'Leary, R. M., Kocsis, B., & Loeb, A. 2009, MNRAS, 395, 2127, 0807.2638

Perets, H. B., & Fabrycky, D. C. 2009, ApJ, 697, 1048, 0901.4328

Shappee, B. J., & Thompson, T. A. 2013, ApJ, 766, 64, 1204.1053

Soderhjelm, S. 1982, A&A, 107, 54

Stone, N., & Loeb, A. 2012, MNRAS, 422, 1933, 1105.4966

Tamayo, D. 2013, ArXiv e-prints, 1312.7020

Teyssandier, J., Naoz, S., Lizarraga, I., & Rasio, F. 2013, ArXiv e-prints, 1310.5048

Thies, I., Kroupa, P., Goodwin, S. P., Stamatellos, D., & Whitworth, A. P. 2011, MNRAS, 417, 1817, 1107.2113

Thomas, F., & Morbidelli, A. 1996, Celestial Mechanics and Dynamical Astronomy, 64, 209

Thompson, T. A. 2011, ApJ, 741, 82, 1011.4322

van Velzen, S. et al. 2011, ApJ, 741, 73, 1009.1627

Veras, D., & Ford, E. B. 2010, ApJ, 715, 803, 1004.1421

Wegg, C., & Bode, N. 2011, ApJ, 738, L8, 1011.5874

Wen, L. 2003, ApJ, 598, 419, astro-ph/0211492

Winn, J. N. et al. 2011, AJ, 141, 63, 1010.1318

Wu, Y., & Lithwick, Y. 2011, ApJ, 735, 109, 1012.3475

Wu, Y., & Murray, N. 2003, ApJ, 589, 605, astro-ph/0303010

Yu, Q., & Tremaine, S. 2001, AJ, 121, 1736, astro-ph/0009255

6.6 Appendix

6.6.1 Dynamics of the Unsimplified Hamiltonian

In our simplified perturbative model, we set $\sqrt{1-\chi^2}$ to be a constant in the Hamiltonian (equation (6.7)) in order to treat this system as a modulated pendulum. Here, we justify this approach by showing that the dynamics with the original Hamiltonian can be well approximated by the simplified version with $\sqrt{1-\chi^2}$ set to be a constant.

Considering each forcing term with frequency s_k at a time, we can plot the critical curve of the trajectories. We show the four critical curves with the different frequency s_k in Figure 6.5. Since most of the forcing terms have librating region far from $\chi = 1$,

the separatrixes are not greatly distorted and are essentially analogous to that with $\sqrt{1-\chi^2}$ constant in Figure 6.2. Because the interaction of the resonant (librating) regions give rise to the dynamical structure of this system, the corresponding overlaps of the separatrixes demonstrate that the dynamics of the original Hamiltonian can be captured by the simplified Hamiltonian.

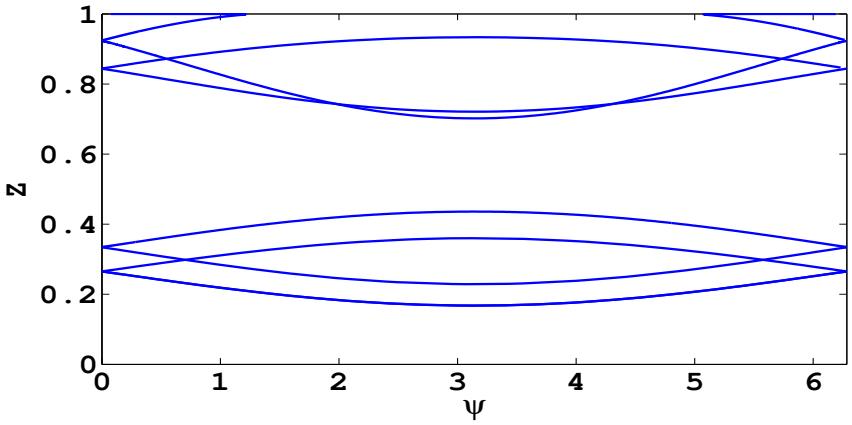

Figure 6.5: The separatrix of the un-simplified Hamiltonian with each frequency s_k. It is analogous to that in Figure 6.2, justifying our approaching with $\sqrt{1-\chi^2}$ set to be a constant.

6.6.2 Double Resonances and Triple Resonances

As explained in the main text, the chaotic zones and the bridge can be approximated as two or three overlapping resonances with equal widths. Here, we demonstrate an analytical way to calculate the Lyapunov exponent and the diffusion coefficient for the double or triple resonances with the same resonant widths. This analytical method can be applied for resonant doublets or triplets with equal widths in general.

For the double resonances, the Hamiltonian can be written as:

$$H_D(p,q,t) = \frac{\beta}{2}p^2 + c(\cos q + \cos(q - \omega_B t)) \tag{6.21}$$

where ω_B is the frequency difference between the two resonances. The half width of each resonant region is $\Delta = 2\sqrt{c/\beta}$, and the libration frequency of each resonant region is $\omega_L = \sqrt{c\beta}$. To illustrate the behavior of this Hamiltonian, in Figure (6.6), we plot the surface of section starting from point $p = 1.5$, $q = 1$ with the total run time $t = 1000$, where we measure time in units of $1/\sqrt{c\beta}$ and action in units of $\sqrt{c/\beta}$. As ω_B decreases, the two resonances are more overlapped.

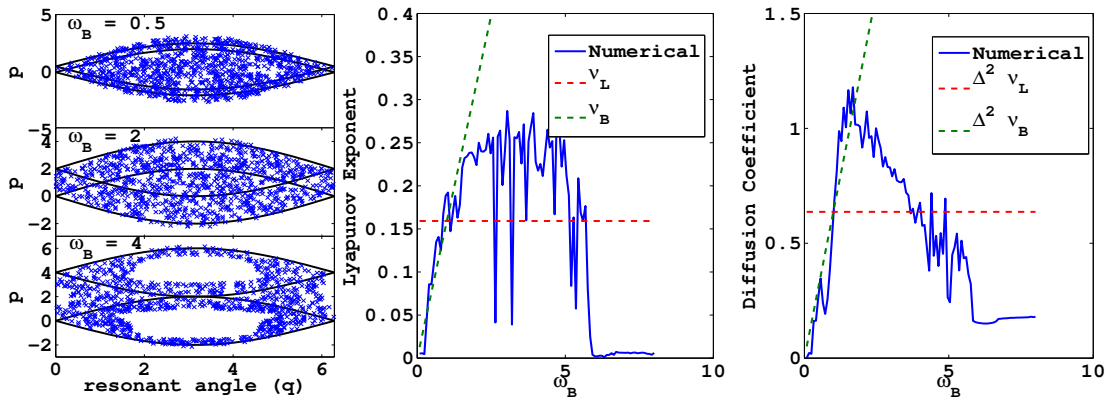

Figure 6.6: The analytical models for the double resonances. Left panel: the surface of section of the double resonances with different overlaps starting with $q = 1$, $p = 1.5$. Middle panel: the numerical and the analytical estimates of the Lyapunov exponent with different overlaps. Right panel: the numerical and analytical estimates of the diffusion coefficient with different overlaps.

Next, we estimate the Lyapunov exponent of the double resonances numerically. Following the method discussed in (Morbidelli 2002), we linearized the hamiltonian H_D to evolve the difference of two trajectories. We start the integration at $p = 1.5$, $q = 1$ arbitrarily, and calculate the Lyapunov exponent as $\frac{1}{t}\ln\frac{\delta(t)}{\delta(0)}$, where we set $t = 1000$ for our integration. We plot the numerical result in the middle panel of Figure (6.6) with

the blue line. To compare with the characteristic frequencies in this system, we over plotted $\nu_B = \omega_B/2\pi$ and $\nu_L = \omega_L/2\pi$.

We notice that when the resonances are closely overlapped $\omega_B < 2$, the Lyapunov exponent can be approximated as ν_B. When the resonances are less overlapped but still attached $2 < \omega_B < 4$, the Lyapunov exponent is approximately constant ($\sim 2\omega_L$). When the resonances are more separated, the Lyapunov exponent falls as the system becomes more regular.

Then, we calculate the diffusion coefficient numerically. To average over the oscillations due to the libration behavior, we take the difference in δp at $t = n/\nu_B$, $n \in Z$, and estimate the diffusion coefficient as $\langle \delta p^2 \nu_B \rangle$. The result is plotted in the right panel in Figure (6.6) with the blue line.

Comparing with the characteristic timescale of the system, we find that the when the two resonant regions are closely overlapped ($\omega_B < 2$), the diffusion coefficient can be well estimated as $\Delta^2 \nu_B$. When the two resonant regions are separated more apart, the diffusion coefficient drops as the system becomes more regular. When $\omega_B = 4$, the diffusion coefficient is approximately $\sim \Delta^2 \nu_L$.

Similarly, for the triple resonances, we use the following simplified Hamiltonian:

$$H_T(p, q, t) = \frac{\beta}{2} p^2 + c(\cos q + \cos(q - \omega_B t) + \cos(q + \omega_B t)) \tag{6.22}$$

Using trigonometric identities, this Hamiltonian can be rewritten as

$$H_T(p, q, t) = \frac{\beta}{2} p^2 + c(1 + 2\cos(\omega_B t)) \cos q \tag{6.23}$$

Thus, H_T can be understood as a "breathing" resonance whose width is changing with frequency ν_B (Morbidelli 2002). We plot the overlap of the resonances in the left panel

of Figure (6.7).

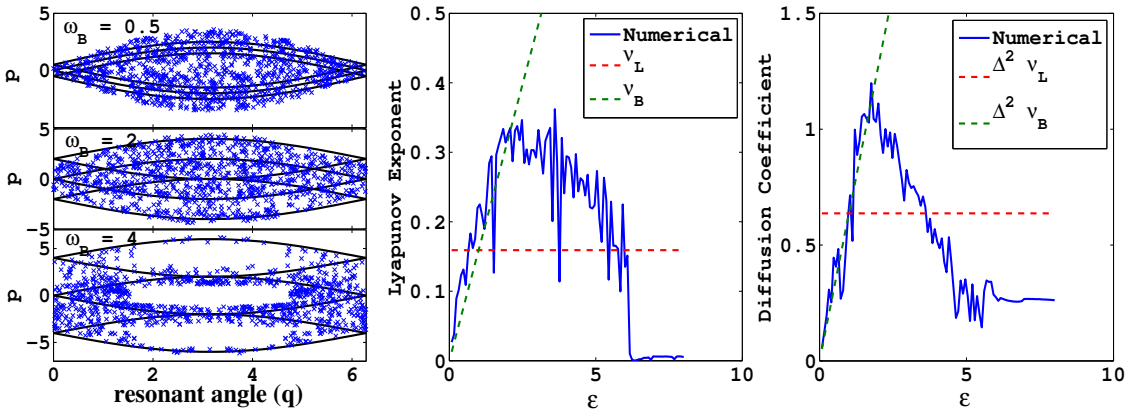

Figure 6.7: The analytical models for the triple resonances analogous to the bridge zone. Left panel: the surface of section of the double resonances with different overlaps starting with $q = 1$, $p = 1.5$. Middle panel: the numerical and the analytical estimates of the Lyapunov exponent with different overlaps. Right panel: the numerical and analytical estimates of the diffusion coefficient with different overlaps.

We numerically calculated the Lyapunov exponent and the diffusion coefficient with the method described for the double resonances. We find that similar to the double resonances, the Lyapunov exponent can be well estimated as ν_B when $\omega_B < 2$, as $\sim 2\nu_L$ when $2 < \omega_B < 4$ and drops when $\omega_B > 4$. For the diffusion coefficient, we find that it can be estimated as $\Delta^2\nu_B$ for $\omega_B < 2$ and it drops for $\omega_B > 2$. At $\omega_B \sim 4$, it can be estimated as $\Delta^2\nu_L$.

Chapter 7

Pre-LHB Evolution of the Earth's Obliquity

This thesis chapter originally appeared in the literature as

Li, G. & Batygin, K. Pre-LHB Evolution of the Earth's Obliquity, *The Astrophysical Journal*, 795, 67, 2014

Abstract

The Earth's obliquity is stabilized by the Moon, which facilitates a rapid precession of the Earth's spin-axis, de-tuning the system away from resonance with orbital modulation. It is however, likely that the architecture of the Solar System underwent a dynamical instability-driven transformation, where the primordial configuration was more compact. Hence, the characteristic frequencies associated with orbital perturbations were likely faster in the past, potentially allowing for secular resonant encounters. In this work

we examine if at any point in the Earth's evolutionary history, the obliquity varied significantly. Our calculations suggest that even though the orbital perturbations were different, the system nevertheless avoided resonant encounters throughout its evolution. This indicates that the Earth obtained its current obliquity during the formation of the Moon.

7.1 Introduction

Obliquity variation plays a major role in the modulation of climate, as it determines the latitudinal distribution of solar radiation. For instance, according to the Milankovitch theory, the ice ages on the Earth are closely associated with the variation in insolation at high latitudes, which depends on the orbital eccentricity and orientation of the spin axis (e.g. Weertman 1976; Hays et al. 1976; Imbrie 1982).

The spin-axis dynamics of the Earth-Moon system has been extensively studied in the literature and is generally well understood. At present, the obliquity variation of the Earth is regular and only undergoes small oscillations between 22.1° and 24.5° with a 41000 year period (e.g. Vernekar 1972; Laskar & Robutel 1993). Without the Moon, the obliquity of the hypothetical Earth is chaotic, but is constrained between $0 - 45°$ over billion year timescales (Laskar et al. 1993; Lissauer et al. 2012; Li & Batygin 2014a).

The difference between obliquity cycles exhibited by a Moon-less Earth and that corresponding to the real Earth arise largely as a consequence of the underlying resonant structure (Laskar 1996). Specifically, the spin-axis of the Earth may exhibit complex behavior if its precession resonates with the secular evolution of the Earth's orbit. The

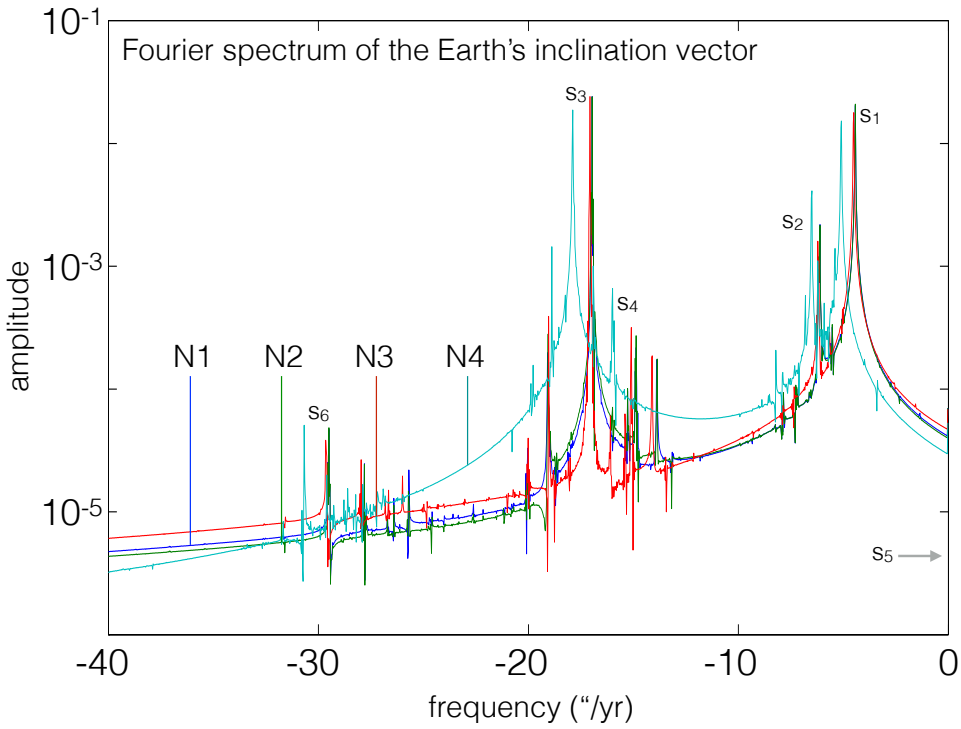

Figure 7.1: The Fourier spectrum of the Earth's orbital parameter ($i_{\oplus}e^{i\Omega_{\oplus}t}$) obtained from an N-body simulation using the *mercury6* program. The initial conditions are those identified in Batygin & Brown (2010), which are compatible with the Nice model. Note that the maximum high-amplitude secular frequencies corresponding to multi-resonant conditions are $\sim -18''/yr$, which is similar to the current maximum secular frequency $s_3 = -18.8512''/yr$. The maximum high-amplitude secular frequencies are within the same order of magnitude for the three cases.

former is dominantly controlled by Solar and Lunar torques, whereas the latter is forced by long-period planet-planet interactions. In absence of the Moon, the Earth would indeed find itself residing within a multi-resonant domain signaling chaotic motion (Chirikov 1979; Laskar et al. 1993). The introduction of the Moon, however, accelerates the precession of the spin-axes, and detunes the system away from resonance yielding quasi-periodic evolution (Neron de Surgy & Laskar 1997).

The aforementioned real vs Moon-less Earth discussion leaves open the question of

how the dynamical state of the spin-axis may have responded to changes in the orbital architecture. After all, if the Earth's orbital evolution was once characterized by more rapid secular evolution, past resonant behavior of the spin-axis cannot be ruled out a-priori. Indeed for the case of Mars, the study of Brasser & Walsh (2011) has shown that the orbital rearrangement of the Solar System has led to a qualitative change in the dynamical behavior of the spin-axis. Hence, it is possible that in the history of the Earth-Moon system, the obliquity variation of the Earth was once significant. Correspondingly, understanding the past variation of the obliquity shines light on how the Earth obtained its current spin-orbit misalignment.

Substantial progress has been made towards the characterization of the early dynamical evolution of the Solar System through the development of the Nice model. Qualitatively, the picture envisioned within the context of the Nice model is one where the giant planets start out on a compact orbital configuration and following a transient instability scatter onto their current orbits (Tsiganis et al. 2005; Levison et al. 2011; Nesvorný 2011; Batygin 2012; Nesvorný & Morbidelli 2012). The numerous successes of the Nice model include a replication of the dynamical architecture of the outer Solar System (Morbidelli et al. 2009), the inner solar system (Brasser et al. 2009; Agnor & Lin 2012), the formation of the Kuiper belt (Levison et al. 2008; Batygin et al. 2011), the chaotic capture of Jupiter and Neptune trojan populations (Morbidelli et al. 2005; Nesvorný et al. 2007) as well as its role as a trigger mechanism for late heavy bombardment (LHB) (Gomes et al. 2005).

Although the primordial state of the Solar System is not well constrained, it is likely that the giant planets resided in a multi-resonant configuration (i.e. a condition where each planet resides in mean motion resonances with each of its neighbors) at the time of

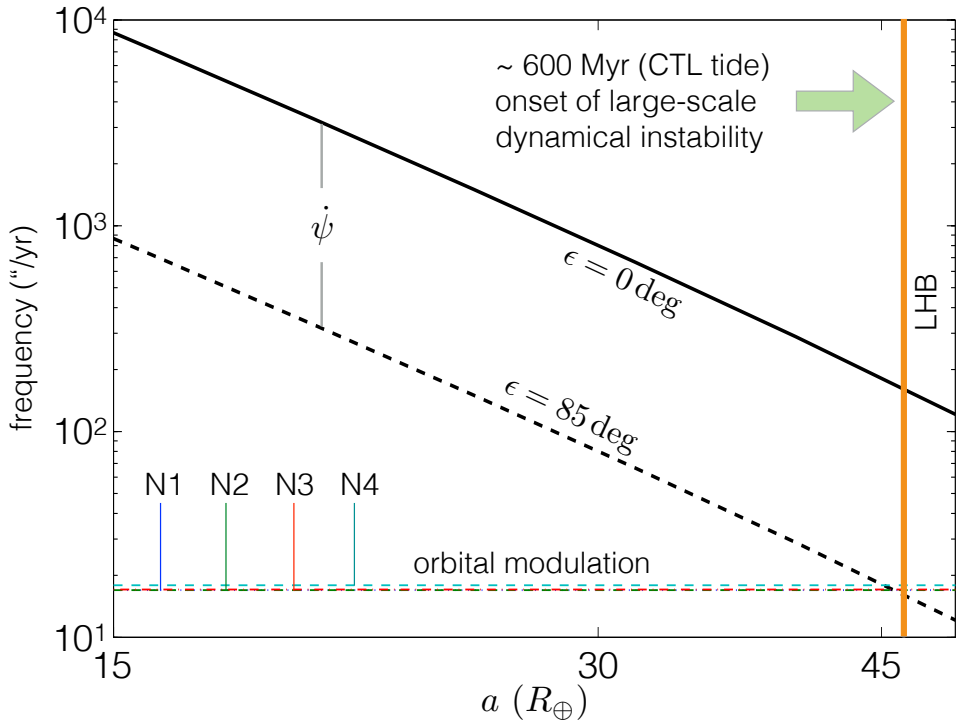

Figure 7.2: The comparison of the maximal secular frequencies of the Earth corresponding to various outer Solar System architectures and the forced spin-axis precession rate of the Earth. The presented analysis shows that the precession frequency is much bigger than the orbital frequency at low obliquity, and this indicates that there are no significant obliquity variations in the history of the Earth-Moon system due to resonances.

nebular dispersion, as such architectures are natural outcomes of disk-driven migration (Masset & Snellgrove 2001; Morbidelli et al. 2007). Under this assumption, a limited number of configurations compatible with the Nice model have been identified (Batygin & Brown 2010; Nesvorný & Morbidelli 2012). Accordingly, in this study we extend the quantification of the Nice model by exploring the spin-axis dynamics of the Earth-Moon system within the context of pre-instability orbital configurations.

The plan of this paper is as follows. In §2, we analyze resonant conditions, and in §3, we study the obliquity variation using numerical simulations. We summarize and discuss our results in §4.

7.2 Spectral Analysis

As already mentioned above, the Sun and the Moon torque the spin axis of the Earth, and the other planets in the solar system perturb the orbit of the Earth. When the two effects share the same frequencies, resonances arise and the spin-orbit angle (obliquity) undergoes large amplitude variations (Colombo 1966; Ward 1973; Henrard & Murigande 1987). Furthermore, if the resonances overlap, the obliquity variation becomes chaotic (Chirikov 1979; Laskar et al. 1993). Therefore, the obliquity variation is sensitive to the two sets of frequencies. Accordingly, in this section, we investigate whether resonant motion was plausible at any point in the system's evolutionary history.

In order to obtain the dominant secular frequencies of the Earth's orbital inclination vector, we performed N-body integrations of the multi-resonant conditions identified by Batygin & Brown (2010) using the *mercury6* orbital integration software package (Chambers 1999). The specific multi-resonant states onto which the giant planets were initialized are delineated in Table (7.1). The rows labeled N1–N4 correspond to different multi-resonant states, while the columns depict neighboring period ratios*. Table (7.2) shows the eccentricity of the four giant planets, which are set to be in the same plane. On the other hand, the terrestrial planets were put in the same location as where they are currently†, motivated by the analysis of Brasser et al. (2009). We ignore the impacts

*Initial conditions where Jupiter and Saturn are locked in a second-order 5:3 resonance were not considered due to their comparatively low capture probability (Pierens & Nelson 2008).

†We note that the angular momentum deficit of the terrestrial planet system may have been somewhat lower in the past. However, this does not affect our analysis appreciably because to leading order, the frequencies of the secular system are set only by the semi-major axes and masses (Murray & Dermott

from scattered planetesimals, since their effects are negligible here. The duration of each integration spanned 50 Myr.

The characteristic secular frequencies, obtained by Fourier analysis of the quantity $z = ie^{\imath\Omega}$, where i is the inclination, Ω is the longitude of ascending node, and $\imath = \sqrt{-1}$ are shown in Figure (1). The curves corresponding to the various multi-resonant giant planet configurations are labeled accordingly. As shown in the figure, the maximum frequencies with non-negligible amplitudes are around $-18^{''}/yr$. This is similar to the current maximum large-amplitude frequency ($s_3 = -18.8512^{''}/yr$) (Laskar 1990).

As a consequence of tidal evolution, the torque exerted on the Earth by the Moon varies as a function of time. Specifically, as the Lunar orbit expands, the spin rate of the Earth slows down and the torque becomes weaker. The tidal dissipation inside the Earth and the Moon depends on the underlying rheology and is generally complicated (see Efroimsky & Williams 2009 for a review). However, as the total angular momentum remains constant under tidal dissipation, the torque and the spin precession frequency caused by the Moon can be evaluated as a function of the Earth-Moon semi-major axis

1999).

Table 7.1:: Multi-resonant states.

	$P_{\text{Jupiter}} : P_{\text{Saturn}}$	$P_{\text{Saturn}} : P_{\text{Uranus}}$	$P_{\text{Uranus}} : P_{\text{Neptune}}$
N1	2 : 3	2 : 3	4 : 5
N2	2 : 3	3 : 4	2 : 3
N3	2 : 3	3 : 4	3 : 4
N4	1 : 2	3 : 4	3 : 4

(a). The expression for the forced spin precession frequency is $\dot{\psi} = \alpha \cos(\varepsilon)$, where ψ is the longitude of the spin-axis, ε is the obliquity, and α is the precession coefficient defined as (Neron de Surgy & Laskar 1997):

$$\alpha = \frac{3G}{2\omega}\Big[\frac{m_\odot}{(a_\oplus\sqrt{1-e_\oplus^2})^3} + \frac{m_M}{(a_M\sqrt{1-e_M^2})^3}(1-\frac{3}{2}\sin^2 i_M)\Big]E_d. \quad (7.1)$$

In the above expression, $m_\odot$ is the mass of the Sun, $a_\oplus$ and $e_\oplus$ are the semi major axis and the eccentricity of the Earth's orbit, m_M is the mass of the moon, $a_M = a$, e_M and i_M are the semi major axis, eccentricity and inclination of the Moon's orbit around the Earth, ω is the spin of the Earth, and $E_d = (2C - A - B)/C$ is the dynamical ellipticity of the Earth, where A, B and C are the moment of inertia in the three principle axes. We set E_d to be proportional to ω^2, as it arises from rotational deformation (e.g. Murray & Dermott 1999). We plot the forced spin-axis precession rate, $\dot{\psi}$ due to both the Sun and the Moon in Figure 7.2, where the solid and the dashed curves corresponds to null ($\epsilon = 0$ deg) and nearly lateral ($\epsilon = 85$ deg) obliquities. Note that in this approach, we require the Moon to be sufficiently far away from the Earth ($a \gtrsim 15R_\oplus$) for the Moon's orbit to precesses about the ecliptic plane. Additionally, we over-plot the maximum orbital frequencies obtained from the N-body simulations (also shown in Figure 7.1).

The denoted curves suggest that for all reasonable choices of parameters, the spin-axis precession frequency has consistently exceeded the maximal secular frequencies significantly, even though the past orbital frequencies are larger than the current ones. Given that the current obliquity is relatively low, this indicates that the spin-axis resonant encounters of low order are unlikely to have played an important role in the past history of the Earth-Moon system. In other words, the Earths obliquity did not

vary substantially throughout the Solar System's lifetime. On the other hand, had the Earths primordial obliquity been greater than $\epsilon \gtrsim 80$ deg, resonant dynamics of the spin-axis could have been possible after a few hundred Myr of tidal evolution.

Moreover, at ~ 600 Myr, the four giant planets reach instability and quickly scatter divergently. The onset of this transient behavior can arise from an encounter of a planet pair with a mean motion resonance (e.g. Jupiter & Saturn's encounter with a 2:1 or a 5:3 MMR; see Tsiganis et al. 2005; Morbidelli et al. 2007; Batygin & Brown 2010), or from the destruction of the resonant phase-protection mechanism by interactions with a distant self-gravitating planetesimal disk (Levison et al. 2011; Nesvorný & Morbidelli 2012). To mark the time when the instability occurs in Figure 7.2, the Earth-Moon distance as a function of time needs to be calculated. Assuming a constant time lag (CTL) tidal model with $t_{\rm diss} = 33.18$ minutes, the Earth-Moon distance at ~ 600 Myr is marked with an orange line in Figure 7.2. The specific choice for $t_{\rm diss}$ is adopted so that the Earth-Moon distance evolves to its current state at ~ 4.5 Gyr.

Shortly after the onset of the instability, the giant planets evolve onto their current locations with higher eccentricities and inclinations, which damp as a result of interactions with a massive planetesimal disk (Levison et al. 2008). Numerical integration shows that the relevant secular frequencies when the eccentricity and inclination are damping are similar to the current frequencies, as the frequencies are largely determined by the semi major axes and masses alone (Murray & Dermott 1999). This suggests that there are no large obliquity variations during the damping era either.

We note that an initial Solar System configuration that harbored more than two ice giants beyond the orbit of Saturn is a distinct possibility within the framework of

the Nice model (Nesvorný 2011; Batygin 2012; Nesvorný & Morbidelli 2012). Although such configurations will yield quantitatively different evolutions from the cases presented here, the synonymity of the Fourier decompositions of the initial conditions presented in this work (see Figure 7.1) suggest that the introduction of additional Neptune-mass planets into the resonant chains is unlikely to alter the results significantly. Accordingly, here we use only the four giant planet models as illustrative examples.

7.3 Numerical Integrations

The analysis performed above suggests that the obliquity does not exhibit large variations due to the resonances as a result of Chirikov diffusion arising from secular spin-orbit resonance overlap at low obliquities. This however does not negate the possibility of substantial obliquity diffusion associated with stochastic pumping arising from a chaotic orbit (Lichtenberg & Lieberman 1983). To illustrate explicitly the evolution of the obliquity as a function of time, we numerically integrate the obliquity variation using the Earth's orbital evolution obtained from N-body simulations. Specifically, we evolve the Earth's obliquity adopting multi-resonant conditions for the giant planets (depicted in Table 1), and taking the precession coefficient to change in accord with the Moon's tidal recession and the Earth's spin-down. As before, a CTL tidal model was employed with $t_{\rm diss} = 33.18$ minutes.

The Hamiltonian describing the evolution of the obliquity is well documented in the literature (e.g. Colombo 1966; Laskar et al. 1993; Touma & Wisdom 1993; Neron de

Surgy & Laskar 1997):

$$\begin{aligned} H(\chi,\psi,t) &= \frac{1}{2}\alpha\chi^2 + \sqrt{1-\chi^2} \\ &\times \quad (A(t)\sin\psi + B(t)\cos\psi)), \end{aligned} \tag{7.2}$$

where $\chi = \cos\varepsilon$, α is the precession coefficient (see eqn 7.1), and

$$A(t) = 2(\dot{q} + p(q\dot{p} - p\dot{q}))/\sqrt{1-p^2-q^2}, \tag{7.3}$$

$$B(t) = 2(\dot{p} - q(q\dot{p} - p\dot{q}))/\sqrt{1-p^2-q^2}, \tag{7.4}$$

where $p = \sin i_\oplus/2\ \sin\Omega_\oplus$ and $q = \sin i_\oplus/2\ \cos\Omega_\oplus$. The integrations are taken to span 600 Myr.

Starting with different initial obliquities, we plot the numerical results in Figure 7.3. The calculations suggest that independent of the initial condition, when $\varepsilon \lesssim 80°$, the obliquity remains nearly constant as a function of time. The obliquity varies substantially and rapidly when $90° \gtrsim \varepsilon \gtrsim 80°$, because the precession frequency ($\alpha\cos\varepsilon$) matches with the orbital perturbation frequency at later times (as shown in Figure 7.2). This is consistent with our analysis of the resonances, indicating the effect of chaotic pumping on the obliquity diffusion is negligible here. As noted above, this suggests that that the Earth's present obliquity has been preserved throughout the system's history.

7.4 Conclusion

It is generally accepted that substantial modulation of the Earths obliquity can result in dynamically-forced climatological changes. In turn, the variation of a planet's obliquity is sensitive to the precession frequency of its spin axis and its secular orbital frequencies.

When the two sets of frequencies match, resonances may arise and the planet's obliquity may undergo large amplitude variations (as the case for the Moonless Earth (e.g. Laskar et al. 1993; Li & Batygin 2014a) or for Mars (Ward 1973; Touma & Wisdom 1993; Laskar & Robutel 1993)). Currently, the Earth's obliquity is regular and oscillates with a very small amplitude ($22.1 - 24.5°$). However, the orbital forcing of the Earth likely underwent significant changes throughout the Solar Systems dramatic history, potentially suggesting that the dynamical state of the Earths spin-axis may have been resonant in the past. In this study, we have quantified this possibility.

We began our investigation by examining the feasible proximity of the pre-instability secular modes that characterize the orbital evolution of the Earth to the precession rate of the Earths spin-axis. To obtain the secular orbital frequencies of the Earth, we computed the orbital evolution of the Earth, adopting Solar System orbital architectures that were previously demonstrated to serve well as initial conditions for the Nice model by Batygin & Brown (2010). Our analysis has shown that even under favorable assumptions, the slow-down in the spin-axis precession frequency associated with the tidal evolution of the Earth-Moon system as well as the increase in the forcing frequencies associated with a more compact giant-planet configuration are insufficient to give rise to secular spin-orbit resonant encounters in the system at low obliquities.

Subsequently, to illustrate the obliquity variation explicitly, we directly integrated the pre-LHB spin-axis evolution of the Earth. We adopted the Earth's orbital evolution from the N-body simulations and calculated the precession coefficient based on the CTL tidal dissipation model for the Earth-Moon system. The numerical results show that only minimal oscillations in the Earths obliquity can be expected for primordial obliquities less than $\epsilon \lesssim 80$ deg. Indeed, this is consistent with our qualitative analysis of spin-axis

resonant conditions.

Cumulatively, our study shows that the dynamical perturbations arising from the other planets are unlikely to have given rise to resonant excitations of the Earths spin-axis at low obliquity. Moreover, chaotic pumping arising from a diffusing orbit also leads to negligible evolution. Thus, the Earth's obliquity likely did not vary substantially throughout the dramatic lifetime of the Solar System, and was probably set in situ by the giant impact associated with the formation of the Moon. This remarkable aspect of Solar System dynamics renders the Earths obliquity one of the few truly primordial features of the Solar System.

Table 7.2:: Orbital properties.

	e_{Jupiter}	e_{Saturn}	e_{Uranus}	e_{Neptune}
N1	0.0060	0.025	0.031	0.0083
N2	0.0038	0.017	0.017	0.0064
N3	0.0069	0.026	0.016	0.018
N4	0.044	0.025	0.053	0.0046
	a_{Jupiter} (AU)	a_{Saturn} (AU)	a_{Uranus} (AU)	a_{Neptune} (AU)
N1	5.88	7.89	10.38	12.01
N2	5.87	8.00	9.98	13.16
N3	5.84	7.83	9.67	11.63
N4	5.48	8.74	10.59	12.86

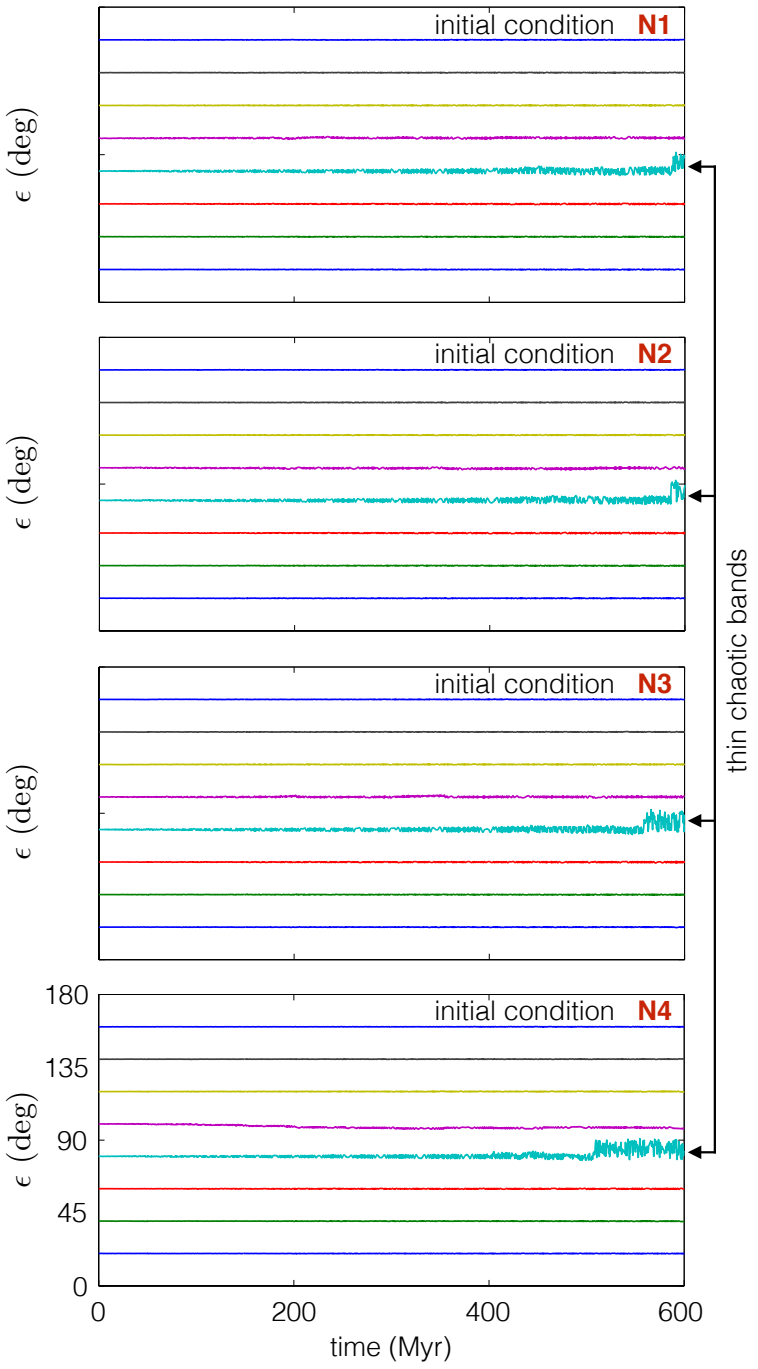

Figure 7.3: The obliquity as a function of time when the giant planets are in resonant states, as presented in table (7.1). The Earth-Moon system is taken to evolve under tidal dissipation with a constant time lag ($t_{\rm diss} = 33.18$ minutes). The obtained solutions suggest that the obliquity remains constant except when it is initialized at $90^\circ \gtrsim \epsilon \gtrsim 80^\circ$.

Section II. Stars around Supermassive Black Holes

Chapter 8

Implications of the Eccentric Kozai-Lidov Mechanism for Stars Surrounding Supermassive Black Hole Binaries

This thesis chapter has been submitted to Monthly Notices of the Royal Astronomical Society, and originally appeared in arXiv as

Li, G., Naoz, S., Kocsis, B. & Loeb, A. Implications of the Eccentric Kozai-Lidov Mechanism for Stars Surrounding Supermassive Black Hole Binaries, 2015

Abstract

An enhanced rate of stellar tidal disruption events (TDEs) may be an important characteristic of supermassive black hole (SMBH) binaries at close separations. Here we study the evolution of the distribution of stars around a SMBH binary due to the eccentric Kozai-Lidov (EKL) mechanism, including octupole effects and apsidal precession caused by the stellar mass distribution and general relativity. We identify a region around one of the SMBHs in the binary where the EKL mechanism drives stars to high eccentricities, which ultimately causes the stars to either scatter off the second SMBH or get disrupted. For SMBH masses $10^7 M_\odot$ and $10^8 M_\odot$, the TDE rate can reach $\sim 10^{-2}$/yr and deplete a region of the stellar cusp around the secondary SMBH in ~ 0.5 Myr. As a result, the final geometry of the stellar distribution between 0.01 and 0.1 pc around the secondary SMBH is a torus. These effects may be even more prominent in nuclear stellar clusters hosting a supermassive and an intermediate mass black hole.

8.1 Introduction

Supermassive black holes (SMBHs) are ubiquitous at the centers of galaxies (Kormendy & Ho 2013). Stars passing close to the SMBH can be tidally disrupted, and the fall back of the stellar debris produces a strong electromagnetic tidal disruption flare (e.g., Gezari 2012). More than a dozen tidal disruption event (TDE) candidates have been observed until present (e.g., Bade et al. 1996; Gezari et al. 2003, 2006, 2008a, 2009; van Velzen et al. 2011; Gezari et al. 2012; Holoien et al. 2014), including two candidates with relativistic jets (Levan et al. 2011; Bloom et al. 2011; Zauderer et al. 2011; Cenko et al.

2012). TDEs can provide valuable information on dormant SMBHs, which are otherwise difficult to detect.

The rate of the TDEs provide information about the SMBH and the stellar distribution in the center of galaxies (Stone & Metzger 2014). The rate of TDEs is highly uncertain observationally due to the small sample size. It is estimated to be in the range of $10^{-5} - 10^{-4}$ per galaxy per year by Donley et al. (2002); Gezari et al. (2008a); Maksym (2012); van Velzen & Farrar (2014). This roughly agrees with the theoretical estimates, discussed by Frank & Rees (1976); Lightman & Shapiro (1977); Cohn & Kulsrud (1978); Magorrian & Tremaine (1999); Wang & Merritt (2004); Brockamp et al. (2011); Stone & Metzger (2014). However, the TDE rate may be enhanced due to the presence of a non-axisymmetric gravitational potential around the SMBH (Merritt & Poon 2004), or due to a massive perturber (Perets et al. 2007). In addition, the TDE rate may be higher in galaxies with more than one SMBH (Ivanov et al. 2005; Chen et al. 2009, 2011; Wegg & Bode 2011), or when the SMBH binary (SMBHB) recoils due to the emission of gravitational waves (Stone & Loeb 2011a; Li et al. 2012; Stone & Loeb 2012). Some TDEs may not appear as flares and therefore be missed in observations(Guillochon & Ramirez-Ruiz 2015).

In this paper, we focus on the impact of SMBHB on the surrounding distribution of stars through hierarchical three body interactions. The outer SMBH perturbs the stellar population around the inner* SMBH, and leads to long-term variations in the eccentricities and inclinations of the stellar orbits while keeping the semimajor axes

*We consider stars that initially orbit the "inner" SMBH and whose orbits are perturbed by the "outer" SMBH regardless of which SMBH is more massive.

of their orbits fixed. In particular, when the orbit of the SMBH secondary is circular and if the mutual inclination between the orbits of the SMBHB and a star is over 40°, the stellar eccentricity and inclination undergo periodic oscillations, known as the quadrupole Kozai-Lidov mechanism (Kozai 1962; Lidov 1962). This is caused by the long-term (orbit-averaged) Newtonian gravitational effect expanded in multipoles to the quadrupole order, i.e. second order in the semimajor axis ratio of the stellar and the outer SMBH's orbit. More generally, it has been found that when the outer orbit is eccentric, the analogous octupole eccentric Kozai-Lidov mechanism (EKL, third order in semi major axis ratio) causes the eccentricity to be excited very close to unity and the inner orbit to flip from prograde to retrograde or vice versa (Naoz et al. 2011; Katz et al. 2011; Lithwick & Naoz 2011; Naoz et al. 2013a,b; Li et al. 2014a; Li et al. 2014b). The TDE rate has been discussed in the literature for stars orbiting an SMBHB, where the quadrupole Kozai-Lidov mechanism can enhance the tidal disruption rate (Ivanov et al. 2005; Chen et al. 2009, 2011; Wegg & Bode 2011). For the Galactic Center, the Kozai-Lidov mechanism driven by the stellar disk has also been discussed and the additional effects of Newtonian apsidal precession were shown to play a significant role (Chang 2009). In light of recent developments in the understanding of hierarchical three body interactions we revisit this problem. Since the stellar eccentricity can be increased to a value much closer to unity by eccentric perturbers, we expect the EKL mechanism to enhance TDE rates with respect to the circular case. We therefore seek to re-evaluate the total number of stars vulnerable to TDE due to EKL.

It is well known that apsidal precession quenches the EKL mechanism (e.g., Ford et al. 2000; Blaes et al. 2002; Naoz et al. 2013b). In galactic nuclei this may be due to the Newtonian (NT) gravitational effect of the spherical stellar cusp or general relativistic

(GR) precession, provided that the corresponding precession timescale is much shorter than the Kozai timescale (Chang 2009). Furthermore, the EKL mechanism may be quenched if the eccentricity of the star is changed by the stellar cluster due to scalar resonant relaxation, or if the orbital plane is reoriented by the stellar cluster due to vector resonant relaxation (Rauch & Tremaine 1996; Kocsis & Tremaine 2011, 2014) or Lense-Thirring precession (Merritt et al. 2010; Merritt & Vasiliev 2012). We find that NT precession and GR precession may have a large effect on the EKL mechanism, but tidal effects, scalar and vector resonant relaxation, and Lense-Thirring precession are typically less important. The timescale on which the EKL mechanism operates increases if the outer SMBH mass is reduced. Thus, GR precession may dominate over and quench the EKL mechanism most efficiently if the outer SMBH is less massive than the inner SMBH (see figure 2 in Naoz & Silk 2014). Similarly, we find that NT precession also suppresses the EKL mechanism most efficiently when the outer SMBH is less massive. Tidal disruption is expected in the opposite regime when the EKL mechanism is very prominent, i.e. when the outer SMBH is more massive than the inner SMBH. We identify the outcome of the EKL mechanism as a function of SMBHB parameters and quantify the TDE rate.

Our discussion is organized as follows. In §2, we describe the adopted methods. In §3, we characterize the parameter space to identify where the EKL mechanism is important. Then, we calculate the tidal disruption rate and discuss the final stellar distribution due to the EKL mechanism with an illustrative example in §4, and for stars surrounding an intermediate-mass black hole in §5. Finally, we summarize our main results in §6.

8.2 Method

We study the tidal disruption of stars due to the EKL mechanism in galaxies that host a SMBHB. The three-body system consists of an "inner binary" comprised of the SMBH and a star, and an "outer binary" comprised of the outer SMBH and the center mass of the inner binary, as shown in Figure 8.1. We denote the masses of the objects by m_1 (inner SMBH), m_2 (star), and m_3 (outer SMBH), and for orbital parameters we use subscript 1 and 2 for the inner and outer binary, respectively. In order for the EKL mechanism to operate, we require the triple system to be in a hierarchical configuration: the inner binary on a much tighter orbit than the third object, such that (e.g., Lithwick & Naoz 2011; Katz et al. 2011),

$$\epsilon = \frac{a_1}{a_2}\frac{e_2}{1-e_2^2} < 0.1\,, \tag{8.1}$$

where a and e are respectively the semimajor axis and eccentricity.

8.2.1 Comparison of Timescales

We examine the range of orbital parameters in oder to identify the regions in which the EKL mechanism may operate. The relevant processes' timescales can be expressed as:

$$t_K = \frac{2\pi a_2^3(1-e_2^2)^{3/2}\sqrt{(m_1+m_2)(1-e_1^2)}}{\sqrt{G}a_1^{3/2}m_3} \tag{8.2}$$

$$t_{oct} = \frac{1}{\epsilon}t_K \tag{8.3}$$

$$t_{GR1} = \frac{2\pi a_1^{5/2}c^2(1-e_1^2)}{3G^{3/2}(m_1+m_2)^{3/2}} \tag{8.4}$$

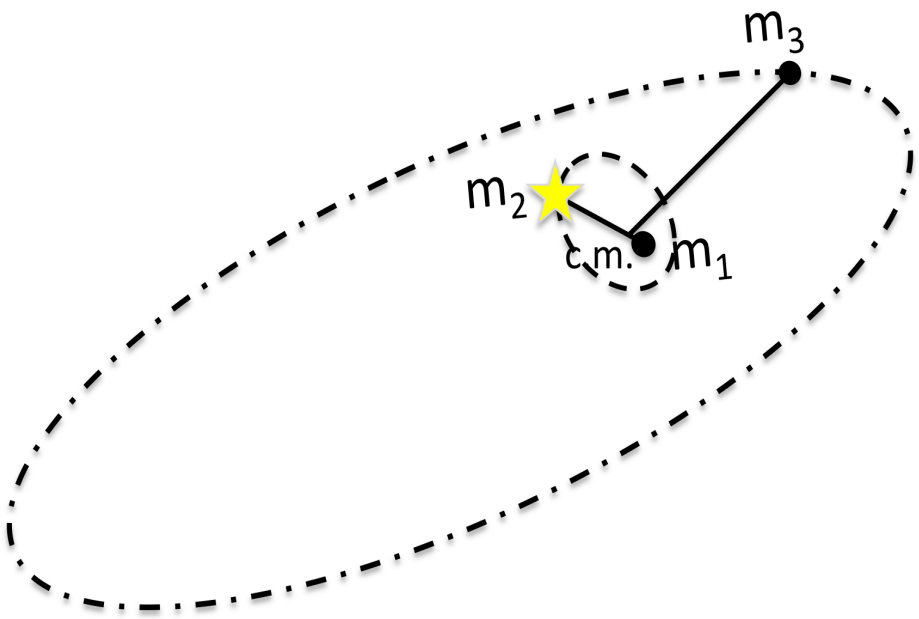

Figure 8.1: The system configuration. 'c.m.' denotes the center of mass of the inner binary, which contains the star (with mass m_2) and SMBH (with mass m_1). The other SMBH (with mass m_3) is on an outer orbit.

$$t_{GR2} = \frac{2\pi a_2^{5/2} c^2 (1-e_2^2)}{3G^{3/2}(m_1+m_2+m_3)^{3/2}} \tag{8.5}$$

$$t_{GR,int} = \frac{16}{9} \frac{a_2^3 c^2 (1-e_2^2)^{3/2} (m_1)^{3/2}}{\sqrt{a} e_1 \sqrt{1-e_1^2} G^{3/2} m_1^2 m_3} \tag{8.6}$$

$$t_{NT} = 2\pi \Big(\frac{\sqrt{G m_1 / a_1^3}}{\pi m_1 e_1} \int_0^\pi d\psi \, M_*(r) \cos\psi \Big)^{-1} \tag{8.7}$$

$$t_{RR,s} = \frac{4\pi\omega}{\beta_s^2 \Omega^2} \frac{m_1^2}{M_*(r) m_2} \tag{8.8}$$

$$t_{RR,v} = \frac{2\pi f_{vrr}}{\Omega} m_1 \frac{1}{\sqrt{M_*(r) m_2}} \tag{8.9}$$

$$t_{rel} = 0.34 \frac{\sigma^3}{G^2 \rho m_2 \ln\Lambda} \tag{8.10}$$

$$t_{LT} = \frac{a^3 c^3 (1-e^2)^{3/2}}{2G^2 m_1^2 s} \tag{8.11}$$

$$t_{GW} = \frac{a_2^4}{4} \frac{5}{64} \frac{c^5}{G^3 m_1 m_3 (m_1+m_3)} \, . \tag{8.12}$$

Here t_K is the quadrupole ($\mathcal{O}(a_1/a_2)^2$) Kozai timescale. Following Naoz et al. (2013b), t_{oct} is the octupole ($\mathcal{O}(a_1/a_2)^3$) Kozai timescale. t_{GR1} and t_{GR2} are the timescales of the first order post Newtonian general relativistic (GR) precession at the quadrupole order ($\mathcal{O}(a_1/a_2)^2$) on the inner and outer orbit, and $t_{GR,int}$ is the timescale associated with the first post-Newtonian order GR interaction between the inner and the outer orbit. Following Kocsis & Tremaine (2011), t_{NT} is the timescale of the Newtonian precession caused by the stellar potential, and $t_{RR,s}$ and $t_{RR,v}$ are the timescales of the scalar and vector resonant relaxation. t_{rel} is the two body relaxation timscale. t_{LT} is the Lense-Thirring precession timescale, and t_{GW} is the timescale of the orbital decay of the binary SMBHB due to gravitational wave radiation. For the resonant relaxation timescales, $M_*(r)$ is the mass of the stars interior to r, ω is the net rate of precession due to GR and NT, β_s is estimated to be 1.05 ± 0.02 by Eilon et al. (2009), Ω is the orbital frequency of the star, and f_{vrr} is estimated to be 1.2 by Kocsis & Tremaine (2014). For

the Lense-Thirring timescale, sGm_1^2/c is the spin angular momentum of the inner SMBH (see references in e.g., Naoz et al. 2013b; Kocsis & Tremaine 2011; Peters 1964). We define some of these effects in more detail in § 8.2.2 below.

The EKL mechanism operates if the following criteria are satisfied:

1. The three-body configuration satisfies the hierarchical condition ($\epsilon < 0.1$, see equation (8.1))
2. The stars stay in the Hill sphere of the inner SMBH in order for them to remain bound to it, i.e. $a_1(1+e_1) < a_2(1-e_2)(m_1/3m_3)^{1/3}$.
3. The quadrupole ($\mathcal{O}(a_1/a_2)^2$) Kozai timescale, t_K, needs to be shorter than the timescales of the other mechanisms that modify the orbital elements, otherwise the EKL mechanism is suppressed. The competing mechanisms include Newtonian precession (NT), general relativistic precession (GR), scalar resonant relaxation, vector resonant relaxation, two-body relaxation, Lense-Thirring precession, and the gravitational radiation.

Note that the secular approximation fails when the perturbation from the outer SMBH is too strong or when the eccentricity reaches values very close to unity (e.g., Antonini & Perets 2012; Katz & Dong 2012; Antognini et al. 2014; Antonini et al. 2014; Bode & Wegg 2013). This means that there are some systems that are poorly described by our approximation. However, we expect that those systems reach even higher eccentricities than the one predicted by the octupole approximation (e.g., Antognini et al. 2013), and thus our overall qualitative conclusions may hold even for those systems, but the quantitative rate values possibly underestimate the true rates.

To calculate the Newtonian timescale, the resonant relaxation timescales, and the two body relaxation timescale, we adopt the spherically symmetric model for the stellar density discussed in O'Leary et al. (2009). Specifically, the stellar density distribution is a power law of semimajor axis and the normalization is fixed by the $M-\sigma$ relation,

$$\rho_*(r) = \frac{3-\alpha}{2\pi}\frac{m_1}{r^3}\left(\frac{GM_0(m_1/M_0)^{1-2/k}}{\sigma_0^2\, r}\right)^{-3+\alpha}, \tag{8.13}$$

where $k=4$, $M_0 = 1.3\times10^8 M_\odot$, $\sigma_0 = 200$km/s (Tremaine et al. 2002), and we set $\alpha = 1.75$.

Figure 8.2 shows the timescales for the case of a $1\,M_\odot$ star orbiting a $10^7\,M_\odot$ SMBH. The separation of the SMBHB is set to 0.3 pc. The upper panel corresponds to $m_3 = 10^6\,M_\odot$, and the lower panel corresponds to $m_3 = 10^9\,M_\odot$. For the Lense-Thirring timescale, s is set to unity. The eccentricity of the star-SMBH system, e_1, is assumed to be 2/3 and e_2 is assumed to be 0.7. The EKL-dominated region is larger for higher e_2 with fixed a_1 and a_2. Figure 8.2 shows that the EKL mechanism is suppressed for a 10^7–$10^6\,M_\odot$ binary at all radii, but it may operate at least in a restricted range for a 10^7–$10^9\,M_\odot$ binary. Note that although the octupole timescale t_{oct} is longer than some of the other secular timescales, our simulations show that the eccentricity can nevertheless reach high values provided that t_K is the shortest timescale and t_{oct} is at most moderately larger than the other timescales. Thus, in the following, we identify the regions where the eccentricity may be excited using conditions 1–3 above irrespective of t_{oct}. Typically, the conditions on the quadrupole Kozai timescale ($t_K < t_{GR}$ and $t_K < t_{NT}$) set the lower limit for a_1 for a fixed a_2, and the hierarchical configuration $\epsilon < 0.1$ and the Hill sphere limit set the upper limit on a_1.

Next, we examine the $a_1 - a_2$ parameter space to identify the parameters where

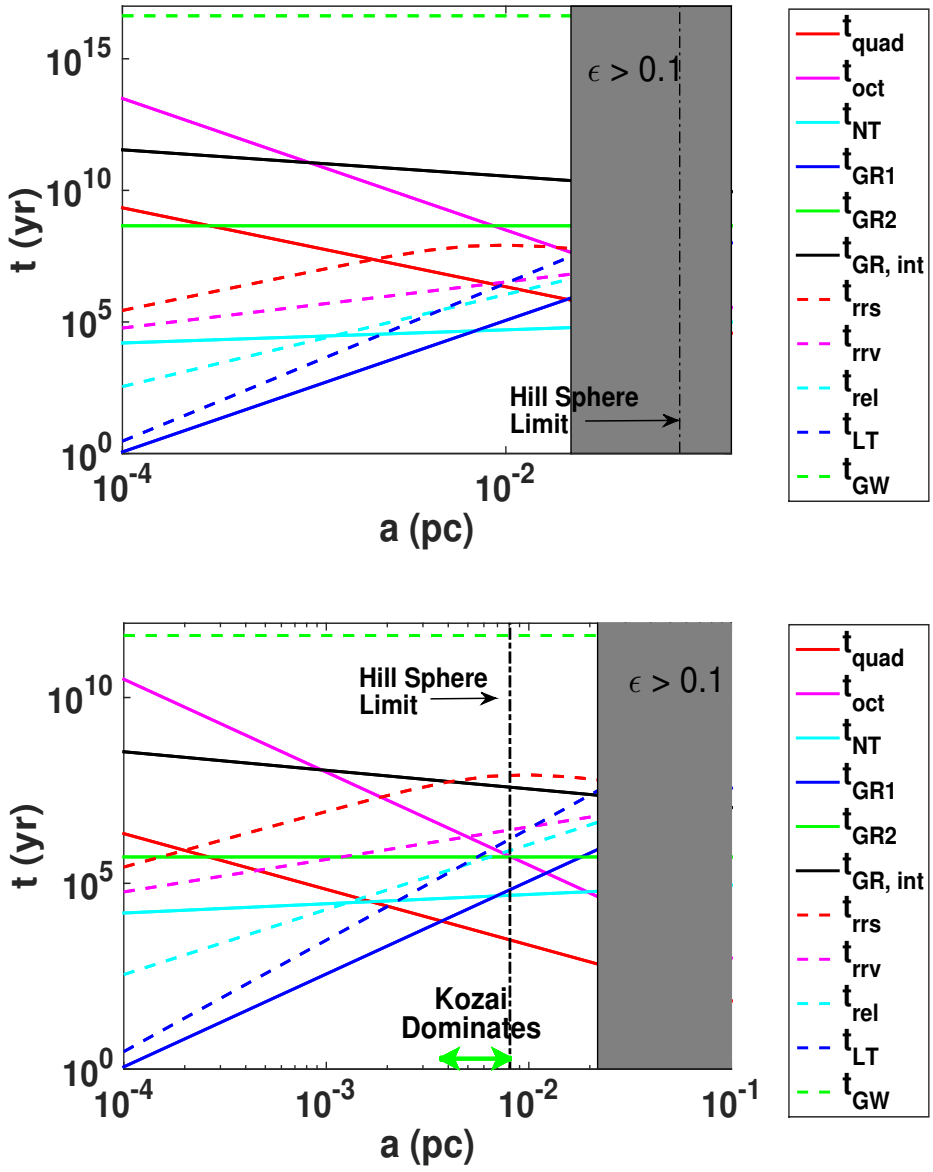

Figure 8.2: The different timescales as a function of the semi major axis of the stars (a_1), where $e_1 = 2/3$, $m_1 = 10^7 M_\odot$, $a_2 = 0.3$ pc, $m_2 = 1 M_\odot$, $e_2 = 0.7$. In the upper panel, $m_3 = 10^6 M_\odot$, and in the lower panel, $m_3 = 10^9 M_\odot$. In the grey region, $\epsilon > 0.1$, the hierarchical approximation is violated. The EKL mechanism does not operate in the grey region and wherever t_{quad} is not the shortest timescale. The quadrupole Kozai timescale is shorter than the other timescales for the semimajor axis range indicated by the light green arrow.

EKL dominates. We plot two examples in Figure 8.3: $m_1 = 10^7\,M_\odot$, $m_2 = 1\,M_\odot$, $m_3 = 10^6\,M_\odot$, $e_2 = 0.7$ in the upper panel, and $m_1 = 10^7\,M_\odot$, $m_2 = 1\,M_\odot$, $m_3 = 10^9\,M_\odot$, $e_2 = 0.7$ in the lower panel. The EKL-dominated region is bigger for larger e_2. To test the dependence on e_1, we include two extreme e_1 values: $e_1 = 0$ (solid lines) and $e_1 = 0.999$ (dashed lines). The parameter space is independent of the mass of the star as long as $m_2 \ll m_1$. The EKL-dominated region is bounded by $t_K = t_{GR}$ (blue line) and $t_K = t_{NT}$ (red line) from above and by the Hill sphere limit (grey line) and the hierarchical condition (black line) from below. In the upper panel, there is no region where the EKL mechanism dominates. In the lower panel, the region where EKL dominates is shaded with horizontal dashed lines for $e_1 = 0.999$ and it is shaded with vertical solid lines for $e_1 = 0$.

We calculate the number of stars affected by the EKL mechanism for the particular stellar density distribution around the inner SMBH (equation (8.13)). In Figure 8.4, we consider the parameter space of different m_1, m_3, a_2, e_2 and show the number of stars in the range of a_1 where all criteria are satisfied for the EKL mechanism to operate. Each panel shows the parameter plane of m_1 and m_3 (assuming $m_2 \ll m_1$), a_2 is varied in different columns of panels from 0.1 to 10 pc, and e_2 is varied in the different rows from 0.1 to 0.7. We set the stellar eccentricity to its typical value $e_1 = 2/3$ in all panels. In regions where the EKL mechanism is important, approximately 10^{5-6} stars are affected. Thus, the EKL mechanism may significantly contribute to the tidal disruption events. Note that the EKL mechanism is more likely to be suppressed for stars orbiting around the more massive SMBH. However, for parameters where the EKL mechanism is not suppressed everywhere around the more massive inner SMBH, the total number of stars affected by EKL may be higher for stars orbiting the more massive SMBH than for those

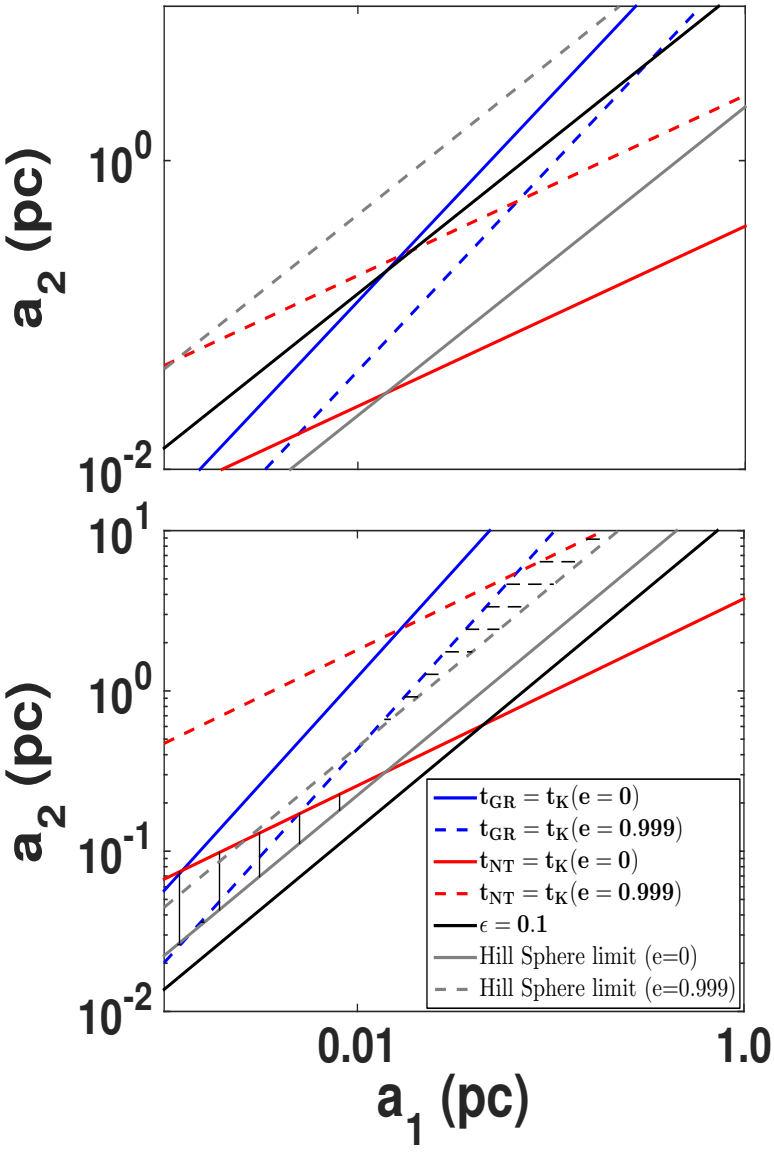

Figure 8.3: The $a_1 - a_2$ parameter space, $m_1 = 10^7 M_\odot$, $m_2 = 1 M_\odot$, $e_2 = 0.7$. In the upper panel, $m_3 = 10^6 M_\odot$, and in the lower panel, $m_3 = 10^9 M_\odot$. The solid blue and red lines represent $e_1 = 0$ and the dashed blue and red lines represent $e_1 = 0.999$. Above the red or blue lines, the EKL mechanism is suppressed by the GR or the Newtonian precession. Below the black line or the grey lines, the hierarchical configuration or the Hill sphere limit is violated. The EKL mechanism is suppressed everywhere in the upper panel, and the EKL mechanism dominates in the shaded regions in the lower panel.

orbiting the less massive SMBH.

8.2.2 Equations of Motion

As shown in the previous section, GR and NT precessions represent important limitations for the EKL mechanism. In this section, we review the equations of motion which govern the long-term evolution of stars due to the EKL mechanism, GR and NT precessions, and tidal effects adopted from Naoz et al. (2013a,b) and Tremaine (2005). We use the Delaunay's elements, which provide a convenient dynamical description of hierarchical three-body systems. The coordinates are the mean anomalies, l_1 and l_2, the arguments of periastron, g_1 and g_2, and the longitude of nodes, h_1 and h_2. Their conjugate momenta are

$$L_1 = \frac{m_1 m_2}{m_1 + m_2}\sqrt{G(m_1 + m_2)a_1} \tag{8.14}$$

$$L_2 = \frac{m_3(m_1 + m_2)}{m_1 + m_2 + m_3}\sqrt{G(m_1 + m_2 + m_3)a_2}$$

$$G_1 = L_1\sqrt{1 - e_1^2}, G_2 = L_2\sqrt{1 - e_2^2} \tag{8.15}$$

$$H_1 = G_1 \cos i_1, \quad H_2 = G_2 \cos i_2, \tag{8.16}$$

where i denotes the inclination relative to the total angular momentum of the three-body system and G without subscript is the gravitational constant. To leading order, the two binaries follow independent Keplerian orbits where l_j are rapidly varying and L_j, G_j, H_j, g_j, and h_j are conserved for $j \in \{1, 2\}$. These quantities are slowly varying over longer timescales due to the superposition of the perturbations: the EKL mechanism, GR and NT precessions, and tidal effects, discussed next.

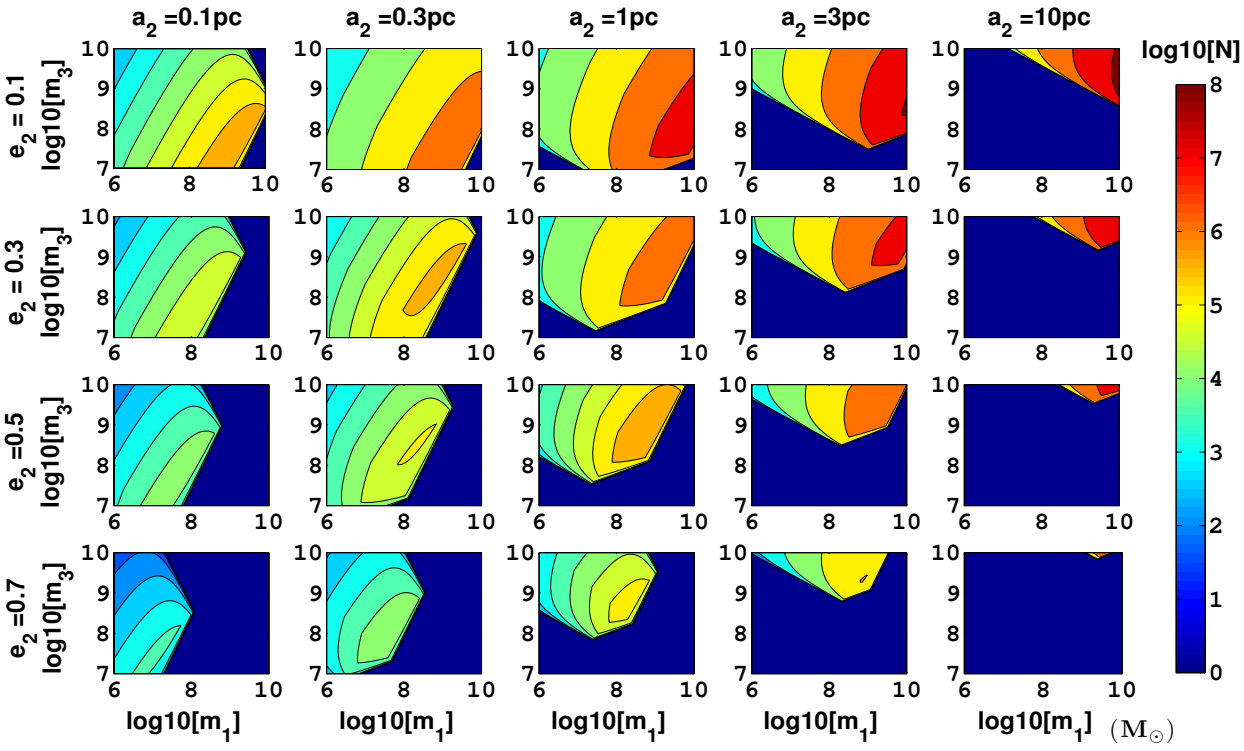

Figure 8.4: The number of stars (N) influenced by the EKL mechanism, assuming a stellar density distribution in equation (8.13), and that the stellar mass is negligible and $e_1 = 2/3$. We determine the range of stellar semimajor axis a_1 where the EKL mechanism operates for a fixed set of SMBH masses, m_1, m_3, and outer orbital parameters, e_2 and a_2. Plotting the corresponding number of stars as a function of m_1 and m_3 for an array of e_2 and a_2 as shown, captures a large parameter space. The EKL mechanism affects a large number of stars over a wide range of SMBH binary parameters when $a_2 \lesssim 3$ pc.

Eccentric Kozai-Lidov Mechanism

The equations of motion for the EKL mechanism may be derived using the double averaged Hamiltonian (i.e. averaged over the rapidly varying l_1 and l_2 elements). We go beyond the analyses of Chen et al. (2011) and Wegg & Bode (2011), who considered only the quadrupole ($\mathcal{O}(a_1/a_2)^2$) Kozai-Lidov mechanism, where the z-component of angular momentum is constant. This assumption does not hold when the orbit of the SMBHB is eccentric, and one needs to include the octupole order terms ($\mathcal{O}(a_1/a_2)^3$) (e.g. Naoz et al. 2013a). The Hamiltonian can be decomposed as

$$\begin{aligned}\mathcal{H}_{Kozai,quad} &= C_2\{(2+3e_1^2)(3\cos^2 i_{tot}-1) \\ &\quad + 15e_1^2\sin^2 i_{tot}\cos 2g_1\} \qquad (8.17)\\ \mathcal{H}_{Kozai,oct} &= \frac{15}{4}\epsilon_M e_1 C_2\{A\cos\phi + 10\cos i_{tot}\sin^2 i_{tot} \\ &\quad \times (1-e_1^2)\sin g_1 \sin g_2\}, \qquad (8.18)\end{aligned}$$

where

$$\epsilon_M = \frac{m_1-m_2}{m_1+m_2}\epsilon \qquad (8.19)$$

$$C_2 = \frac{G^2}{16}\frac{(m_1+m_2)^7}{(m_1+m_2+m_3)^3}\frac{m_3^7}{(m_1m_2)^3}\frac{L_1^4}{L_2^3G_2^3} \qquad (8.20)$$

$$A = 4+3e_1^2-\frac{5}{2}B\sin^2 i_{tot} \qquad (8.21)$$

$$B = 2+5e_1^2-7e_1^2\cos 2g_1 \qquad (8.22)$$

$$\cos\phi = -\cos g_1\cos g_2 - \cos i_{tot}\sin g_1\sin g_2 \qquad (8.23)$$

The equations of motion for the EKL mechanism are given by Hamilton's equations (eqn (A26-35) in Naoz et al. 2013a).

GR Effects

Next, we consider the leading order (first Post-Newtonian, 1PN) effects of GR. We follow Naoz et al. (2013b), who derived the double averaged 1PN Hamiltonian to the octupole ($\mathcal{O}(a_1/a_2)^3$) order. The Hamiltonian consists of four terms: $\mathcal{H}_{a_1}$, $\mathcal{H}_{a_2}$, $\mathcal{H}_{a_1a_2}$, $\mathcal{H}_{int}$ (Naoz et al. 2013b). Here $\mathcal{H}_{a_1a_2}$ does not contribute to the dynamical evolution, and the long-term effect of $\mathcal{H}_{int}$ is typically negligible, as its timescale is longer than that of the Kozai timescale and the GR precession of the inner and outer orbit as long as the star stays within the Hill sphere of the inner SMBH. Thus, we only consider the effects of $\mathcal{H}_{a_1}$ and $\mathcal{H}_{a_2}$ which cause the GR precession of the arguments of periapsides,

$$\frac{dg_1}{dt}\Big|_{1PN,a_1} = -\frac{3G^{3/2}(m_1+m_2)^{3/2}}{a_1^{5/2}c^2(1-e_1^2)}\,, \tag{8.24}$$

$$\frac{dg_2}{dt}\Big|_{1PN,a_2} = -\frac{3G^{3/2}(m_1+m_2+m_3)^{3/2}}{a_2^{5/2}c^2(1-e_2^2)}\,. \tag{8.25}$$

Given that we neglect $\mathcal{H}_{int}$, and higher order Post-Newtonian corrections such as Lense-Thirring precession and gravitational radiation, the other conserved quantities, L_j, G_j, H_j, h_j, are not effected for $j \in \{1,2\}$.

NT Precession

The Newtonian potential of a spherical stellar cusp causes apsidal precession at the rate (Tremaine 2005):

$$\dot{g}_{1,NT} = \frac{(1-e_1^2)^{1/2}}{(Gm_1/a_1^3)^{1/2}a_1e_1}\frac{d\Phi_*}{dr}\cos\psi, \tag{8.26}$$

where Φ_* is the stellar potential, r is the distance to the central SMBH and ψ is the true anomaly of the inner orbit. The averaged precession rate of g_1 due to Newtonian

precession is expressed below:

$$\dot{g}_{1,NT} = \frac{(Gm_1/a_1^3)^{1/2}}{\pi m_1 e_1} \int_0^\pi d\psi \, M_*(r) \cos\psi, \tag{8.27}$$

where $M_*(r)$ is the mass of the stellar system interior to r and $r \equiv r(\psi) = a_1(1-e_1^2)/(1+e\cos\psi)$ from Kepler's equation. Explicit analytic expressions for the apsidal precession rate are given in Appendix A of Kocsis & Tremaine (2014).

Tidal Dissipation

To investigate if tides can suppress eccentricity excitation, we consider the "equilibrium tide" with constant time lag to calculate the inner binary's orbital evolution when the pericenter distance is larger than $2R_t$. Similarly to Naoz et al. (2012) and Naoz & Fabrycky (2014), we include the differential equation governing the orbital evolution following Eggleton et al. (1998); Eggleton & Kiseleva-Eggleton (2001) and Fabrycky & Tremaine (2007). For the star, we assume the viscous timescale is 10 yr, which corresponds to the quality factor (Goldreich & Soter 1966) $Q \sim 10^5$ for a 10 day orbit (or $Q \sim 4 \times 10^8$ for a 100 year orbit).

In Figure 8.5 we show a representative example of the evolution with and without tides. The effect of tides is negligible mainly because the orbital period is long and Q is low.

8.3 SMBH-binary System

Requiring the criteria listed in §8.2.1, the minimum and the maximum distance of the star affected by the EKL mechanism from the inner SMBH can be calculated. However,

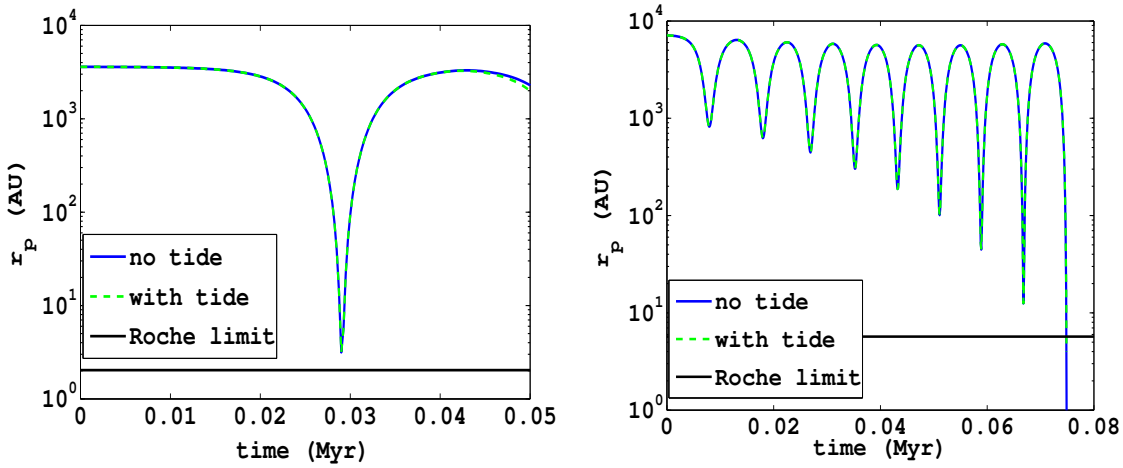

Figure 8.5: Comparison of the runs with tidal effects and the runs with no tidal effects. The dashed green line indicates the case with tidal effects and the blue lines indicates the case without tidal effects. The two lines are nearly identical, suggesting that tidal effects are negligible in these runs. The left panel shows a case when a 1 $M_\odot$ star orbits around a $10^7 M_\odot$ SMBH with $a_1 = 0.017$ pc and $e_1 = 0.001$, and is perturbed by a $10^9 M_\odot$ outer SMBH with $a_2 = 1$ pc. The right panel shows a case when a 10 $M_\odot$ star orbits around a $10^7 M_\odot$ SMBH with $a_1 = 0.035$ pc and $e_1 = 0.01$, and is perturbed by a $10^9 M_\odot$ outer SMBH with $a_2 = 1$ pc, $e_2 = 0.7$. We used the constant time lag prescription for the tides, and the quality factor Q was set to $\sim 10^5$ for a 10 day orbit ($Q \sim 4 \times 10^8$ for a 100 year orbit).

not all stars in this region will be disrupted, since the excitation of the eccentricity depends sensitively on the orbital orientation, and the parameter region where the eccentricity can be excited is complicated (Li et al. 2014b). In addition, when the Kozai timescale is only slightly smaller than the GR or the NT timescale (with t_K still being the smallest), the evolution of the inner orbit is complex. For instance, the eccentricity of the inner orbit can be excited in configurations where the eccentricity cannot be excited due to the Kozai-Lidov mechanism alone. This excitation may be caused by the resonances between the NT, GR or Kozai-Lidov precessions (Naoz et al. 2013b).

We consider the following illustrative example: $m_1 = 10^7 M_\odot$, $m_2 = 10^8 M_\odot$, $a_2 = 0.5$ pc, $e_2 = 0.5$. We adopt the isotropic stellar distribution function of equation (8.13), assuming the stars have a solar mass, and that the eccentricity distribution is thermal ($dN/de = 2e$). We run large Monte-Carlo simulations, integrating the equations presented in §8.2, where the equations of motion for the EKL mechanism are given by Hamilton's equations (eqs. (A26-35) in Naoz et al. 2013a), and $\dot{g}_1 = \dot{g}_{1,EKL} + \dot{g}_{1,GR} + \dot{g}_{1,NT}$, $\dot{g}_2 = \dot{g}_{2,EKL} + \dot{g}_{2,GR}$. We distinguish three outcomes for the EKL evolution: "TDE", "scattered by the SMBH companion", and "surviving", as explained now.

The eccentricity of the star needs to reach very close to unity to cause tidal disruption. The tidal radius is $R_t = 5 \times 10^{-6}$ pc around a $10^7 M_\odot$ SMBH. We identify the TDE with $a_1(1 - e_1) < 3R_t$, since the stars may still be disrupted due to accumulated heating under the strong tide outside the tidal radius (Li & Loeb 2013). Since the size of the Hill sphere of the less massive SMBH is small (i.e. 0.08 pc in our example), the star may reach the apocenter outside the Hill sphere before disruption as the eccentricity increases. Namely, the gravitational pull of the companion SMBH (m_3) will be larger than m_1. We refer to this as a "scattering event" ($a_1(1 + e_1) > a_2(1 - e_2)(m_1/(3m_3))^{1/3}$).

Note that the secular approximation is no longer valid for the scattering events. Three-body integrations of the dynamical evolution of scattering events show that they may either lead to an exchange interaction, where the star is captured by the outer SMBH, they may cause the ejection of the star producing a hyper-velocity star (Samsing 2014; Guillochon & Loeb 2014), or they may be tidally disrupted. The scattering events resulting in a capture may systematically increase the eccentricity distribution of stars orbiting the companion SMBH. For the third category, we label the stars neither disrupted nor scattered by the companion after 1 Gyr as "survivors".

Figure 8.6 shows the results of the numerical simulation in the final $a_1 - i$ and $a_1 - e_1$ planes. We use open circles to mark stars that underwent TDEs, crosses for stars that were scattered by the companion, and full circles for stars that survived. The disruption/scattering time is color coded, and it indicates that most of the disruption events occur within ~ 0.5 Myr. This corresponds to the octupole Kozai timescale, which is roughly $0.2 - 2$ Myr for these systems at $a_1 = 0.03 - 0.08$ pc. Out of all 1,000 stars between $a_1 = 0.0275$ pc and 0.075 pc, 57 are disrupted, and 726 are scattered by the outer black hole. According to the stellar density distribution in equation (8.13), there are $\sim 10^5$ stars in this semi-major axis range. Normalized by the total number of stars in this semi-major axis range, it indicates that the tidal disruption rate is $\sim 10^{-2}$/yr in the first ~ 0.5 Myr for the less massive black hole due to EKL, while $\sim 7 \times 10^4$ stars undergo scattering events by the outer SMBH.

Since the eccentricity of the stars with high inclinations are more likely to be excited, the stars with high inclinations are more vulnerable to tidal disruption, the final inclination distribution is no longer isotropic (the lower panels in Figure 8.7) and the stars around the SMBH form a torus-like configuration (see Naoz & Silk (2014) for

similar results). The stars with larger semi major axis have higher probability to be scattered when their eccentricity become excited due to the EKL mechanism, and thus the final distribution of stars surrounding the less massive black hole will be truncated at a larger semimajor axis. In addition, the distribution of the eccentricity of the surviving stars shows deviations from thermal distribution with a suppression of very eccentric stars (as expected since they get scattered by m_3 more easily, and their eccentricity can be excited more easily at a lower inclination (Li et al. 2014a)). Furthermore, as shown in Figure 8.8, the stars that are closer to m_1 ($\lesssim 0.04$ pc) have an eccentricity distribution closer to thermal. The stars that are closer to m_3 ($\gtrsim 0.04$ pc) have systematically smaller eccentricities. The thermal distribution for closely separated stars ($\lesssim 0.04$ pc) is similar to the observed S stars in the center of the Milky-Way galaxy (Genzel et al. 2010), which shows a steeper slope.

8.4 SMBH-IMBH System

Let us consider next the perturbations of a SMBH on stars orbiting an intermediate mass black hole (IMBH). IMBHs may form through runaway mergers during core collapse in globular clusters (Portegies Zwart & McMillan 2002). Since globular clusters sink to the galactic center through dynamical friction, and the disrupted globular cluster could contribute to most of the mass in nuclei stellar cluster for galaxies with total mass below $10^{11}M_{\odot}$, this setup may be common in the Universe(Portegies Zwart et al. 2006; Antonini 2013; Gnedin et al. 2014). Alternatively, IMBH may form at cosmologically early times from population III stars in galactic nuclei (Madau & Rees 2001), or in accretion disks around SMBHs (Goodman & Tan 2004; McKernan et al. 2012, 2014).

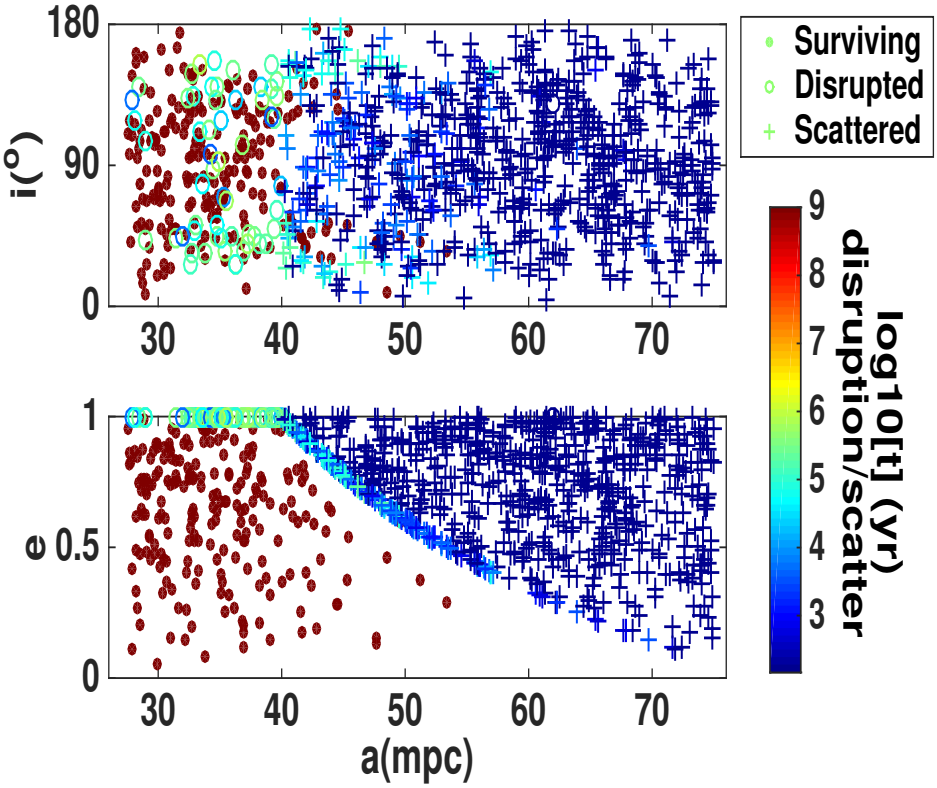

Figure 8.6: The outcome of the evolution around a SMBH binary with $m_1 = 10^7 M_\odot$, $m_3 = 10^8 M_\odot$, $a_2 = 0.5$ pc, $e_2 = 0.5$. We plot the final i_1 versus a_1 and e_1 versus a_1 for stars that survived, were disrupted, or were scattered in the simulation after 1 Gyr. The color code indicates the time when the star is disrupted or is scattered. Out of the 1,000 stars between $a_1 = 0.0275$ pc and 0.075 pc, 57 are disrupted, and 726 are scattered by the outer black hole. The number of stars in this range according to the distribution of equation (8.13) is $\sim 10^5$ (assuming the stars are 1 solar mass). This suggests that the tidal disruption rate is $\sim 10^{-2}$/yr in the first ~ 0.5 Myr for the less massive black hole.

In the Milky Way center, the orbits of the S-stars are consistent with that caused by the dynamical interactions of IMBHs (Merritt et al. 2009). In addition, IRS 13E may potentially host an IMBH, though its existence is controversial (Maillard et al. 2004; Schödel et al. 2005; Fritz et al. 2010). The TDE rate has been discussed by Chen & Liu (2013) and Mastrobuono-Battisti et al. (2014). Here, we consider the interactions of stars surrounding IMBHs in the center of galaxies with the central SMBH due to the hierarchical three body interactions, and consider the re-distribution of the stars as a result of the interaction.

We set the IMBH mass to $10^4 M_\odot$ at a distance of 0.1 pc from Sgr A* ($a_2 = 0.1pc$, $e_2 = 0.7$, $m_1 = 10^4 M_\odot$ and $m_3 = 4 \times 10^6 M_\odot$). These parameters for the IMBH are allowed according to limits on the astrometric wobble of the radio image of Sgr A* (Hansen & Milosavljević 2003; Reid & Brunthaler 2004), the study of hypervelocity stars (Yu & Tremaine 2003), and the study of the orbits of S stars (Gualandris & Merritt 2009). We set the distance of stars to be uniformly distributed between 0.00045 pc and 0.0028 pc. The tidal disruption radius for $1\,M_\odot$ stars is 4.89×10^{-7} pc. The minimum distance is set by requiring the GR precession timescale to be longer than the Kozai timescale, and the maximum distance is set by requiring the stars to stay in the Hill sphere of the IMBH. Note that in this case the hierarchical criterion 1 in Sec. 8.2.1, $\epsilon < 0.1$, is satisfied as long as the stars are within the IMBH's Hill sphere. We assume the distribution of the stellar eccentricity to be uniform. We take into account GR precession, NT precession and EKL at octupole order in the integration.

In $1,000$ runs, we find that ~ 40 end up in tidal disruption and ~ 500 are scattered as shown in Figure 8.9. The tidal disruption/scattering time (color coded) is around 10^5 yrs. As shown in Figure 8.10, we predict that the surviving stars form a torus-like

configuration (similarly to the result achieved by Naoz & Silk (2014) for dark matter particles). The predicted distribution may be resolved if the angular resolution of the instrument is better than that corresponding to the Hill sphere around the IMBH, in this case 0.07 arcsec. This can be achieved in near infrared by the Gemini, VLT and Keck telescopes. In addition, the EKL mechanism also produces scattering events which may be responsible for the observed hypervelocity stars. The TDE rate may reach $\sim 10^{-4}$/ yr for a short $\sim 10^5$ yr duration episode after the globular cluster first approaches the galactic nucleus at a distance of 0.1 pc, assuming there are ~ 200 stars in a globular cluster around an $10^4 M_{\odot}$-IMBH in the EKL-dominated region according to the density distribution in equation (8.13).

8.5 Conclusion

SMBH binaries are natural outcomes of galaxy mergers. An SMBH binary may show an enhanced TDE rates due to the eccentric Kozai-Lidov (EKL) mechanism and chaotic three body interactions (Ivanov et al. 2005; Chen et al. 2009, 2011; Wegg & Bode 2011). The higher tidal disruption rates may in turn serve as a flag to identify closely separated black hole binaries on subparsec scale, which are difficult to detect otherwise. We focused on the effect of the EKL mechanism (see Naoz et al. 2011, 2013a) on the surrounding stars in SMBHB. This mechanism can excite the stars' eccentricity to values very close to unity (e.g., Naoz et al. 2013a,b; Li et al. 2014a; Li et al. 2014b). We identified the range of physical parameters where EKL is important.

We first compared the Kozai timescale with the secular timescales of other mechanisms that may suppress EKL in galactic nuclei. These include Newtonian (NT)

precession, general relativistic (GR) precession, resonant relaxation, two body relaxation, Lense-Thirring precession and orbital decay due to gravitational wave emission. We have found that for the SMBHB cases we considered, NT precession and GR precession may suppress EKL, especially when the inner SMBH is more massive than the outer SMBH (as shown in Figure 8.4). This is consistent with the results by Naoz & Silk (2014) for dark matter particles around SMBH binaries, as well as the three body scattering experiments done by Chen et al. (2009); Wegg & Bode (2011); Chen et al. (2011), who observed that the tidal disruption events were dominated by the three body chaotic interactions rather than EKL mechanism for stars surrounding the more massive black hole. However, we found that a massive outer binary allows a non-negligible region of parameter space where the EKL mechanism may operate and lead to TDEs. We also demonstrated that tidal effects are typically negligible for the stellar orbital evolution (see Figure 8.5).

To illustrate the EKL effects on stars surrounding the less massive black hole, we ran 1,000 numerical experiments with different initial conditions for a star cluster surrounding a $10^7 M_\odot$ black hole, which is being perturbed by a $10^8 M_\odot$ outer black hole. We have found over ~ 50 out of the 1,000 runs stars are disrupted in ~ 0.5 Myr. Scaled with the total number of stars according to equation (8.13), this corresponds to a TDE rate of 10^{-2}/yr for the first ~ 0.5 Myr. In contrast, Chen et al. (2011) considered tidal disruption rates for stars surrounding the more massive SMBH, using numerical three body scattering experiments. They estimated the tidal disruption rate to be as high as 0.2 per year mainly due to three-body scattering effects[†], in the first 3×10^5 yrs for stars

[†]since, as we showed, the EKL is suppressed in this case

surrounding a $10^7 M_\odot$ SMBH perturbed by an 81 times less massive outer SMBH. For the same SMBHB configuration, EKL only affects at most $\sim 10^3$ stars surrounding the less massive SMBH as shown in Figure 8.4, and affects at most $\sim 10^3$ stars surrounding the more massive SMBH. Thus, EKL contributes negligibly to the total tidal disruption rate in this case, but EKL contributes significantly to the TDE rate of stars around the secondary SMBH.

The EKL mechanism also affects the stellar distribution for stars surrounding the less massive SMBH. As shown in Figure 8.7, the survived stars within a particular range of radii are distributed in the shape of a torus (Naoz & Silk 2014). In addition, a large number of stars orbiting the less massive black hole will be scattered by the outer black hole following the EKL-induced eccentricity increase. In our illustrative example, ~ 670 out of 1000 stars are eventually transferred to an orbit around the outer, more massive SMBH. This may produce hyper-velocity stars (Guillochon & Loeb 2014).

Finally, we studied the tidal disruption of stars by an IMBH during mergers of globular clusters with galactic nuclei. For an IMBH of mass $10^4\,M_\odot$ at a distance of 0.1 pc from Sgr A*, 4% of stars get disrupted within the relevant distance range around the IMBH, and $\sim 50\%$ get scattered within 10^5 yrs. This yields a tidal disruption rate of $\sim 10^{-4}$/yr. Some of the scattering events may produce hypervelocity stars or additional TDEs. The EKL mechanism produces a torus-like stellar distribution for the surviving stars, which may be resolved by the Gemini, VLT and Keck telescopes in near infrared. Further investigations of this process using numerical scattering experiments would be a worthwhile in the future.

Acknowledgments

This work was supported in part by NSF grant AST-1312034. BK was supported in part by the W.M. Keck Foundation Fund of the Institute for Advanced Study and NASA grants NNX11AF29G and NNX14AM24G. The numerical calculations were performed at the Harvard-Smithsonian Center for Astrophysics, the Institute for Theory and Computation, on Harvard Odyssey cluster.

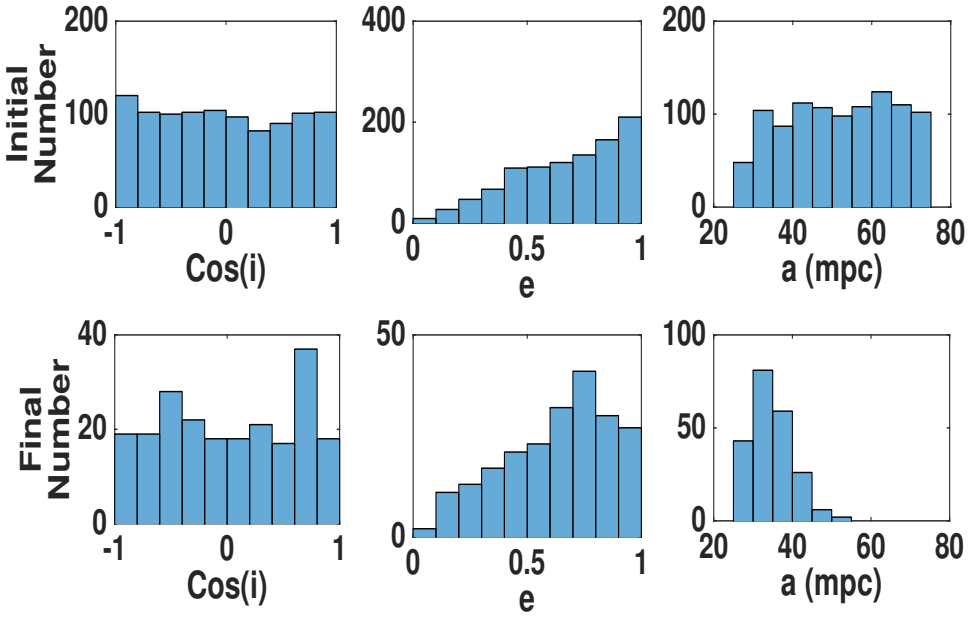

Figure 8.7: The initial distribution and the final distribution of the stars after 1 Gyr in our illustrative example shown in Figure 8.6. The final distribution represent the surviving stars.

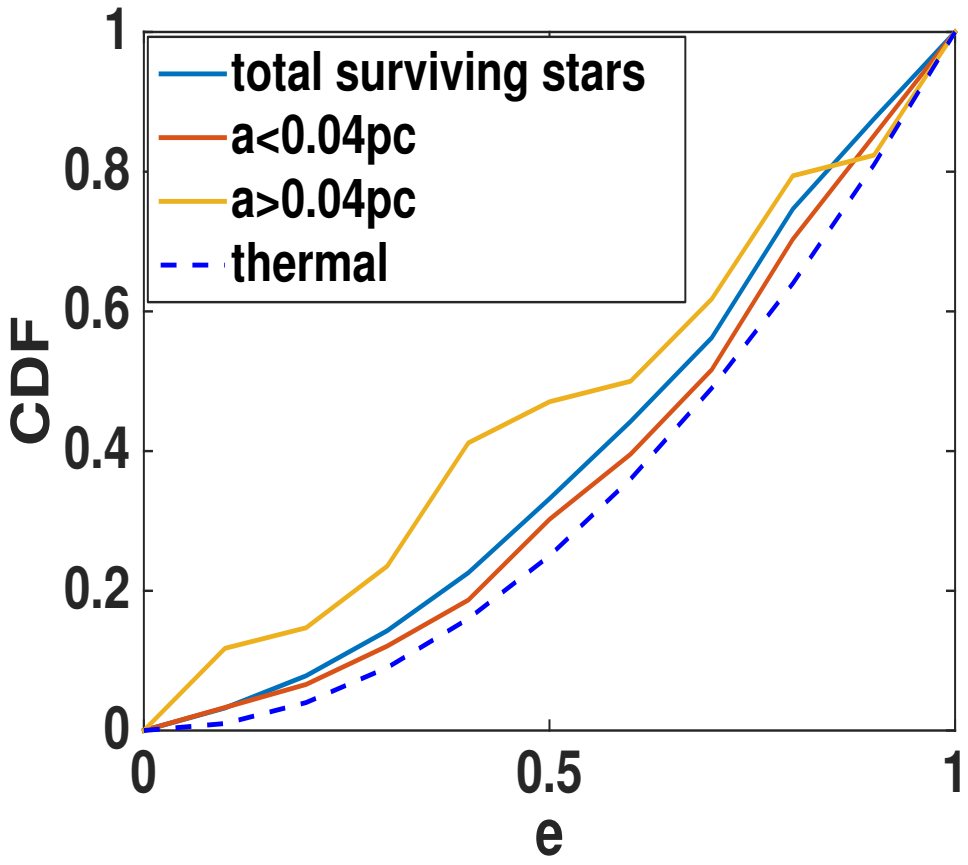

Figure 8.8: The final cumulative distribution of the eccentricity of stars in our illustrative example for $m_1 = 10^7 M_\odot$, $m_3 = 10^8 M_\odot$ separated by 0.5 pc in an eccentric orbit with $e_2 = 0.5$. For stars at distance larger than 0.04 pc, the final eccentricity distribution becomes shallower than that inside of 0.04 pc.

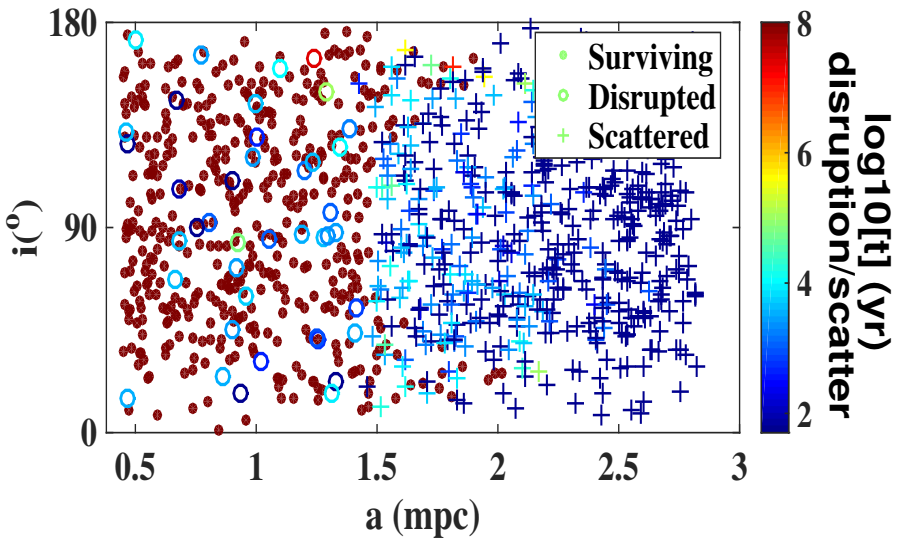

Figure 8.9: The final distribution of stars surrounding a $10^4 M_\odot$ IMBH at a distance of 0.1 pc from Sgr A^* after 100 Myr. The open circles represent stars that get tidally disrupted, and the crosses represent stars that get scattered. Both are colored according to the time of tidal disruption/scattering. We find that $\sim$ 50% of the stars survived tidal disruption and scattering. The final distribution of the star has a deficiency at high inclination relative to the orbital plane of IMBH.

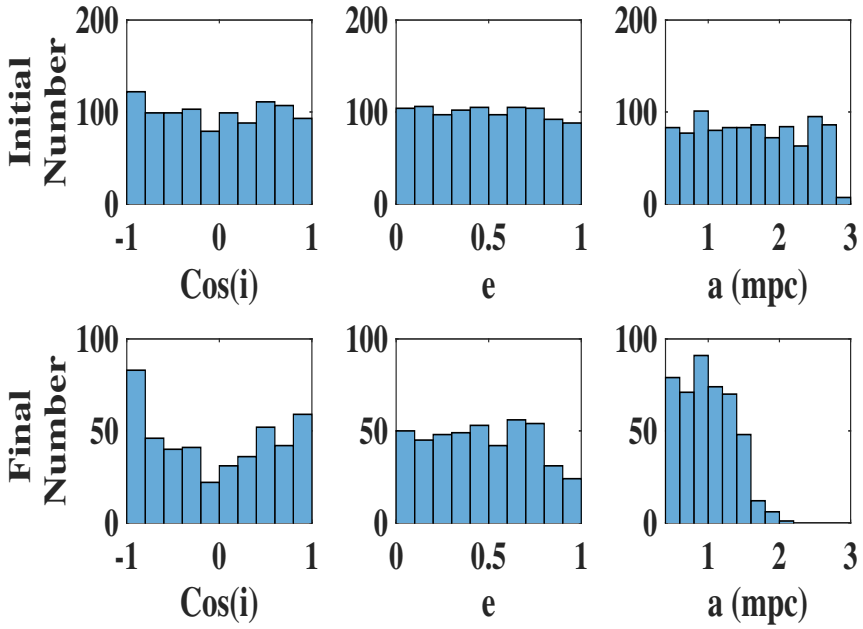

Figure 8.10: The initial distribution and the final distribution of the stars after 100Mr in our illustrative example for the IMBH, as shown in Figure 8.9.

Chapter 9

Accumulated Tidal Heating of Stars Over Multiple Pericenter Passages Near SgrA*

This thesis chapter originally appeared in the literature as

Li, G. & Loeb, A. Accumulated Tidal Heating of Stars Over Multiple Pericenter Passages Near SgrA*, *Monthly Notices of the Royal Astronomical Society*, 429, 3040, 2013

It is presented here with minor modifications.

Abstract

We consider the long-term tidal heating of a star by the supermassive black hole at the Galactic center, SgrA*. We show that gravitational interaction with background stars

leads to a linear growth of the tidal excitation energy with the number of pericenter passages near SgrA*. The accumulated heat deposited by excitation of modes within the star over many pericenter passages can lead to a runaway disruption of the star at a pericenter distance that is 4-5 times farther than the standard tidal disruption radius. The accumulated heating may explain the lack of massive ($\gtrsim 10M_{\odot}$) S-stars closer than several tens of AU from SgrA*.

9.1 Introduction

Near the Galactic center, stars may get scattered into orbits for which the tide raised by the supermassive black hole, SgrA*, at pericenter is large but not strong enough to disrupt the stars. The scattering rate into those orbits is larger than that of immediate tidal disruptions orbits, where the pericenter distances are smaller than the tidal radius, $r_p \lesssim r_t = R_*(M_{\rm BH}/M_*)^{\frac{1}{3}}$ (Magorrian & Tremaine 1999; Alexander & Livio 2001). Here $M_{\rm BH} = 4 \times 10^6 M_{\odot}$ is the mass of SgrA* (Ghez et al. 2008; Genzel et al. 2010), and M_* and R_* are the mass and radius of the star. In the near miss regime, stars with $r_p \gtrsim r_t$ are not disrupted during their first passage near SgrA*, their tidal heating and bloating could still be substantial after multiple passages due to the tidal distortion and the excitation of internal oscillation modes. In principle, a sufficiently large number of close passages may lead to the disruption of these stars (Rees 1988; Novikov et al. 1992; Kosovichev & Novikov 1992; Diener et al. 1995; Alexander & Morris 2003; Antonini et al. 2011; Guillochon & Ramirez-Ruiz 2012). Various tidal effects at $r_p \gtrsim r_t$ were considered in the literature, including relativistic effects (Luminet & Marck 1985; Gomboc & Čadež 2005; Ivanov & Chernyakova 2006; Kostić et al. 2009), tidal heating of planets by stars

(Ivanov & Papaloizou 2004a, 2007, 2011), and tidal heating in close binary systems (Press & Teukolsky 1977; Kochanek 1992; Mardling 1995a,b; Lai 1997; Ho & Lai 1999; Ivanov & Papaloizou 2004b; Lai & Wu 2006; Fuller & Lai 2011; Weinberg et al. 2012).

In this paper we consider the heating of stars at distances $r_p \gtrsim 3r_t$ from SgrA*. Since each pericenter passage is associated with a small distortion in the shape of stars, one may adopt a linear description for the tidal excitation of stellar modes (Novikov et al. 1992; Kosovichev & Novikov 1992). The associated theory of linear mode excitation has been calibrated recently by new data on stellar binaries from the Kepler satellite (Fuller & Lai 2012; Burkart et al. 2012). The underlying theory was also recently extended to describe nonlinear coupling of the excited modes (Weinberg et al. 2012). We use the latest results from these studies to calculate the tidal excitation and heating of stars in the vicinity of SgrA*.

Our goal is to find the maximum distance from SgrA* at which the accumulated heating due to numerous pericenter passages can lead to tidal disruption of stars around SgrA*. The accumulated heating would lead to the absence of massive stars on eccentric orbits interior to a spherical region around SgrA*, whose radius depends on $M_\star$ and exceeds the standard tidal disruption radius r_t. Our predictions could be tested by future searches for stars at closer separations than the known S-stars, which have $r_p \gtrsim 10^2$ AU (Ghez et al. 2008; Genzel et al. 2010).

SgrA* is surrounded by a circumnuclear disk of young stars (Genzel et al. 2010). Inside the inner radius of this disk, there is the S-cluster of young main sequence B-stars (Ghez et al. 2003; Eisenhauer et al. 2005), with random orbital orientations and high orbital eccentricities (Gillessen et al. 2009). All the known S-stars have $r_p \gg r_t$, but

it is possible that the lack of S-stars inside 100 AU is caused by the accumulated tidal heating over multiple pericenter passages. Our predictions can be tested as new stars, such as SO-102 (Meyer et al. 2012), are being discovered and new instruments, such as the second-generation VLTI instrument GRAVITY (Bartko et al. 2009), are being constructed.

The outline of the paper is as follows. In §10.2 we describe the method we use to calculate the heating due to tidal excitation and the response of the stars. In §10.3 we show examples of these effects in the Galactic center using two stellar models produced by MESA stellar evolution code (Paxton et al. 2011) and present the results. In §10.4, we summarize our main conclusions.

9.2 Heating of Stars by Tidal Excitation of Modes

The tidal force from SgrA* can excite internal oscillation modes within an orbiting star during its pericenter passages. At distances $r_p \gtrsim 3r_t$, the energy gain by tidal excitation per pericenter passage is low, but the accumulated energy after many passages can heat the star significantly.

9.2.1 Mode Excitation and Interference in Multiple Pericenter Passages

To calculate the low energy gain per orbit at $r_p \gtrsim 3r_t$, it is appropriate to use the linear perturbation formalism of Press & Teukolsky (1977) (see also Novikov et al. 1992; Kosovichev & Novikov 1992). We denote the separation of the star from SgrA* at time t

by $r(t)$. For a single passage, the energy of an excited stellar mode can be expressed as,

$$\Delta E_{0,nml} = 2\pi^2 \Big(\frac{GM_*^2}{R_*}\Big)\Big(\frac{M_{\rm BH}}{M_*}\Big)^2\Big(\frac{R_*}{r_p}\Big)^{2l+2}|Q_{nl}|^2|K_{nlm}|^2, \tag{9.1}$$

where n is the mode order and $\{l, m\}$ are the two spherical harmonic indices. The excited modes have $l > 1$, $-l < m < l$, and we adopt the convention in which $n < 0$ for g-modes and $n > 0$ for p-modes. The coefficient K_{nlm} represents the coupling to the orbit,

$$K_{nlm} = \frac{W_{lm}}{2\pi}\int_{-\infty}^{\infty} dt\Big(\frac{r_p}{r(t)}\Big)^{l+1}\exp\{\mathrm{i}[\omega_{\rm n}\mathrm{t} + \mathrm{m}\Phi(\mathrm{t})]\}, \tag{9.2}$$

where ω_n is the mode frequency, $\Phi(t)$ is the true anomaly, and $W_{lm} = (-1)^{(l+m)/2}[\frac{4\pi}{(2l+1)}(l-m)!(l+m)!]^{1/2}/[2^l\frac{(l-m)}{2}!\frac{(l+m)}{2}!]$. The 'tidal overlap integral' Q_{nl} represents the coupling of the tidal potential to a given mode,

$$Q_{nl} = \int_0^1 R^2 dR\rho(R) l R^{l-1}[\xi_{nl}^{\mathcal{R}} + (l+1)\xi_{nl}^{\mathcal{S}}]. \tag{9.3}$$

where $\rho(R)$ is the stellar density profile as a function of radius R. $\xi(R) = [\xi_{nl}^{\mathcal{R}}(R)\hat{e}_R + \xi_{nl}^{\mathcal{S}}(R)R\nabla]Y_{lm}(\theta,\phi)$ is the mode eigenfunction, with $\xi_{nl}^{\mathcal{R}}$ being its radial component and $\xi_{nl}^{\mathcal{S}}$ being its the poloidal component. The total energy transferred from the orbit to the star in a single passage is

$$\Delta E_0 = \sum_{nlm}\Delta E_{0,nml} \quad . \tag{9.4}$$

Next, we consider the evolution of the modes as a result of multiple pericenter passages. If the dissipation timescale of the modes is longer than the orbital period, the modes remain excited and interfere with newly excited modes during subsequent passages. Mardling (1995a,b) considered this problem numerically and found two orbital parameter regions. In one of them the energy exchange between the mode and the orbits

is quasi-periodic and the amplitudes of the modes remain small. In the other region, chaotic behavior is exhibited. Ivanov & Papaloizou (2004b) (hereafter IP04) further explored this stability boundary using a proxy α, which characterizes the change of the phase due to the orbital period change, where the period change is caused by the energy transferred to the modes. By mapping the mode amplitude and phase of a particular passage to those values at an earlier passage, IP04 found that when α is larger than a threshold value α_c, there is a secular increase of mode energy. α_c depends on the phase of the mode in the first passage.

For Galactic center stars with $r_p \gtrsim 3r_t$ around SgrA*, the change in orbital period per passage provided by the exchange between tidal excitation energy and orbital energy is too small to increase the mode amplitude. Below we show that gravitational scattering on stars and compact objects in the Galactic center could naturally lead to a drift in the orbital period that allows the amplitude of the excited modes to increase stochastically.

Similar to IP04, we introduce the two-dimensional vectors $\mathbf{x}_i$ to characterize the amplitude A_i and the phase ψ_i of the excited modes at the i^{th} passage:

$$\begin{aligned} x_i^1 &= A_i \cos(\psi_i), \\ x_i^2 &= A_i \sin(\psi_i). \end{aligned} \tag{9.5}$$

Because different stellar modes act independently in the linear regime, we focus here on one mode with frequency ω_n. For the $(i+1)^{th}$ passage,

$$\mathbf{x}_{i+1} = \mathcal{R}(\phi_i)[\mathbf{x}_i + \mathbf{e}], \tag{9.6}$$

where $\phi_i = \omega_n P_{orb,i}$ (with $P_{orb,i}$ being the orbital period for the i^{th} passage), $e^1 = 1$, $e^2 = 0$ and $\mathcal{R}$ is the rotation matrix.

Defining $\alpha_i = \omega_n \Delta P_{orb,i}$ where $\Delta P_{orb,i}$ is the change in the orbital period in the i^{th} passage, we get $\phi_{i+1} = \phi_i + \alpha_i$. In difference from IP04, α_i is a random variable. Given the initial condition $\mathbf{x}_0 = (1, 0)$ (without loss of generality) and equation (9.6), we examine numerically how the mode amplitude changes as a function of the number of passages. First, we examined the case when α is drawn from a uniform distribution between $-2\alpha_m$ to $2\alpha_m$, $\langle|\alpha|\rangle = \alpha_m$. We characterize the growth in the mode amplitude by the power-law index of its evolution with the number of passages (using a total of 10^6 passages). Figure 9.1 shows that for $\langle|\alpha|\rangle > 0.1$ the amplitude increases with a power-law index of 0.5, so the energy of the mode increases linearly with time. We also examined an alternative case with α drawn from a Poisson distribution and the result was the same .

Note that in difference from IP04, the increase in the amplitude is caused by the stochastic nature of α. We also find that the threshold value does not show any dependence on ϕ_0.

Next we examine the value of $\langle|\alpha|\rangle$ due to gravitational perturbers in the Galactic center. We start by expressing α in terms of the fractional change in the orbital period assuming the primary excited mode has frequency $\omega_n \sim \sqrt{N_{pm} G M_* / R_*^3}$ (with a typical value $N_{pm} \sim 10$),

$$\begin{aligned} \alpha &= \omega_n \Delta P_{orb} \\ &\sim 3300 \frac{\Delta P_{orb}}{P_{orb}} \Big[\sqrt{\frac{N_{pm}}{10}} \Big(\frac{1 - 0.9}{1 - e} \Big)^{3/2} \Big(\frac{r_p / r_t}{3} \Big)^{3/2} \Big], \end{aligned} \tag{9.7}$$

where e is the orbital eccentricity. Thus, when $\frac{|\Delta P_{orb}|}{P_{orb}} \gtrsim 3 \times 10^{-5}$ the amplitude of the modes increases stochastically.

We calculate the expected $|\Delta P_{orb}|/P_{orb}$ due to gravitational scatterings using the N-body code BHINT (Löckmann & Baumgardt 2008) to track the orbits of the stars

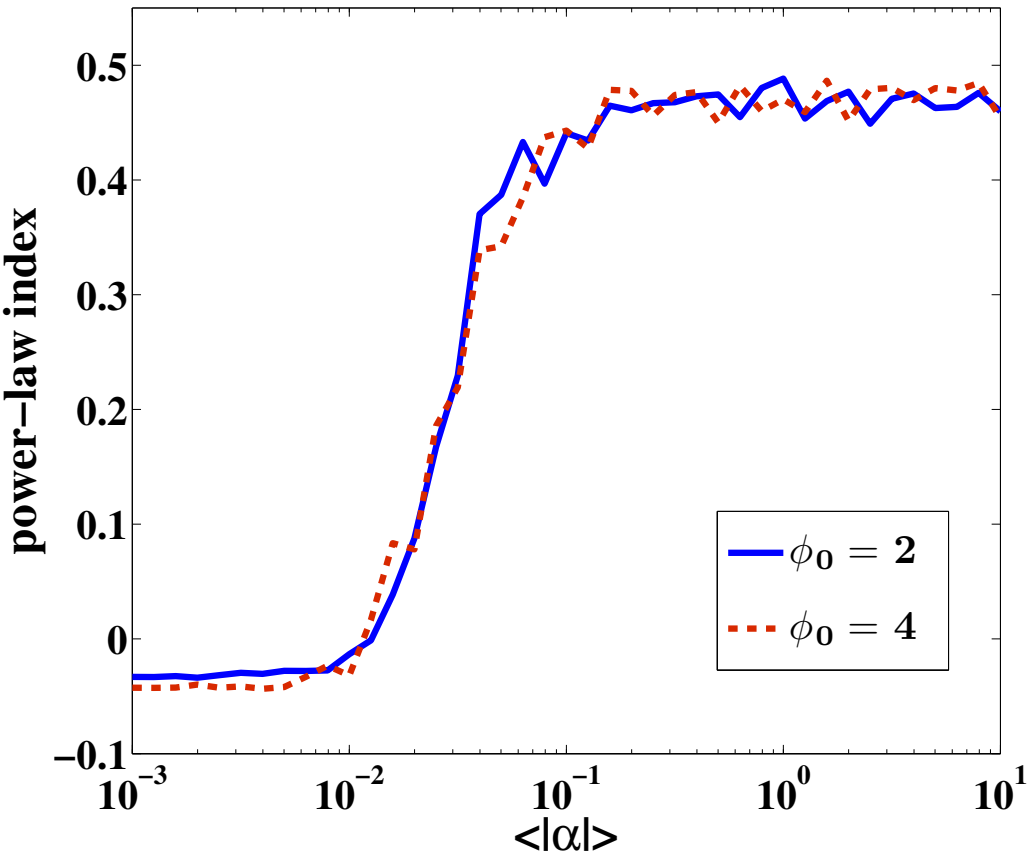

Figure 9.1: The power-law index of the mode amplitude growth with time during multiple passages as a function of the average magnitude of $\alpha = \omega_n \Delta P_{orb}$. When the power-law index is around 0.5, the amplitude growth resembles a random walk and the energy of the mode is growing linearly with the number of passages. We find this scaling when $\langle|\alpha|\rangle > 0.1$, independent of the value of $\phi_0 = \omega_n P_{orb,0}$ (shown by the different lines).

and compact objects in the Galactic center. We estimate $|\Delta P_{orb}|/P_{orb}$ for each passage, and the expectation value is calculated by averaging $|\Delta P_{orb}|/P_{orb}$ over ~ 50 passages. We performed a convergence test and verified that our numerical errors are small and the results are robust. The fractional change in the orbital period of a test star depends on the semi-major axis a and eccentricity e of its orbit and the distribution of perturbers within the S-cluster. We assume an outer radius of ~ 0.04 pc ($= 1''$) for the S-cluster, and estimate the period change for typical S-stars with eccentricities in the range of 0.85–0.95. We consider the initial mass function (IMF) that matches the mass distribution of S-stars inside $0.8''$ ($dN/dm \propto m^{-2.15\pm0.3}$) (Bartko et al. 2010)). The fractional change of the orbital period is most sensitive to the massive stars (Murray-Clay & Loeb 2011). We normalize the IMF so that it gives ~ 3 S-stars with $M \sim 20M_{\odot}$ as observed. In the mass range of 0.3–$25M_{\odot}$, the IMF yields a total of 800 stars.

We also considered the effects of scattering on stellar-mass black holes (SBH) and a hypothetical intermediate-mass black hole (IMBH). SBHs are more massive than the background stars and therefore are expected to segregate in the Galactic center (Morris 1993; Miralda-Escudé & Gould 2000; Freitag et al. 2006). We normalize the number of SBHs (each having $10M_{\odot}$) within 0.04 pc to be 1400, based on Miralda-Escudé & Gould (2000) and Freitag et al. (2006). An IMBH was hypothesized as an agent for randomizing the inclinations of stars in the S-cluster, potentially creating the hyper-velocity stars and the stellar disk (Yu & Tremaine 2003; Sesana et al. 2006; Yu et al. 2007; Gualandris & Merritt 2009; Perets & Gualandris 2010; Yu 2010). To gauge its effect on ΔP_{orb} we assume an IMBH mass of $10^3 M_{\odot}$ (Yu 2010) with either $a = 10^{-3}$pc ($= 206$AU)) and $e = 0.80$ or $a = 3 \times 10^{-4}$pc and $e = 0.26$. The scattering due to the SBH and IMBH dominate the fractional change in the orbital periods.

Figure 9.2 shows the results from the numerical runs of the N-body code. We find that the fractional changes of the orbital period are higher than the minimum value required to increase the mode amplitudes stochastically, implying that the energy of the excited modes would increase linearly with the number of pericenter passages. Because the scattering of the orbit is fully random and the change of the orbit is typically small ($\sim 10^{-4}$–10^{-3}), we neglect the orbital evolution. For a random walk, the period is expected to change significantly only after 10^6–10^8 passages, beyond the number of passages considered here.

Similar to the study on the variation of orbital period, we quantify the change in eccentricity using N-body integration code BHINT. We use the same configuration of the stars and we do not consider the effect of SBHs or IMBHs for simplicity. Figure 9.3 shows the changes in eccentricity for a star at $a = 0.01$ pc, $e = 0.998$ versus time. Assuming $\delta e(t) \propto \sqrt{t}$, the changes in $1 - e$ over ~ 1 Myr timescale, during which the star accumulates a large amount of energy, is $\delta(1 - e) \sim 0.25(1 - e_0)$. Thus, the eccentricity variation due to the perturbation from the surrounding stars can affect the heating process. The increase of the eccentricity may increase the heating, and the decrease of the eccentricity can weaken the tidal excitation of the modes and delay tidal disruption. Since $\delta(1 - e)/\delta(1 - e_0)$ is less than an order of unity before the star accumulates the heating energy, heating of the star will not be completely suppressed due to the variation in eccentricity. We ignore the variation in eccentricity for the rest of this section for simplicity.

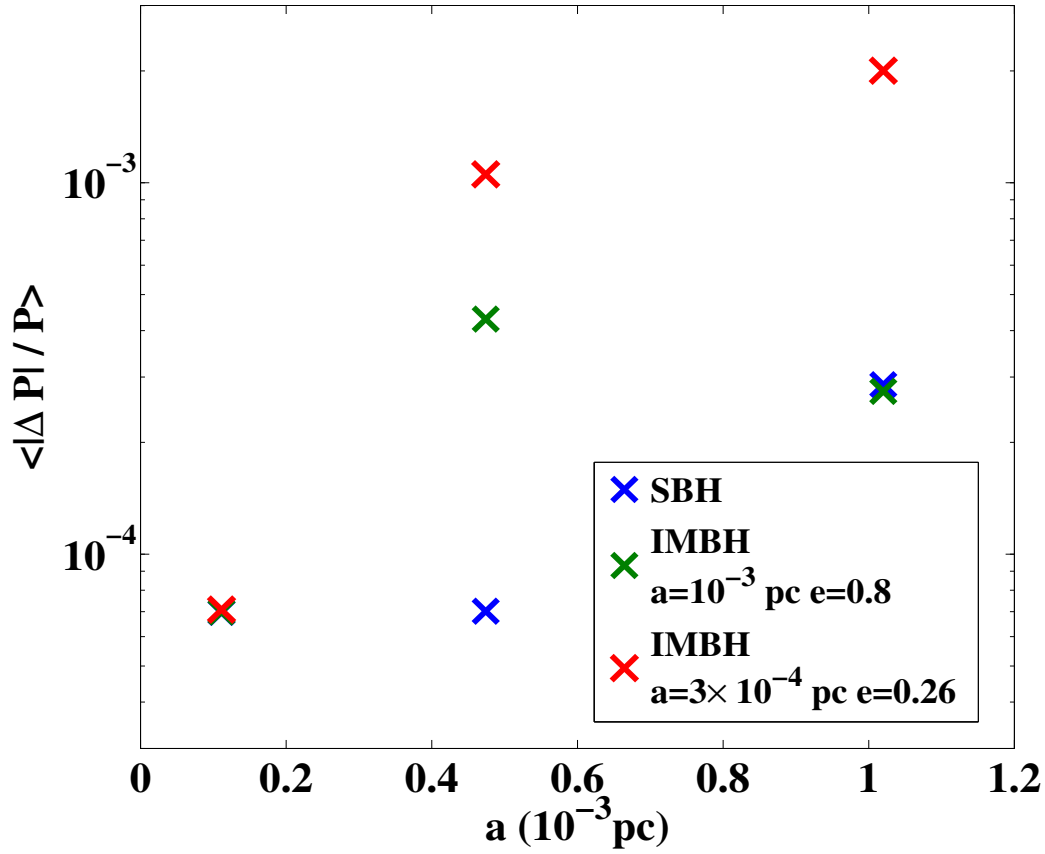

Figure 9.2: The average of the fractional change in orbital period per pericenter passage, $\langle|\Delta P_{orb}|/P_{orb}\rangle$, for stars on orbits with different semi-major axis a. The x-axis is in unit of 10^{-3} pc $= 206$ AU. We include 800 stars with an initial mass function $(dN_*/dM_*) \propto M_*^{-2.15}$ (Bartko et al. 2010) in the mass range 0.3–25$M_\odot$, providing about three $20M_\odot$ stars. We also consider scattering on a population of $1,400$ stellar-mass black holes (SBH) within 0.04 pc from Sgr A* (Miralda-Escudé & Gould 2000; Freitag et al. 2006), or an intermediate mass black hole (IMBH) with a mass of $10^3 M_\odot$ on two possible orbits.

9.2.2 Tidal Heating of Stars

Since the expected fractional change in the orbital period per pericenter passage in Figure 9.2 is higher than 3×10^{-5}, the tidally-excited mode energy is expected to increase linearly with the number of pericenter passages. Cumulatively, a significant amount of heat might be deposited inside the star during multiple passages. In this section, we consider the dissipation of the mode energy and the resultant heating of the star.

Previous studies showed that when the amplitude of the excited modes increases over some parametric instability threshold, the excited mode begins to transfer its energy to lower frequency daughter modes which dissipate rapidly (Dziembowski 1982; Kumar & Goodman 1996; Wu & Goldreich 2001; Arras et al. 2003; Weinberg & Quataert 2008; Weinberg et al. 2012). We set $n_{crit} = E_{th}/\Delta E_0$ to be the number of pericenter passages after which the amplitude of the mode exceeds this threshold, where E_{th} is the threshold energy when non-linear coupling occurs. As the dissipation time of the excited daughter modes is typically short compared with the orbital period in the Galactic center, the thermal energy gain in the stellar interior is:

$$E_{t,n_p} = (n_p/n_{crit})E_{th} = n_p \Delta E_0, \tag{9.8}$$

where E_t is the thermal energy gained during this process, n_p is the number of pericenter passages and ΔE_0 is the energy gain of the excited modes during the first passage. When $n_p \gg n_{crit}$, the thermal energy added to the star is independent of the parametric instability threshold.

The heat generated around a radius R within the star at time t_0 will be trapped inside the star for a finite time, $(t - t_0) < t_c(R)$, where $t_c(R)$ is the characteristic time it takes heat to leak out. We estimate $t_c(R)$ as the minimum between the photon diffusion

time, $t_{diff} = \int dR\{\tau(R) - (R_* - R)[d\tau(R)/dR]\}/c$, and the turbulent convection time, $t_t = \int dR/v_c(R)$, for each spherical shell inside the star. Here $\tau(R)$ is the scattering optical depth and $v_c(R)$ is the convective velocity. At late times $t > t_c(R)$, the heating at radius R will saturate and reach a steady state where it is balanced by cooling. This sets the upper limit of the maximum heat stored at a radius R.

As the non-linear coupling excites a large number ($> 10^3$) of daughter modes, most of the energy is redistributed. Typically, the daughter modes consist of high order g-modes and so the energy is redistributed mostly in the radiative zone. Weinberg et al. (2012) investigated modes inside solar-type stars and found that most of the energy is transferred to the radiative core of the star. For simplicity, we will assume that the energy is uniformly distributed per unit mass within the radiative zone.

The energy gained can be expressed as follows,

$$E_t(R) = \begin{cases} n_{crit}\Delta E_0(R) & \text{if } t_c(R) < P_{orb} n_{crit} \\ \frac{t_c(R)}{P_{orb}}\Delta E_0(R) & \text{if } t_c(R) > P_{orb} n_{crit} \end{cases} \tag{9.9}$$

Assuming that energy is evenly deposited throughout the entire radiative zone of the star, we find $E_0(R)$ and obtain the thermal energy stored at a radius R, $E_t(R)$. Typically for stars at $r_p \gtrsim 3r_t$ around SgrA*, $n_{crit} \ll t_c(R)/P_{orb}$, and so the total stored heat is independent of n_{crit}. Finally, integrating $E_t(r)$ over the interior of the star yields the total heating inside the star, E_H.

As a result of the additional source of energy, the star expands. So far, we did not include the increase of the size of the star in our calculation. As the stellar radius increases, the tidal effects become stronger with $\Delta E \propto R_*^6$. A decrease in the mode frequency $\sim \sqrt{GM_*/R_*^3}$ brings ω_n closer to the orbital frequency and increases K_{nl}.

Thus, ignoring the variation in the tidal overlap integral (Q_{nl}), the tidal excitation becomes stronger as the size of the star increases. In addition, the rate of the expansion and the final size of the star depend on where the heat is deposited (Podsiadlowski 1996). We examine this process more closely with MESA stellar evolution simulations (Paxton et al. 2011) in the next section.

As the star gains energy, its energy gain rate increases due to its increasing size. The resulting runaway process could lead to the disruption of the star. In order to find the minimum heating at saturation ($t > t_c(R = 0)$) that may lead to disruption, we express the radius of the star after the n^{th} pericenter passage as, $R_*(n) = R_{*,0}(1 + \epsilon_n)$, where $R_{*,0}$ is the original radius of the star. Assuming $\Delta E \propto R_*(n)^6$ and ignoring the change in entropy within the star, we find

$$1/(1 + \epsilon_n) - 1/(1 + \epsilon_{n+1}) = \Delta\tilde{E}_0((1 + \epsilon_n)^6 - 1), \tag{9.10}$$

where $\Delta\tilde{E}_0 = \Delta E_0/(GM_*^2/R_{*,0})$. Figure 9.4 shows the growth of $R_*(n)$ as a function of the number of pericenter passages starting with the saturation value of $\epsilon_0 = 0.01$. Our results demonstrate that at $r_p/r_t \sim 4$ the stored heat can approach the binding energy of the star after $\sim 10^6$ pericenter passages following saturation, even if the total heat gained at saturation is only $\sim 1\%$ of the binding energy. This threshold increases as r_p/r_t increases.

During its lifetime, a massive star can achieve $\gtrsim 10^7$ pericenter passages at the corresponding distances from SgrA*. For example, a 20 $M_\odot$ star with $e = 0.9$ and $r_p \sim 5r_t$ around SgrA* has an orbital period of ~ 0.8 years. Thus, during its lifetime the star encounters $\sim 10^7$ pericenter passages. The maximum number of pericenter passages is also limited by gravitational scatterings on other stars. According to Figure 9.2, with

stochastic scatterings on SBH or one hypothesized IMBH, the maximum number of passages at the original pericenter is $\sim 10^6 - 10^8$. Thus, for $r_p/r_t < 5$, the star will be significantly heated even if the total heat gained at saturation is only $\sim 1\%$ of the binding energy.

Non-linear effects are expected to dominate in the last phase of the disruption process. When the star is distorted, the energy transfer from the orbit to the modes can be either positive or negative depending on the phases of the modes and the orientation of the ellipsoid at the time of the pericenter passage. Diener et al. (1995) studied this effect statistically and found that the probability of a positive transfer of energy from the orbit to the star is high.

9.3 Results

Based on the formalism presented in §10.2, we calculated the tidal heating of stars in the Galactic center. We consider two steller masses: $1M_\odot$ (representing low-mass stars) and $20M_\odot$ (representing high mass stars, similar to SO-2 (Martins et al. 2008)). The other properties of the two stars are summarized in Table 9.1.

Table 9.1:: Properties of stellar models

Mass ($M_\odot$)	Metallicity	Radius ($R_\odot$)	Age (yrs)
1	$Z = Z_\odot$	1	4.5×10^9
20	$Z = Z_\odot$	10	7×10^6

Since the energy gain in each passage depends on $\left(R_*/r_p\right)^{2l+2}$, and because the value of Q_{nl} and K_{nlm} are similar for modes with different values of l, the quadrupole ($l = 2$) modes gain the most energy during the tidal excitation (whereas $l = 0$ and $l = 1$ modes are not excited). Thus, we focus on the $l = 2$ modes.

We calculate the overlap integral (Q_{nl}) and the orbit coupling (K_{nlm}) using the MESA stellar model (Paxton et al. 2011). The adiabatic normal modes are computed with the ADIPLS code (Christensen-Dalsgaard 2008). For illustration, we show in Figure 9.5 the values of $\sum_m |Q_{n,l=2}|^2 |K_{n,l=2,m}|^2$ for a $20M_\odot$ star in orbit around Sgr A* with $a = 7 \times 10^{-3}$ pc and $e = 0.9$. As expected (e.g. Press & Teukolsky 1977; Burkart et al. 2012), we find that lower order g-modes are excited the most. The energy gain in one passage, ΔE_0, can then be found from equation (9.4).

To calculate the time it takes for the deposited heat to travel to the surface (t_c) as described in §9.2.2, we obtain the optical depth and the convective velocity profile in the interior of the stars from the MESA code (Paxton et al. 2011). Figure 9.6 shows the cooling time as a function of radius for the two stars.

The threshold for non-linear coupling has been discussed by Weinberg et al. (2012) for three mode coupling in a solar-mass star. If the daughter modes only couple to one other daughter mode, the threshold is $E_{th} \sim 10^{-19} GM_*^2/R_*$; however, if the daughter modes couple to multiple daughters, $E_{th} \sim 10^{-16} GM_*^2/R_*$. In both cases, $(t_c/t_{orb}) \gg n_{crit}$ in the interior of the stars for $r_p \gtrsim 3r_t$. Thus, the heating of the star is independent of the value of n_{crit}. Conservatively, we calculate the heating using the high energy threshold.

As the daughter modes consist of high order g-modes, energy is redistributed mostly in the radiative zone of the star. For simplicity, we assume that the distribution is

uniform per unit mass in the radiative zone and integrate equation (9.9) over the interior of the star. Figure 9.7 shows the heat gained by the stars (E_H) in units of their binding energy (E_B) obtained from MESA, at the saturation time $t = t_c(R = 0)$. The increase in the stellar radius is not included in this calculation.

Taking account of the runaway increase in the stellar radius, the net heat deposited could approach the binding energy and hence lead to disruption when the heating at saturation approaches 1% of the binding energy. We estimate that the heating could be substantial at $r_p \sim 4.5 r_t$ for $20 M_\odot$ stars.

Next we analyse the heating effect more accurately using MESA stellar evolution simulations. We estimate the heating rate by $\Delta E_0 / P_{orb}$, and assume that the heat is deposited uniformly in the radiative zone. We take account of the change in $|Q_{nl=2}|^2 |K_{nl=2m}|^2$ due to the change of the stellar structure through iterations. For our first iteration, we assume a constant $|Q_{nl=2}|^2 |K_{nl=2m}|^2$ and obtain the structure of the heated stars with different radii at different times. Then we calculate the increase in $|Q_{nl=2}|^2 |K_{nl=2m}|^2$ as a function of the increase in stellar radius for the heated stars. For our second iteration, we simulate the heated stars with a changing $|Q_{nl=2}|^2 |K_{nl=2m}|^2$ as a function of stellar radius. We calculate $|Q_{nl=2}|^2 |K_{nl=2m}|^2$ and continue iterating until the dependence of $|Q_{nl=2}|^2 |K_{nl=2m}|^2$ on radius converges. In the examples we consider, convergence is reached within two iterations.

Our convergent results for the 20 $M_\odot$ star indicate that the size of the convective core decreases and the central temperature stays approximately constant during the heating. For the 1 $M_\odot$ star, the size of the radiative core increases and the central temperature drops significantly. Figure 9.8 shows the radius of the heated star as a

function of time. We compare the results of the two iterations for the 20 $M_\odot$ star at $r_p/r_t = 4.5$ and for the 1 $M_\odot$ star at $r_p/r_t = 5$, and find that the disruption time depends only weakly on the change in $|Q_{nl=2}|^2|K_{nl=2m}|^2$. For other pericenter distances we show only the results of the first iteration (assuming $|Q_{nl=2}|^2|K_{nl=2m}|^2$ =const). Requiring the heating timescale to be shorter than the orbital scattering timescale and the stellar lifetime, we find that the maximum r_p for disruption is $\sim 4.5r_t$ for a 20 $M_\odot$ star and $\sim 5r_t$ for a 1 $M_\odot$ star.

For simplicity, we only considered non-rotating stars. As discussed by Fuller & Lai (2012), the mode frequencies are modified for rotating stars by $mC_{nl}\Omega_*$, where Ω_* is the rotation rate of the star and $C_{nl} = \int_0^{R_*} \rho R^2(2\xi^{\mathcal{R}}\xi^{\mathcal{S}} + \xi^{\mathcal{S}2})\, dR$. Because Q_{nl} are unchanged by rotation, the dominant modes shift to higher order g-modes which have smaller values of Q_{nl}. Thus, rotation would lower the excitation energies. In addition, the rotation may modify the modes themselves (Burkart et al. 2012), and further complicate the calculation. Treatment of tidal excitation in misaligned spin-orbit systems were discussed by Ho & Lai (1999) and Lai & Wu (2006).

Finally, we discuss the observational signature of a tidally heated star. Using the MESA simulation, we plot the Hertzsprung-Russell (HR) diagram of the heated stars in Figure 9.9. Because our calculation is not appropriate in the non-linear regime when the tidal radius of the heated star approaches $\sim (r_p/2.7)$, we stop the calculation when $r_p \sim 2.7r_{t,heated}$, where $r_{t,heated}$ is the tidal radius of the heated star. We find that a 1 $M_\odot$ star at $r_p \sim 2.7r_{t,heated}$ acquires a luminosity L that is ~ 3 times higher than if it were on the main sequence and an effective temperature T_{eff} that is $\sim 12\%$ lower than the main sequence star. A $20M_\odot$ star at $r_p \sim 2.7r_{t,heated}$ acquires a luminosity that is $\sim 44\%$ times higher and an effective temperature that is $\sim 20\%$ lower than that on the

main sequence. Photometrically, the heated stars could be confused with giant stars that evolved off the main sequence (illustrated by the blue lines in the plot).

9.4 Conclusion

We considered the tidal excitation of oscillation modes in stars orbiting SgrA*. When the dissipation timescale of the modes is longer than the orbital period, the modes excited in each passage interfere. Due to the gravitational scatterings on nearby stars or stellar-mass black holes, the orbital period of the excited star changes stochastically and the energy of the excited modes increases approximately linearly with the number of pericenter passages. As non-linear coupling of the stellar modes dissipate the kinetic energy of the modes, the excited star is heated. Once the deposited heat is significant, the star bloats and its tidal heating accelerates, until non-linearities lead to the final mass loss and possible disruption of the star.

We calculated the thermal energy gain by a star as a function of the semi-major axis and eccentricity of its orbit around Sgr A*. We have found that the maximum pericenter distance where the heat gained by the star approaches its binding energy is $r_p \sim 5r_t$ (~ 3.7 AU) for a 1 $M_\odot$ star and $r_p \sim 4.5r_t$ (~ 13 AU) for a 20 $M_\odot$ star. The accumulated heating may explain the lack of massive ($\gtrsim 10M_\odot$) S-stars closer than several tens of AU from SgrA* (Genzel et al. 2010).

The heating process may be most effective for the highest-mass stars ($\gtrsim 100M_\odot$), where radiation pressure nearly balances gravity and reduces the binding energy considerably relative to GM_*^2/R_* (Shapiro & Teukolsky 1986). This makes these stars

more vulnerable to disruption through heating. However, the heating is not important for giant stars evolved off the main sequence, because for $r_p/r_t \sim 5$ the orbital period of a giant star is too long to allow sufficient number of pericenter passages during the star's lifetime.

The expected radius of the cavity produced by tidal disruption of stars depends on stellar mass (Alexander & Livio 2001). Since gravitational scatterings on other objects could change the orbital period on a timescale much shorter than the lifetime of a low mass star but similar to the lifetime of the high mass star ($\sim 20M_\odot$), the net number of pericenter passages is similar in the two cases. Of course, the tidal distance of a high mass star is larger than that of a low mass star, and so a lower mass star may approach Sgr A* at a closer distance (having a shorter orbital time and more pericenter passages) before being tidally disrupted.

The removal of tidally-heated stars makes it more difficult to test the no hair theorem of general relativity based on stellar orbits, as the precession produced by the quadruple moment of SgrA* decreases with increasing distance. For example, the precession rate due to the quadruple moment of SgrA* is only $\sim 0.4\mu$as/yr for a $20M_\odot$ star with $r_p = 4.5r_t$, and is $\sim 4\mu$as/yr for a $1M_\odot$ star with $r_p = 5r_t$, assuming a normalized spin of 0.7 for SgrA* (Will 2008). Gravitational deflections by other stars or compact objects contaminate the precession signal and require the monitored stars to be within $\sim 2 \times 10^{-4}$ pc from SgrA* (Merritt et al. 2010). We find that only low mass stars (which cannot be detected at present) would be viable targets for testing the no hair theorem around SgrA*.

As new stars, such as SO102 (Meyer et al. 2012), are being discovered in the Galactic

center, our predictions for the tidal cavity radius as a function of stellar mass may be tested. In particular, the second-generation VLTI instrument GRAVITY will be able to resolve faint stars with a K-band magnitude $m_K = 18$ ($\sim 3M_\odot$) (Bartko et al. 2009) and test our predictions in the coming years.

Acknowledgments

We thank Charlie Conroy, James Fuller, Bence Kocsis, Leo Meyer, Sterl Phinney, Eliot Quataert and Nick Stone for helpful comments. GL benefitted significantly from the MESA 2012 summer school. This work was supported in part by NSF grant AST-0907890 and NASA grants NNX08AL43G and NNA09DB30A.

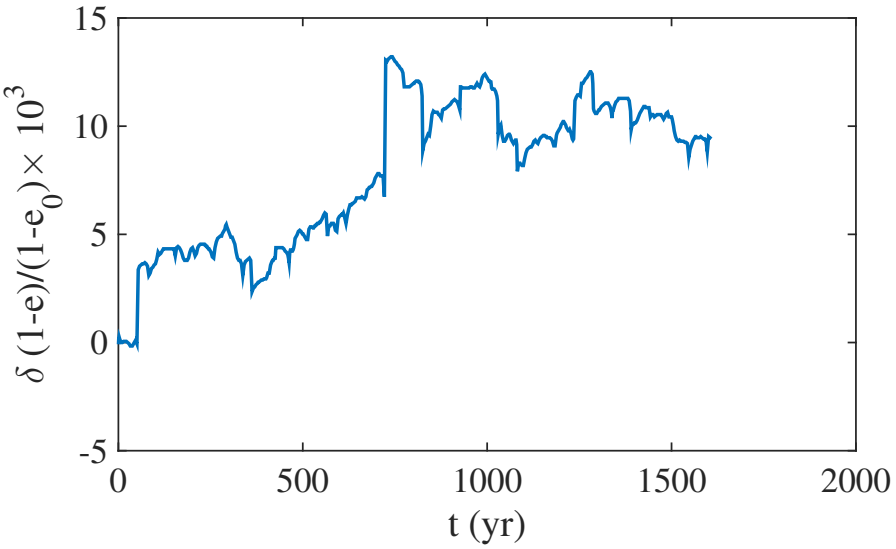

Figure 9.3: The change in eccentricity of a star at 0.01 pc with $e = 0.998$ due to surrounding stars. The configuration of the stellar cluster is the same as that shown in Figure 9.2. The changes in eccentricity can affect heating, but cannot completely suppress the heating process.

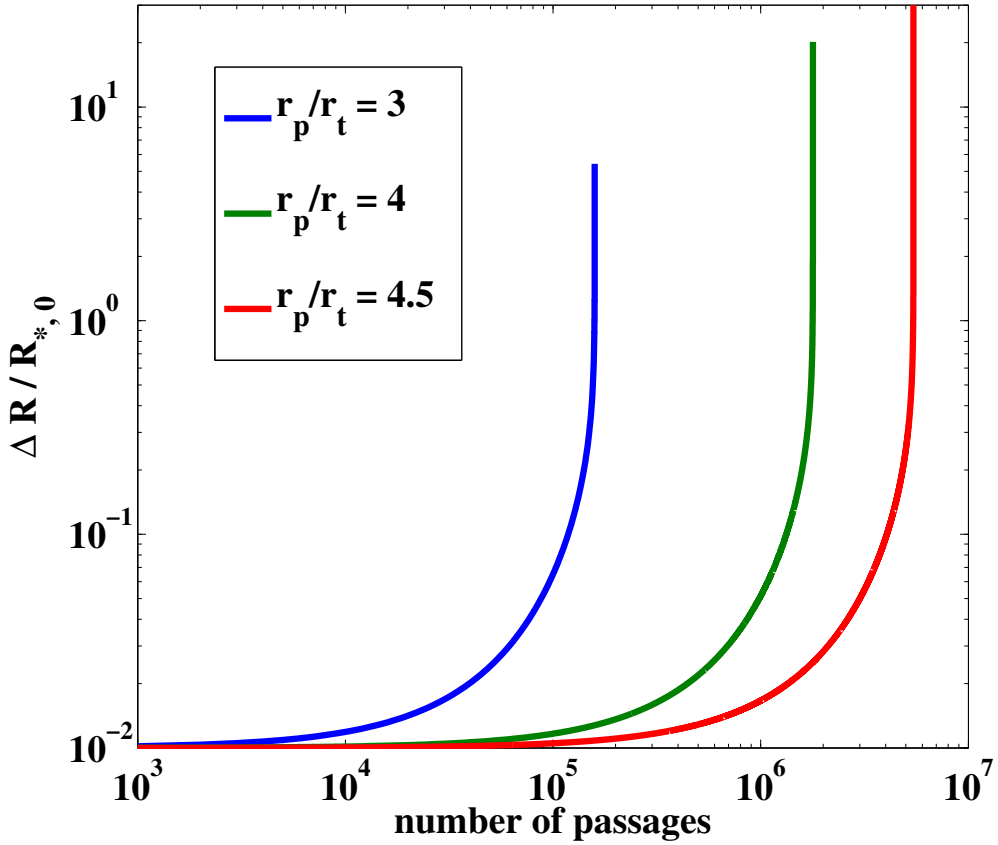

Figure 9.4: Radius of the star as a function of the number of passages after saturation when $t > t_c(R = 0)$, assuming $\Delta R/R_{*,0}(n = 0) = 0.01$. We find that a star can be heated significantly after $\sim 10^6$ passages even if the thermal energy it stores at saturation is only 1% of its binding energy. This threshold increases as r_p/r_t increases.

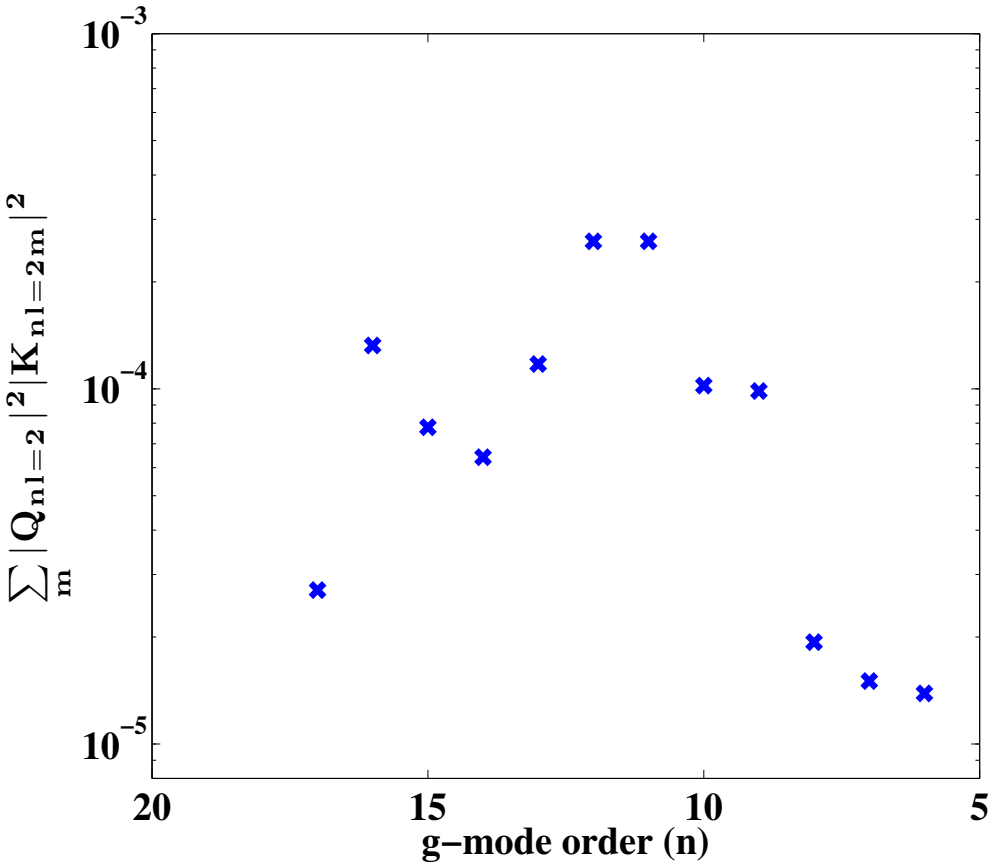

Figure 9.5: $\sum_m |Q_{n,l=2}|^2 |K_{n,l=2,m}|^2$ as a function of the mode order (n) for stellar modes computed with the ADIPLS code (Christensen-Dalsgaard 2008) based on the stellar structure from the MESA stellar model (Paxton et al. 2011). The mass ($20M_\odot$) and radius ($10R_\odot$) of the star resemble those of SO-2 (Martins et al. 2008).

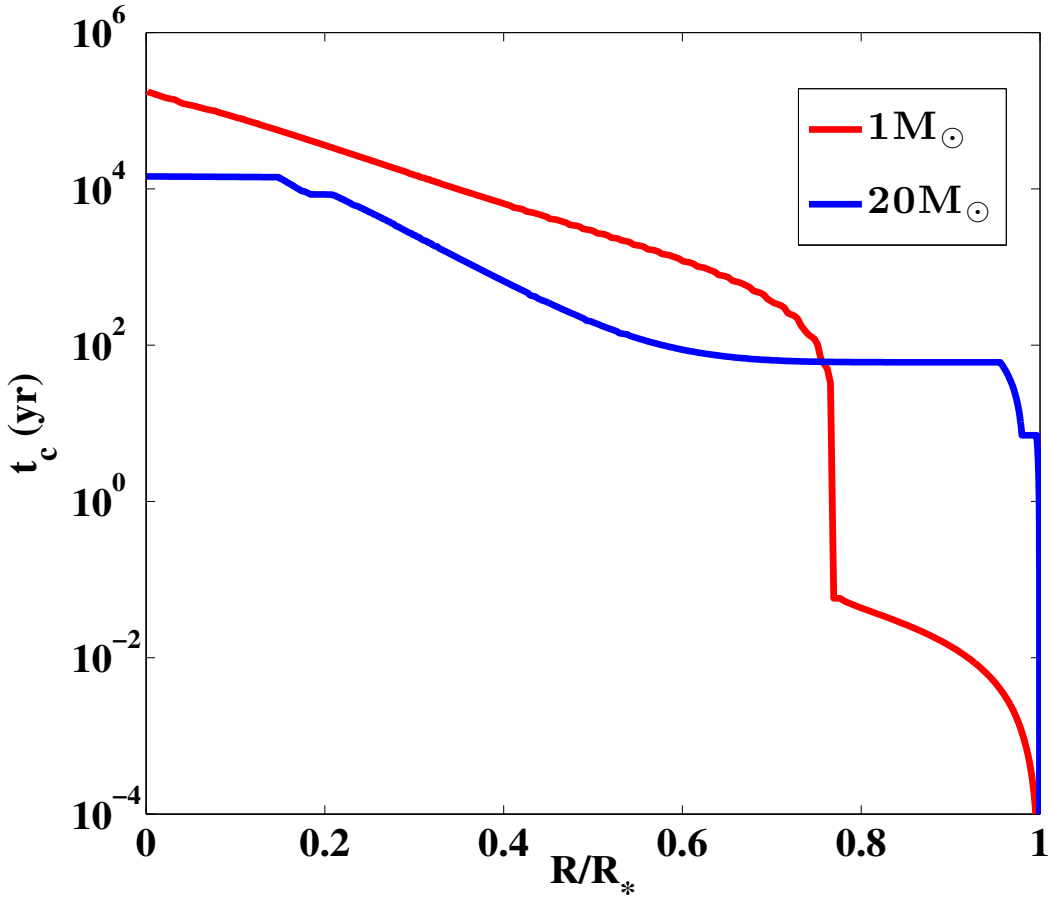

Figure 9.6: The cooling time (t_c) as a function of radius for the two stars in Table 9.1.

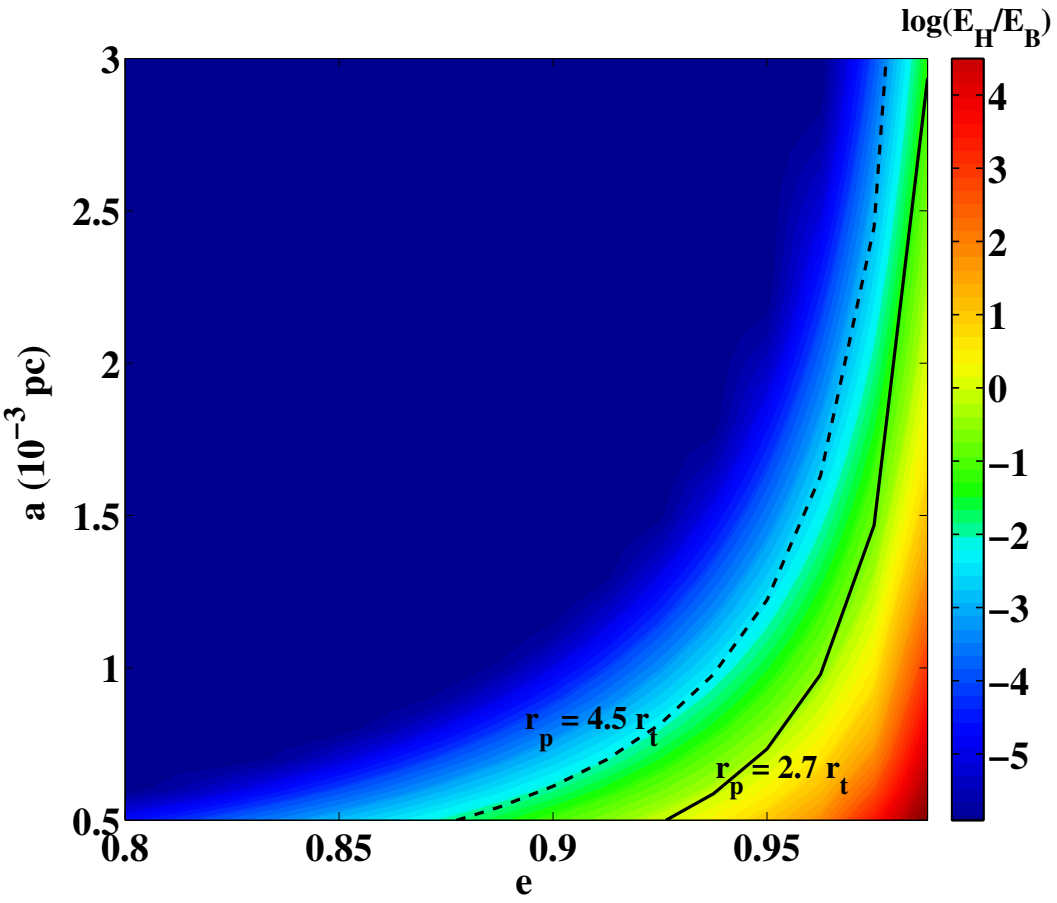

Figure 9.7: Maximum amount of heat gained at saturation in units of the binding energy of the star as a function of its orbital parameters a and e for a $20M_\odot$ star. The solid black line indicates the pericenter distance boundary $r_p = 2.7r_t$ below which the linear tidal excitation formalism is not applicable (Novikov et al. 1992). The dashed black line delineates the threshold $E_H/E_B \sim 0.01$, beyond which the star can potentially be disrupted in $\lesssim 10^6$ pericenter passages. We find that $20M_\odot$ stars are significantly heated at $r_p \sim 4.5r_t$.

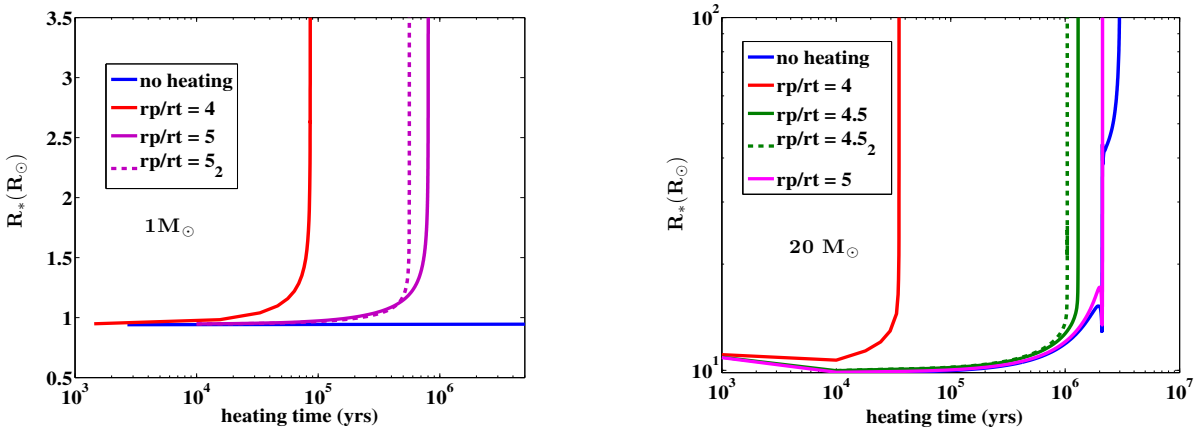

Figure 9.8: Stellar radius versus heating time. *Left panel:* $1M_\odot$ star; *Right panel:* $20M_\odot$ star. Blue lines indicate the radius change by stellar evolution. Requiring the heating time to be shorter than the orbital scattering timescale ($\sim 10^6$ yrs) and the lifetime of the unheated stars, the maximum r_p for which the stellar radius significantly is $\sim 4.5r_t$ for the 20 $M_\odot$ star, and $\sim 5r_t$ for the 1 $M_\odot$ star. At these limiting cases, the dashed lines show results from a second iteration in which $|Q_{nl=2}|^2|K_{nl=2m}|^2$ is updated as the stellar radius increases.

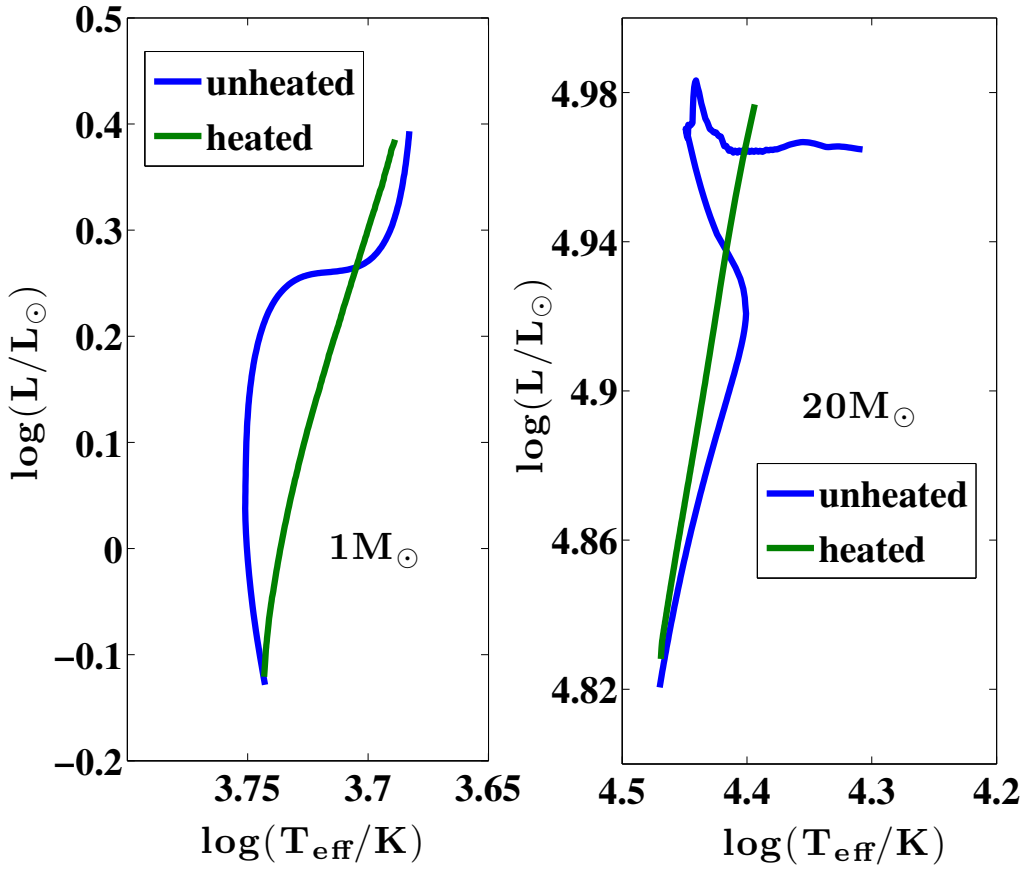

Figure 9.9: HR diagram of heated stars with masses of $1M_\odot$ (left panel) and $20M_\odot$ (right panel). Blue lines indicate the evolution track of giant stars with the same masses as they evolve off the main sequence. The HR diagrams of the heated stars stop at the point when the tidal radii of the heated stars approach $(r_p/2.7)$, at which point the linear tidal excitation approach breaks down.

Chapter 10

Gravitational Wave Heating of Stars and Accretion Disks

This thesis chapter originally appeared in the literature as

Li, G., Kocsis, B & Loeb, A. Gravitational Wave Heating of Stars and Accretion Disks, *Monthly Notices of the Royal Astronomical Society*, 425, 2407, 2012

Abstract

We investigate the electromagnetic (EM) counterpart of gravitational waves (GWs) emitted by a supermassive black hole binary (SMBHB) through the viscous dissipation of the GW energy in an accretion disk and stars surrounding the SMBHB. We account for the suppression of the heating rate if the forcing period is shorter than the turnover time of the largest turbulent eddies. We find that the viscous heating luminosity in

$0.1M_{\odot}$ stars can be significantly higher than their intrinsic luminosity, but still too low to be detected for extragalactic sources. The relative brightening is small for accretion disks.

10.1 Introduction

The coalescence of supermassive black hole binaries (SMBHBs) generates gravitational waves (GW) which are a primary source for the proposed Laser Interferometric Space Antenna (LISA*). SMBHBs are inevitable outcomes of galaxy mergers. Spatially-resolved active galactic nuclei have been observed (Komossa et al. 2003; Bianchi et al. 2008; Green et al. 2010; Koss et al. 2011; Fabbiano et al. 2011). In addition, spectroscopic surveys (Comerford et al. 2009; Smith et al. 2010; Liu et al. 2010b) and observations that combine ground-based imaging show numerous systems containing compelling SMBHB candidates with pc to kpc separations (Rodriguez et al. 2006; Liu et al. 2010a; Shen et al. 2011; Fu et al. 2011; McGurk et al. 2011). Hydrodynamic simulations of galaxy mergers also predict SMBHB pair formation (e.g. Escala et al. 2004, 2005; Di Matteo et al. 2005; Robertson et al. 2006; Hopkins et al. 2006; Callegari et al. 2009; Colpi & Dotti 2011; Blecha et al. 2012).

Electromagnetic (EM) counterparts to GW sources complements the GW detection by determining the host galaxy redshift and the environment of the sources (Kocsis et al. 2006; Phinney 2009). A large variety of EM signatures have been proposed to accompany the coalescence of SMBHBs (Schnittman 2011; Haiman et al. 2009). In the

*http://lisa.nasa.gov/

pre-merger phase, the torques of the SMBHB excavates a hollow region in the disk and leads to periodic accretion across the gap on the orbital timescale (Cuadra et al. 2009; MacFadyen & Milosavljević 2008; Hayasaki et al. 2008). After the merger, the recoil of the black hole remnant and its sudden mass loss due to the final GW burst produce shocks in the accretion disk which lead to EM signals (Bode & Phinney 2007; Lippai et al. 2008; Schnittman & Krolik 2008; Shields & Bonning 2008; O'Neill et al. 2009; Rossi et al. 2010). The recoil of the black hole remnant changes the tidal disruption rate of stars due to the refilling of the loss cone and the wandering of black hole remnant (Stone & Loeb 2011a, 2012; Li et al. 2012). Finally, the infall of gas onto the black hole remnant produces an EM afterglow (Milosavljević & Phinney 2005; Tanaka & Menou 2010).

In this paper, we consider the viscous dissipation of GWs generated by a SMBHB in a neighboring gaseous medium. In particular, the velocity shear induced by GWs in the gas is damped by viscosity. The dissipated GW energy turns into heat, and produces an electromagnetic flare. Unlike other EM counterparts, the brightening here follows promptly within a few hours to days after the coalescence of the SMBHB (Kocsis & Loeb 2008). The effect provides a unique test of general relativity for the interaction of GWs with matter. In § 10.2 and 10.3 we investigate GW dissipation in a gaseous accretion disk and stars in the vicinity of the SMBHB. We examine the suppression of the effect if the forcing period is shorter than the turnover time of the largest eddies (Krolik 2010), in analogy to a similar treatment of tidal heating in binary stars (Zahn 1966; Goldreich & Keeley 1977). Finally, we discuss our conclusions and their implications in § 10.4.

10.2 Method

We start by presenting our approach for estimating the GW heating inside an accretion disk and stars due to turbulent viscosity. Following Kocsis & Loeb (2008), we approximate the GW luminosity by matching the Newtonian inspiral luminosity prior to merger ($t < 0$), the peak luminosity at the merger ($t = 0$) and the decay luminosity afterwards ($t > t_1$), where t_1 can be fixed from this matching procedure. Specifically, in the Newtonian inspiral regime, the luminosity is

$$L_{\rm GW\,inspiral} = \frac{32}{5}\frac{G^4}{c^5}\frac{M^3\mu^2}{a^5}, \tag{10.1}$$

where $M = M_1 + M_2$ is the sum of the masses of the SMBHB members, $\mu = M_1 M_2/M$ is the reduced mass of the SMBHB and a is the separation between the SMBHB, which can be expressed as

$$a = \left[\frac{256}{5}\frac{G^3}{c^5}\mu M^2(t_1 - t)\right]^{1/4}, \tag{10.2}$$

assuming a circular orbit. The peak luminosity is approximated from numerical simulations (Berti et al. 2007; Buonanno et al. 2007) as

$$L_{\rm GW\,peak} \approx 10^{-3}\frac{c^5}{G}\left(\frac{\mu}{M}\right)^2, \tag{10.3}$$

and the ringdown luminosity is set to be

$$L_{\rm GW\,ringdown} = L_{\rm GW\,peak}\exp\left(-\frac{c(t - t_1)}{5R_{\rm g}}\right), \tag{10.4}$$

where $R_{\rm g} = GM/c^2$ is the gravitational radius of the SMBHB. The peak luminosity is modified by a factor of two (Berti et al. 2007; Buonanno et al. 2007) due to different magnitudes and orientation of the spin of the SMBHB. In this paper, we assume the masses of the two black holes are the same.

With the approximated expression of GW luminosity as a function of time, the dissipation of GW energy inside a viscous medium can be calculated by solving the weak-field Einstein equation (Hawking 1966; Weinberg 1972):

$$\dot{e}_{\rm heat} = \frac{16\pi G\eta}{c^2} e_{\rm GW}, \tag{10.5}$$

where $\dot{e}_{\rm heat}$ is the dissipation rate, η is the dynamical viscosity and $e_{\rm GW}$ is the GW energy density. $e_{\rm GW}$ can be obtained from $e_{\rm GW} = Y(\theta)\frac{L_{\rm GW}}{4\pi c r^2}$, where θ is the angle relative to the total angular momentum vector, $Y(\theta) = 5/2[\sin^8(\theta/2) + \cos^8(\theta/2)]$. We use the average value $\langle Y\rangle = 1$ below. With $L_{\rm GW}$ derived, the only unknown parameter is the dynamical viscosity of the medium that the GW passes through. The dissipation rate of the GW energy gives the heating rate of any gaseous medium such as an accretion disk and stars.

Next, we estimate the dynamical viscosity for stars. We use stellar models produced by Modules for Experiments in Stellar Astrophysics (MESA[†]) (Paxton et al. 2011), a 1D stellar evolution code, and we consider stellar models, whose properties are included in Table 10.1. We associate the dynamical viscosity with the mixing length theory diffusion coefficient, which is directly provided in the simulated models by MESA. When the period of the driving force is smaller than the largest eddy turnover time, the eddy viscosity depends on the ratio of the period to the largest eddy turnover time in one of two possible ways:

$$\eta = \eta_i \ \min\left[\left(\frac{\tau_{\rm GW}}{2\tau_l}\right), 1\right], \tag{10.6}$$

or

$$\eta = \eta_i \ \min\left[\left(\frac{\tau_{\rm GW}}{2\pi\tau_l}\right)^2, 1\right], \tag{10.7}$$

[†]http://mesa.sourceforge.net/

where η_i is the intrinsic viscosity in the absence of shear force with short period, τ_l is the largest eddy turnover timescale and $\tau_{\rm GW}$ is the shear force period, which is calculated as $2\pi/\omega_{\rm GW}$, where $\omega_{\rm GW} = 2\sqrt{GM/a^3}$ in the inspiral phase $a < 6R_{\rm g}$ and $0.25/(GM/c^3)$] after the ringdown, and extrapolate linearly during the transition according to Buonanno et al. (2007). The viscosity scaling given by Eq. (10.6) is discussed in Zahn (1966, 1989); Zahn & Bouchet (1989) and Eq. (10.7) in Goldreich & Keeley (1977); Goldreich & Nicholson (1989). Observations are more consistent with Zahn's scaling for pulsating stars in the red edge of the instability strip (Gonczi 1982), for tidal circularization of binary stars (Verbunt & Phinney 1995; Meibom & Mathieu 2005), while the damping of the solar p-mode oscillations is more consistent with the Goldreich's scaling (Goldreich & Kumar 1988; Goldreich et al. 1994). Recently, Penev et al. (2009) studied turbulent viscosity in low mass stars using the perturbative approach of Goodman & Oh (1997), taking into account compressible fluid and anisotropic viscosity. Their simulation suggests a linear scaling. However, Ogilvie & Lesur (2012) found results more consistent with Goldreich's scaling when studying the limit of a low amplitude short oscillation period shear. We considered both scalings for stars in this paper.

With the viscosity for stars and $L_{\rm GW}(t)$ in hand, the GW heating rate can be estimated using Eq. (10.5). The EM luminosity increase can be estimated by solving the radiative transfer equation:

$$t_c(r)\frac{d}{dt}\Delta f(r) + \Delta f(r) = \dot{e}_{\rm heat}, \tag{10.8}$$

$$L_{\rm GWH} = \int_{\rm star} \Delta f(r)\ dV, \tag{10.9}$$

where $\Delta f(r)$ is the excess EM signal produced per unit volume as a function of location in the star, $L_{\rm GWH}$ is the excess EM luminosity associated to GW heating, and $t_c(r)$ is the

cooling time as a function of the location, which characterizes the time it takes for heat to travel to the surface. We estimate the latter by taking the integral of the minimum of the photon diffusion time, $dr/c \times [\tau(r) - (R_* - r)\frac{d\tau(r)}{dr}]$, and the turbulent convection time, $dr/v_c(r)$, in each spherical shell inside the star, where the optical depth, $\tau(r)$, and the convective velocity, $v_c(r)$ are obtained from the MESA simulation, and R_* is the radius of the star.

Finally, we estimate the heating in accretion disks. We adopt the geometrically thin, optically thick, standard accretion disk model, where the angular momentum transport is associated with the internal stresses due to turbulence (Shakura & Sunyaev 1973; Novikov & Thorne 1973). Heat is dissipated locally by turbulent viscosity, and transported vertically outward by photon diffusion or advection. Specifically, the viscosity of the accretion disk is

$$\eta_i(r) = \frac{2}{3}\frac{\alpha P(r)}{\Omega(r)}, \tag{10.10}$$

where $\Omega^2(r) = GM/r^3$ is the angular velocity, α is a constant which we assume to be 0.3 (King et al. 2007), and P is the total (gas+radiation) pressure in the α disk model, and gas pressure in the β model. In these models, the physical characteristics of the disk is fixed by the following parameters: the accretion rate in Eddington units ($\dot{m}$), the radiation efficiency (ϵ), and the SMBHB mass (M) (Goodman 2003; Goodman & Tan 2004). We set $\dot{m}$ to be 0.1, ϵ to be 0.1, and discuss the effects caused by different SMBHB masses.

Similarly to stars, we account for the frequency dependence of viscosity when the period of the driving force is smaller than the largest eddy turnover time, and estimate the effective viscosity according to the perturbative methods as discussed in Goodman

& Oh (1997). Specifically, for incompressible fluid with isotropic viscosity, the viscosity as a function of driving force frequency can be expressed in terms of the frequency spectrum of the average kinetic energy per unit mass. For accretion disks, where the Kolmogorov scalings may not be applicable to obtain the energy spectrum, we adopt the energy spectrum from recent magnetohydrodynamic (MHD) disk simulations. Flock et al. (2011) present a full 2π three dimensional simulation on a stratified accretion disk, where the turbulence is driven by magnetorotational instability (MRI) and the kinetic spectra is obtained in the ϕ direction, and Fromang (2010) investigate the MRI in a shearing box with zero net flux. Flock et al. (2011) and Fromang (2010) estimate the kinetic energy spectrum exponent to be 11/9 and 1.5, respectively. We estimate the viscous heating in accretion disk with the Flock et al. (2011) exponent as well as the Kolmogorov scaling exponent 2.

Similarly to the calculation for stars, the GW heating rate can be estimated using Eq. (10.5). The corresponding EM signals can be estimated by solving the radiative transfer equation following Kocsis & Loeb (2008):

$$t_c(r)\frac{d}{dt}\Delta F(r,t) + \Delta F(r,t) = H\dot{e}_{\rm heat}(r,t), \tag{10.11}$$

$$L_{\rm GWH}(t) = \int_{r_{\rm min}}^{r_{\rm max}} 2\pi r \Delta F(r,t)\, dr, \tag{10.12}$$

where $F(r)$ is the excess EM flux due to GW heating in the accretion disk, H is the scaleheight, $L_{\rm GWH}$ is the corresponding excess EM luminosity, and $t_c(r)$ is the cooling time. Here, we assume the disk is face on, and account for the different light-travel time from different annuli in the disk. The brightening can be somewhat larger in an inclined or edge-on configuration (by up to a factor of ~ 3) where the peak GW flux is observed coincidentally at the inner and outer radii along the line of sight (Kocsis & Loeb 2008).

10.3 Results

First, we consider the GW heating of nearby stars. As an example, we examine the GW heating light curve for a 0.1 $M_\odot$ star (stellar model 2) surrounding an $M = 10^7$ or an $10^9 M_\odot$ SMBHB, respectively. Using Eqs. (10.8) and (10.9), we calculate $F(t)$ and plot the GW heating light curve in Figure 10.1. We assume that the star is located at $d = 5$ tidal radii from the SMBHB (corresponds to 320 and 15 $R_{\rm g}$ for a 10^7 and a 10^9 $M_\odot$ SMBHB, respectively). Note that since the GW luminosity is proportional to $(d/R_{\rm g})^{-2}$, the GW heating effect is much larger around more massive SMBHBs because the viscosity suppression for a high mass SMBHB is smaller.

Figure 10.1 shows that the excess luminosity of the star surrounding the $10^9 M_\odot$ SMBHB is much higher than the intrinsic luminosity of the star ($L = 2.6 \times 10^{30}$erg s^{-1}). In fact, the net dissipated GW energy can exceed the gravitational binding energy near the stellar surface, and could generate a stellar wind. However, as the viscosity is strongly suppressed in the stellar interior ($\frac{\tau_{\rm GW}}{\tau_l(r)} \ll 1$ for $r \lesssim 0.99 R_{star}$), the heating effect is negligible to the star as a whole. In addition, these stars are very faint; the absolute peak GW heating luminosity in the star is typically too faint to be observed outside of the Galaxy.

Since the turnover time of turbulent eddies is much longer in the interior of the star than that at the surface, the energy is mostly dissipated at the surface. Since the cooling time near the surface (~ 200 s) is short compared to the peak GW timescale ($\sim 10\, R_g/c \sim 500\,{\rm s}\, M_{\rm BH}/10^7\, M_\odot$), the light curve of the star closely tracks the luminosity curve of the GW. When the GW driving period is shorter than the eddy turnover time, the viscosity caused by the eddy depends on the ratio $\tau_{\rm GW}/\tau_l$, where the exact scaling is

uncertain as discussed in § 10.2. For stars surrounding a $10^9\,M_\odot$ SMBHB, the differences between the two scalings are smaller as the period of peak GW emission for this SMBHB mass is more comparable to the surface eddy turnover time in a $0.1\,M_\odot$ star.

To examine the influence of the GW heating in different types of stars, we consider stellar models of different stellar masses and ages as included in Table 1. We include the extreme cases with $0.1\,M_\odot$ and $100\,M_\odot$ stars. We plot the ratio of the peak heating luminosity to the intrinsic luminosity for different stellar models in Figure 2 with Zahn's scaling. We find that the influence of the GW heating is more significant as the metallicity of the star increases, and GW heating is not significant for very massive ($M_* \geq 100 M_\odot$) stars.

Next, we discuss the heating effects in accretion disks. For α and β disks, we solve Eqs. (10.11) and (10.12) for the heating flux, and plot the heating light curve of the disk due to GW heating in Figure 3. The accretion disk is punctured with an inner hole. This geometry is essentially "frozen" during the final GW merger timescale with a gap radius $\gtrsim 100M$ for α–disks (Milosavljević & Phinney 2005). Recent MHD simulations by Noble et al. (2012) indicate that the stresses may be enhanced in a binary, such that gap decoupling occurs further in, at $20R_{\rm g}$. We optimistically adopt this value for our estimates, which implies a larger heating rate than that for a larger gap radius. We integrate over the accretion disks between the inner and outer boundary. We set the latter to $2 \times 10^4 R_{\rm g}$, but this value does not influence our result as the heating in the outer accretion disk is negligible. We include the different light travel time from different accretion disk surface elements along the line of sight. Our calculation of the heating in the accretion disks improves the simplified treatment of Kocsis & Loeb (2008) by including the dependence of viscosity on the ratio of the GW driving period to the

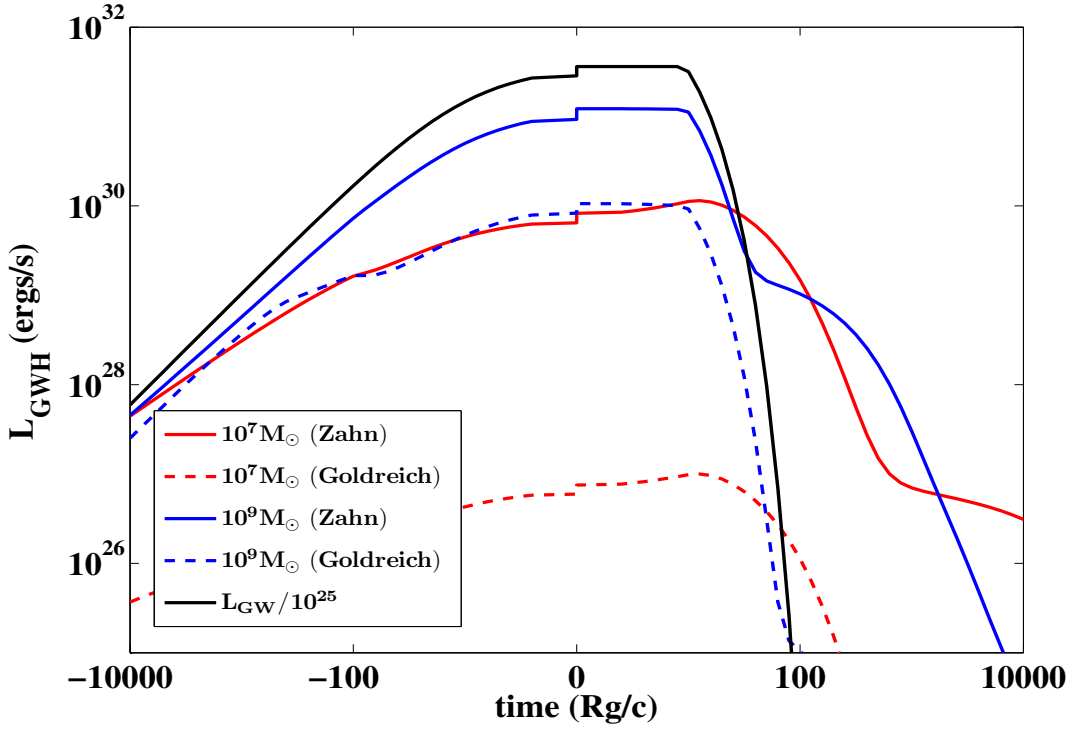

Figure 10.1: The light curve of a GW heated star (based on star model 2 with an intrinsic luminosity: $L = 2.6 \times 10^{30}$erg s^{-1}). The time axis is in units of R_g/c, and is shown on a logarithmic scale at both negative and positive values (causing the discontinuity at $t = 0$). The star is located 5 tidal radii away from the SMBHB (320 and 15 R_g for a $10^7\,M_\odot$ and $10^9\,M_\odot$ SMBHB, respectively). The black line indicates the GW luminosity scaled down by 25 order of magnitude in order to fit in this figure. The red and blue lines indicate the light curve of a star surrounding a 10^7 and a $10^9\,M_\odot$ SMBHB, respectively, with solid and dashed lines corresponding to the viscosity dependence with $(\tau_{GW}/2\tau_l)$ and $(\tau_{GW}/2\pi\tau_l)^2$, respectively. The light curve closely tracks the GW light curve. Interestingly, the peak luminosity surrounding the $10^9\,M_\odot$ SMBHB is much higher than the intrinsic luminosity of this star.

Table 10.1:: Properties of stellar models

No.	Mass ($M_\odot$)	Metallicity (Z)	Radius ($R_\odot$)	Luminosity ($L_\odot$)	Age (yrs)
1	0.1	0.16	3.3	0.00079	2×10^4
2	0.1	0.16	3	0.00066	5×10^6
3	0.1	0.16	0.57	5.5×10^{-5}	2×10^9
4	0.1	0.01	2.4	0.43	2×10^4
5	0.1	0.01	0.44	0.022	5×10^6
6	0.1	0.01	0.12	0.0012	2×10^9
7	100	0.04	21	1.4×10^6	1×10^4
8	100	0.04	36	1.7×10^6	1×10^6
9	100	0.04	960	2.1×10^6	2×10^6

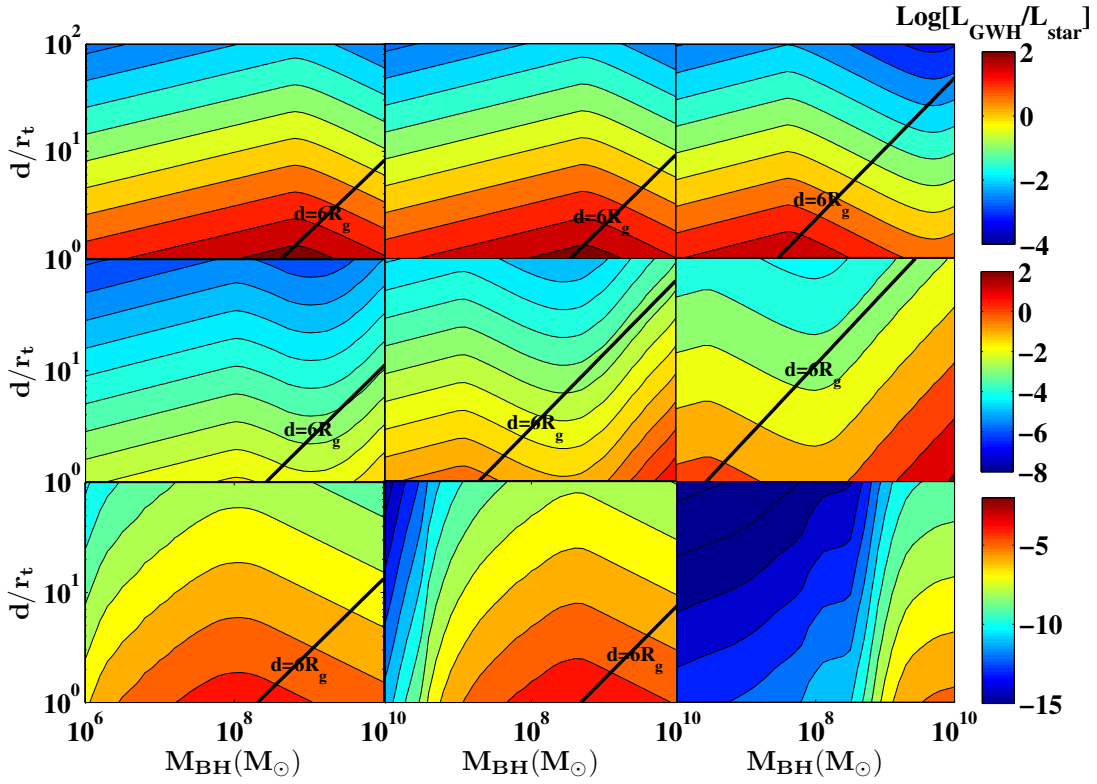

Figure 10.2: Ratio of the peak GW heating luminosity to the intrinsic stellar luminosity. The horizontal axis shows the mass of the SMBHB, and the vertical axis plots the distance (d) between the star and the SMBHB in units of the tidal radius (r_t). First row: model 1, 2, 3; second row: model 4, 5, 6, third row: model 7, 8, 9. Solid black line indicates where the distance between the star and black hole binary is 6 $R_{\rm g}$, the radius of the innermost stable circular orbit (ISCO) around a non-spinning black hole. In the last panel, the points in the figure lie out of 6 $R_{\rm g}$, and so the black line is not shown. The first two rows correspond to 0.1 $M_\odot$ stars with metallicity $Z = 0.16$ and $Z = 0.01$ respectively, and the last row corresponds to 100 $M_\odot$ stars. GW heating is most significant for high metallicity low mass stars.

largest eddy turnover time, which suppresses the dissipation of GWs. We consider two cases in this plot. Following the perturbative turbulence derivation by Goodman & Oh (1997), the power-law index is 2 for Kolmogorov turbulent scaling, and $\frac{11}{9}$ according to MHD disk simulation by Flock et al. (2011). The eddy turnover time increases rapidly as the radius increases, and so the suppression of the GW heating is less significant for disks truncated closer to the SMBHB. Therefore, the heating luminosity is more significant for disks that are truncated closer to the SMBHB.

10.4 Discussion

In this paper, we considered the dissipation of GWs in an accretion disk or stars surrounding a SMBHB. We have found that the GW heating luminosity of the accretion disk and stars are low, and make no significant EM flare relative to their intrinsic luminosity except for low mass stars ($\sim 0.1 M_\odot$). The integrated excess luminosity from heated low mass stars is too low to be observed in galactic nuclei as they are faint. Assuming a Bahcall-Wolf distribution of stars or assuming a collision timescale larger than 1 Myr, we find that only a few stars are expected to be within 5 tidal radii of a coalescing SMBHB, where the GW heating effect is significant. Therefore the overall brightening of the stellar cluster is negligible.

In order to be heated significantly by GWs, the stars need to be close to the SMBHB. One possible avenue is that stars get caught in mean motion resonances (such as Trojan resonances) and move inwards as the SMBHB merge (Seto & Muto 2010; Schnittman 2010). This is only effective for SMBHB with an unequal mass ratio $q \lesssim 10^{-2}$; the stars get ejected before the coalescence otherwise. Another possibility is for stars to get

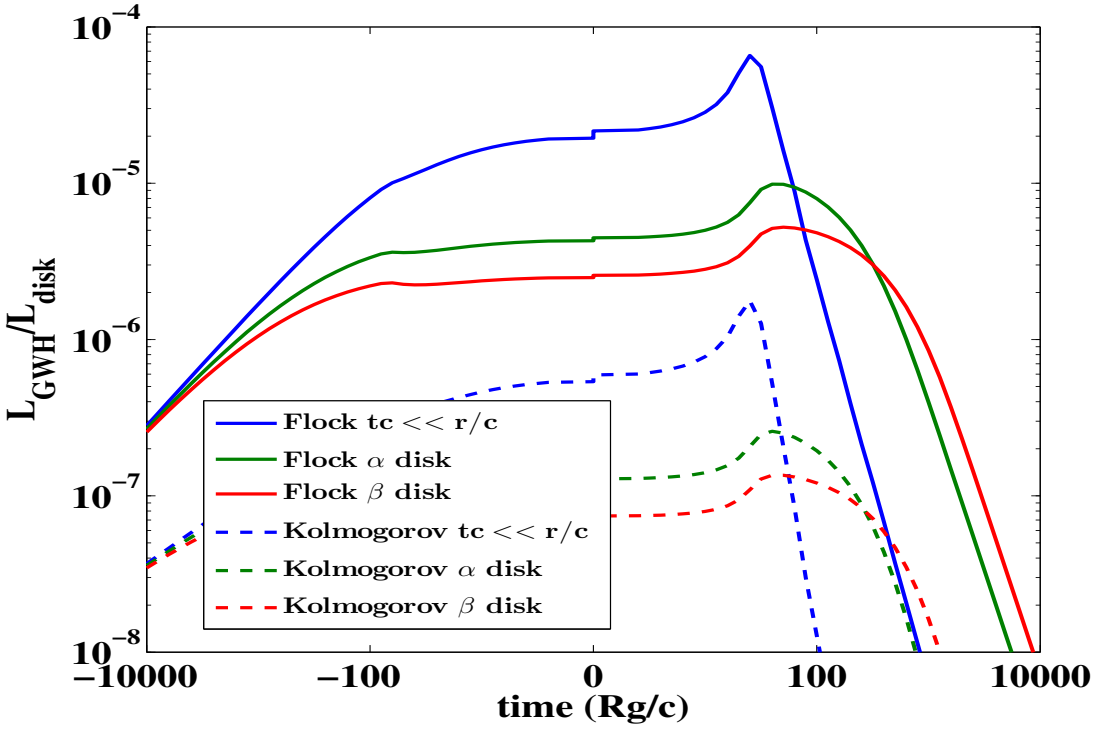

Figure 10.3: The excess luminosity relative to the disk luminosity due to GW heating on an accretion disk (inner disk truncated at 20 $R_{\rm g}$) before ($t < 0$) and after ($t > 0$) the binary coalescence event. The time axis is shown on a logarithmic scale at both negative and positive values (in units of $R_{\rm g}$). The SMBHB mass is $10^7 M_\odot$. Solid lines corresponds to the frequency dependence $(\tau_{\rm GW}/2\pi\tau_l)^{\frac{11}{9}}$ derived according to the energy spectrum of accretion disk based on MHD simulations by Flock et al. (2011), and the dashed lines correspond to the scaling $(\tau_{\rm GW}/2\pi\tau_l)^2$, assuming Kolmogorov turbulence.

captured or form in the outer parts of accretion disks, and migrate inwards by processes analogous to planetary migration (Miralda-Escudé & Kollmeier 2005; Karas & Šubr 2001; Levin 2007).

We assumed that GW energy is dissipated locally through turbulent viscosity. The damping of shear stress by eddy viscosity in stars was found to be consistent with observations in the context of the tidal circularization of binaries (Verbunt & Phinney 1995; Meibom & Mathieu 2005). The underlying accretion disk model is uncertain since the disk structure is unstable to both thermal and viscous instabilities. Recently, Blaes et al. (2011) found that radiation-dominated disks differ significantly from the standard disk models, where the dissipation associated with the turbulent cascade and radiative damping dissipate energy non-locally. It remains to be seen whether the GW heating effect is more prominent in alternative disk models.

Acknowledgments

We thank Eliot Quataert, Sterl Phinney and Paul Groot for helpful discussions. This work was supported in part by NSF grant AST-0907890 and NASA grants NNX08AL43G and NNA09DB30A. BK acknowledges support from NASA through Einstein Postdoctoral Fellowship Award Number PF9-00063 issued by the Chandra X-ray Observatory Center, which is operated by the Smithsonian Astrophysical Observatory for and on behalf of the National Aeronautics Space Administration under contract NAS8-03060.

References

Adams, F. C. 2010, ARA&A, 48, 47

Adams, F. C., & Fatuzzo, M. 1996, ApJ, 464, 256

Adams, F. C., & Laughlin, G. 2001, Icarus, 150, 151

Adams, F. C., Proszkow, E. M., Fatuzzo, M., & Myers, P. C. 2006, ApJ, 641, 504

Adams, F. C., & Spergel, D. N. 2005, AsBio, 5, 497

Agnor, C. B., & Lin, D. N. C. 2012, ApJ, 745, 143, 1110.5042

Albrecht, S., Winn, J. N., Johnson, J. A., Howard, A. W., Marcy, G. W., Butler, R. P., Arriagada, P., Crane, J. D., Shectman, S. A., Thompson, I. B., Hirano, T., Bakos, G., and Hartman, J. D. (2012). Obliquities of Hot Jupiter Host Stars: Evidence for Tidal Interactions and Primordial Misalignments. ApJ, 757:18.

Albrecht, S., Winn, J. N., Marcy, G. W., Howard, A. W., Isaacson, H., & Johnson, J. A. 2013, ApJ, 771, 11, 1302.4443

Alexander T., Livio M., 2001, ApJ, 560, L143

Alexander T., Morris M., 2003, ApJ, 590, L25

Allen, L. et al. 2007, in Protostars & Planets V, ed. B. Reipurth, D. Jewitt, K. Keil, pp. 361–376, (Tucson: Univ. Arizona Press)

Antonini F., Lombardi Jr. J. C., Merritt D., 2011, ApJ, 731, 128

Antognini J. M., Shappee B. J., Thompson T. A., Amaro-Seoane P., 2014, MNRAS, 439, 1079

Antonini F., 2013, ApJ, 763, 62

Antonini F., Murray N., Mikkola S., 2014, ApJ, 781, 45

Antonini F., Perets H. B., 2012, ApJ, 757, 27

Arras P., Flanagan E. E., Morsink S. M., Schenk A. K., Teukolsky S. A., Wasserman I., 2003, ApJ, 591, 1129

Bade, N., Komossa, S., and Dahlem, M. (1996). Detection of an extremely soft X-ray outburst in the HII-like nucleus of NGC 5905. A&A, 309:L35–L38.

Barenblatt, G. I. 2003, Scaling (Cambridge: Cambridge Univ. Press)

Bartko H., Martins F., Trippe S., et al. 2010, ApJ, 708, 834

Barclay, T. et al. 2013, ApJ, 768, 101, 1304.4941

Bartko H., Perrin G., Brandner W., et al. 2009, New Astron. Rev, 53, 301

Bate, M. R., Lodato, G., & Pringle, J. E. 2010, MNRAS, 401, 1505, 0909.4255

Batalha, N. M., Rowe, J. F., Bryson, S. T.. Barclay, T. et al. 2013, ApJS, 204, 24

Battinelli, P., & Capuzzo-Dolcetta, R. 1991, MNRAS, 249, 76

Batygin, K., & Laughlin, G. 2008, ApJ, 683, 1207

Batygin, K., & Brown, M. E. 2010, ApJ, 716, 1323

Batygin, K., Brown, M. E., & Fraser, W. C. 2011, ApJ, 738, 13, 1106.0937

Batygin, K., Brown, M. E., & Betts, H. 2012, ApJ, 744, L3, 1111.3682

Batygin, K. 2012, Nature, 491, 418

Batygin, K., & Morbidelli, A. 2013, A&A, 556, 28

Batygin, K., Morbidelli, A., & Tsiganis, K. 2011, A&A, 533, 8

Batygin, K. (2012). A primordial origin for misalignments between stellar spin axes and planetary orbits. Nature, 491:418–420.

Bear, E., & Soker, N. 2011a, MNRAS, 414, 1788, 1102.5487

Bear, E., Kashi, A., and Soker, N. (2011). Mergerburst transients of brown dwarfs with exoplanets. MNRAS, 416:1965–1970.

——. 2012, ApJ, 749, L14, 1202.1168

Berti E., Cardoso V., Gonzalez J. A., Sperhake U., Hannam M., Husa S., Brügmann B., 2007, Phys. Rev. D, 76, 064034

Bianchi S., Chiaberge M., Piconcelli E., Guainazzi M., Matt G., 2008, MNRAS, 386, 105

Blaes, O., Lee, M. H., and Socrates, A. (2002). The Kozai Mechanism and the Evolution of Binary Supermassive Black Holes. ApJ, 578:775–786.

Blaes O., Krolik J. H., Hirose S., Shabaltas N., 2011, ApJ, 733, 110

Blecha L., Loeb A., Narayan R., 2013, MNRAS, 429, 2594

Bloom J. S., Giannios D., Metzger B. D., et al. 2011, Science, 333, 203

Bode N., Phinney S., 2007, APS April Meeting Abstracts, 1010

Bode J. N., Wegg C., 2014, MNRAS, 438, 573

Boley, A. C., Payne, M. J., and Ford, E. B. (2012). Interactions between Moderate- and Long-period Giant Planets: Scattering Experiments for Systems in Isolation and with Stellar Flybys. ApJ, 754:57.

Bonfils, X. et al. 2013, in European Physical Journal Web of Conferences, Vol. 47, European Physical Journal Web of Conferences, 5004

Borucki, W. J. et al. 2013, Science, 340, 587, 1304.7387

——. 2012, ApJ, 745, 120, 1112.1640

Boué, G., & Fabrycky, D. 2014, ArXiv e-prints, 1405.7636

Bowler, B. P. et al. 2010, ApJ, 709, 396, 0912.0518

Brasser, R., Morbidelli, A., Gomes, R., Tsiganis, K., & Levison, H. F. 2009, A&A, 507, 1053, 0909.1891

Brasser, R., & Walsh, K. J. 2011, Icarus, 213, 423, 1102.0868

Brasser, R., Duncan, M. J., Levison, H. F., Schwamb, M. E., & Brown, M. E. 2012, Icarus, 217, 1

Breslau, A., Steinhausen, M., Vincke, K., & Pfalzner, S. 2014, A&A, 565, 130

Brockamp M., Baumgardt H., Kroupa P., 2011, MNRAS, 418, 1308

Brouwer, D., & van Woerkom, A. J. J. 1950, Astron. Papers Amer. Ephem., 13, 81

Brown, W. R., Geller, M. J., Kenyon, S. J., & Kurtz, M. J. 2005, ApJ, 622, L33, astro-ph/0501177

Bruhwiler, D. L., & Cary, J. R. 1989, Physica D Nonlinear Phenomena, 40, 265

Buonanno A., Cook G. B., Pretorius F., 2007, Phys. Rev. D, 75, 124018

Burkart J., Quataert E., Arras P., Weinberg N. N., 2012, MNRAS, 421, 983

Callegari S., Mayer L., Kazantzidis S., Colpi M., Governato F., Quinn T., Wadsley J., 2009, ApJ, 696, L89

Cameron, A.G.W., & Truran, J. W. 1977, Icarus, 30, 447

Campbell, B., Walker, G. A. H., & Yang, S. 1988, ApJ, 331, 902

Cary, J. R., Escande, D. F., & Tennyson, J. L. 1986, Phys. Rev. A, 34, 4256

Chabrier, G. 2003, PASP, 115 763

Chambers, J. E., & Migliorini, F. 1997, in Bulletin of the American Astronomical Society, Vol. 29, AAS/Division for Planetary Sciences Meeting Abstracts #29, 1024–+

Chambers, J. E. 1999, MNRAS, 304, 793

Chandler, M. A., & Sohl, L. E. 2000, J. Geophys. Res., 105, 20737

Chatterjee, S., Ford, E. B., Geller, A. M., & Rasio, F. A. 2012, MNRAS, 427, 1587

Chaplin, W. J. et al. 2013, ApJ, 766, 101, 1302.3728

Chatterjee, S., Ford, E. B., Matsumura, S., & Rasio, F. A. 2008, ApJ, 686, 580, arXiv:astro-ph/0703166

Chirikov, B. V. 1979, Phys. Rep., 52, 263

Cenko, S. B., Krimm, H. A., Horesh, A., Rau, A., Frail, D. A., Kennea, J. A., Levan, A. J., Holland, S. T., Butler, N. R., Quimby, R. M., Bloom, J. S., Filippenko, A. V., Gal-Yam, A., Greiner, J., Kulkarni, S. R., Ofek, E. O., Olivares E., F., Schady, P., Silverman, J. M., Tanvir, N. R., and Xu, D. (2012). Swift J2058.4+0516: Discovery of a Possible Second Relativistic Tidal Disruption Flare? ApJ, 753:77.

Chang P., 2009, MNRAS, 393, 224

Chatterjee, S., Ford, E. B., and Rasio, F. A. (2011). How planet-planet scattering can create high-inclination as well as long-period orbits. In Sozzetti, A., Lattanzi, M. G., and Boss, A. P., editors, *IAU Symposium*, volume 276 of *IAU Symposium*, pages 225–229.

Chen, X., Madau, P., Sesana, A., and Liu, F. K. (2009). Enhanced Tidal Disruption Rates from Massive Black Hole Binaries. ApJ, 697:L149–L152.

Chen, X., Sesana, A., Madau, P., and Liu, F. K. (2011). Tidal Stellar Disruptions by Massive Black Hole Pairs. II. Decaying Binaries. ApJ, 729:13.

Chen X., Liu F. K., 2013, ApJ, 762, 95

Chirikov, B. V. 1979, Phys. Rep., 52, 263

Christensen-Dalsgaard J., 2008, Ap&SS, 316, 113

Cohn H., Kulsrud R. M., 1978, ApJ, 226, 1087

Colombo, G. 1966, AJ, 71, 891

Colpi M., Callegari S., Dotti M., Mayer L., 2009, Classical and Quantum Gravity, 26, 094029

Colpi, M. and Dotti, M. (2011). Massive Binary Black Holes in the Cosmic Landscape. *Advanced Science Letters*, 4:181–203.

Comerford J. M., Gerke B. F., Newman J. A., Davis M., Yan R., Cooper M. C., Faber S. M., Koo D. C., Coil A. L., Rosario D. J., Dutton A. A., 2009, ApJ, 698, 956

Correia, A. C. M., Laskar, J., Farago, F., and Boué, G. (2011). Tidal evolution of hierarchical and inclined systems. *Celestial Mechanics and Dynamical Astronomy*, 111:105–130.

Craig, J., & Krumholz, M. R. 2013, ApJ, 769, 150

Cuadra J., Armitage P. J., Alexander R. D., Begelman M. C., 2009, MNRAS, 393, 1423

Ćuk, M., & Stewart, S. T. 2012, Science, 338, 1047

Cumming, A., Butler, R. P., Marcy, G. W., Vogt, S. S., Wright, J. T., & Fischer, D. A. 2008, PASP, 120, 531, 0803.3357

Dauphas, N., & Chaussidon, M. 2011, AREPS, 39, 351

Dawson, R. I. 2014, ApJ, 790, L31, 1405.1735

Di Matteo T., Springel V., Hernquist L., 2005, Nature, 433, 604

Donley J. L., Brandt W. N., Eracleous M., Boller T., 2002, AJ, 124, 1308

Dressing, C. D., & Charbonneau, D. 2013, ApJ, 767, 95, 1302.1647

——. 2015, ArXiv e-prints, 1501.01623

Dukes, D., & Krumholz, M. R. 2012, ApJ, 754, 56

Duquennoy, A., & Mayor, M. 1991, A&A, 248, 485

Diener P., Kosovichev A. G., Kotok E. V., Novikov I. D., Pethick C. J., 1995, MNRAS, 275, 498

Dziembowski W., 1982, Acta Astron, 32, 147

Efroimsky, M., & Williams, J. G. 2009, Celestial Mechanics and Dynamical Astronomy, 104, 257, 0803.3299

Eggleton, P. P., Kiseleva, L. G., and Hut, P. (1998). The Equilibrium Tide Model for Tidal Friction. ApJ, 499:853.

Eggleton, P. P. and Kiseleva-Eggleton, L. (2001). Orbital Evolution in Binary and Triple Stars, with an Application to SS Lacertae. ApJ, 562:1012–1030.

Eilon E., Kupi G., Alexander T., 2009, ApJ, 698, 641

Eisenhauer F., Genzel R., Alexander T., et al. 2005, ApJ, 628, 246

Escala A., Larson R. B., Coppi P. S., Mardones D., 2004, ApJ, 607, 765

—, 2005, ApJ, 630, 152

Fabbiano G., Wang J., Elvis M., Risaliti G., 2011, Nature, 477, 431

Fabrycky, D. and Tremaine, S. (2007). Shrinking Binary and Planetary Orbits by Kozai Cycles with Tidal Friction. ApJ, 669:1298–1315.

Fabrycky, D. C., & Winn, J. N. 2009, ApJ, 696, 1230, 0902.0737

Fanale, F. P., Salvail, J. R., Banerdt, W. B., & Saunders, R. S. 1982, Icarus, 50, 381

Fang, J., & Margot, J.-L. 2012, ApJ, 761, 92, 1207.5250

Fatuzzo, M., & Adams, F. C. 2008, ApJ, 675, 1361

Ferrarese, L., & Ford, H. 2005, Space Sci. Rev., 116, 523, astro-ph/0411247

Ferrarese, L., & Merritt, D. 2000, ApJ, 539, L9, astro-ph/0006053

Fielding, D. B., McKee, C. F., Socrates, A., Cunningham, A. J., & Klein, R. I. 2014, ArXiv e-prints, 1409.5148

Flock M., Dzyurkevich N., Klahr H., Turner N. J., Henning T., 2011, ApJ, 735, 122

Ford, E. B., Kozinsky, B., and Rasio, F. A. (2000). Secular Evolution of Hierarchical Triple Star Systems. ApJ, 535:385–401.

Ford, E. B. and Rasio, F. A. (2008). Origins of Eccentric Extrasolar Planets: Testing the Planet-Planet Scattering Model. ApJ, 686:621–636.

Francois, L. M., Walker, J. C. G., & Kuhn, W. R. 1990, J. Geophys. Res., 95, 14761

Frank J., Rees M. J., 1976, MNRAS, 176, 633

Freitag M., Amaro-Seoane P., Kalogera V., 2006, ApJ, 649, 91

Fritz T. K., Gillessen S., Dodds-Eden K., Martins F., Bartko H., Genzel R., Paumard T., Ott T., Pfuhl O., Trippe S., Eisenhauer F., Gratadour D., 2010, ApJ, 721, 395

Fromang S., 2010, A&A, 514, L5

Fu H., Zhang Z.-Y., Assef R. J., Stockton A., Myers A. D., Yan L., Djorgovski S. G., Wrobel J. M., Riechers D. A., 2011, ApJ, 740, L44

Fuller J., Lai D., 2011, MNRAS, 412, 1331

Fuller J., Lai D., 2012, MNRAS, 420, 3126

Gebhardt, K. et al. 2000, ApJ, 539, L13, astro-ph/0006289

Genzel R., Eisenhauer F., Gillessen S., 2010, Reviews of Modern Physics, 82, 3121

Gezari, S., Chornock, R., Rest, A., Huber, M. E., Forster, K., Berger, E., Challis, P. J., Neill, J. D., Martin, D. C., Heckman, T., Lawrence, A., Norman, C., Narayan, G., Foley, R. J., Marion, G. H., Scolnic, D., Chomiuk, L., Soderberg, A., Smith, K., Kirshner, R. P., Riess, A. G., Smartt, S. J., Stubbs, C. W., Tonry, J. L., Wood-Vasey, W. M., Burgett, W. S., Chambers, K. C., Grav, T., Heasley, J. N., Kaiser, N., Kudritzki, R.-P., Magnier, E. A., Morgan, J. S., and Price, P. A. (2012). An ultraviolet-optical flare from the tidal disruption of a helium-rich stellar core. Nature, 485:217–220.

Gezari S., 2012, in European Physical Journal Web of Conferences Vol. 39 of European Physical Journal Web of Conferences, Ultraviolet and optical observations of tidal disruption events. p. 3001

Gezari S., Basa S., Martin D. C., Bazin G., Forster K., Milliard B., Halpern J. P., Friedman P. G., Morrissey P., Neff S. G., Schiminovich D., Seibert M., Small T., Wyder T. K., 2008, ApJ, 676, 944

Gezari, S., Dessart, L., Basa, S., Martin, D. C., Neill, J. D., Woosley, S. E., Hillier, D. J., Bazin, G., Forster, K., Friedman, P. G., Le Du, J., Mazure, A., Morrissey, P., Neff, S. G., Schiminovich, D., and Wyder, T. K. (2008). Probing Shock Breakout with Serendipitous GALEX Detections of Two SNLS Type II-P Supernovae. ApJ, 683:L131–L134.

Gezari, S., Halpern, J. P., Komossa, S., Grupe, D., and Leighly, K. M. (2003). Follow-Up Hubble Space Telescope/Space Telescope Imaging Spectroscopy of Three Candidate Tidal Disruption Events. ApJ, 592:42–51.

Gezari, S., Heckman, T., Cenko, S. B., Eracleous, M., Forster, K., Gonçalves, T. S., Martin, D. C., Morrissey, P., Neff, S. G., Seibert, M., Schiminovich, D., and Wyder, T. K. (2009). Luminous Thermal Flares from Quiescent Supermassive Black Holes. ApJ, 698:1367–1379.

Gezari, S., Martin, D. C., Milliard, B., Basa, S., Halpern, J. P., Forster, K., Friedman, P. G., Morrissey, P., Neff, S. G., Schiminovich, D., Seibert, M., Small, T., and Wyder, T. K. (2006). Ultraviolet Detection of the Tidal Disruption of a Star by a Supermassive Black Hole. ApJ, 653:L25–L28.

Ghez A. M., Duchêne G., Matthews K., Hornstein S. D., Tanner A., Larkin J., Morris M., Becklin E. E., Salim S., Kremenek T., Thompson D., Soifer B. T., Neugebauer G., McLean I., 2003, ApJ, 586, L127

Ghez A. M., Salim S., Weinberg N. N., Lu J. R., Do T., Dunn J. K., Matthews K., Morris M. R., Yelda S., Becklin E. E., Kremenek T., Milosavljevic M., Naiman J., 2008, ApJ, 689, 1044

Gillessen S., Eisenhauer F., Trippe S., Alexander T., Genzel R., Martins F., Ott T., 2009, ApJ, 692, 1075

Gnedin O. Y., Ostriker J. P., Tremaine S., 2014, ApJ, 785, 71

Goldreich P., Keeley D. A., 1977, ApJ, 212, 243

Goldreich P., Soter S., 1966, ICARUS, 5, 375

Goldreich P., Kumar P., 1988, ApJ, 326, 462

Goldreich P., Murray N., Kumar P., 1994, ApJ, 424, 466

Goldreich P., Nicholson P. D., 1989, ApJ, 342, 1079

Goldstein, H. 1950, Classical mechanics

Gomes, R., Levison, H. F., Tsiganis, K., & Morbidelli, A. 2005, Nature, 435, 466

Gonczi G., 1982, A&A, 110, 1

Goodman J., 2003, MNRAS, 339, 937

Goodman J., Tan J. C., 2004, ApJ, 608, 108

Goodman J., Oh S. P., 1997, ApJ, 486, 403

Goodman J., Tan J. C., 2004, ApJ, 608, 108

Gomboc A., Čadež A., 2005, ApJ, 625, 278

Green P. J., Myers A. D., Barkhouse W. A., Mulchaey J. S., Bennert V. N., Cox T. J., Aldcroft T. L., 2010, ApJ, 710, 1578

Gualandris A., Merritt D., 2009, ApJ, 705, 361

Guillochon J., Ramirez-Ruiz E., 2012, ArXiv e-prints

Guillochon J., Loeb A., 2014, ArXiv e-prints

Guillochon J., Ramirez-Ruiz E., 2015, ArXiv e-prints

Haiman Z., Kocsis B., Menou K., Lippai Z., Frei Z., 2009, Classical and Quantum Gravity, 26, 094032

Hansen B. M. S., Milosavljević M., 2003, ApJ, 593, L77

Hansen, B. M. S. (2010). Calibration of Equilibrium Tide Theory for Extrasolar Planet Systems. ApJ, 723:285–299.

Hao, W., Kouwenhoven, M.B.N., Spurzem, R. 2013, MNRAS, 433, 867

Harrington, R. S. (1968). Dynamical evolution of triple stars. AJ, 73:190–194.

Harrington, R. S. (1969). The Stellar Three-Body Problem. *Celestial Mechanics*, 1:200–209.

Hawking S. W., 1966, ApJ, 145, 544

Hayasaki K., Mineshige S., Ho L. C., 2008, ApJ, 682, 1134

Hays, J. D., Imbrie, J., & Shackleton, N. J. 1976, Science, 194, 1121

Hébrard, G. et al. 2008, A&A, 488, 763, 0806.0719

Hébrard, G. et al. 2013, A&A, 549, A134, 1211.0810

Heggie, D. C., & Rasio, F. A. 1996, MNRAS, 282, 1064

Hellier, C., Anderson, D. R., Collier Cameron, A., Gillon, M., Hebb, L., Maxted, P. F. L., Queloz, D., Smalley, B., Triaud, A. H. M. J., West, R. G., Wilson, D. M., Bentley, S. J., Enoch, B., Horne, K., Irwin, J., Lister, T. A., Mayor, M., Parley, N., Pepe, F., Pollacco, D. L., Segransan, D., Udry, S., and Wheatley, P. J. (2009). An orbital period of 0.94days for the hot-Jupiter planet WASP-18b. Nature, 460:1098–1100.

Henrard, J., & Murigande, C. 1987, Celestial Mechanics, 40, 345

Henrard, J., & Morbidelli, A. 1993, Physica D Nonlinear Phenomena, 68, 187

Hester, J. J., Desch, S. J., Healy, K. R., & Leshin, L. A. 2004, Science, 304, 1116

Hillenbrand L. A., & Hartmann L. W., 1998, ApJ, 492, 540

Hills, J. G. 1988, Nature, 331, 687

Hirano, T. et al. 2012, ApJ, 759, L36, 1209.4362

Ho W. C. G., Lai D., 1999, MNRAS, 308, 153

Ho, S., & Turner, E. L. 2011, ApJ, 739, 26, 1003.4738

Holman, M., Touma, J., and Tremaine, S. (1997). Chaotic variations in the eccentricity of the planet orbiting 16 Cygni B. Nature, 386:254–256.

Holoien T. W.-S., Prieto J. L., Bersier D., Kochanek C. S., Stanek K. Z., Shappee B. J., Grupe D., Basu U., Beacom J. F., Brimacombe J., Brown J. S., Davis A. B., Jencson J., Pojmanski G., Szczygieł D. M., 2014, MNRAS, 445, 3263

Hopkins P. F., Somerville R. S., Hernquist L., Cox T. J., Robertson B., Li Y., 2006, ApJ, 652, 864

Huang, S.-S. 1959, PASP, 71, 421

Huber, D. et al. 2013, Science, 342, 331, 1310.4503

Hut, P. (1981). Tidal evolution in close binary systems. A&A, 99:126–140.

Imbrie, J. 1982, Icarus, 50, 408

Innanen, K. A., Zheng, J. Q., Mikkola, S., & Valtonen, M. J. 1997, AJ, 113, 1915

Ivanov P. B., Papaloizou J. C. B., 2004a, MNRAS, 353, 1161

Ivanov P. B., Papaloizou J. C. B., 2004b, MNRAS, 347, 437

Ivanov P. B., Polnarev A. G., Saha P., 2005, MNRAS, 358, 1361

Ivanov P. B., Chernyakova M. A., 2006, A&A, 448, 843

Ivanov P. B., Papaloizou J. C. B., 2007, MNRAS, 376, 682

Ivanov P. B., Papaloizou J. C. B., 2011, Celestial Mechanics and Dynamical Astronomy, 111, 51

Ivanov, P. B., Polnarev, A. G., and Saha, P. (2005). The tidal disruption rate in dense galactic cusps containing a supermassive binary black hole. MNRAS, 358:1361–1378.

Ivanova, N., Chaichenets, S., Fregeau, J., Heinke, C. O., Lombardi, Jr., J. C., & Woods, T. E. 2010, ApJ, 717, 948, 1001.1767

Jenkins, G. S. 2000, J. Geophys. Res., 105, 7357

Jewitt, D. J. 2001, ApJ, 123, 1039

Johnson, J. A. et al. 2007, ApJ, 665, 785, 0704.2455

Kaib, N. A., Raymond, S. N., & Duncan, M. J. 2011, ApJ, 742, L24, 1110.5911

Kaib, N. A., Roskar, R., & Quinn, T. 2011, Icarus, 215, 491

Karas V., Šubr L., 2001, A&A, 376, 686

Kasting, J. F., Whitmire, D. P., & Reynolds, R. T. 1993, ICARUS, 101, 108

Katz, B. and Dong, S. (2012). The rate of WD-WD head-on collisions may be as high as the SNe Ia rate. *ArXiv e-prints*.

Katz, B., Dong, S., and Malhotra, R. (2011). Long-Term Cycling of Kozai-Lidov Cycles: Extreme Eccentricities and Inclinations Excited by a Distant Eccentric Perturber. *Physical Review Letters*, 107(18):181101.

Kenyon, S. J., & Bromley, B. C. 2004, Nature, 432, 598

King A. R., Pringle J. E., Livio M., 2007, MNRAS, 376, 1740

Kipping, D. M., Forgan, D., Hartman, J., Nesvorny, D., Bakos, G. Á., Schmitt, A. R., & Buchhave, L. A. 2013a, ArXiv e-prints, 1306.1530

Kipping, D. M., Hartman, J., Buchhave, L. A., Schmitt, A. R., Bakos, G. Á., & Nesvorný, D. 2013b, ApJ, 770, 101, 1301.1853

Kiseleva, L. G., Eggleton, P. P., and Mikkola, S. (1998). Tidal friction in triple stars. MNRAS, 300:292–302.

Kochanek C. S., 1992, ApJ, 385, 604

Kocsis B., Frei Z., Haiman Z., Menou K., 2006, ApJ, 637, 27

Kocsis B., Loeb A., 2008, Physical Review Letters, 101, 041101

Kocsis B., Tremaine S., 2011, MNRAS, 412, 187

Kocsis, B. and Levin, J. (2012). Repeated bursts from relativistic scattering of compact objects in galactic nuclei. Phys. Rev. D, 85(12):123005.

Kocsis B., Tremaine S., 2014, ArXiv e-prints

Komossa, S. and Greiner, J. (1999). Discovery of a giant and luminous X-ray outburst from the optically inactive galaxy pair RX J1242.6-1119. A&A, 349:L45–L48.

Komossa S., Burwitz V., Hasinger G., Predehl P., Kaastra J. S., Ikebe Y., 2003, ApJ, 582, L15

Kormendy J., Ho L. C., 2013, ArXiv e-prints

Kosovichev A. G., Novikov I. D., 1992, MNRAS, 258, 715

Koss M., Mushotzky R., Treister E., Veilleux S., Vasudevan R., Miller N., Sanders D. B., Schawinski K., Trippe M., 2011, ApJ, 735, L42

Kostić U., Čadež A., Calvani M., Gomboc A., 2009, A&A, 496, 307

Kozai, Y. (1962). Secular perturbations of asteroids with high inclination and eccentricity. AJ, 67:591.

Kratter, K. M., & Perets, H. B. 2012, ApJ, 753, 91, 1204.2014

Krolik J. H., 2010, ApJ, 709, 774

Kroupa, P., Aarseth, S., & Hurley, J. 2001, MNRAS, 321, 699

Kumar P., Goodman J., 1996, ApJ, 466, 946

Lada, C. J., & Lada, E. A. 2003, ARA&A, 41, 57

Lai D., 1997, ApJ, 490, 847

Lai, D., Foucart, F., & Lin, D. N. C. 2010, ArXiv e-prints, 1008.3148

Lai D., Wu Y., 2006, Phys. Rev. D, 74, 024007

Lamers, H.J.G.L.M., Gieles, M., & Portegies Zwart, S. F. 2005, A&A, 429, 173

Laskar, J. 1989, Nature, 338, 237

——. 1990, Icarus, 88, 266

Laskar, J., & Robutel, P. 1993, Nature, 361, 608

Laskar, J., Joutel, F., & Robutel, P. 1993, Nature, 361, 615

——. 1996, Celestial Mechanics and Dynamical Astronomy, 64, 115

Laskar, J., Correia, A. C. M., Gastineau, M., Joutel, F., Levrard, B., & Robutel, P. 2004, Icarus, 170, 343

Laskar, J., & Gastineau, M. 2009, Nature, 459, 817

Laskar, J. 2013, Progress in Mathematical Physics, 66, 239

Latham, D. W., Stefanik, R. P., Mazeh, T., Mayor, M., & Burki, G. 1989, Nature, 339, 38

Laughlin, G., & Adams, F. C. 2000, Icarus, 145, 614

Lee, M. H. and Peale, S. J. (2003). Secular Evolution of Hierarchical Planetary Systems. ApJ, 592:1201–1216.

Levan A. J., Tanvir N. R., Cenko S. B., et al. 2011, Science, 333, 199

Le Verrier, U.-J. 1855, Annales de l'Observatoire de Paris, 1, 258

Levin Y., 2007, MNRAS, 374, 515

Levison, H. F., & Morbidelli, A. 2007, Icarus, 189, 196

Levison, H. F., Morbidelli, A., Van Laerhoven, C., Gomes, R., & Tsiganis, K. 2008, Icarus, 196, 258, 0712.0553

Levison, H. F., Morbidelli, A., Tsiganis, K., Nesvorný, D., & Gomes, R. 2011, AJ, 142, 152

Li S., Liu F. K., Berczik P., Chen X., Spurzem R., 2012, ApJ, 748, 65

Li, G., Kocsis, B. & Loeb, A. 2012, MNRAS, 425, 2407, 2012

Li, G., & Loeb, A. 2013, MNRAS, 429, 3040, 1209.1104

Li, G., & Batygin, K. 2014, ApJ, 790, 67

Li, G., & Batygin, K. 2014, ApJ, 795, 69

Li G., Naoz S., Kocsis B., Loeb A., 2014a, ApJ, 785, 116

Li, G., Naoz, S., Holman, M., & Loeb, A. 2014b, 791, 86, 2014

Li, G., Naoz, S., Valsecchi, F., Johnson, J. A., & Rasio, F. A. 2014, ApJ, 794, 131, 1407.2249

Li, G., & Adams, F. C. 2015, MNRAS, 448, 344, 1501.00911

Li G., Naoz S., Kocsis B., Loeb A., 2015, arXiv: 1502, 03825

Li S., Liu F. K., Berczik P., Chen X., Spurzem R., 2012, ArXiv e-prints

Lidov, M. L. (1962). The evolution of orbits of artificial satellites of planets under the action of gravitational perturbations of external bodies. Planet. Space Sci., 9:719–759.

Lidov, M. L. and Ziglin, S. L. (1974). The Analysis of Restricted Circular Twice-averaged Three Body Problem in the Case of Close Orbits. *Celestial Mechanics*, 9:151–173.

Lichtenberg, A. J., & Lieberman, M. A. 1983, Regular and stochastic motion

Lichtenberg, A. & Lieberman, M. 1992, Regular and Chaotic Dynamics, Applied Mathematical Sciences (New York: Springer)

Lightman A. P., Shapiro S. L., 1977, ApJ, 211, 244

Lillo-Box, J. et al. 2014, A&A, 562, A109, 1312.3943

Lin, D. N. C. and Papaloizou, J. (1986). On the tidal interaction between protoplanets and the protoplanetary disk. III - Orbital migration of protoplanets. ApJ, 309:846–857.

Lippai Z., Frei Z., Haiman Z., 2008, ApJ, 676, L5

Lissauer, J. J. et al. 2011, ApJS, 197, 8, 1102.0543

Lissauer, J. J., Barnes, J. W., & Chambers, J. E. 2012, Icarus, 217, 77

Lithwick, Y. and Naoz, S. (2011). The Eccentric Kozai Mechanism for a Test Particle. ApJ, 742:94.

Liu X., Greene J. E., Shen Y., Strauss M. A., 2010a, ApJ, 715, L30

Liu X., Shen Y., Strauss M. A., Greene J. E., 2010b, ApJ, 708, 427

Löckmann U., Baumgardt H., 2008, MNRAS, 384, 323

Luminet J.-P., Marck J.-A., 1985, MNRAS, 212, 57

MacFadyen A. I., Milosavljević M., 2008, ApJ, 672, 83

Madau P., Rees M. J., 2001, ApJ, 551, L27

Magorrian J., Tremaine S., 1999, MNRAS, 309, 447

Maillard J. P., Paumard T., Stolovy S. R., Rigaut F., 2004, A&A, 423, 155

Maksym W. P., 2012, in European Physical Journal Web of Conferences Vol. 39 of European Physical Journal Web of Conferences, Tidal flares and rates from an archival cluster survey. p. 5002

Malmberg, D., Davies, M. B., Heggie, D. C. 2011, MNRAS, 411, 859

Malmberg, D., de Angeli, F., Davies, M. B., Church, R. P., Mackey, D., & Wilkinson, M. I. 2007, MNRAS, 378, 1207

Marcy, G. W., Butler, R. P., Williams, E., Bildsten, L., Graham, J. R., Ghez, A. M., & Jernigan, J. G. 1997, ApJ, 481, 926

Mardling R. A., 1995a, ApJ, 450, 722

Mardling R. A., 1995b, ApJ, 450, 732

Mardling, R. A. 2010, MNRAS, 407, 1048, 1001.4079

Martins F., Gillessen S., Eisenhauer F., Genzel R., Ott T., Trippe S., 2008, ApJ, 672, L119

Masset, F., & Snellgrove, M. 2001, MNRAS, 320, L55, astro-ph/0003421

Masset, F. S., & Papaloizou, J. C. B. 2003, ApJ, 588, 494, arXiv:astro-ph/0301171

Mastrobuono-Battisti A., Perets H. B., Loeb A., 2014, ApJ, 796, 40

Matsumura, S., Peale, S. J., and Rasio, F. A. (2010). Tidal Evolution of Close-in Planets. ApJ, 725:1995–2016.

Mayor, M., & Queloz, D. 1995, Nature, 378, 355

Mazeh, T. and Shaham, J. (1979). The orbital evolution of close triple systems - The binary eccentricity. A&A, 77:145–151.

McGurk R. C., Max C. E., Rosario D. J., Shields G. A., Smith K. L., Wright S. A., 2011, ApJ, 738, L2

McKernan B., Ford K. E. S., Kocsis B., Lyra W., Winter L. M., 2014, MNRAS, 441, 900

McKernan B., Ford K. E. S., Lyra W., Perets H. B., 2012, MNRAS, 425, 460

Meibom S., Mathieu R. D., 2005, ApJ, 620, 970

Merritt D., Alexander T., Mikkola S., Will C. M., 2010, Phys. Rev. D, 81, 062002

Merritt D., Gualandris A., Mikkola S., 2009, ApJ, 693, L35

Merritt D., Poon M. Y., 2004, ApJ, 606, 788

Merritt D., Vasiliev E., 2012, Phys. Rev. D, 86, 102002

Meyer L., Ghez A. M., Schoedel R., Yelda S., Boehle A., Lu J. R., Do T., Morris M. R., Becklin E. E., Matthews K., 2012, submitted to Science

Miller, M. C. and Hamilton, D. P. (2002). Four-Body Effects in Globular Cluster Black Hole Coalescence. ApJ, 576:894–898.

Milosavljević M., Phinney E. S., 2005, ApJ, 622, L93

Miralda-Escudé J., Kollmeier J. A., 2005, ApJ, 619, 30

Morbidelli, A. 2002, Modern celestial mechanics : aspects of solar system dynamics

Morbidelli, A., Levison, H. F., Tsiganis, K., & Gomes, R. 2005, Nature, 435, 462

Morbidelli, A., Tsiganis, K., Crida, A., Levison, H. F., & Gomes, R. 2007, AJ, 134, 1790, 0706.1713

Morbidelli, A., Brasser, R., Tsiganis, K., Gomes, R., & Levison, H. F. 2009, A&A, 507, 1041

Morton, T. D., & Johnson, J. A. 2011, ApJ, 729, 138, 1010.4025

Moutou, C. et al. 2011, A&A, 533, A113, 1105.3849

Murray, C. D., & Dermott, S. F. 1999, Solar System Dynamics (Cambridge: Cambridge Univ. Press)

Miralda-Escudé J., Gould A., 2000, ApJ, 545, 847

Morris M., 1993, ApJ, 408, 496

Murray, N. W., Lieberman, M. A., & Lichtenberg, A. J. 1985, Phys. Rev. A, 32, 2413

Murray, N., & Holman, M. 1997, AJ, 114, 1246

Murray-Clay R. A., Loeb A., 2011, ArXiv e-prints

Nagasawa, M., Ida, S., & Bessho, T. 2008, ApJ, 678, 498, 0801.1368

Nagasawa, M. and Ida, S. (2011). Orbital Distributions of Close-in Planets and Distant Planets Formed by Scattering and Dynamical Tides. ApJ, 742:72.

Nakamura, T., & Tajika, E. 2003, Geophys. Res. Lett., 30, 1685

Naoz, S., Farr, W. M., Lithwick, Y., Rasio, F. A., and Teyssandier, J. (2011). Hot Jupiters from secular planet-planet interactions. Nature, 473:187–189.

Naoz, S., Farr, W. M., Lithwick, Y., Rasio, F. A., and Teyssandier, J. (2013a). Secular dynamics in hierarchical three-body systems. MNRAS, 431:2155–2171.

Naoz, S., Farr, W. M., and Rasio, F. A. (2012). On the Formation of Hot Jupiters in Stellar Binaries. ApJ, 754:L36.

Naoz, S., Kocsis, B., Loeb, A., and Yunes, N. (2013b). Resonant Post-Newtonian Eccentricity Excitation in Hierarchical Three-body Systems. ApJ, 773:187.

Naoz S., Silk J., 2014, ApJ, 795, 102

Naoz S., Fabrycky D. C., 2014, ApJ, 793, 137

Neron de Surgy, O., & Laskar, J. 1997, A&A, 318, 975

Nesvorný, D., Vokrouhlický, D., & Morbidelli, A. 2007, AJ, 133, 1962

Nesvorný, D. 2011, ApJ, 742, L22, 1109.2949

Nesvorný, D., & Morbidelli, A. 2012, AJ, 144, 117

Noble S. C., Mundim B. C., Nakano H., Krolik J. H., Campanelli M., Zlochower Y., Yunes N., 2012, ArXiv e-prints

Nordhaus, J., Spiegel, D. S., Ibgui, L., Goodman, J., & Burrows, A. 2010, MNRAS, 408, 631, 1002.2216

Novikov I. D., Thorne K. S., 1973, in Black Holes (Les Astres Occlus), C. Dewitt & B. S. Dewitt, ed., pp. 343–450

Novikov I. D., Pethick C. J., Polnarev A. G., 1992, MNRAS, 255, 276

Ogilvie G. I., Lesur G., 2012, ArXiv e-prints

O'Leary, R. M., Kocsis, B., and Loeb, A. (2009). Gravitational waves from scattering of stellar-mass black holes in galactic nuclei. MNRAS, 395:2127–2146.

O'Neill S. M., Miller M. C., Bogdanović T., Reynolds C. S., Schnittman J. D., 2009, ApJ, 700, 859

Oort, J. 1950, Bull. Astron. Inst. Neth., 11, 91

Pacucci, F., Ferrara, A., & D'Onghia, E. 2013, ApJL, 778, L42

Paczyński, B. 1971, ARA&A, 9, 183

Parker, R. J., & Quanz, S. P. 2012, MNRAS, 419, 2448

Paxton B., Bildsten L., Dotter A., Herwig F., Lesaffre P., Timmes F., 2011, ApJS, 192, 3

Paxton, B. et al. 2013, ApJS, 208, 4, 1301.0319

Penev K., Sasselov D., Robinson F., Demarque P., 2009, ApJ, 704, 930

Perets H. B., Hopman C., Alexander T., 2007, ApJ, 656, 709

Peters P. C., 1964, Physical Review, 136, 1224

Petrovich C., 2015, ApJ, 799, 27

Perets, H. B. and Fabrycky, D. C. (2009). On the Triple Origin of Blue Stragglers. ApJ, 697:1048–1056.

Perets H. B., Gualandris A., 2010, ApJ, 719, 220

Pfalzner, S. 2013, A&A, 549, 82

Phinney E. S., 2009, in ArXiv Astrophysics e-prints, Vol. 2010, astro2010: The Astronomy and Astrophysics Decadal Survey, p. 235

Picogna, G., & Marzari, F. 2014, A&A, 564, 28

Pierens, A., & Nelson, R. P. 2008, A&A, 482, 333, 0802.2033

Podsiadlowski P., 1996, MNRAS, 279, 1104

Pollack, J. B., & Toon, O. B. 1982, Icarus, 50, 259

Porras, A., et al. 2003, AJ, 126, 1916

Portegies Zwart, S. F. 2009, ApJL, 696, L13

Portegies Zwart S. F., Baumgardt H., McMillan S. L. W., Makino J., Hut P., Ebisuzaki T., 2006, ApJ, 641, 319

Portegies Zwart S. F., McMillan S. L. W., 2002, ApJ, 576, 899

Press W. H., Teukolsky S. A., 1977, ApJ, 213, 183

Press, W. H., Flannery, B. P., Teulkolsky, S. A., & Vetterling, W. T. 1986, Numerical Recipes: The art of scientific computing (Cambridge: Cambridge Univ. Press)

Proszkow, E. M., & Adams, F. C. 2009, ApJS, 185, 486

Rafikov, R. R. 2006, ApJ, 648, 666, astro-ph/0405507

Ramírez, I., Bajkova, A. T., Bobylev, V. V., Roederer, I. U., Lambert, D. L., Endl, M., Cochran, W. D., MacQueen, P. J., & Wittenmyer, R. A 2014, ApJ, 787, 154

Rasio, F. A., & Ford, E. B. 1996, Science, 274, 954

Rauch K. P., Tremaine S., 1996, Nature, 1, 149

Rees M. J., 1988, Nature, 333, 523

Reid M. J., Brunthaler A., 2004, ApJ, 616, 872

Roberts, M. 1957, PASP, 69, 406

Robertson B., Bullock J. S., Cox T. J., Di Matteo T., Hernquist L., Springel V., Yoshida N., 2006, ApJ, 645, 986

Rodriguez C., Taylor G. B., Zavala R. T., Peck A. B., Pollack L. K., Romani R. W., 2006, ApJ, 646, 49

Rogers, T. M., Lin, D. N. C., & Lau, H. H. B. 2012, ApJ, 758, L6, 1209.2435

Rogers, T. M., Lin, D. N. C., McElwaine, J. N., & Lau, H. H. B. 2013, ApJ, 772, 21, 1306.3262

Rossi E. M., Lodato G., Armitage P. J., Pringle J. E., King A. R., 2010, MNRAS, 401, 2021

Samsing J., 2014, ArXiv e-prints

Sanchis-Ojeda, R. et al. 2012, Nature, 487, 449, 1207.5804

Sato, B. et al. 2008, PASJ, 60, 1317, 0807.0268

Schlaufman, K. C., & Winn, J. N. 2013, ApJ, 772, 143, 1306.0567

Schnittman J. D., 2010, ApJ, 724, 39

—, 2011, Classical and Quantum Gravity, 28, 094021

Schnittman J. D., Krolik J. H., 2008, ApJ, 684, 835

Schödel R., Eckart A., Iserlohe C., Genzel R., Ott T., 2005, ApJ, 625, L111

Seto N., Muto T., 2010, Phys. Rev. D, 81, 103004

Sesana A., Haardt F., Madau P., 2006, ApJ, 651, 392

Shapiro S. L., Teukolsky S. A., 1986, Black Holes, White Dwarfs and Neutron Stars: The Physics of Compact Objects

Shappee, B. J. and Thompson, T. A. (2013). The Mass-loss-induced Eccentric Kozai Mechanism: A New Channel for the Production of Close Compact Object-Stellar Binaries. ApJ, 766:64.

Shakura N. I., Sunyaev R. A., 1973, A&A, 24, 337

Shen Y., Liu X., Greene J. E., Strauss M. A., 2011, ApJ, 735, 48

Shields G. A., Bonning E. W., 2008, ApJ, 682, 758

Smith K. L., Shields G. A., Bonning E. W., McMullen C. C., Rosario D. J., Salviander S., 2010, ApJ, 716, 866

Soderhjelm, S. (1982). Studies of the stellar three-body problem. A&A, 107:54–60.

Soto, A., Mischna, M. A., & Richardson, M. I. 2012, in Lunar and Planetary Institute Science Conference Abstracts, Vol. 43, Lunar and Planetary Institute Science Conference Abstracts, 2783

Spalding, C., & Batygin, K. 2014, ApJ

Spiegel, D. S., Menou, K., & Scharf, C. A. 2009, ApJ, 691, 596, 0807.4180

Steffen, J. H., & Farr, W. M. 2013, ApJ, 774, L12, 1306.3526

Stone N., Loeb A., 2011a, MNRAS, 412, 75

Stone, N. and Loeb, A. (2012). Tidal disruption flares of stars from moderately recoiled black holes. MNRAS, 422:1933–1947.

Stone N. C., Metzger B. D., 2014, ArXiv e-prints

Spiegel, D. S., Menou, K., & Scharf, C. A. 2009, ApJ, 691, 596, 0807.4180

Spurzem, R., Giersz, M., Heggie, D. C., Lin, D.N.C. 2009, ApJ, 697, 458

Storch, N. I., & Lai, D. 2015, MNRAS, 448, 1821

Sussman, G. J., & Wisdom, J. 1992, Science, 257, 56

Swift, J. J., Johnson, J. A., Morton, T. D., Crepp, J. R., Montet, B. T., Fabrycky, D. C., & Muirhead, P. S. 2013, ApJ, 764, 105, 1301.0023

Takeda, G., Kita, R., & Rasio, F. A. 2008, ApJ, 683, 1063, 0802.4088

Tamayo, D., Burns, J. A., Hamilton, D. P., & Nicholson, P. D. 2013, AJ, 145, 54, 1212.0028

Tamayo, D. (2013). Consequences of an Eccentric Orbit for Fomalhaut b. *ArXiv e-prints*.

Tanaka T., Menou K., 2010, ApJ, 714, 404

Teitler, S., & Königl, A. 2014, ArXiv e-prints, 1403.5860

Teyssandier, J., Naoz, S., Lizarraga, I., and Rasio, F. (2013). Extreme orbital evolution from hierarchical secular coupling of two giant planets. *ArXiv e-prints*.

Thies, I., Kroupa, P., Goodwin, S. P., Stamatellos, D., and Whitworth, A. P. (2011). A natural formation scenario for misaligned and short-period eccentric extrasolar planets. MNRAS, 417:1817–1822.

Thomas, F. and Morbidelli, A. (1996). The Kozai Resonance in the Outer Solar System and the Dynamics of Long-Period Comets. *Celestial Mechanics and Dynamical Astronomy*, 64:209–229.

Thompson, T. A. (2011). Accelerating Compact Object Mergers in Triple Systems with the Kozai Resonance: A Mechanism for "Prompt" Type Ia Supernovae, Gamma-Ray Bursts, and Other Exotica. ApJ, 741:82.

Thompson, T. A. 2013, MNRAS, 431, 63

Toon, O. B., Pollack, J. B., Ward, W., Burns, J. A., & Bilski, K. 1980, Icarus, 44, 552

Touma, J., & Wisdom, J. 1993, Science, 259, 1294

——. 1998, AJ, 115, 1653

Tremaine S., Gebhardt K., Bender R., Bower G., Dressler A., Faber S. M., Filippenko A. V., Green R., Grillmair C., Ho L. C., Kormendy J., Lauer T. R., Magorrian J., Pinkney J., Richstone D., 2002, ApJ, 574, 740

Tremaine S., 2005, ApJ, 625, 143

Tremaine, S., Touma, J., & Namouni, F. 2009, AJ, 137, 3706, 0809.0237

Tremaine, S. 2011, in IAC Talks, Astronomy and Astrophysics Seminars from the Instituto de Astrofísica de Canarias, 227

Triaud, A. H. M. J. et al. 2010, A&A, 524, A25+, 1008.2353

Trilling, D. E., Benz, W., Guillot, T., Lunine, J. I., Hubbard, W. B., & Burrows, A. 1998, ApJ, 500, 428, arXiv:astro-ph/9801292

Tsiganis, K., Gomes, R., Morbidelli, A., & Levison, H. F. 2005, Nature, 435, 459

Valluri, M., Merritt, D., & Emsellem, E. 2004, ApJ, 602, 66, astro-ph/0210379

Valsecchi, F., Farr, W. M., Willems, B., Deloye, C. J., & Kalogera, V. 2012, ApJ, 745, 137, 1105.4837

Valsecchi, F., & Rasio, F. A. 2014a, ArXiv e-prints, 1403.1870

——. 2014b, ArXiv e-prints, 1402.3857

van Velzen, S., Farrar, G. R., Gezari, S., Morrell, N., Zaritsky, D., Östman, L., Smith, M., Gelfand, J., and Drake, A. J. (2011). Optical Discovery of Probable Stellar Tidal Disruption Flares. ApJ, 741:73.

Van Eylen, V. et al. 2014, ApJ, 782, 14, 1312.4938

van Velzen S., Farrar G. R., 2014, ApJ, 792, 53

Veras, D. and Ford, E. B. (2010). Secular Orbital Dynamics of Hierarchical Two-planet Systems. ApJ, 715:803–822.

Veras, D., Hadjidemetriou, J. D., & Tout, C. A. 2013, MNRAS, 435, 2416, 1308.0599

Verbunt F., Phinney E. S., 1995, A&A, 296, 709

Vernekar, A. D. 1972, in Atmospheric Radiation, 228

Wang J., Merritt D., 2004, ApJ, 600, 149

Ward, W. R. 1973, Science, 181, 260

Weertman, J. 1976, Nature, 261, 17

Wegg, C. and Bode, N. (2011). Multiple Tidal Disruptions as an Indicator of Binary Supermassive Black Hole Systems. ApJ, 738:L8.

Weinberg S., 1972, Gravitation and Cosmology: Principles and Applications of the General Theory of Relativity, Weinberg, S., ed.

Weinberg N. N., Quataert E., 2008, MNRAS, 387, L64

Weinberg N. N., Arras P., Quataert E., Burkart J., 2012, ApJ, 751, 136

Wen, L. (2003). On the Eccentricity Distribution of Coalescing Black Hole Binaries Driven by the Kozai Mechanism in Globular Clusters. ApJ, 598:419–430.

Whitmore, B. C., Chandar, R., & Fall, S. M. 2007, AJ, 133, 1067

Will C. M., 2008, ApJ, 674, L25

Williams, D. M., & Kasting, J. F. 1997, Icarus, 129, 254

Williams, J. P. 2010, ConPhy, 51, 381

Williams, J. P., & Gaidos, E. 2007, ApJ, 663, 33

Winn, J. N., Fabrycky, D., Albrecht, S., & Johnson, J. A. 2010, ApJ, 718, L145, 1006.4161

Winn, J. N., Howard, A. W., Johnson, J. A., Marcy, G. W., Isaacson, H., Shporer, A., Bakos, G. Á., Hartman, J. D., Holman, M. J., Albrecht, S., Crepp, J. R., and Morton, T. D. (2011). Orbital Orientations of Exoplanets: HAT-P-4b is Prograde and HAT-P-14b is Retrograde. AJ, 141:63.

Wolszczan, A., & Frail, D. A. 1992, Nature, 355, 145

Wu, Y. and Lithwick, Y. (2011). Secular Chaos and the Production of Hot Jupiters. ApJ, 735:109.

Wu, Y. and Murray, N. (2003). Planet Migration and Binary Companions: The Case of HD 80606b. ApJ, 589:605–614.

Wu, Y., & Lithwick, Y. 2011, ApJ, 735, 109, 1012.3475

Wu Y., Goldreich P., 2001, ApJ, 546, 469

Yu, Q. and Tremaine, S. (2001). Resonant Capture by Inward-migrating Planets. AJ, 121:1736–1740.

Yu Q., Tremaine S., 2003, ApJ, 599, 1129

Yu Q., Lu Y., Lin D. N. C., 2007, ApJ, 666, 919

Yu Q., 2010, in Dynamics from the Galactic Center to the Milky Way Halo Limits on a black hole companion to SgrA*

Zahn J. P., 1966, Annales d'Astrophysique, 29, 489

Zahn J.-P., 1989, A&A, 220, 112

Zahn J.-P., Bouchet L., 1989, A&A, 223, 112

Zauderer B. A., Berger E., Soderberg A. M., et al. 2011, Nature, 476, 425